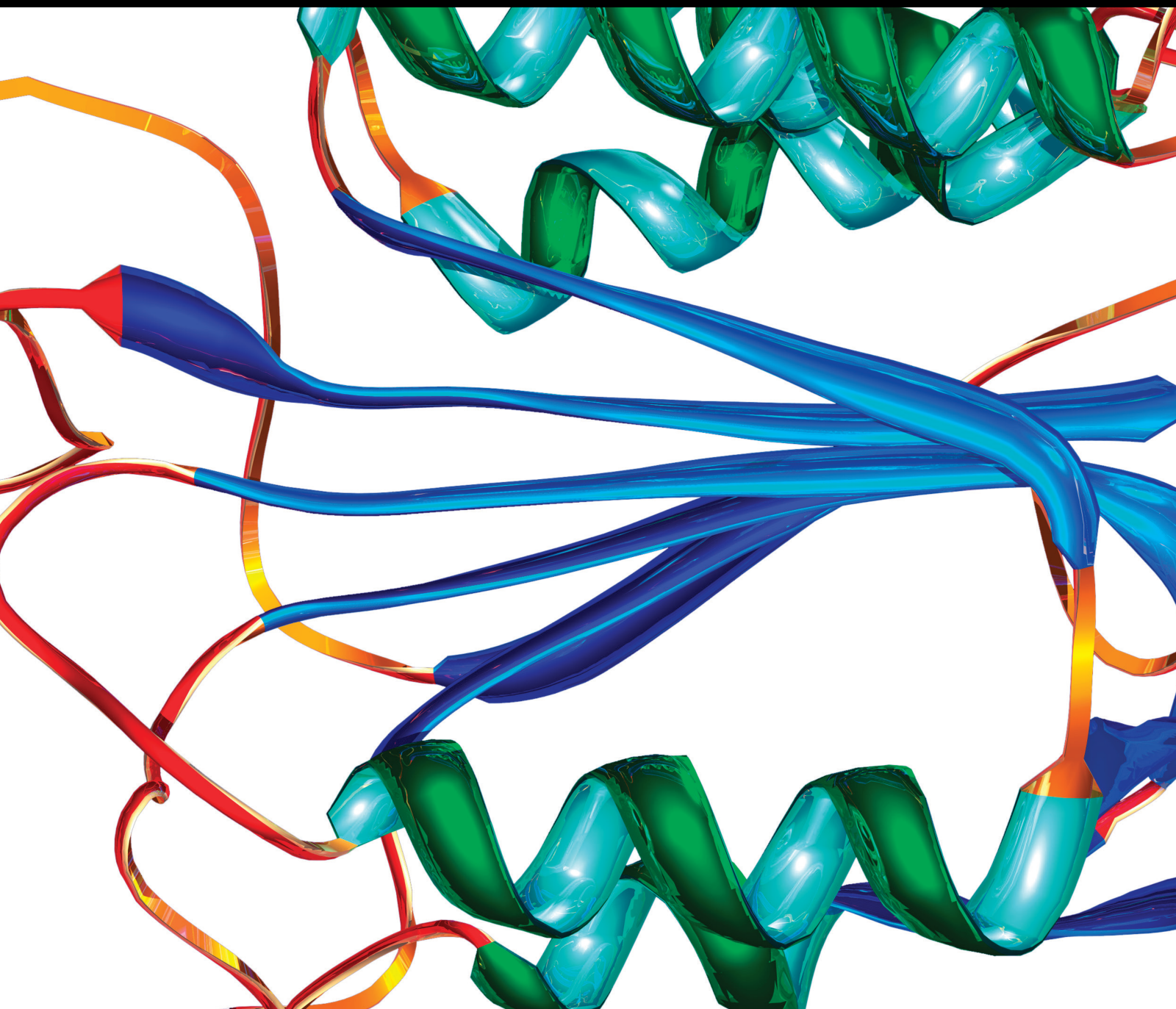# Neuroimaging Biomarkers for Chronic Diseases

Lead Guest Editor: Yi Shao
Guest Editors: Dai Xi-jian, Ting Su, and Wensi Tao

Neuroimaging Biomarkers for Chronic Diseases

Neuroimaging Biomarkers for Chronic Diseases

Lead Guest Editor: Yi Shao
Guest Editors: Dai Xi-jian, Ting Su, and Wensi Tao

Chief Editor

Paola Gazzaniga, Italy

Alexander G. Mathioudakis, United Kingdom
Andrea Maugeri, Italy
Prasenjit Mitra, India
Ekansh Mittal, USA
Hiroshi Miyamoto, USA
Naoshad Muhammad, USA
Chiara Nicolazzo, Italy
Xing Niu, China
Dong Pan, USA
Dr.Krupakar Parthasarathy, India
Robert Pichler, Austria
Dimitri Poddighe, Kazakhstan
Roberta Rizzo, Italy
Maddalena Ruggieri, Italy
Tamal Sadhukhan, USA
Pier P. Sainaghi, Italy
Cristian Scheau, Romania
Jens-Christian Schewe, Germany
Alexandra Scholze, Denmark
Shabana, Pakistan
Anja Hviid Simonsen, Denmark
Eric A. Singer, USA
Daniele Sola, Italy
Timo Sorsa, Finland
Yaying Sun, China
Mohammad Tarique, USA
Jayaraman Tharmalingam, USA
Sowjanya Thatikonda, USA
Stamatios E. Theocharis, Greece
Tilman Todenhöfer, Germany
Anil Tomar, India
Alok Tripathi, India
Drenka Trivanović, Germany
Natacha Turck, Switzerland
Azizah Ugusman, Malaysia
Shailendra K. Verma, USA
Aristidis S. Veskoukis, Greece
Arianna Vignini, Italy
Jincheng Wang, Japan
Zhongqiu Xie, USA
Yuzhen Xu, China
Zhijie Xu, China
Guan-Jun Yang, China
Yan Yang, USA

Chengwu Zeng, China
Jun Zhang Zhang, USA
Qun Zhang, China
Changli Zhou, USA
Heng Zhou, China
Jian-Guo Zhou, China

Contents

Contents

Hindawi

Retraction

Retracted: Development and Validation of Diagnostic Models for Hand-Foot-and-Mouth Disease in Children

Disease Markers

This article has been retracted by Hindawi following an investigation undertaken by the publisher [1]. This investigation has uncovered evidence of one or more of the following indicators of systematic manipulation of the publication process:

(1) Discrepancies in scope

(2) Discrepancies in the description of the research reported

(3) Discrepancies between the availability of data and the research described

(4) Inappropriate citations

(5) Incoherent, meaningless and/or irrelevant content included in the article

(6) Peer-review manipulation

The presence of these indicators undermines our confidence in the integrity of the article's content and we cannot, therefore, vouch for its reliability. Please note that this notice is intended solely to alert readers that the content of this article is unreliable. We have not investigated whether authors were aware of or involved in the systematic manipulation of the publication process.

Wiley and Hindawi regrets that the usual quality checks did not identify these issues before publication and have since put additional measures in place to safeguard research integrity.

We wish to credit our own Research Integrity and Research Publishing teams and anonymous and named external researchers and research integrity experts for contributing to this investigation.

The corresponding author, as the representative of all authors, has been given the opportunity to register their agreement or disagreement to this retraction. We have kept a record of any response received.

References

[1] F. Zhuo, M. Yu, Q. Chen et al., "Development and Validation of Diagnostic Models for Hand-Foot-and-Mouth Disease in Children," *Disease Markers*, vol. 2021, Article ID 1923636, 9 pages, 2021.

Hindawi

Retraction

Retracted: Identification of Ferroptosis-Related Long Noncoding RNA and Construction of a Novel Prognostic Signature for Gastric Cancer

Disease Markers

This article has been retracted by Hindawi following an investigation undertaken by the publisher [1]. This investigation has uncovered evidence of one or more of the following indicators of systematic manipulation of the publication process:

(1) Discrepancies in scope

(2) Discrepancies in the description of the research reported

(3) Discrepancies between the availability of data and the research described

(4) Inappropriate citations

(5) Incoherent, meaningless and/or irrelevant content included in the article

(6) Peer-review manipulation

The presence of these indicators undermines our confidence in the integrity of the article's content and we cannot, therefore, vouch for its reliability. Please note that this notice is intended solely to alert readers that the content of this article is unreliable. We have not investigated whether authors were aware of or involved in the systematic manipulation of the publication process.

In addition, our investigation has also shown that one or more of the following human-subject reporting requirements has not been met in this article: ethical approval by an Institutional Review Board (IRB) committee or equivalent, patient/participant consent to participate, and/or agreement to publish patient/participant details (where relevant).

Wiley and Hindawi regrets that the usual quality checks did not identify these issues before publication and have since put additional measures in place to safeguard research integrity.

We wish to credit our own Research Integrity and Research Publishing teams and anonymous and named external researchers and research integrity experts for contributing to this investigation.

The corresponding author, as the representative of all authors, has been given the opportunity to register their agreement or disagreement to this retraction. We have kept a record of any response received.

References

[1] W. Chen, Z. Feng, J. Huang et al., "Identification of Ferroptosis-Related Long Noncoding RNA and Construction of a Novel Prognostic Signature for Gastric Cancer," *Disease Markers*, vol. 2021, Article ID 7724997, 2021.

Retraction

Retracted: Probiotic Supplement Preparation Relieves Test Anxiety by Regulating Intestinal Microbiota in College Students

Disease Markers

This article has been retracted by Hindawi following an investigation undertaken by the publisher [1]. This investigation has uncovered evidence of one or more of the following indicators of systematic manipulation of the publication process:

(1) Discrepancies in scope

(2) Discrepancies in the description of the research reported

(3) Discrepancies between the availability of data and the research described

(4) Inappropriate citations

(5) Incoherent, meaningless and/or irrelevant content included in the article

(6) Peer-review manipulation

The presence of these indicators undermines our confidence in the integrity of the article's content and we cannot, therefore, vouch for its reliability. Please note that this notice is intended solely to alert readers that the content of this article is unreliable. We have not investigated whether authors were aware of or involved in the systematic manipulation of the publication process.

Wiley and Hindawi regrets that the usual quality checks did not identify these issues before publication and have since put additional measures in place to safeguard research integrity.

We wish to credit our own Research Integrity and Research Publishing teams and anonymous and named external researchers and research integrity experts for contributing to this investigation.

The corresponding author, as the representative of all authors, has been given the opportunity to register their agreement or disagreement to this retraction. We have kept a record of any response received.

References

[1] Q. Qin, H. Liu, Y. Yang et al., "Probiotic Supplement Preparation Relieves Test Anxiety by Regulating Intestinal Microbiota in College Students," *Disease Markers*, vol. 2021, Article ID 5597401, 8 pages, 2021.

Research Article

Brain Functional Network Analysis of Patients with Primary Angle-Closure Glaucoma

Dan Liu,[1] **Junwei Gao,**[2] **Tao You,**[3] **Shenghong Li,**[2] **Fengqin Cai,**[2] **Chonggang Pei,**[4] **and Xianjun Zeng** [2]

[1]*Department of Radiology, Hubei Cancer Hospital, Tongji Medical College, Huazhong University of Science and Technology, Wuhan, 430079 Hubei Province, China*
[2]*Department of Radiology, The First Affiliated Hospital of Nanchang University, Nanchang, 330006 Jiangxi Province, China*
[3]*Department of Radiology, Chinese PLA General Hospital of Central Theater Command, Wuhan, 430070 Hubei Province, China*
[4]*Department of Ophthalmology, The First Affiliated Hospital of Nanchang University, Nanchang, 330006 Jiangxi Province, China*

Correspondence should be addressed to Xianjun Zeng; ndyfy00930@ncu.edu.cn

Dan Liu, Junwei Gao, and Tao You contributed equally to this work.

Objectives. Recent resting-state functional magnetic resonance imaging (fMRI) studies have focused on glaucoma-related neuronal degeneration in structural and spontaneous functional brain activity. However, there are limited studies regarding the differences in the topological organization of the functional brain network in patients with glaucoma. In this study, we aimed to assess both potential alterations and the network efficiency in the functional brain networks of patients with primary angle-closure glaucoma (PACG). *Methods.* We applied resting-state fMRI data to construct the functional connectivity network of 33 patients with PACG (54.21 ± 7.21 years) and 33 gender- and age-matched healthy controls (52.42 ± 7.80 years). The differences in the global and regional topological brain network properties between the two groups were assessed using graph theoretical analysis. Partial correlations between the altered regional values and clinical parameters were computed for patients with PACG. *Results.* No significant differences in global topological measures were identified between the two groups. However, significant regional alterations were identified in the patients with PACG, including differences within visual and nonvisual (somatomotor and cognition-emotion) regions. The normalized clustering coefficient and normalized local efficiency of the right superior parietal gyrus were significantly correlated with the retinal fiber layer thickness (RNFLT) and the vertical cup to disk ratio (V C/D). In addition, the normalized node betweenness of the left middle frontal gyrus (orbital portion) was significantly correlated with the V C/D in the patients with PACG. *Conclusions.* Our results suggest that regional inefficiency with decrease and compensatory increase in local functional properties of visual and nonvisual nodes preserved the brain network of the PACG at the global level.

1. Introduction

Glaucoma is an age-related, blindness-causing disease characterized by the progressive death of retinal ganglion cells (RGCs) in association with increased intraocular pressure (IOP). Glaucoma may be classified into primary open-angle glaucoma (POAG) and primary angle-closure glaucoma (PACG) according to the anatomy of the anterior chamber angle [1]. However, in China, PACG is still the most common type of glaucoma [2, 3]. Moreover, recent pathological data have demonstrated that neurodegenerative processes in the central nervous system of patients with glaucoma, such as apoptosis and reactive oxygen species production, were similar to the processes identified in Alzheimer's disease (AD) [4, 5], which suggests that glaucoma is a neurodegenerative disease. Therefore, potential alterations in the central nervous system of patients with PACG should receive greater emphasis.

Structural neuroimaging, including voxel-based morphometry (VBM) and diffusion tensor imaging (DTI), indicates an atrophic optic nerve (ON) and lateral geniculate body (LGN), damaged optic radiation (OR), and a thinning visual cortex in glaucoma patients [6–9]. Functional magnetic resonance imaging (fMRI) has demonstrated several forms of visual task-related deactivation in glaucoma [10], including decreased visual functional connectivity (FC) [11], decreased and/or increased amplitude of low-frequency fluctuations (ALFF) in the cuneus and occipital lobe/inferior temporal gyrus [12–14], and decreased regional homogeneity (ReHo) in the calcarine area [15]. In addition, structural and functional studies have indicated alterations in the extravisual system, such as the hippocampus [16], anterior thalamic radiation, superior longitudinal fascicle [17], and executive network [18]. However, these mentioned studies have primarily focused on regional alterations in structures and/or functions of the brain [6–18] and ignored alterations in the functional network architecture and information transfer which may indicate the changes of visual and nonvisual pathway in patients with PACG. Thus, there might need some other researches for a more comprehensive understanding of visual and extravisual processes changes of patients with PACG.

Recent graph theoretical developments have become increasingly popular for describing the structural and functional network maps of the human brain. The human brain is a complex and interconnected network characterized by efficient, coordinated, and integrated neuronal activities, with nodes that represent neurons and edges that represent internodal neural connections [19, 20]. The topological features have been well defined, such as small-worldness [21–23], global and local efficiency [24], and highly connected hubs [25], which contain node degree, node betweenness, and so on. The brain network features have been characterized in AD [26, 27], schizophrenia [28], multiple sclerosis [29], and other conditions. Moreover, several analyses have indicated that patients with PACG exhibit signs of changes in brain network properties that were identified in previous resting-state fMRI studies. For example, Cai et al. identified altered features of degree centrality (DC) at voxel levels in patients with PACG [30]. Based on the different patterns of functional connectivity between PACG and POAG patients, it is reasonable to question whether the topological properties of the whole brain network are also altered in patients with PACG.

We hypothesized that patients with PACG would exhibit significantly altered global network topological properties, such as small-worldness, global efficiency, or normalized clustering coefficients. The areas considered in the assessment of this hypothesis included 116 regions defined by the Automated Anatomical Labeling (AAL) atlas. The alterations in the brain network pattern were correlated with clinical parameters to investigate the potential relationship between network topological properties and clinical parameters. It may provide for PACG a unique opportunity to understand how the brain network topological organization changes in response to ocular hypertension and secondary neural degeneration.

2. Materials and Methods

2.1. Subjects. Thirty-three patients with PACG (13 M/20 F, mean age 54.21 ± 7.21 years) were recruited from the Department of Ophthalmology of the First Affiliated Hospital of Nanchang University. Thirty-three age- and gender-matched healthy controls were recruited through local advertisements. All subjects were right-handed and participated in this study after providing written informed consent. The study was conducted in accordance with the Declaration of Helsinki. The study protocol was approved by the Institutional Review Board of the First Affiliated Hospital of Nanchang University. All patients with PACG underwent a detailed ophthalmological examination, including gonioscopy, IOP assessment, fundoscopy, and standard automated perimetry.

The inclusion criteria for the patients with PACG were as follows: (1) narrow anterior chamber angle in one or both eyes, (2) characteristic optic disc damage (optic disc cupping or thinning), and (3) typical glaucomatous visual field loss (tubular vision or central island). The exclusion criteria for the patients were as follows: (1) secondary glaucoma or other ocular disorders; (2) neural-associated diseases, chronic pain, hypertension, diabetes, or a history of brain surgery; or (3) inability to attend MRI scanning because of metal implantation or a history of claustrophobia or other psychological disorders.

2.2. MRI Data Acquisition. All MRI data were collected on a 3.0 T (Trio Tim, Siemens, Erlangen, Germany) scanner using an 8-channel phased-array head coil. During the MRI scanning, each participant laid in the supine position, with the head in a neutral position and fixed comfortably by a belt and foam pads. All participants were required to relax, think of nothing in particular, remain awake, and keep their eyes closed. (1) The resting-state functional MRI (fMRI) data were acquired using a gradient-echo echo-planer imaging (EPI) sequence with the following parameters: repetition time (TR) = 2,000 ms, echo time (TE) = 40 ms, flip angle = 90°, slice thickness/gap = 4.0/1 mm, field of view (FOV) = 240 mm × 240 mm, in − plane resolution = 64 × 64, 30 axial slices that covered the whole brain, and 240 volumes acquired in 8 min. (2) The high-resolution brain structural images of each subject were acquired using a T1-weighted 3D MP-RAGE sequence as follows: TR = 1,900 ms, TE = 2.26 ms, flip angle = 9°, matrix = 256 × 256, FOV = 240 mm × 240 mm, thickness = 1.0 mm, and 176 sagittal slices.

2.3. MRI Data Preprocessing. The Data Processing Assistant for Resting-State fMRI (DPARSF, http://www.restfmri.net), which is based on Statistical Parametric Mapping (SPM8) (http://www.fil.ion.ucl.ac.uk) and the Resting-State Data Analysis Toolkit (REST, http://www.restfmri.net), was used for all fMRI data preprocessing. The first ten volumes of the resting-state fMRI data were discarded for each participant to remove potential effects of scanner instability and adjust for the surroundings. The remaining 230 volumes were corrected for slice timing. The resultant images were realigned to correct for small movements. In addition,

participants with head displacements that exceeded 3 mm in the cardinal directions (x, y, z) and $3°$ of rotation (x, y, z) were excluded. The T1-weighted structural images used for segmentation were coregistered to the corrected functional images for each individual and segmented into GM, WM, and CSF [31]. Based on the transformation matrix, the functional images were spatially normalized to standard Montreal Neurological Institute (MNI) space and subjected to nonlinear modulation to compensate for spatial normalization effects. All the standard MNI space functional images were smoothed with a 6 mm full-width at half maximum Gaussian kernel [32].

To further remove the effects of nuisance covariates, the signals from the white matter, cerebrospinal fluid, global signals from the entire brain, and six head realignment parameters used for rigid body head motion correction were removed from the data through linear regression [33]. Temporal filtering (0.01-0.1 Hz) of the time series was subsequently performed to remove very low-frequency drifts and physiological high-frequency noise.

2.4. Network Construction. A brain network may be considered as a graph, G (V, E), composed of vertex (V) and edge (E). The 116 brain regions from the AAL template [34] are the vertexes in the graph, and the Pearson coefficients of each region pair (e.g., the i-th region and the j-th region) represent the edges between two vertexes (wij). First, the time series of each node were extracted by averaging the time series of all voxels in the same nodal areas. Then, the Pearson correlation coefficients between the time series of each possible node pair were calculated. Thus, a functional correlation matrix was generated for each subject [35]. To improve the normality of the correlation coefficient, Fisher's r-to-z transformation was applied to the correlation matrices [36].

A previous study suggested that the brain network of each normal subject differs in both the number of significant edges and their weights [37]. Therefore, the threshold method was used to determine the available edges in the matrix and binarize the entire matrix. As there is no consensus in regard to the setting of functional-network-threshold to date, we employed a wide range of sparsity thresholds (range from 0.1 to 0.6, with step = 0.01) to analyse alterations in the topological properties of the brain network in the two groups. The minimum network sparseness can ensure that all nodes in the network are connected, and the maximum network sparseness can maintain the small-world attributes of the network.

2.5. Network Analysis. The network analysis toolbox, GRETNA (Version 1.0, http://www.nitrc.Org/projects/gretna/), running on a matrix laboratory platform (MATLAB R2010a; Natick, MA, USA), was used to estimate the topological properties of the networks [38]. Five small-world parameters and two efficiency parameters were used to assess the global topological organization of the functional brain networks in the PACG and HC groups. Four regional parameters were computed to characterize the properties of the 116 brain regions. Table 1 provides a brief description of

TABLE 1: Brief description of network properties in this study.

Global network properties.	
Clustering coefficient C_p	C_i is formed by a direct connection to the nearest neighbours of the node i, which measures the segregation of the network [39].
	The C_p of a network is the average of C_i over all nodes [39].
Characteristic path length L_p	L_p is the average of all of the shortest path lengths between two pairs of nodes, which may be regarded as a measurement of network integration [40].
Normalized clustering coefficient γ	γ is the average of C_p, which is further normalized by comparing to 1000 matched random networks [40].
Normalized characteristic path length λ	λ is the average of L_p, which is further normalized by comparing to 1000 matched random networks [40].
Small-worldness σ	σ is the ratio of γ to λ. The network topology may be considered to correspond to a "small world" if $\gamma > 1$, $\lambda \approx 1$, or if $\sigma > 1$ [39].
Global efficiency E_{glob}	E_{glob} and E_{loc} are the biologically sensible topological features of the brain networks, which describe the global and local efficiency of information transmission of the network [24].
Local efficiency E_{loc}	

Regional network properties	
Normalized degree, Deg (i)	Normalized Deg(i) is the mean Deg(i) of 1000 matched random networks. Deg(i) is the number of connections of node i that connect it to the rest of the network.
Normalized node betweenness, NB(i)	Normalized NB(i) is the mean NB(i) of 1000 matched random networks. NB(i) may be used to compute the effects node i that has over the stream of information between all other nodes in the network.
Normalized local efficiency $E_{loc}(i)$	Normalized $E_{loc}(i)$ is the mean $E_{loc}(i)$ of 1000 matched random networks. $E_{loc}(i)$ is defined as the inverse of the average shortest path length between node i and all other nodes. This variable is a measure of information transfer from node i to all other nodes of a network [41].
Normalized clustering coefficient $\gamma(i)$	$\gamma(i)$ is the mean γ of 1000 matched random networks.

the network properties, and Supplementary Materials 1 provides the definitions and calculations.

2.6. Statistical Analysis. Differences in the global (C_p, L_p, λ, γ, σ, E_{glob}, and E_{loc}) and regional (normalized Deg(i), NB(i),

$E_{loc}(i)$, and $\gamma(i)$) topological parameters between the PACG and HC groups were examined in MATLAB. The network measure data basically complied with the normality which were tested by using SPSS to apply the Kolmogorov-Smirnov test. Regional differences were also identified at a minimum sparsity of 0.32, which maintains the integrity of functional networks, whereas D_{max} was set at 0.42 to ensure the small-worldness of the two groups. As a result, differences in the global network properties and regional network properties between the PACG and HC groups were compared using a two-sample t-test (false discovery rate (FDR), $p < 0.05$) over the small-world network sparsity threshold (from 0.32 to 0.42). We ultimately correlated the regional values of the altered regions in the patients with PACG with the RNFL, V C/D, and IOP at a minimum sparsity of 0.32. SPSS v.17.0 was used for this analysis.

3. Results

3.1. Participant Characteristics. The demographic information of the patients with PACG and controls is listed in Table 2. There was no significant difference in age and gender between the 33 PACG group and 33 HC group ($p < 0.05$).

3.2. Global Network Property Changes. The global functional network properties and two efficiency parameters in the two groups are presented in Figure 1. The networks of both the PACG and HC groups exhibited small-world characteristics ($\gamma > 1$, $\lambda \approx 1$, or $\sigma > 1$) at all network sparsities (0.1-0.6).

Over the sparsity range of 0.32 to 0.42, the functional brain networks in the PACG group exhibited a slightly lower clustering coefficient ($p = 0.904 \sim 0.999$) and normalized clustering coefficient ($p = 0.283 \sim 0.453$), similar characteristic path length ($p = 0.545 \sim 0.996$) and normalized characteristic path length ($p = 0.463 \sim 0.993$), and slightly lower small-worldness ($p = 0.322 \sim 0.548$) compared with the HCs. No statistically significant differences were identified in these regards ($p > 0.05$) (Figure 2). Moreover, the PACG group exhibited a similar mean local efficiency and whole brain global efficiency compared with the HC group.

3.3. Regional Network Property Changes. The differences in the regional normalized clustering coefficients and local efficiencies between the two groups are presented in Figure 3 at a sparsity threshold of 0.32. Compared with the HC group, a decreased normalized clustering coefficient and local efficiency were identified in the dorsal visual pathway brain regions (right superior parietal gyrus and right angular gyrus) and nonvisual pathway brain regions (right postcentral gyrus and right supramarginal gyrus) in the PACG group. In contrast, these metrics were increased in the left superior frontal gyrus (orbital portion).

The difference in the regional normalized node degree between the two groups is presented in Figure 4 at a sparsity threshold of 0.32. The PACG patients exhibited a decreased normalized degree in the primary and secondary visual cortices (bilateral calcarine, left superior occipital gyrus, right inferior occipital gyrus, and bilateral cuneus). An increased

TABLE 2: Demographics and clinical characteristics of patients with PACG and controls.

	PACG	HCs	p value
Age (years old)	54.21 ± 7.21	52.42 ± 7.80	0.337
Sex (M/F)	13/20	13/20	0.999
Handedness	33R	33R	0.999
RNFL (μm)	80.83 ± 17.69		
Vision	0.46 ± 0.34		
V C/D	0.68 ± 0.17		
IOP (mmHg)	26.86 ± 9.44		

RNFL: retina nerve fiber layer; RNFLT: retina nerve fiber layer thickness; V C/D: vertical cup to disc ratio; IOP: intraocular pressure; M: male; F: female; R: right.

normalized degree was identified in the dorsal visual pathway brain regions (right thalamus and bilateral middle temporal gyrus), as well as nonvisual pathway brain regions (bilateral supplementary motor area, right parahippocampal, right paracentral lobule, and right inferior frontal (opercular portion)).

Figure 4 and Table 3 indicate differences in the normalized node betweenness between the PACG and HC groups. The normalized node betweenness in the dorsal visual pathway brain regions (left superior occipital gyrus, left inferior occipital gyrus, bilateral cuneus, and left lingual gyrus) was decreased in the patients with PACG. A decrease was also identified in the nonvisual regions, including the left superior frontal gyrus, left superior frontal gyrus (orbital portion), left middle frontal gyrus (orbital portion), left hippocampus, left putamen, left cerebellum, and vermis. Furthermore, the patients with PACG exhibited significant increases in the normalized node betweenness in the dorsal/ventral visual pathway (right middle temporal gyrus, right middle temporal pole, and left inferior temporal gyrus) as well as in nonvisual areas (right parahippocampal, right paracentral lobule, bilateral inferior frontal gyrus (opercular portion), and bilateral supramarginal gyrus) ($p < 0.05$).

3.4. Correlation between Altered Regional Values in Patients with PACG and Clinical Parameters. We correlated the clinical parameters with the regional values of brain areas that exhibited alterations in the patients with PACG (Figure 5). We determined that the normalized clustering coefficient of the right superior parietal gyrus was negatively correlated with the RNFL ($r = -0.384$, $p = 0.028$) and positively correlated with the V C/D ($r = 0.384$, $p = 0.028$). Similarly, the normalized local efficiency of the right superior parietal gyrus was negatively correlated with the RNFL ($r = -0.376$, $p = 0.031$) and positively correlated with the V C/D ($r = 0.346$, $p = 0.049$). In addition, the normalized node betweenness of the left middle frontal gyrus (orbital region) was positively correlated with the V C/D ($r = 0.406$, $p = 0.019$).
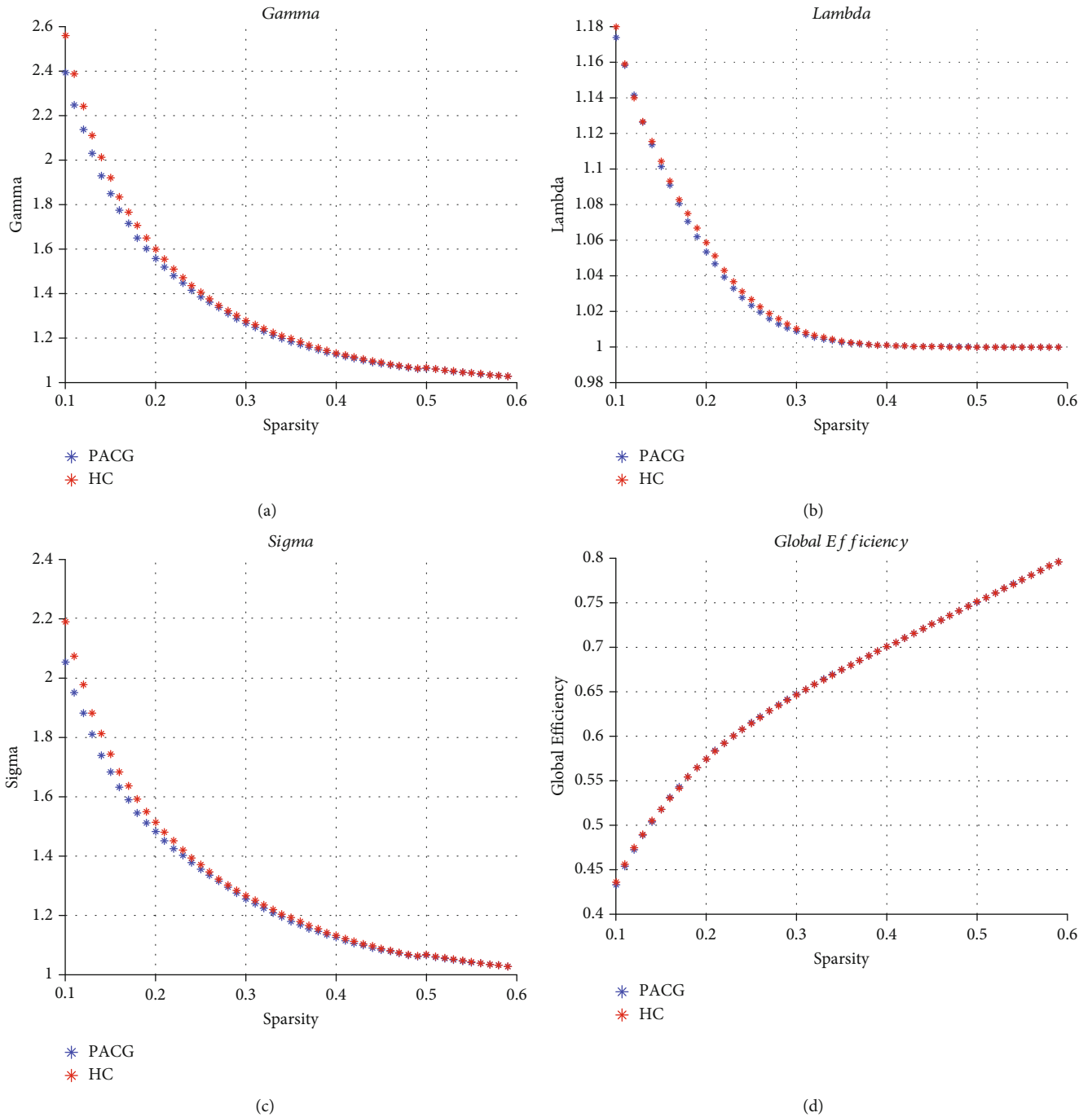
FIGURE 1: Changes in global network property measures as a function of network sparsity (from 0.1 to 0.6). The normalized clustering coefficient γ (a), normalized characteristic path length λ (b), small-world index σ (c), and global efficiency (d) of both the PACG and HC networks. Both networks follow a small-world organization.

4. Discussion

The present study investigated the topological properties of the functional brain networks of patients with PACG at both global and regional levels. Our main findings are as follows: (1) an economical and stabilized small-world property is identified in the whole brain functional networks of patients with PACG; (2) patients with PACG exhibit significantly altered regional characteristics

(normalized degree, node betweenness, local efficiency, and clustering coefficient) in several regions, including visual and nonvisual pathways; and (3) in patients with PACG, the normalized clustering coefficient and local efficiency of the right superior parietal gyrus were significantly correlated with the RNFL and V C/D, whereas the normalized node betweenness of the left middle frontal gyrus (orbital portion) was significantly correlated with the V C/D.

(a)

(b)

(c)

(d)
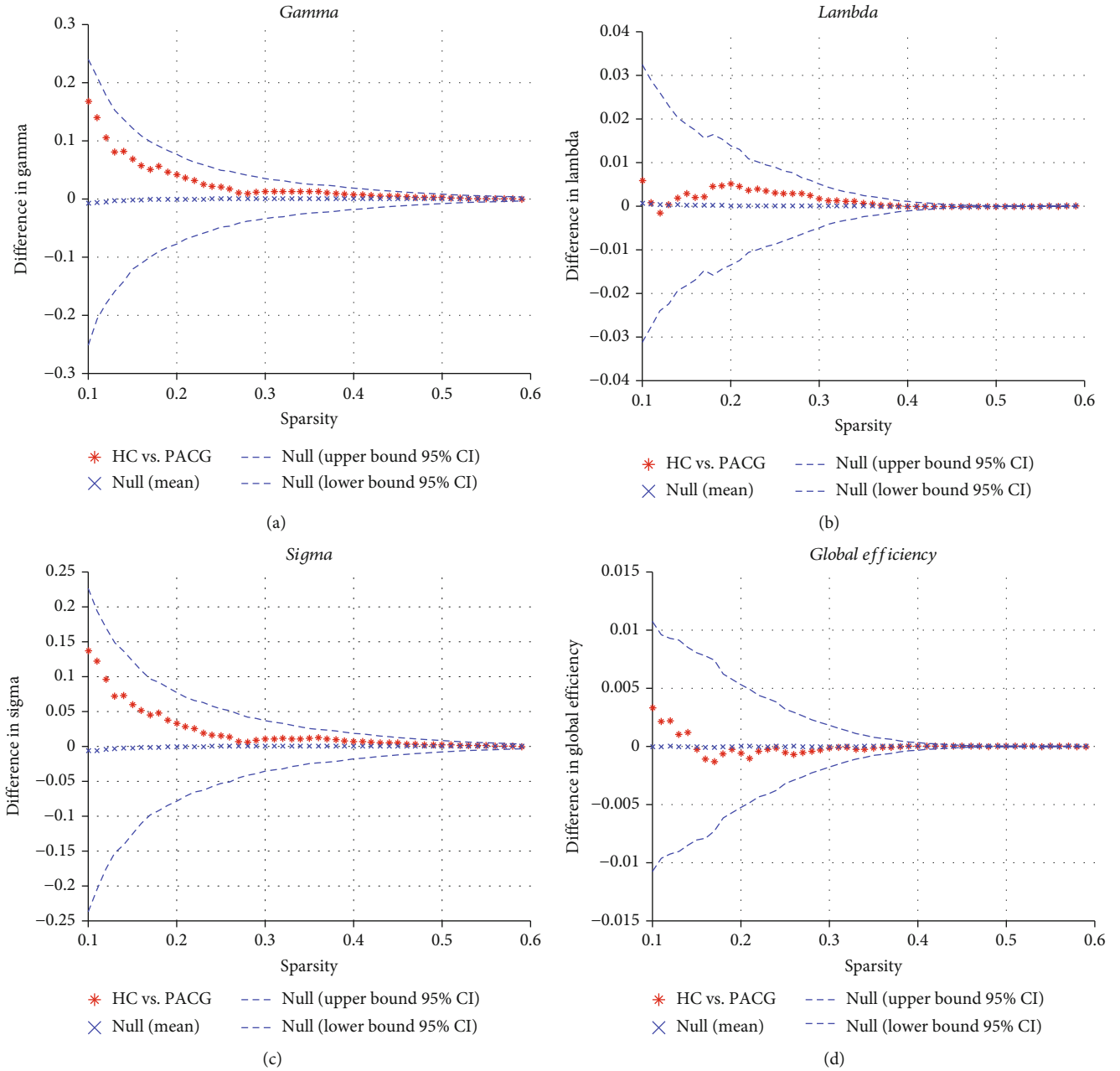
FIGURE 2: Between-group differences in global network measures as a function of small-world network sparsity (from 0.32 to 0.42). The 95% confidence intervals and between-group differences for the normalized clustering coefficient γ (a), normalized path length λ (b), small-world index σ (c), and global efficiency (d). Compared with the HC network, the global network normalized clustering coefficient and small-world index in the PACG network were slightly different across the small-world network sparsity range.

4.1. Economical and Stabilized Global Network Properties.

The small-world network is considered to be well balanced with local brain specialization and global integration. Our study indicated that the networks of the two groups had economic small-world characteristics ($\gamma > 1$, $\lambda \approx 1$, or $\sigma > 1$).

In our study, the specific maximum and minimum sparsity thresholds were set to range from 0.32 to 0.42 to avoid the existence of isolated nodes and ensure small-worldness in both group networks. We determined that the global features of the brain network did not exhibit significant changes

in patients with PACG above the sparsity threshold. Recently, Wang et al. [42] employed graph theoretical analysis and reported no statistical changes in global brain properties in POAG patients, which suggests that the efficiency of functional brain network information transmission was conserved. Consistent with this previous study, our results indicated that the brain network was homogeneous [[43]] in glaucoma patients. However, the clustering coefficient (λ) and small-worldness (σ) were slightly decreased ($p > 0.05$), which indicates that the global brain network characteristics
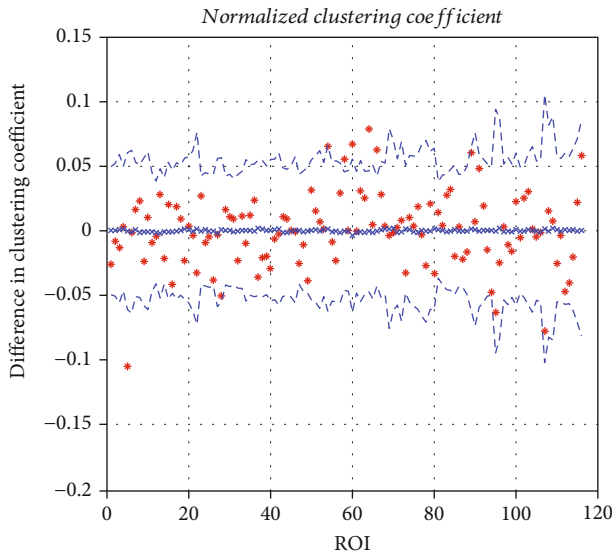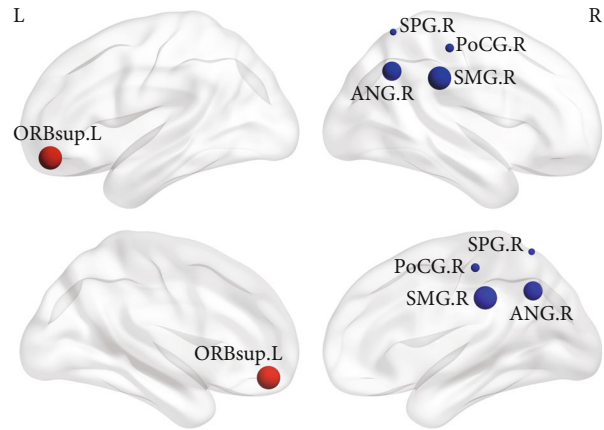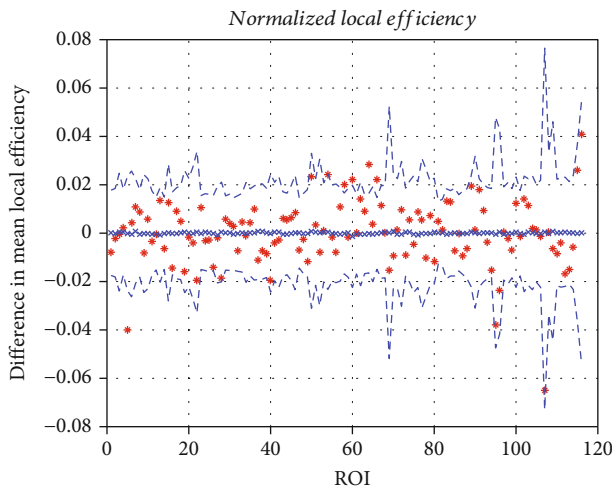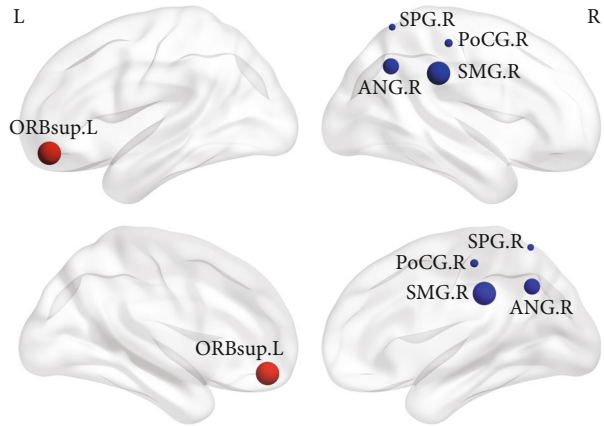
FIGURE 3: Regional alterations in normalized clustering coefficiencies and normalized local efficiencies in functional brain networks at a minimum sparsity of 0.32. Statistical graphs of each node are presented on the left (a, b), and a three-dimensional view of the corresponding significant nodes are shown on the right (c, d). The significantly increased regional nodal parameters (normalized clustering coefficient and local efficiency) of patients with PACG are indicated by the red spheres, and significantly increased regional nodal parameters of the HC group are indicated by the blue spheres. The sphere sizes represent the significance values ($p < 0.05$, FDR correction); larger spheres indicate greater significance and smaller p values.

of patients with PACG tend to decrease. This finding suggests that the balance of local specialization and global integration in patients with PACG was disrupted, which caused the brain network in patients with PACG to tend towards a lower efficiency random network.

4.2. Alteration of Regional Network Properties. The analysis of regional network properties in patients with PACG indicated differences in the normalized node degree and normal-ized node betweenness in both visual and nonvisual pathways. The node degree and node betweenness are well established to indicate the significance of a node and represent the number of connections with and degree of information processing to all other nodes in a network, respectively [30].

Over the sparsity range of 0.32-0.42, our results indicated a significantly decreased normalized degree in the primary and secondary visual cortices (bilateral calcarine, left

(a)

(b)

(c)

(d)

FIGURE 4: Regional alterations in normalized node degree and normalized node betweenness in functional brain networks at the minimum sparsity of 0.32. Graphs of each node are presented on the left (a, b), and a three-dimensional view of the corresponding significant brain regions are shown on the right (c, d). The significantly increased regional nodal parameters (normalized node degree and normalized node betweenness) of the patients with PACG are indicated by the red spheres, and the significantly increased regional nodal parameters of the HC group are indicated by the blue spheres. The sphere size represents significance ($p < 0.05$); a larger sphere size indicates greater significance and a smaller p value.

superior occipital gyrus, right inferior occipital gyrus, and bilateral cuneus) in patients with PACG, as well as significantly decreased normalized node betweenness in the dorsal visual pathway regions (extending from the left superior occipital gyrus to the left inferior occipital gyrus, bilateral cuneus, and left lingual gyrus). The primary visual cortex (calcarine, occipital lobe, and cuneus) receives direct visual information from the ON and LGN. The primary cortex sends most of its projections to the secondary visual cortex (occipital lobe). Notably, reduced visual stimulation in the visual cortices may lead to a loss of projections from these areas in glaucoma, an effect that leads to impairments in the primary and secondary visual cortices [44]. As similar with previous researches, these impairments include struc-

tural damage and functional impairment in the calcarine area, cuneus [[45, 46]], and occipital lobe [[45, 47]]. Similarly, the DC is decreased in the superior/inferior occipital and lingual gyri. As a result, the integrity of brain regions in the dorsal visual pathway, which plays an important role in visuospatial function, is further affected. Previous studies have also reported structural changes in the occipital lobe and altered cortical thickness in the cuneus and lingual gyrus [30], which strongly affect visuospatial and motion processing in glaucoma patients. Consistent with these findings, the observed decrease in the normalized node degree and normalized node betweenness indicates a lower efficiency of functional communication through these regions. This negative effect particularly affects visual projection and

TABLE 3: Between-group comparisons of PACG vs. HCs in regional network properties at a minimum sparsity of 0.32.

| Normalized node betweenness | | Normalized degree | |
Regions	p value	Regions	p value
PACG > HCs		PACG > HCs	
L. inferior frontal gyrus (opercular portion), IFGoperc.L	0.040	R. inferior frontal gyrus (opercular portion), IFGoperc.R	0.042
R. inferior frontal gyrus (opercular portion), IFGoperc.R	0.024	L. supplementary motor area, SMA.L	0.013
R. parahippocampal gyrus, PHG.R	0.013	R. supplementary motor area, SMA.R	0.041
L. supramarginal gyrus, SMG.L	0.036	R. parahippocampal gyrus, PHG.R	0.012
R. supramarginal gyrus, SMG.R	0.003	R. paracentral lobule, PCL.R	0.002
R. paracentral lobule, PCL.R	≤0.001	R. thalamus, THA.R	0.044
R. middle temporal gyrus, MTG.R	0.025	R. middle temporal gyrus, MTG.R	0.047
R. temporal pole:middle temporal gyrus, TPOmid.R	0.040	L. temporal pole:middle temporal gyrus, TPOmid.L	0.018
L. inferior temporal gyrus, ITG.L	0.012	R. temporal pole:middle temporal gyrus, TPOmid.R	0.038
PACG < HCs		PACG < HCs	
L. dorsal lateral superior frontal gyrus, SFGdor.	0.043	L. calcarine, CAL.L	0.007
L. superior frontal gyrus (orbital portion), ORBsup.L	0.049	R. calcarine, CAL.R	0.032
L. middle frontal gyrus (orbital portion), ORBmid.L	0.049	L. cuneus, CUN.L	≤0.001
L. hippocampus, HIP.L	0.009	R. cuneus, CUN.R	0.004
L. cuneus, CUN.L	0.004	L. superior occipital gyrus, SOG.L	0.040
R. cuneus, CUN.R	≤0.001	R. inferior occipital gyrus, IOG.R	0.042
L. lingual gyrus, LING.L	0.014		
L. superior occipital gyrus, SOG.L	0.012		
L. inferior occipital gyrus, IOG.L	0.047		
L. putamen, PUT.L	0.007		
L. cerebellum 6, CRBL6.L	0.026		
Vermis 6, Vermis6	0.015		

L: left; R: right; PACG > HCs: increased regional network properties in PACG compared with HCs; PACG < HCs: decreased regional network properties in PACG compared with HCs.

processing, thereby contributing to an increasing body of evidence of impaired spatial orientation in patients with PACG.

Moreover, the brain regions of the dorsal visual pathway (right thalamus and bilateral middle temporal gyrus) exhibited an increase in the normalized degree, and the dorsal/ventral visual pathway brain regions (right middle temporal gyrus, right middle temporal pole, and left inferior temporal gyrus) exhibited increased normalized node betweenness. Areas that extend from the primary visual cortex to the temporal lobes (middle and right inferior temporal gyrus) may be associated with visual memory or episodic memory imagery [48]. The primary visual cortex and the inferior temporal gyrus are thought to play a role in connecting visual, auditory, and tactile stimulation [49]. Analogous results have also been reported in terms of the synchronization of spontaneous activity [50], and functional integration in the temporal lobe and middle/inferior temporal gyrus exhibits compensatory increases in glaucoma. This effect may be related to neuroplasticity and compensatory mechanisms. Specifically, glaucomatous visual loss may lead to a loss of inhibition inputs of the primary visual regions, following which the dorsal/ventral visual regions are further compensatory increased [51, 52]. Our preliminary study of increased visual cortices in postoperative patients with PACG supports this interpretation [53]. Consistent with these results, our

finding of an increased normalized node degree and normalized node betweenness in visual cortices may suggest a compensatory response of visual memory and the integration of visual, auditory, and tactile inputs.

Moreover, we identified a significantly altered normalized node degree and normalized node betweenness in nonvisual cortices, including (i) cognition-emotion processing brain regions, such as the left superior frontal gyrus, left superior/middle frontal gyrus (orbital portion), bilateral inferior frontal lobe (opercular portion), left hippocampus, right parahippocampus, left cerebellum and vermis and (ii) the somatomotor cortex (bilateral supplementary motor area, right paracentral lobule, and bilateral supramarginal gyrus along with left putamen). A recent study suggested that glaucoma patients, particularly patients with PACG, are at a higher risk of anxiety and depression [[54]]. Moreover, the cerebellum and hippocampus [55], which play an important role in cognition-emotion processing, as well as the frontal lobe (orbital portion) and inferior frontal gyrus (opercular portion) [56] are functionally and structurally disrupted in this condition. In addition, the functional connectivity of somatomotor regions is altered in patients with glaucoma. Consistent with these findings, an altered normalized node degree and normalized node betweenness in nonvisual cortices suggest that the efficiency of cognition-emotion and somatomotor processing is impaired in
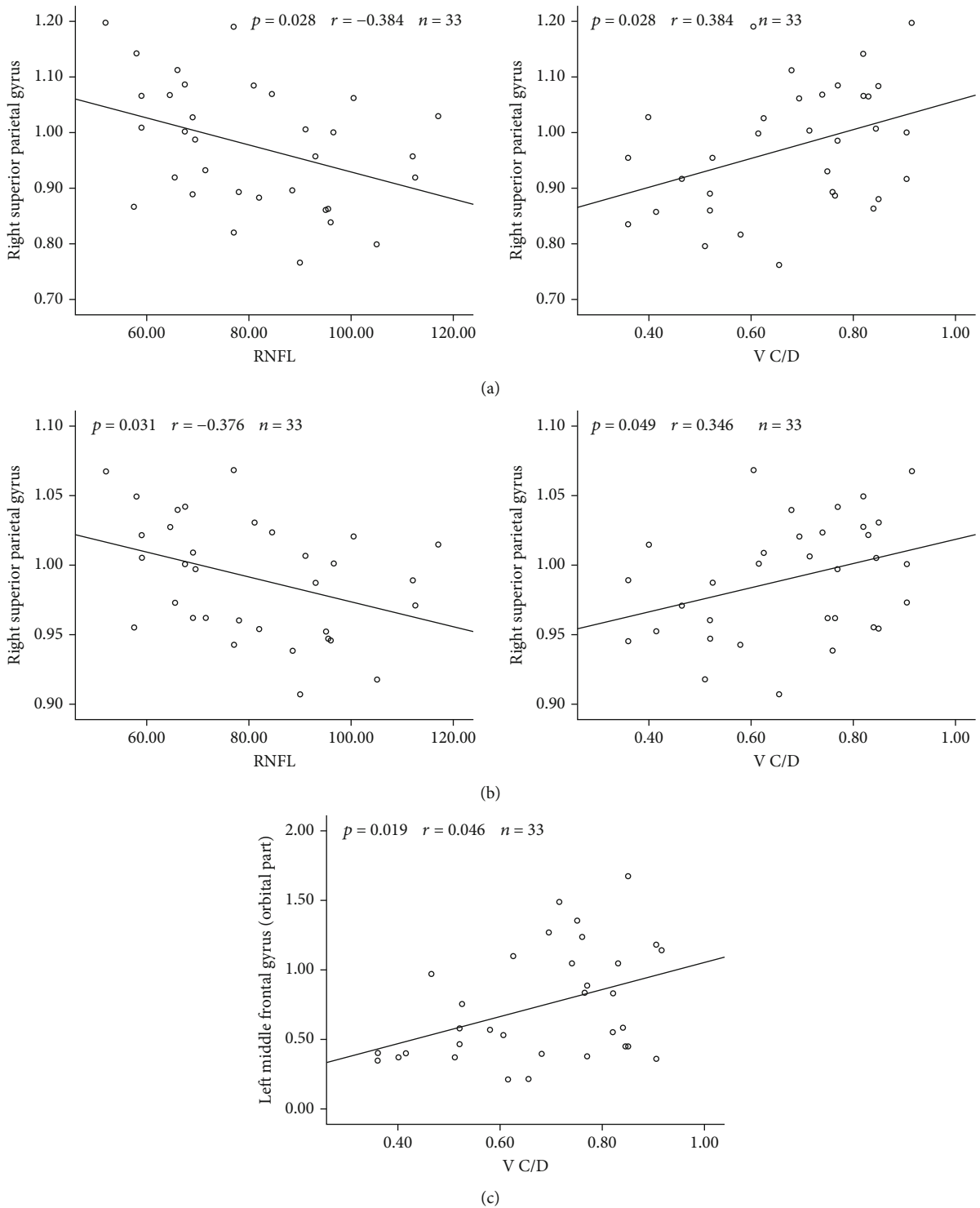
FIGURE 5: Correlation between altered regional values in patients with PACG and clinical parameters. The right superior parietal gyrus of the normalized clustering coefficient is correlated with the RNFL and V C/D (a), the right superior parietal gyrus normalized local efficiency is correlated with the RNFL and V C/D (b), and the left middle frontal gyrus (orbital portion) normalized node betweenness is correlated with the V C/D (c).

patients with PACG. This result implies that glaucoma is a widespread brain disorder.

Interestingly, the identified alterations in the normalized clustering coefficients of the dorsal visual pathway and the somatomotor and cognition-emotion regions were similar to the alterations in the normalized local efficiency in patients with PACG. These results are consistent with the hypothesis that the normalized clustering coefficient is a

good approximation of efficiency [57]. A substantial proportion of fMRI studies have reported that glaucoma is not simply an ophthalmic disease but rather a more complex, widespread disorder that through visual and nonvisual cortices [50, 58, 59]. Therefore, with the changed visual and nonvisual pathways of normalized clustering coefficient and normalized local efficiency, our results also provided a growing evidence of the conception that glaucoma was not only an ocular disease but also a more widespread brain syndrome.

In our study, the normalized clustering coefficient and normalized local efficiency of the right superior parietal gyrus were negatively correlated with the RNFL and positively correlated with the V C/D. In addition, the decrease in the node betweenness of the left middle frontal gyrus (orbital portion) was positively correlated with the V C/D. The RNFL and V C/D are considered to be important measures of glaucoma severity; i.e., more severe glaucoma is associated with a thicker RNFL and higher V C/D. As a result, these significant correlations indicate that the altered regional properties of the right superior parietal gyrus and left middle frontal gyrus (orbital portion) are correlated with the PACG severity.

5. Limitations

Several limitations of this study should be addressed. First, being identified from functional brain network connectivity metrics, the structural brain network is not yet described or characterized as a within-group description; thus, the correlation between structural and functional network should be considered in the future. Second, the PACG sample size was relatively small, and a large longitudinal sample is required for further analysis. Third, our study adopted a binary, undirected network analysis. To address the connectivity strength, a weighted network with a sparsity threshold or an effective connectivity network should also be considered in future analyses. The severity of the damage to the eyes caused by PACG is variable. Moreover, it is doubtful that alterations in brain network properties will be similar between different disease stages and/or severities.

6. Conclusions

In conclusion, we investigated the intrinsic functional brain network in patients with PACG using graph theoretical analysis. No significant differences were identified in the global topological measures of patients with PACG; however, significant alterations were identified in the local properties of visual, somatomotor, and cognition-emotional regions. Taken together, our findings indicate that reduced efficiencies in visual and nonvisual processing regions are accompanied by compensatory increases in the local functional properties of visual and nonvisual nodes, which thereby preserve the global network stabilization in patients with PACG. Our framework may help to promote further studies towards a better understanding of the neurological basis of PACG.

Data Availability

The raw/processed data required to reproduce these findings cannot be shared at this time as the data also forms part of an ongoing study.

Conflicts of Interest

The authors declare that there is no conflict of interest regarding the publication of this paper.

Authors' Contributions

Dan Liu, Junwei Gao and Tao You are co-authors and contributed equally to this work.

Acknowledgments

Supplementary Materials

1: the definitions and calculations of network measures. *(Supplementary Materials)*

References

[1] J. N. He, S. Lu, L. J. Chen et al., "Coding region mutation screening in optineurin in Chinese normal-tension glaucoma patients," *Disease Markers*, vol. 2019, Article ID 5820537, 5 pages, 2019.

[2] X. Kong, X. Liu, X. Huang, Z. Mao, Y. Zhong, and W. Chi, "Damage to the blood-aqueous barrier in eyes with primary angle closure glaucoma," *Molecular Vision*, vol. 16, pp. 2026–2032, 2010.

[3] P. J. Foster and G. J. Johnson, "Glaucoma in China: how big is the problem?," *The British Journal of Ophthalmology*, vol. 85, no. 11, pp. 1277–1282, 2001.

[4] S. J. Mckinnon, "The cell and molecular biology of glaucoma: common neurodegenerative pathways and relevance to glaucoma," *Investigative Ophthalmology & Visual Science*, vol. 53, no. 5, pp. 2485–2487, 2012.

[5] P. Wostyn, K. Audenaert, and P. P. De Deyn, "Alzheimer's disease: Cerebral glaucoma?," *Medical Hypotheses*, vol. 74, no. 6, pp. 973–977, 2010.

[6] H. D. Brown, R. L. Woodall, R. E. Kitching, H. A. Baseler, and A. B. Morland, "Using magnetic resonance imaging to assess visual deficits: a review," *Ophthalmic & Physiological Optics*, vol. 36, no. 3, pp. 240–265, 2016.

[7] D. M. Borucki, A. Toutonji, C. Couch, K. Mallah, B. Rohrer, and S. Tomlinson, "Complement-mediated microglial phagocytosis and pathological changes in the development and degeneration of the visual system," *Frontiers in Immunology*, vol. 11, article 566892, 2020.

[8] H. V. Danesh-Meyer and L. A. Levin, "Glaucoma as a neurodegenerative disease," *Journal of Neuro-Ophthalmology*, vol. 35, Supplement 1, pp. S22–S28, 2015.

[9] Q. Wang, W. Chen, H. Wang et al., "Reduced functional and anatomic interhemispheric homotopic connectivity in primary open-angle glaucoma: a combined resting state-fMRI and DTI study," *Investigative Ophthalmology & Visual Science*, vol. 59, no. 5, pp. 1861–1868, 2018.

[10] C. P. B. Gracitelli, V. M. Gerente, R. L. Furlanetto, E. Amaro, and A. Paranhos, "Magnetic resonance imaging for glaucoma evaluation," *Journal of Glaucoma*, vol. 29, no. 8, pp. 622–626, 2020.

[11] Y. Y. Wu, S. F. Wang, P. W. Zhu et al., "Altered intrinsic functional connectivity of the primary visual cortex in patients with neovascular glaucoma: a resting-state functional magnetic resonance imaging study," *Neuropsychiatric Disease and Treatment*, vol. Volume 16, pp. 25–33, 2020.

[12] Z. Y. Peng, Y. X. Liu, and B. Li, "Altered spontaneous brain activity patterns in patients with neovascular glaucoma using amplitude of low-frequency fluctuations: a functional magnetic resonance imaging study," *Brain and Behavior: A Cognitive Neuroscience Perspective*, vol. 11, no. 3, article e02018, 2021.

[13] H. Dai, J. N. Morelli, F. Ai et al., "Resting-state functional MRI: functional connectivity analysis of the visual cortex in primary open-angle glaucoma patients," *Human Brain Mapping*, vol. 34, no. 10, pp. 2455–2463, 2013.

[14] T. Li, Z. Liu, J. Li et al., "Altered amplitude of low-frequency fluctuation in primary open-angle glaucoma: a resting-state FMRI study," *Investigative Ophthalmology & Visual Science*, vol. 56, no. 1, pp. 322–329, 2014.

[15] Y. Song, K. Mu, J. Wang et al., "Altered spontaneous brain activity in primary open angle glaucoma: a resting-state functional magnetic resonance imaging study," *PLoS One*, vol. 9, no. 2, article e89493, 2014.

[16] P. Frezzotti, A. Giorgio, F. Toto, A. de Leucio, and N. de Stefano, "Early changes of brain connectivity in primary open angle glaucoma," *Human Brain Mapping*, vol. 37, no. 12, pp. 4581–4596, 2016.

[17] P. Frezzotti, A. Giorgio, I. Motolese et al., "Structural and functional brain changes beyond visual system in patients with advanced glaucoma," *PLoS One*, vol. 9, no. 8, article e105931, 2014.

[18] Q. Wang, X. Qu, W. Chen et al., "Altered coupling of cerebral blood flow and functional connectivity strength in visual and higher order cognitive cortices in primary open angle glaucoma," *Journal of Cerebral Blood Flow and Metabolism*, vol. 41, no. 4, pp. 901–913, 2021.

[19] E. Bullmore and O. Sporns, "Complex brain networks: graph theoretical analysis of structural and functional systems," *Nature Reviews. Neuroscience*, vol. 10, no. 3, pp. 186–198, 2009.

[20] C. Y. Lo, Y. He, and C. P. Lin, "Graph theoretical analysis of human brain structural networks," *Reviews in the Neurosciences*, vol. 22, no. 5, pp. 551–563, 2011.

[21] W. H. Lee, E. Bullmore, and S. Frangou, "Quantitative evaluation of simulated functional brain networks in graph theoretical analysis," *NeuroImage*, vol. 146, pp. 724–733, 2017.

[22] W. Yuan, S. K. Holland, J. S. Shimony et al., "Abnormal structural connectivity in the brain networks of children with hydrocephalus," *NeuroImage: Clinical*, vol. 8, pp. 483–492, 2015.

[23] H. Lv, Z. Wang, E. Tong et al., "Resting-state functional MRI: everything that nonexperts have always wanted to know," *AJNR. American Journal of Neuroradiology*, vol. 39, no. 8, pp. 1390–1399, 2018.

[24] Z. Chen, M. Liu, D. W. Gross, and C. Beaulieu, "Graph theoretical analysis of developmental patterns of the white matter network," *Frontiers in Human Neuroscience*, vol. 7, p. 716, 2013.

[25] J. Wang, X. Wang, M. Xia, X. Liao, A. Evans, and Y. He, "GRETNA: a graph theoretical network analysis toolbox for imaging connectomics," *Frontiers in Human Neuroscience*, vol. 9, p. 386, 2015.

[26] L. Kuang, Y. Gao, Z. Chen, J. Xing, F. Xiong, and X. Han, "White matter brain network research in Alzheimer's disease using persistent features," *Molecules*, vol. 25, no. 11, p. 2472, 2020.

[27] S. Y. Lin, C. P. Lin, T. J. Hsieh et al., "Multiparametric graph theoretical analysis reveals altered structural and functional network topology in Alzheimer's disease," *NeuroImage: Clinical*, vol. 22, article ???, 2019.

[28] P. Finotelli, C. G. Forlim, L. Klock et al., "New graph-theoretical-multimodal approach using temporal and structural correlations reveals disruption in the thalamo-cortical network in patients with schizophrenia," *Brain Connectivity*, vol. 9, no. 10, pp. 760–769, 2019.

[29] G. Fadda, R. A. Brown, G. Longoni et al., "MRI and laboratory features and the performance of international criteria in the diagnosis of multiple sclerosis in children and adolescents: a prospective cohort study," *Lancet Child Adolesc Health*, vol. 2, no. 3, pp. 191–204, 2018.

[30] F. Cai, L. Gao, H. Gong et al., "Network centrality of resting-state fMRI in primary angle-closure glaucoma before and after surgery," *PLoS One*, vol. 10, no. 10, article e0141389, 2015.

[31] S. Rupprechter, L. Romaniuk, P. Series et al., "Blunted medial prefrontal cortico-limbic reward-related effective connectivity and depression," *Brain*, vol. 143, no. 6, pp. 1946–1956, 2020.

[32] J. Chang and R. Yu, "Hippocampal connectivity in the aftermath of acute social stress," *Neurobiol Stress*, vol. 11, article 100195, 2019.

[33] X. Chen, X. He, L. Tao et al., "The working memory and dorsolateral prefrontal-hippocampal functional connectivity changes in long-term survival breast cancer patients treated with tamoxifen," *The International Journal of Neuropsychopharmacology*, vol. 20, no. 5, pp. 374–382, 2017.

[34] N. Tzourio-Mazoyer, B. Landeau, D. Papathanassiou et al., "Automated anatomical labeling of activations in SPM using a macroscopic anatomical parcellation of the MNI MRI single-subject brain," *NeuroImage*, vol. 15, no. 1, pp. 273–289, 2002.

[35] X. Chen, L. Chen, S. Zheng et al., "Disrupted brain connectivity networks in aphasia revealed by resting-state fMRI," *Frontiers in Aging Neuroscience*, vol. 13, article 666301, 2021.

[36] Q. Su, D. Yao, M. Jiang et al., "Decreased interhemispheric functional connectivity in insula and angular gyrus/supramarginal gyrus: significant findings in first-episode, drug-naive somatization disorder," *Psychiatry Research: Neuroimaging*, vol. 248, pp. 48–54, 2016.

[37] W. Wen, W. Zhu, Y. He et al., "Discrete neuroanatomical networks are associated with specific cognitive abilities in old age," *The Journal of Neuroscience*, vol. 31, no. 4, pp. 1204–1212, 2011.

[38] for the Alzheimer's Disease Neuroimaging Initiative, H. Chen, X. Sheng et al., "The compensatory phenomenon of the

functional connectome related to pathological biomarkers in individuals with subjective cognitive decline," *Translational Neurodegeneration*, vol. 9, no. 1, p. 21, 2020.

[39] T. X. Zou, L. She, C. Zhan, Y. Q. Gao, and H. J. Chen, "Altered topological properties of gray matter structural covariance networks in minimal hepatic encephalopathy," *Frontiers in Neuroanatomy*, vol. 12, p. 101, 2018.

[40] D. J. Watts and S. H. Strogatz, "Collective dynamics of 'small-world' networks," *Nature*, vol. 393, no. 6684, pp. 440–442, 1998.

[41] Z. Gao, X. Liu, D. Zhang, M. Liu, and N. Hao, "The indispensable role of the cerebellum in visual divergent thinking," *Scientific Reports*, vol. 10, no. 1, p. 16552, 2020.

[42] J. Wang, T. Li, N. Wang, J. Xian, and H. He, "Graph theoretical analysis reveals the reorganization of the brain network pattern in primary open angle glaucoma patients," *European Radiology*, vol. 26, no. 11, pp. 3957–3967, 2016.

[43] J. Wang, X. Wang, M. Xia, X. Liao, A. Evans, and Y. He, "Corrigendum: GRETNA: a graph theoretical network analysis toolbox for imaging connectomics," *Frontiers in Human Neuroscience*, vol. 9, p. 458, 2015.

[44] Q. Wang, W. Chen, X. Qu et al., "Reduced cerebral blood flow in the visual cortex and its correlation with glaucomatous structural damage to the retina in patients with mild to moderate primary open-angle glaucoma," *Journal of Glaucoma*, vol. 27, no. 9, pp. 816–822, 2018.

[45] C. P. B. Gracitelli, G. L. Duque-Chica, L. G. Sanches et al., "Structural analysis of glaucoma brain and its association with ocular parameters," *Journal of Glaucoma*, vol. 29, no. 5, pp. 393–400, 2020.

[46] G. Kitsos, A. K. Zikou, E. Bagli, P. Kosta, and M. I. Argyropoulou, "Conventional MRI and magnetisation transfer imaging of the brain and optic pathway in primary open-angle glaucoma," *The British Journal of Radiology*, vol. 82, no. 983, pp. 896–900, 2009.

[47] F. Jiang, C. Yu, M. J. Zuo et al., "Frequency-dependent neural activity in primary angle-closure glaucoma," *Neuropsychiatric Disease and Treatment*, vol. Volume 15, pp. 271–282, 2019.

[48] Y. Wang, J. Wang, Y. Jia et al., "Shared and specific intrinsic functional connectivity patterns in unmedicated bipolar disorder and major depressive disorder," *Scientific Reports*, vol. 7, no. 1, p. 3570, 2017.

[49] J. Zhang, Y. L. Wu, J. Su et al., "Assessment of gray and white matter structural alterations in migraineurs without aura," *The Journal of Headache and Pain*, vol. 18, no. 1, p. 74, 2017.

[50] X. Huang, Y. L. Zhong, X. J. Zeng et al., "Disturbed spontaneous brain activity pattern in patients with primary angle-closure glaucoma using amplitude of low-frequency fluctuation: a fMRI study," *Neuropsychiatric Disease and Treatment*, vol. 11, pp. 1877–1883, 2015.

[51] N. Plange, M. Kaup, O. Arend, and A. Remky, "Asymmetric visual field loss and retrobulbar haemodynamics in primary open-angle glaucoma," *Graefe's Archive for Clinical and Experimental Ophthalmology*, vol. 244, no. 8, pp. 978–983, 2006.

[52] M. Sullivan-Mee, M. T. Karin Tran, D. Pensyl, G. Tsan, and S. Katiyar, "Prevalence, features, and severity of glaucomatous visual field loss measured with the 10-2 achromatic threshold visual field test," *American Journal of Ophthalmology*, vol. 168, pp. 40–51, 2016.

[53] S. P. Gennari, R. E. Millman, M. Hymers, and S. L. Mattys, "Anterior paracingulate and cingulate cortex mediates the effects of cognitive load on speech sound discrimination," *NeuroImage*, vol. 178, pp. 735–743, 2018.

[54] D. Zhang, Z. Fan, X. Gao et al., "Illness uncertainty, anxiety and depression in Chinese patients with glaucoma or cataract," *Scientific Reports*, vol. 8, no. 1, p. 11671, 2018.

[55] C. Han, F. Li, J. Ma et al., "Distinct behavioral and brain changes after different durations of the modified multiple platform method on rats: an animal model of central fatigue," *PLoS One*, vol. 12, no. 5, article e0176850, 2017.

[56] L. Schlaffke, A. Leemans, L. M. Schweizer, S. Ocklenburg, and T. Schmidt-Wilcke, "Learning Morse code alters microstructural properties in the inferior longitudinal fasciculus: a DTI study," *Frontiers in Human Neuroscience*, vol. 11, p. 383, 2017.

[57] S. Achard and E. Bullmore, "Efficiency and cost of economical brain functional networks," *PLoS Computational Biology*, vol. 3, no. 2, article e17, 2007.

[58] A. Giorgio, J. Zhang, F. Costantino, N. de Stefano, and P. Frezzotti, "Diffuse brain damage in normal tension glaucoma," *Human Brain Mapping*, vol. 39, no. 1, pp. 532–541, 2018.

[59] W. Chen, L. Zhang, Y. G. Xu, K. Zhu, and M. Luo, "Primary angle-closure glaucomas disturb regional spontaneous brain activity in the visual pathway: an fMRI study," *Neuropsychiatric Disease and Treatment*, vol. Volume 13, pp. 1409–1417, 2017.

Research Article

USP1 Promotes GC Metastasis via Stabilizing ID2

Nuoya Li,[1] Lei Wu,[1] Xingye Zuo,[2] Huilong Luo,[1] Yanling Sheng [iD],[3] and Jinlong Yan [iD][1]

[1]*Department of General Surgery, Second Affiliated Hospital of Nanchang University, Nanchang, 330006 Jiangxi Province, China*
[2]*Department of General Surgery, Yongxin County People's Hospital, Ji'an, 343000 Jiangxi Province, China*
[3]*Department of Ultrasound, The Affiliated Hospital of Jiangxi University of Traditional Chinese Medicine, Nanchang, 330006 Jiangxi Province, China*

Correspondence should be addressed to Yanling Sheng; 498437800@qq.com and Jinlong Yan; yjl19880608@126.com

Gastric cancer (GC) is one of the most common malignant tumors all over the world. And recurrence and metastasis are still the main causes of low survival rate for advanced GC. USP1 has been shown overexpressed in multiple cancers, which indicate its important biomarker in tumorigenesis and development. Our study is aimed at defining the exact role of USP1 on GC metastasis and the underlying mechanism. USP1 was firstly found overexpressed in GC tissues and relatively high-expression levels conferred poor survival rates. Then, real-time cellular analysis (RTCA) showed that USP1 knockdown inhibited GC metastasis both in vitro and in vivo. Mechanically, we demonstrated that USP1 promoted GC metastasis via upregulating ID2 expression and further confirmed that USP1 stabilized ID2 expression through deubiquitinating ID2 in GC. In conclusion, our study showed that USP1 promoted GC metastasis via stabilizing ID2 expression, which provides a potential biomarker and therapy target for GC.

1. Introduction

Gastric cancer (GC) is one of the most common malignant tumors all over the world, with estimated 951,600 new cases and 723,100 deaths occurring in 2012 [1]. Although most countries have shown declining trend in incidence and mortality rates of GC over the past decades [2, 3], the absolute incidence is increasing owing to the growth and aging of population worldwide [4]. Endoscopic submucosal dissection or surgical resection of stomach is still the best choice for early GC, but for advanced patients, even with maximal treatments, the overall survival rates for 5 years are still low owing to recurrence and metastasis [5]. Molecular target treatment has shown its advantages in improving the prognosis of advanced GC patients in recent years [6]. Thus, it is necessary to further explore the molecular mechanisms of GC metastasis and search for new treatment strategies for GC.

Ubiquitination is an important posttranscriptional modification (PTM) which participate in a number of cellular processes, such as protein degradation, gene expression, and DNA repair [7]. Similar to other posttranscriptional modifications, ubiquitin modification is also a reversible process. Deubiquitinases (DUBs) can exert deubiquitination effect by hydrolyzing the isopeptide (or peptide) bond between ubiquitin or ubiquitin-like proteins and target proteins, so as to inhibit protein degradation and rescue their initial functions [8, 9]. Based on the Ub-protease domains in the human genome, DUBs are divided into 5 subclasses, of which ubiquitin-specific protease (USP) is the largest subclass [10]. USP has been indicated its regulatory effects on the development and progression of cancer [11–13]. As a member of USPs, USP1 plays important role in DNA repair through deubiquitinating Fanconi anemia complementation group I (FANCI), Fanconi anemia group D2 (FANCD2), and proliferating cell nuclear antigen (PCNA) [10, 14, 15]. Thus, USP1 is associated with multiple diseases including cancer. Previous studies have shown that USP1 is overexpressed in multiple cancers, such as osteosarcoma, multiple myeloma, glioblastoma, and non-small-cell lung cancer (NSCLC) [16–19]. But in the research of Zhiqiang et al., low expression of USP1 was found in non-small-cell lung

cancer tissues and overexpressing USP1 inhibited lung cancer cell proliferation [20]. Thus, it is controversial whether USP1 acts as an oncogene or tumor suppressor in the tumorigenesis and progression. In our study, we aimed to define the exact role of USP1 in GC metastasis and further to explore the underlying mechanism.

DNA-binding protein inhibitor ID-2 is a protein that in humans is encoded by the ID2 gene. ID2 may play a role in negatively regulating cell differentiation. Recently, its roles in cancers have been increasingly studied [21]. A research from Italian researchers states that ID2 protein has a relevant role in the development and resistance to therapies of glioblastoma, the most aggressive of brain cancers [22]. Another study found an inhibitor of DNA binding 2 (ID2) as a novel molecule involved in the regulation of invasion and LNM of HNSCC and further verified its functional role. Overexpression of ID2-induced invasion and LNM of HNSCC cells was observed in vitro and in vivo. By contrast, knockdown of the ID2 gene diminished invasion and LNM of HNSCC cells [23]. In addition, targeting ID2 could significantly inhibit the proliferation of colorectal cancer cells in mice [24]. However, the regulation of ID2 in gastric cancer remains unclear.

2. Materials and Methods

2.1. Patients and Samples. GC specimens were collected from 188 patients who underwent GC resection at the Second Affiliated Hospital of Nanchang University between January 2010 and May 2014. Informed consent was obtained from each patient, and the study protocol was approved by the Ethics Committee of the Second Affiliated Hospital of Nanchang University.

2.2. Cell Culture. The human GC cell lines BGC-823 and MGC-803 and human gastric mucosal cell line GES-1 were purchased from the Shanghai Cell Bank, Type Culture Collection Committee of Chinese Academy of Science (Shanghai, China). All cell lines were authenticated using short tandem repeat profiling by the Cell Bank. The cells were cultured in DMEM or MEM (Gibco, Grand Island, NY, USA) supplemented with 10% fetal bovine serum (Gibco, Grand Island, NY, USA) at 37°C and under 5% $CO2$.

2.3. Plasmids and Reagents. Based on the USP1 (NM_ 001017415.2) and ID2 (NM_002166.5) sequences, two shRNAs were designed using the siRNA Target Finder (InvivoGen). The target sites of shRNAs are detailed in Supplementary Table S1. The interference effects were confirmed by Western blotting (Figure 1(c)). The shUSP1 and shID2 construct that produced the most significant knockdown effect was used to transduce GC cells. Stably transfected GC cells were selected based on resistance to hygromycin (600 μg/ml) (Invitrogen, Carlsbad, CA, USA), and GC cells transfected with a negative control vector (shNC) were included as a control. pCMV-flag-USP1, pCMV-HA-Ub, and pCMV-his-ID2-expressing GC cells

were selected using G418 (700 μg/ml) (Invitrogen), and an empty vector was used as the negative control. After four weeks of selection, individual colonies were isolated and expanded. All primers are listed in Supplementary Table S1.

The following antibodies and reagents/kits were used: USP1, ID2, flag, his, HA, and Tubulin (Proteintech, Chicago, IL, USA); ubiquitin (Ub) (Nova Biomedical, MA, USA); protein A/G PLUS-agarose (Santa Cruz, CA, USA); DMEM, fetal bovine serum, and Lipofectamine® 3000 (Invitrogen); total protein extraction kit (Applygen, Beijing, China); BCA protein quantitation kit (Beyotime, Jiangsu, China); CHX [25] and PS-341 [26]; and MG132 [27] (Selleck, Houston, USA).

2.4. Immunohistochemistry (IHC). 188 GC and adjacent tissue (nontumor) sections were treated with xylene and graded alcohol and then subjected to antigen retrieval in 0.01 M citrate buffer. Hydrogen peroxide was used for blockage. The sections were incubated with goat serum for 30 min and then with anti-USP1 polyclonal antibodies (Proteintech, Chicago, IL, USA, 1 : 100 dilution) overnight at 4°C. A 2-step immunohistochemical method (catalog no.: PV-9000; ZSGB-BIO Co., Ltd., Beijing, China) was adopted for immunostaining. The staining intensity and percentage of positive cells were scored semiquantitatively by 3 pathologists who were blind to the clinical parameters.

2.5. Real-Time Quantitative Polymerase Chain Reaction (qRT-PCR), Western Blot Analysis, and Coimmunoprecipitation (Co-IP). qRT-PCR, Western blotting, and Co-IP were performed as previously described [28, 30]. The primers for q-PCR were included in Supplementary Table 1.

2.6. Transwell Assay. To determine cell invasion and migration, the cells were seeded on the top chamber of a Transwell (Corning, USA) with serum free medium, while complete medium containing 10% FBS were added in the lower chamber. After 24-hour incubation, the migrated cells were fixed with 4% PFA and then stained with 0.1% crystal violet (Sigma, USA) for 20 minutes. The results were photographed under an invert microscope. We also detected the cell invasion with the same protocol, but the membranes were coated with Matrigel (Stemcell, USA).

2.7. Real-Time Proliferation Assay (RTCA). Real-Time Cell Kinetic Analyzer xCELLigence RTCA (ACEA Biosciences) was used to monitor cell invasion and migration. Data were analyzed using the RTCA Control Unit and the preinstalled RTCA software. For real-time proliferation assay, CIA-plate 16 was used. Cells were seeded directly onto the CIA-plate. Changes in baseline impedance resulting from an increase in cell number were monitored by gold microelectrodes located at the bottom of CIA-plate 16. The proportional changes in impedance were recorded continuously and expressed as cell index. Changes in cell index over time were monitored continuously.

2.8. Establishment of Liver Metastasis Model of Gastric Cancer in Nude Mice. MGC-803 cells were transfected with

(a)

(b)

(c)

(d)

(e)

(f)

(g)
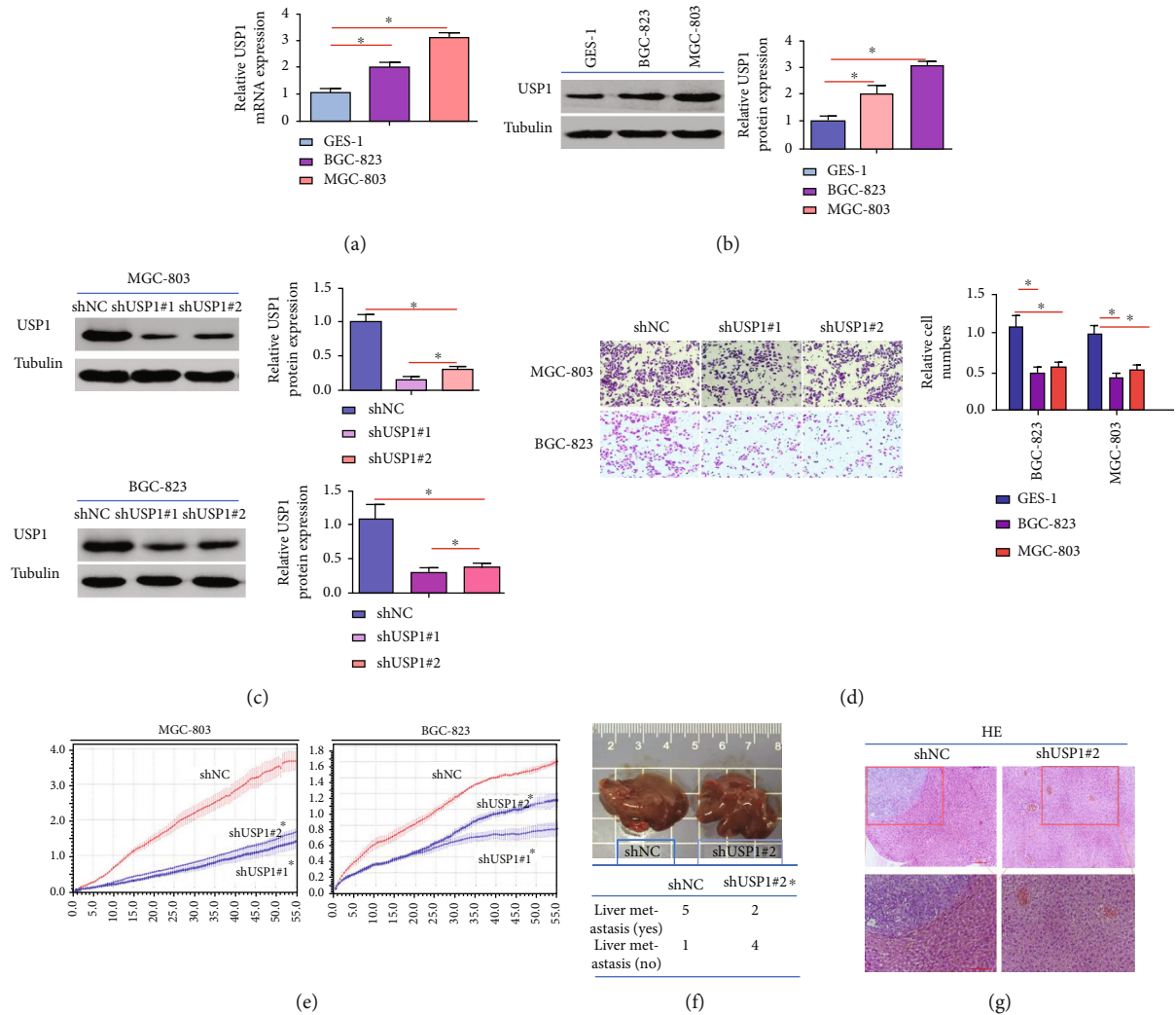
Figure 1: Stable knockdown of USP1 inhibits GC metastasis both in vitro and in vivo. (a, b) mRNA and protein expression levels of USP1 in normal gastric mucosa cells and two human GC cells (GES-1, BGC-823, and MGC-803) were detected by RT-qPCR and Western blot; (c) the efficacy of shRNA1 and shRNA2 mediated knockdown of USP1 was detected by Western blot; (d, e) in vitro experiments, MGC-803 and BGC-823 cells were transfected with shUSP1#1 or shUSP1#2; the real-time cellular analysis (RTCA) were used to evaluate cell migration; (f) in vivo experiments, MGC-803 cells transfected with shUSP1 or shNC were injected into the tail veins of nude mice; the representative images of HE staining of liver tissues with metastatic cells and the number of mice with liver metastasis were shown ($^{**}p < 0.01$; $^{*}p < 0.05$).

USP1 interference empty plasmid (shNC) and USP1 interference plasmid (shUSP1) before injection. The concentration was 1×0.2 ml of 10^7 human gastric cancer cell MGC-803 suspension inoculated under the splenic capsule of nude mice. The mice were killed at the 4th week after operation. The liver metastasis was observed by HE staining. There were 6 nude mice in the two groups. Animal: all the animal work was approved by the Ethics Committee for Animal Experiments of the Second Affiliated Hospital of Nanchang University.

2.9. Statistical Analysis. Data were analyzed using GraphPad Prism v7.0 (GraphPad Software Inc., USA). Survival curves were generated using the Kaplan-Meier method. Differences between groups were analyzed using Student's t-test when comparing two groups or by one-way analysis of variance

(ANOVA) when comparing more than two groups. $p < 0.05$ or 0.01 was considered significant.

3. Results

3.1. USP1 Is Overexpressed in in GC Tissues, and Relatively High Expression Levels of USP1 Correlate with Poor Survival. RT-qPCR and Western blot results further showed that the mRNA levels and protein levels of USP1 in GC tissues were higher than that in adjacent normal tissues (Figures 2(a) and 2(b)). In order to compare the expression levels USP1 on GC tissues and adjacent normal tissues from 116 patients, immunohistochemistry (IHC) was performed. The results showed that more intensive USP1 staining was found in GC tissues than that in adjacent normal tissues (Figure 2(c)). Kaplan-Meier analysis indicated that patients

(a)

(b)

(c)

(d)

(e)
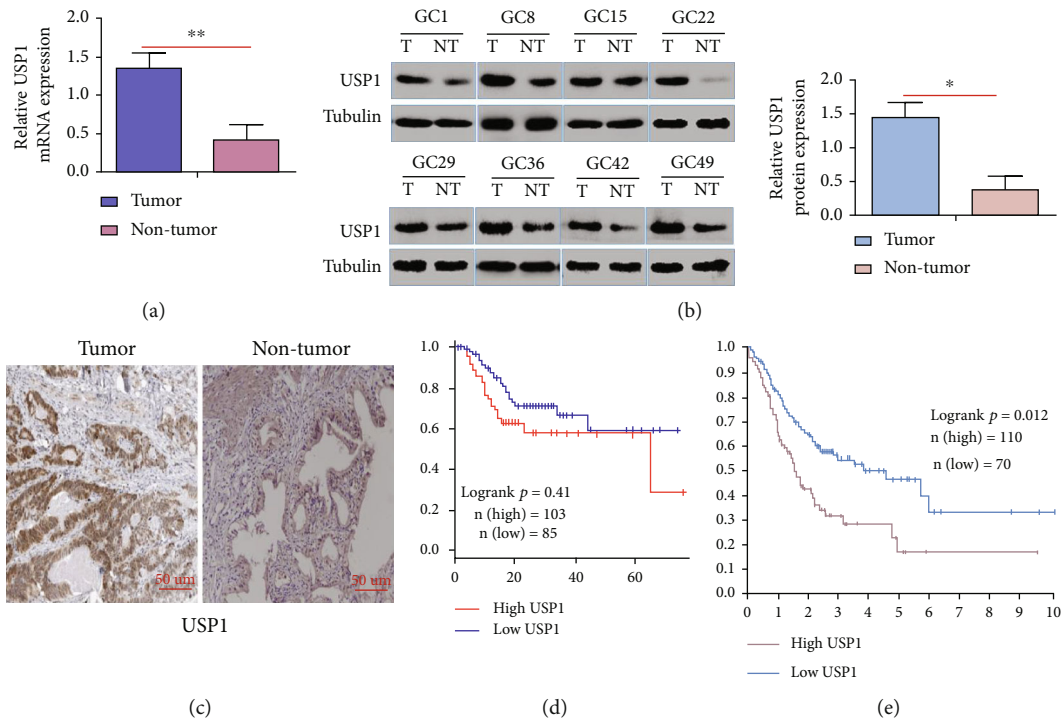
FIGURE 2: USP1 is overexpressed in in GC tissues and relatively high expression levels of USP1 correlates with poor survival. (a, b) mRNA and protein expression levels of USP1 were detected by RT-qPCR and Western blot; β-Tubulin was used as an internal control; (c) the representative images of USP1 staining in GC tissues and adjacent normal tissues were shown by immunohistochemistry (IHC); (d) based on the USP1 expression, the overall survival of GC patients were analyzed by Kaplan-Meier curve; (e) data from the TCGA database was further used to analyze the overall survival rate of GC patients ($^{**}p < 0.01$; $^{*}p < 0.05$).

with relatively high expression levels had lower survival rates than those with low expression levels (Figure 2(d)), which was further confirmed by data from TCCA database (Figure 2(e)).

3.2. Stable USP1 Knockdown Inhibits GC Metastasis Both In Vitro and In Vivo. In order to define the exact role of USP1 on GC, USP1 knockdown was performed both in vitro and in vivo. USP1 was highly expressed in all human GC cells compared with normal control (Figures 1(a) and 1(b)). MGC-803 and BGC-823 cells which had relatively higher expression levels of USP1 were transfected with shUSP#1 or shUSP#2, and the efficacy of USP1 knockdown was detected by Western blot (Figure 1(c)). As shown in Figure 1(d), USP1 knockdown significantly inhibited cell migration in MGC-803 and BGC-823 cells in Transwell experiments (Figure 1(d)). Real-time dynamic curves further showed that less number of migrated cells were observed when transfected with shUSP1 (Figure 1(e)). In order to evaluate the effects of USP1 on distant metastasis in vivo, MGC-803 cells transfected with shUSP1 or shNC were inoculated under the splenic capsule of nude mice. USP1 knockdown significantly decreased the number of mice with liver metastasis (Figures 1(f) and 1(g)). Overall, these results demonstrate that USP1 knockdown inhibits GC migration both in vitro and in vivo.

3.3. USP1 Promotes GC Metastasis by Upregulating ID2 Expression. Previous studies have shown that inhibitor of

DNA binding-2 (ID2) is overexpressed in multiple cancers including gastric cancer [28–31]. To define the correlation between USP1 and ID2 in GC, the expression levels of USP1 and ID2 were firstly detected by RT-qPCR and Western blot (Figures 3(a) and 3(b)). Conversely, flag-USP1-mediated USP1 overexpression increased the expression levels of ID2 (Figure 3(c)). Then, BGC-823 and MGC-803 cells were transfected with shUSP1; Western blot results showed that USP1 knockdown significantly decreased the expression levels of ID2 (Figure 3(d)). Thus, we speculated that the mechanism by which USP1-promoted GC migration was associated with upregulating ID2 expression. To confirm our hypothesis, BGC-823 were transfected with shUSP1 and/or his-ID2; Western blot results showed that USP1 knockdown significantly decreased the expression levels of ID2 and reduced the number of migrated cells, which was rescued by ID2 overexpression (Figure 3(e)). Conversely, USP1 overexpression significantly increased the expression levels of ID2 and increased the number of migrated cells, which was inhibited by ID2 knockdown (Figure 3(f)). Overall, these results demonstrate that USP1 promotes GC metastasis by upregulating ID2 expression.

3.4. The Degradation of ID2 Depends on Ub-Proteasome Way in GC. Previous study has shown that ID2 is normally polyubiquitinated and can be rapidly degraded by the Ub-proteasome pathway [31]. For further confirming the ubiquitination and degradation of ID2 in GC, Co-IP assay

(a)

(b)

(c)

(d)
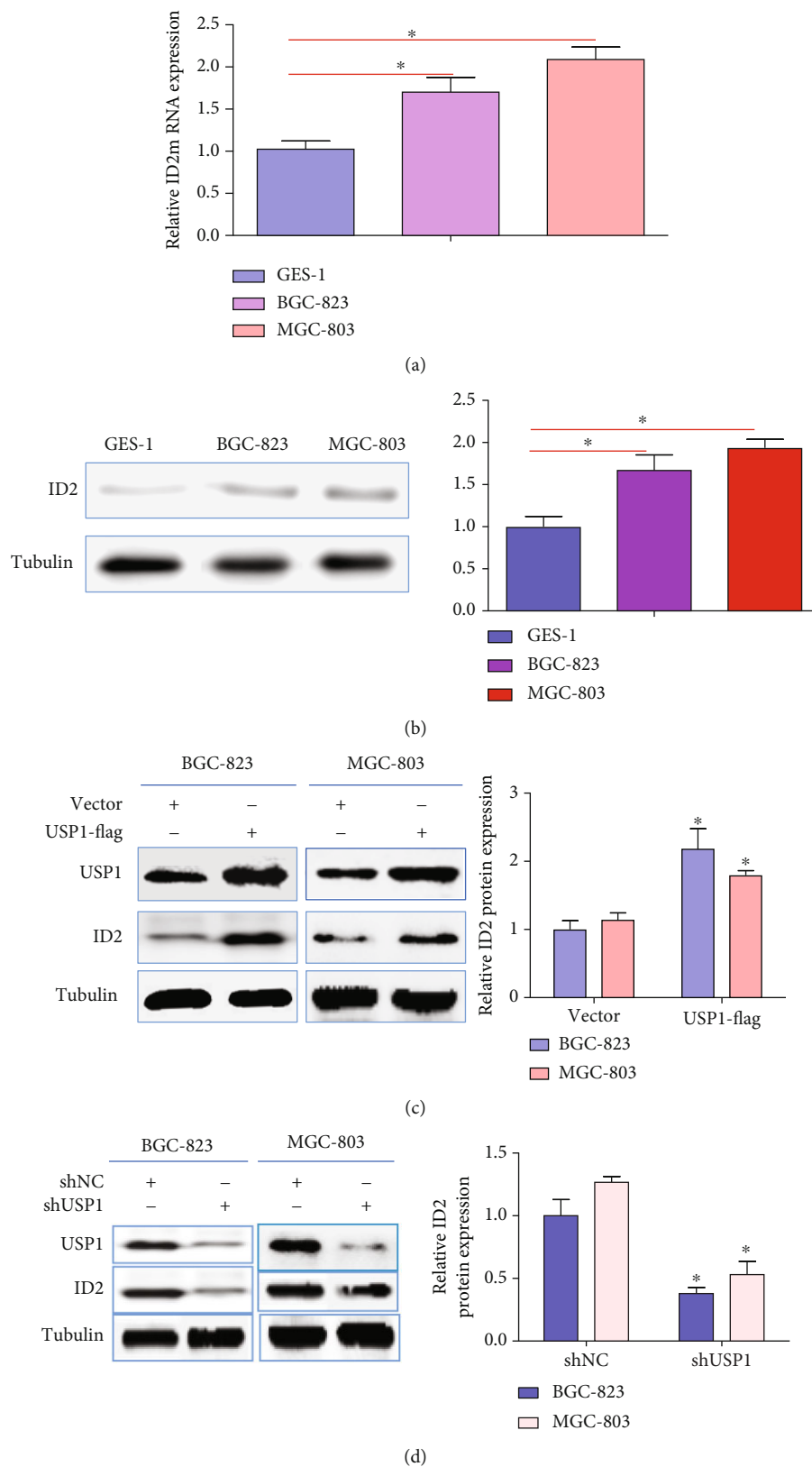
FIGURE 3: Continued.

(e)

(f)
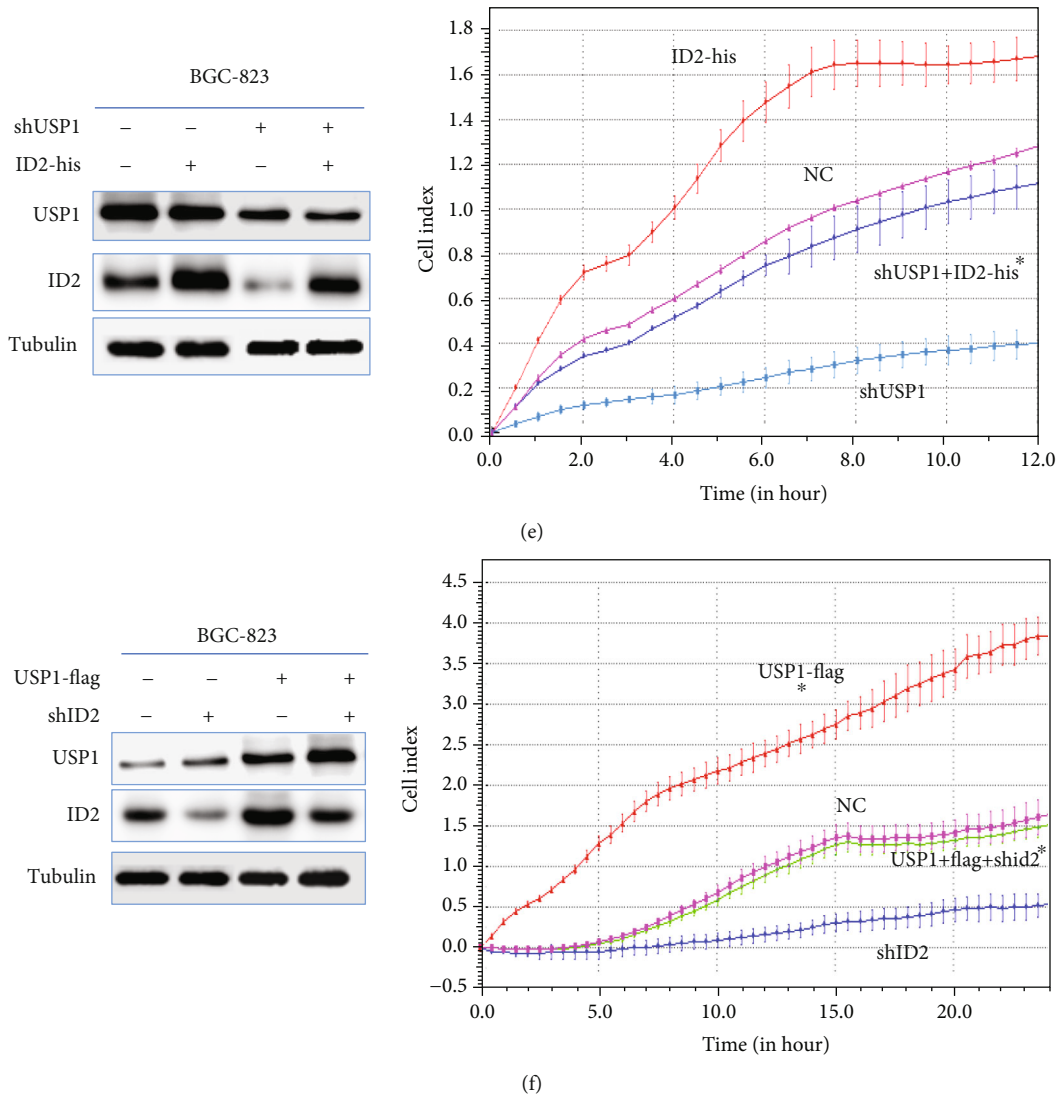
FIGURE 3: USP1 promotes GC metastasis by upregulating ID2 expression. (a, b) The mRNA and protein levels of ID2 in normal gastric mucosa cells and two human GC cells were detected by RT-qPCR and Western blot; (c) MGC-803 and BGC-823 cells were transfected with flag-vector or USP1-flag; the protein expression levels of USP1 and ID2 were detected by Western blot; (d) MGC-803 and BGC-823 cells were transfected with shNC or shUSP1; the protein expression levels of USP1 and ID2 were detected by Western blot; (e) BGC-823 cells were transfected with shUSP11 and/or his- ID2, the protein expression levels of USP1 and ID2 were detected by Western blot, and the effects of cell migration were detected by RTCA. (f) BGC-823 cells were transfected with flag-USP1 and/or shID2, the protein expression levels of USP1 and ID2 were detected by Western blot, and the effects of cell migration were detected by RTCA ($^{**}p < 0.01$; $^{*}p < 0.05$).

between endogenous ID2 and Ub was firstly performed in MGC-803 and BGC-823 cells. As shown in Figure 4(a), ID2 could be detected when Ub was immunoprecipitated. Then, MGC-803 and BGC-823 cells were transfected with increasing amount of HA-Ub and exposed to cycloheximide(CHX). CHX can inhibit protein synthesis by interfering the translation of mRNA [25]. Western blot results showed that the expression levels of ID2 were decreased with increasing expression levels of Ub (Figure 4(b)). In order to define the effect of proteasome on the degradation of ID2, proteasome inhibitors (MG132 and PS-341) [26, 27] were added to MGC-803 and BGC-823 cells; Western blot was used to detect the expression levels of ID2. As shown

in Figures 4(c) and 4(d), endogenous ID2 was accumulated with increasing time. Overall, these results demonstrate that the degradation of ID2 depends on Ub-proteasome way in GC.

3.5. USP1 Stabilizes ID2 Expression through Deubiquitinating ID2 in GC. As a deubiquitinase, USP1 can remove ubiquitin from target protein, so as to inhibit their degradation, whether USP1 stabilizing ID2 expression through its deubiquitination activity in GC was further explored. As shown in Figure 5(a), USP1 overexpression or knockdown increased or decreased ID2 expression, respectively, which was counteracted by proteasome inhibitor PS-341 (Figure 5(a)). Next, in order
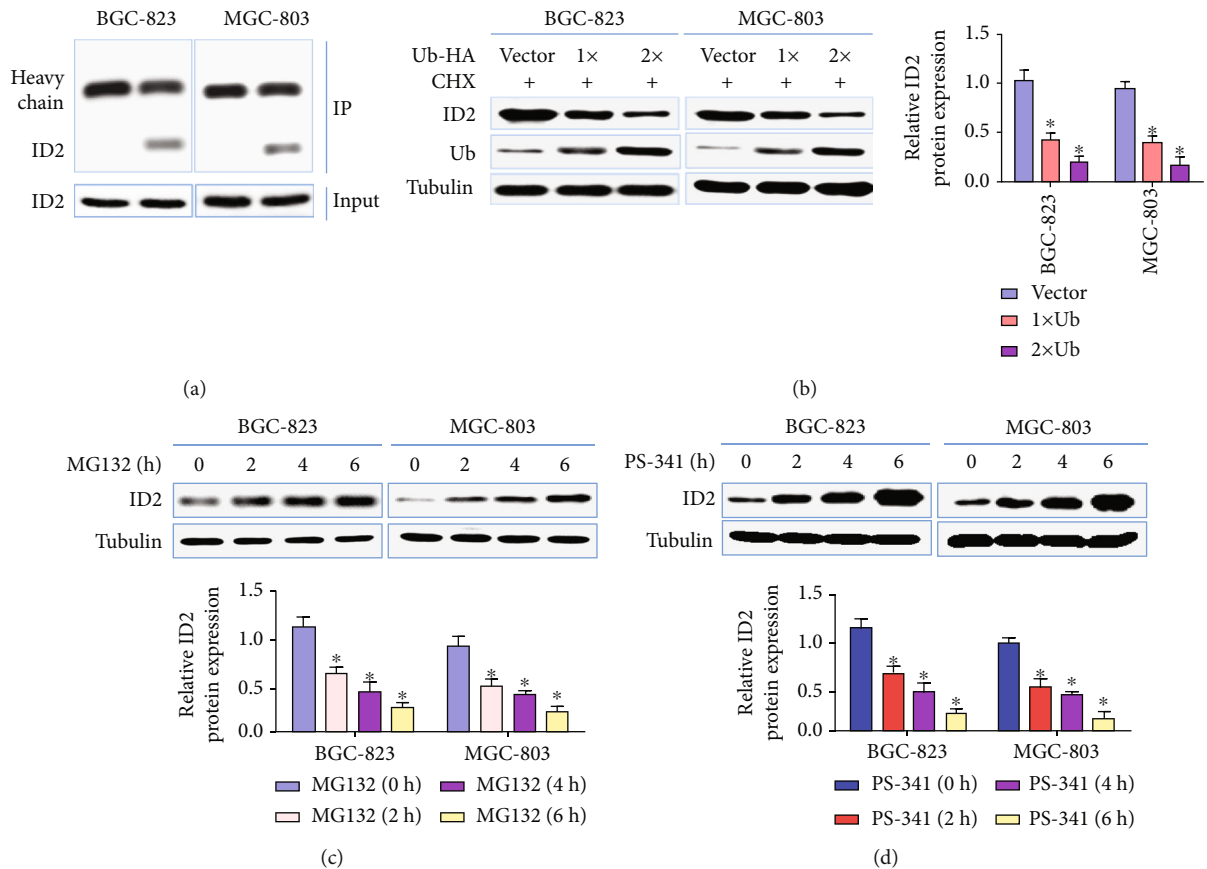
FIGURE 4: ID2 degradation depends on Ub-proteasome way. (a) Coimmunoprecipitation assay was used to detected ubiquitinated ID2 in MGC-803 and BGC-823 cells; (b) MGC-803 and BGC-823 cells were transfected with increasing amounts of HA-Ub, then exposed to CHX; the protein expression levels of ID2 and Ub were detected by Western blot; (c, d), GC-803 and BGC-823 cells were exposed to proteasome inhibitors-MG132 and PS-341, respectively; the protein expression levels of ID2 were detected by Western blot at indicated time after treatment ($^{**}p < 0.01$; $^*p < 0.05$).

to detect the influences of USP1 on the rate of ID21degradation, MGC-803 and BGC-823 cells were transfected with his-ID2 and flag-USP1. As shown in Figure 5(b), USP1 overexpression significantly increased the half-life of ID2. The two experiments confirmed that USP1 stabilized ID2 expression. To test whether USP1 regulates the deubiquitination of ID2, Co-IP assay was firstly performed to define the interaction between endogenous USP1 and ID2. As shown in Figure 5(c), ID2 could be detected when USP1 was immunoprecipitated. Further experiments showed that USP1 knockdown or overexpression significantly increased or decreased the protein expression levels of ubiquitinated ID2, respectively (Figure 5(d)). Overall, these results demonstrate that USP1 stabilizes ID2 expression through deubiquitinating ID2 in GC.

4. Discussion

USP1 is a member of USPs which consists of 785 amino acids with a speculated molecular mass of 88.2 kDa [32]. As a member of USP, USP1 has been indicated important in regulating cancer proliferation and metastasis, such as in osteosarcoma and lung cancer [16, 20]. But the exact role

of USP1 on GC metastasis and the underlying mechanism are still unclear. Our study is the first time to demonstrate that USP1 can promote GC metastasis by stabilizing ID2 expression via deubiquitinating ID2. Firstly, we examined the expression levels of USP1 in GC tissues and adjacent normal tissues and found that USP1 was overexpressed in the GC tissues, and relatively high-expression levels of USP1 conferred poor survival. Consistently, higher expression levels of USP1 were also found in all human GC cells compared with normal control, and USP1 knockdown significantly inhibited GC cell migration and distant liver metastasis. Thus, these results indicated that ID2 may function as an oncogene in GC.

ID2 is a member of four homologous proteins (Id1-Id4) which can dimerize with basic helix-loop-helix (bHLH) proteins and preventing them from binding DNA, so as to negatively regulate their biological functions, such as cell proliferation and differentiation [33, 34]. ID2 has been shown overexpressed in several cancer tissues or cells, such as salivary gland cancer and bladder cancer, and promote cancer invasion, proliferation, and metastasis [35–39]. In our study, consistent with the results in GC tissues [29], ID2 was also overexpressed in GC cells, and USP1 positively

(a)

(b)

(c)

(d)
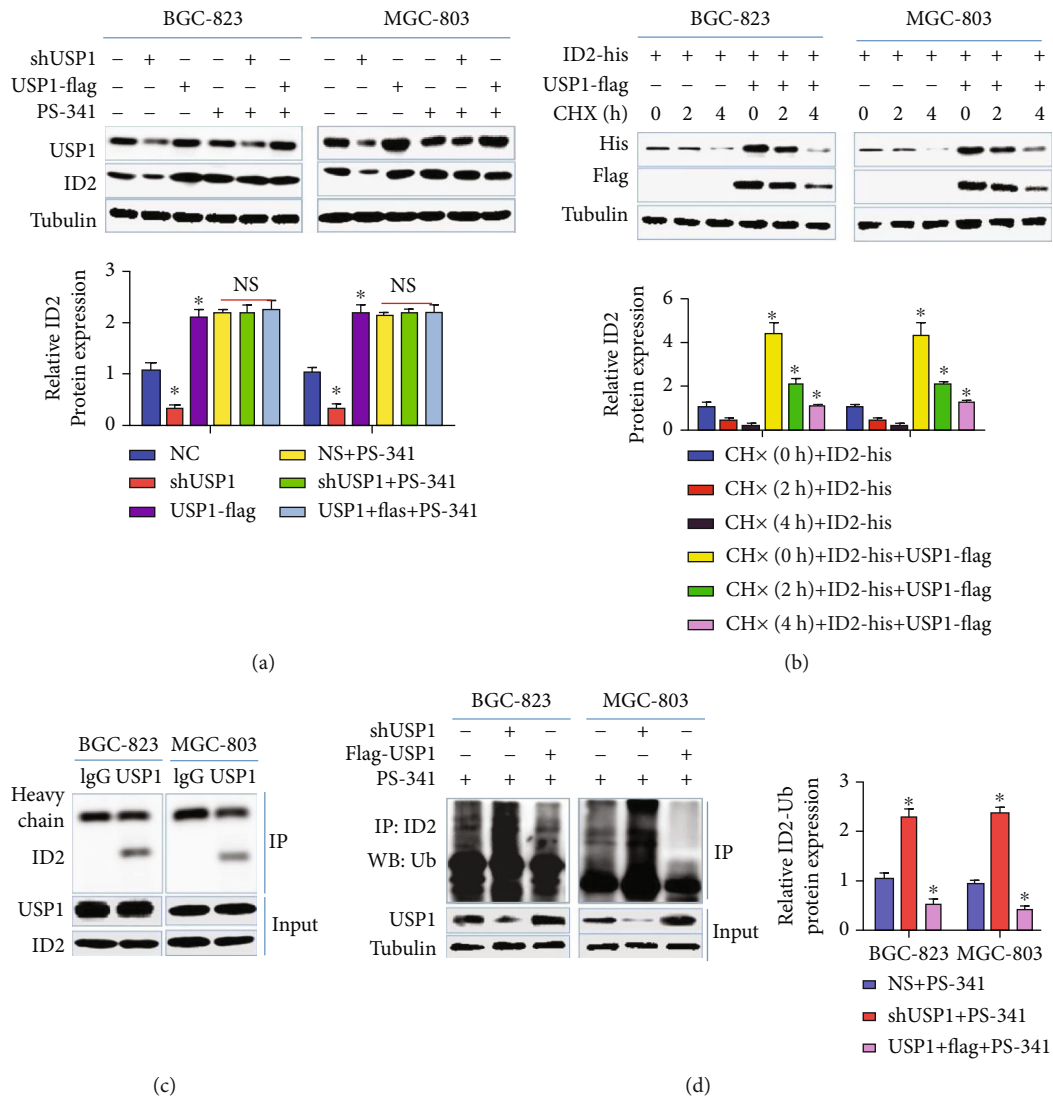
Figure 5: USP1 stabilizes ID2 expression through deubiquitinating ID2. (a) MGC-803 and BGC-823 cells were transfected with shUSP1 or flag-USP1, then exposed to PS-341 or not; the protein expression levels of USP1 and ID2 were detected by Western blot; (b) MGC-803 and BGC-823 cells were transfected with his-ID2 or flag-USP1, then exposed to CHX; the protein expression levels of his-ID2 and flag-USP1 were detected by Western blot at indicated time; (c) the interaction between USP1 and Ub was detected by Co-IP assay in MGC-803 and BGC-823 cells; (d) MGC-803 and BGC-823 cells were transfected with shUSP1 or flag-USP1, then exposed to PS-341; ubiquitinated ID2 was detected by Co-IP assay ($^{**}p < 0.01$; $^*p < 0.05$).

regulated ID2 expression. Moreover, we demonstrated that USP1 promoted GC metastasis by upregulating ID2 expression. And the mechanism by which USP1 regulated ID expression was further explored. Since Ub-proteasome pathway is an important degradation way for ID2, our results confirmed that the degradation of ID2 also depended on Ub-proteasome way in GC cells. As a deubiquitinase, USP1 has been shown to stabilize ID proteins in osteosarcoma cells [40–42]. Our study further confirmed that USP1 can stabilized ID2 expression through deubiquitinating ID2 in GC.

In conclusion, we firstly found that USP1 is overexpressed in GC tissues compared with adjacent normal tissues, and relatively high levels of USP1 conferred poor survival. Mechanically, we demonstrated that USP1 knockdown inhibits GC metastasis, and USP1 promoted GC metastasis

via upregulating ID2 expression. And we further confirmed that USP1 stabilized ID2 expression through deubiquitinating ID2 in GC. Thus, our study provided a new biomarker therapy target for GC.

Data Availability

The data used to support the findings of this study are included within the article.

Conflicts of Interest

The authors declare that they have no competing interest.

Acknowledgments

Supplementary Materials

Supplementary Table 1: primary sequences. *(Supplementary Materials)*

References

[1] L. A. Torre, F. Bray, R. L. Siegel, J. Ferlay, J. Lortet-Tieulent, and A. Jemal, "Global cancer statistics, 2012," *CA: A Cancer Journal for Clinicians.*, vol. 65, no. 2, pp. 87–108, 2015.

[2] L. A. Torre, R. L. Siegel, E. M. Ward, and A. Jemal, "Global cancer incidence and mortality rates and trends-an update," *Cancer Epidemiology and Prevention Biomarkers*, vol. 25, no. 1, pp. 16–27, 2016.

[3] A. Ferro, B. Peleteiro, M. Malvezzi et al., "Worldwide trends in gastric cancer mortality (1980-2011), with predictions to 2015, and incidence by subtype," *European Journal of Cancer*, vol. 50, no. 7, pp. 1330–1344, 2014.

[4] J. Ferlay, I. Soerjomataram, R. Dikshit et al., "Cancer incidence and mortality worldwide: sources, methods and major patterns in GLOBOCAN 2012," *International Journal of Cancer*, vol. 136, no. 5, pp. E359–E386, 2015.

[5] M. Martin-Richard, A. Custodio, C. García-Girón et al., "Seom guidelines for the treatment of gastric cancer 2015," *Clinical and Translational Oncology*, vol. 17, no. 12, pp. 996–1004, 2015.

[6] W. Yang, A. Raufi, and S. J. Klempner, "Targeted therapy for gastric cancer: molecular pathways and ongoing investigations," *Biochimica et Biophysica Acta (BBA) - Reviews on Cancer*, vol. 1846, no. 1, pp. 232–237, 2014.

[7] F. E. Reyes-Turcu, K. H. Ventii, and K. D. Wilkinson, "Regulation and cellular roles of ubiquitin-specific deubiquitinating enzymes," *Annual Review of Biochemistry*, vol. 78, no. 1, pp. 363–397, 2009.

[8] D. Komander, M. J. Clague, and S. Urbé, "Breaking the chains: structure and function of the deubiquitinases," *Nature reviews Molecular cell biology*, vol. 10, no. 8, pp. 550–563, 2009.

[9] K. D. Wilkinson, "Regulation of ubiquitin-dependent processes by deubiquitinating enzymes," *The FASEB Journal*, vol. 11, no. 14, pp. 1245–1256, 1997.

[10] S. M. Nijman, M. P. Luna-Vargas, A. Velds et al., "A genomic and functional inventory of deubiquitinating enzymes," *Cell*, vol. 123, no. 5, pp. 773–786, 2005.

[11] Y. Wang, J. Wang, J. Zhong et al., "Ubiquitin-specific protease 14 (USP14) regulates cellular proliferation and apoptosis in epithelial ovarian cancer," *Medical oncology*, vol. 32, no. 1, p. 379, 2015.

[12] Y. Li, D. Jiang, Q. Zhang, X. Liu, and Z. Cai, "Ubiquitin-specific protease 4 inhibits breast cancer cell growth through the upregulation of PDCD4," *International Journal of Molecular Medicine*, vol. 38, no. 3, pp. 803–811, 2016.

[13] C. Song, W. Liu, and J. Li, "USP17 is upregulated in osteosarcoma and promotes cell proliferation, metastasis, and epithe-

lial–mesenchymal transition through stabilizing SMAD4," *Tumor Biology*, vol. 39, no. 7, p. 101042831771713, 2017.

[14] S. M. B. Nijman, T. T. Huang, A. M. G. Dirac et al., "The deubiquitinating enzyme USP1 regulates the Fanconi anemia pathway," *Molecular Cell*, vol. 17, no. 3, pp. 331–339, 2005.

[15] T. T. Huang, S. M. B. Nijman, K. D. Mirchandani et al., "Regulation of monoubiquitinated PCNA by DUB autocleavage," *Nature Cell Biology*, vol. 8, no. 4, pp. 341–347, 2006.

[16] J. Liu, H. Zhu, N. Zhong et al., "Gene silencing of USP1 by lentivirus effectively inhibits proliferation and invasion of human osteosarcoma cells," *International Journal of Oncology*, vol. 49, no. 6, pp. 2549–2557, 2016.

[17] Y. Liu, X. Luo, H. Hu et al., "Integrative proteomics and tissue microarray profiling indicate the association between overexpressed serum proteins and non-small cell lung cancer," *PLoS One*, vol. 7, no. 12, p. 51748, 2012.

[18] D. S. Das, A. Das, A. Ray et al., "Blockade of deubiquitylating enzyme USP1 inhibits DNA repair and triggers apoptosis in multiple myeloma cells," *Clinical Cancer Research*, vol. 23, no. 15, pp. 4280–4289, 2017.

[19] J. Lee, N. Chang, Y. Yoon et al., "USP1 targeting impedes GBM growth by inhibiting stem cell maintenance and radioresistance," *Neuro-Oncology*, vol. 18, no. 1, pp. 37–47, 2016.

[20] Z. Zhiqiang, Y. Qinghui, Z. Yongqiang et al., "USP1 regulates AKT phosphorylation by modulating the stability of PHLPP1 in lung cancer cells," *Journal of cancer research and clinical oncology*, vol. 138, no. 7, pp. 1231–1238, 2012.

[21] E. Hara, T. Yamaguchi, H. Nojima et al., "Id-related genes encoding helix-loop-helix proteins are required for G1 progression and are repressed in senescent human fibroblasts," *Journal of Biological Chemistry*, vol. 269, no. 3, pp. 2139–2145, 1994.

[22] S. B. Lee, V. Frattini, M. Bansal et al., "An ID2-dependent mechanism for VHL inactivation in cancer," *Nature*, vol. 529, no. 7585, pp. 172–177, 2016.

[23] H. R. Kim, J. H. Moon, J. H. Lee, and Y. C. Lim, "Inhibitor of DNA binding 2 (ID2): a novel marker for lymph node metastasis in head and neck squamous cell carcinoma," *Annals of Surgical Oncology*, vol. 28, no. 11, pp. 6479–6488, 2021.

[24] M. J. Gray, N. A. Dallas, G. van Buren et al., "Therapeutic targeting of Id2 reduces growth of human colorectal carcinoma in the murine liver," *Oncogene*, vol. 27, no. 57, pp. 7192–7200, 2008.

[25] T. Schneider-Poetsch, J. Ju, D. E. Eyler et al., "Inhibition of eukaryotic translation elongation by cycloheximide and lactimidomycin," *Nature Chemical Biology*, vol. 6, no. 3, pp. 209–217, 2010.

[26] J. Adams, V. J. Palombella, E. A. Sausville et al., "Proteasome inhibitors: a novel class of potent and effective antitumor agents," *Cancer Research*, vol. 59, no. 11, pp. 2615–2622, 1999.

[27] K. Harhouri, C. Navarro, D. Depetris et al., "MG132-induced progerin clearance is mediated by autophagy activation and splicing regulation," *EMBO Molecular Medicine*, vol. 9, no. 9, pp. 1294–1313, 2017.

[28] Y. Qiu, D. Huang, Y. Sheng et al., "Deubiquitinating enzyme USP46 suppresses the progression of hepatocellular carcinoma by stabilizing MST1," *Experimental Cell Research*, vol. 405, no. 1, p. 112646, 2021.

[29] H. Y. Yang, H. L. Liu, J. Ke et al., "Expression and prognostic value of id protein family in human breast carcinoma," *Oncology Reports*, vol. 23, no. 2, pp. 321–328, 2010.

[30] Y. Z. Li and P. Zhao, "Expressions and clinicopathologic significance of Id2 and NF-κB/P65 in gastric cancer," *Zhonghua Yi Xue Za Zhi*, vol. 98, no. 11, pp. 846–850, 2018.

[31] S. Zhang, N. Li, Y. Sheng et al., "Hepatitis B virus induces sorafenib resistance in liver cancer via upregulation of cIAP2 expression," *Infect Agent Cancer*, vol. 16, no. 1, p. 20, 2021.

[32] J. P. Coppe, Y. Itahana, D. H. Moore, J. L. Bennington, and P. Y. Desprez, "Id-1 and Id-2 proteins as molecular markers for human prostate cancer progression," *Clinical Cancer Research*, vol. 10, no. 6, pp. 2044–2051, 2004.

[33] M. A. BOUNPHENG, J. J. DIMAS, S. G. DODDS, and B. A. CHRISTY, "Degradation of Id proteins by the ubiquitin-proteasome pathway," *The FASEB Journal*, vol. 13, no. 15, pp. 2257–2264, 1999.

[34] T. Fujiwara, A. Saito, M. Suzuki et al., "Identification and chromosomal assignment of USP1, a novel gene encoding a human ubiquitin-specific protease," *Genomics*, vol. 54, no. 1, pp. 155–158, 1998.

[35] X. H. Sun, N. G. Copeland, N. A. Jenkins, and D. Baltimore, "Id proteins Id1 and Id2 selectively inhibit DNA binding by one class of helix-loop-helix proteins," *Molecular and Cellular Biology*, vol. 11, no. 11, pp. 5603–5611, 1991.

[36] J. D. Norton, R. W. Deed, G. Craggs, and F. Sablitzky, "Id helix–loop–helix proteins in cell growth and differentiation," *Trends in Cell Biology*, vol. 8, no. 2, pp. 58–65, 1998.

[37] S. Zeng, Y. Zhang, J. Ma et al., "BMP4 promotes metastasis of hepatocellular carcinoma by an induction of epithelial-mesenchymal transition via upregulating ID2," *Cancer Letters*, vol. 390, pp. 67–76, 2017.

[38] J. Ma, S. Zeng, Y. Zhang et al., "BMP4 enhances hepatocellular carcinoma proliferation by promoting cell cycle progression via ID2/CDKN1B signaling," *Molecular carcinogenesis*, vol. 56, no. 10, pp. 2279–2289, 2017.

[39] T. Sumida, A. Ishikawa, H. Nakano, T. Yamada, Y. Mori, and P. Y. Desprez, "Targeting ID2 expression triggers a more differentiated phenotype and reduces aggressiveness in human salivary gland cancer cells," *Genes to Cells*, vol. 21, no. 8, pp. 915–920, 2016.

[40] M. Luo, Z. Li, W. Wang, Y. Zeng, Z. Liu, and J. Qiu, "Upregulated H19 contributes to bladder cancer cell proliferation by regulating ID2 expression," *The FEBS Journal*, vol. 280, no. 7, pp. 1709–1716, 2013.

[41] Y. U. Kamata, T. Sumida, Y. Kobayashi, A. Ishikawa, W. Kumamaru, and Y. Mori, "Introduction of ID2 enhances invasiveness in ID2-null oral squamous cell carcinoma cells via the SNAIL axis," *Cancer genomics & proteomics*, vol. 13, no. 6, pp. 493–497, 2016.

[42] S. A. Williams, H. L. Maecker, D. M. French et al., "USP1 deubiquitinates ID proteins to preserve a mesenchymal stem cell program in osteosarcoma," *Cell*, vol. 146, no. 6, pp. 918–930, 2011.

Research Article

Research on the Segmentation of Biomarker for Chronic Central Serous Chorioretinopathy Based on Multimodal Fundus Image

Jianguo Xu,[1] **Jianxin Shen** [iD],[1] **Qin Jiang,**[2] **Cheng Wan,**[3] **Zhipeng Yan,**[2] **and Weihua Yang** [iD][2]

[1]*College of Mechanical and Electrical Engineering, Nanjing University of Aeronautics and Astronautics, Nanjing 210016, China*
[2]*The Affiliated Eye Hospital of Nanjing Medical University, Nanjing 210029, China*
[3]*College of Electronic and Information Engineering, Nanjing University of Aeronautics and Astronautics, Nanjing 210016, China*

Correspondence should be addressed to Jianxin Shen; cadatc@nuaa.edu.cn and Weihua Yang; benben0606@139.com

At present, laser surgery is one of the effective ways to treat the chronic central serous chorioretinopathy (CSCR), in which the location of the leakage area is of great importance. In order to alleviate the pressure on ophthalmologists to manually label the biomarkers as well as elevate the biomarker segmentation quality, a semiautomatic biomarker segmentation method is proposed in this paper, aiming to facilitate the accurate and rapid acquisition of biomarker location information. Firstly, the multimodal fundus images are introduced into the biomarker segmentation task, which can effectively weaken the interference of highlighted vessels in the angiography images to the location of biomarkers. Secondly, a semiautomatic localization technique is adopted to reduce the search range of biomarkers, thus enabling the improvement of segmentation efficiency. On the basis of the above, the low-rank and sparse decomposition (LRSD) theory is introduced to construct the baseline segmentation scheme for segmentation of the CSCR biomarkers. Moreover, a joint segmentation framework consisting of the above method and region growing (RG) method is further designed to improve the performance of the baseline scheme. On the one hand, the LRSD is applied to offer the initial location information of biomarkers for the RG method, so as to ensure that the RG method can capture effective biomarkers. On the other hand, the biomarkers obtained by RG are fused with those gained by LRSD to make up for the defect of undersegmentation of the baseline scheme. Finally, the quantitative and qualitative ablation experiments have been carried out to demonstrate that the joint segmentation framework performs well than the baseline scheme in most cases, especially in the sensitivity and F1-score indicators, which not only confirms the effectiveness of the framework in the CSCR biomarker segmentation scene but also implies its potential application value in CSCR laser surgery.

1. Introduction

CSCR is a macular disease which is characterized by neurosensory retinal detachment (NRD) with or without pigment epithelium detachment (PED) [1–3] and may result in blurred vision, central scotoma, deformed vision, and even permanent visual loss in serious cases. In general, the CSCR can be divided into acute and chronic types [4, 5], among which most acute CSCR patients can be self-healing within 3-4 months without any treatment [6]. However, the chronic cases are difficult to automatically return to normal and have to rely on surgery or drug intervention to block the deterioration of the course. In recent years, the laser surgery intervention has become one of the important means of CSCR

therapy, which plays an effective role in inhibiting the development of CSCR. The traditional laser photocoagulation and micropulse laser photocoagulation are commonly used in CSCR laser surgery. The former employs a laser spot with a diameter of 50 to 100μm to directly act on the leakage area (i.e., the biomarkers), which can block the leakage outlet smoothly. Compared with the former, the latter has a wider range of work, which covers the entire CSCR edema area based on the multipoint scanning mode. In this paper, we mainly focus on the former laser surgery scheme, where the fast and accurate segmentation of biomarkers is the most critical step. Usually, before the traditional laser photocoagulation, the ophthalmologists either manually mark the position of biomarkers on the color fundus image by referring

to the angiography image or mark the position of biomarkers directly on the angiography image (refer to Figure 1) and then make the real-time determination of the laser photocoagulation position according to the marking position and the real fundus field of view during the operation. The time-consuming and laborious situation of manual labeling of biomarkers in the above process is an important factor to drive the related research in this paper. In addition, the exploration of automatic segmentation of biomarkers can also lay a foundation for automatic laser photocoagulation.

As far as we know, the automatic segmentation of CSCR biomarkers in the angiography image has not been widely studied. To the best of our knowledge, Ferreira has carried out relevant research so far [7] and achieved certain success. Specifically, the image processing skills such as image registration, blood vessel segmentation, optic disc detection, image inpainting, and image segmentation were combined to locate the biomarkers based on the angiography image sequence. Despite all this, some of the existing biomarker segmentation methods in fundus images and optical coherence tomography (OCT) images or target detection schemes in natural scenes can provide inspiration for our research work. The automated detection methods [8, 9] were presented to quantify the diabetic macular edema (DME) leakage area based on the angiography image sequence. With the help of image registration, image frame subtraction and vessel segmentation, the interference of normal fundus tissue such as the optic disc and vessels to segment DME biomarkers can be effectively weakened, but the difference is that the Gaussian mixture model is adopted by [9] in the final step for the biomarker segmentation, while Rabbani [8] employed the active contour segmentation algorithm to achieve the above task. Both methods performed well in the segmentation of DME biomarkers. Martinez-Costa [10] designed a scheme for leakage detection, the principle of which is to classify those pixels with a high increment in gray level within the closest area to the foveal center as the biomarkers due to retinal vein occlusion. However, this method requires manual location of the macular center. A biomarker detection framework [11] of choroidal neovascularization (CNV) was proposed, which is of great significance for the qualitative analysis of age-related macular degeneration (AMD), but more analytical techniques need to be introduced to fully count biomarker information. For studying the malarial retinopathy, a novel framework [12] was put forward to automatically detect the corresponding biomarkers, the performance of which was excellent with the introduction of saliency technique. On this basis, they developed the saliency detection method based on the intensity and compactness [13], further highlighting the advantages of the framework in the detection of biomarkers for malaria retinopathy and diabetic retinopathy.

In addition, with the development of machine learning technology, many methods based on this paradigm have emerged in the biomarker detection scenarios of various diseases, such as the discovery of biomarkers for early lung cancer diagnosis [14], predicting long-term mortality [15], the exploration of electroencephalography biomarker for Parkinson's disease classification [16], the biomarker localization of pectoralis muscle area, subcutaneous fat area and liver mass area [17], and the detection of biomarkers for multiple myeloma discrimination [18]. Besides, the machine learning method also shows its capability in the task of biomarker detection of fundus diseases. Based on the Adaboost algorithm, Tsai [19] developed an automatic biomarker segmentation method for accurate diagnosis of choroidal neovascularization. With the help of the same classifier and context knowledge, Trucco [20] achieved the localization of ischemic regions in the angiography images. To realize the joint segmentation and quantification of chorioretinal biomarkers, a residual learning-based framework integrating the atrous spatial pyramid pooling, coherent preprocessing, and postprocessing mechanisms was established, and 11 biomarkers were successfully detected [21]. Although the machine learning based method has achieved remarkable performance in all kinds of biomarker detection, this scheme is mostly driven by a large number of the labeled data, which will cause high cost of data collection and label making. Moreover, the small proportion of CSCR biomarkers in the whole image will lead to the imbalance between target pixels and background pixels, weakening the ability of machine learning method in the biomarker detection task.

However, the recently popular LRSD theory provides an effective solution for small target detection. Inspired by this theory, Gao [22] regarded the small target detection in infrared image as an optimization problem of recovering the low-rank and sparse matrices, and the scheme gained better detection performance. A LRSD-based method was put forward by Biondi [23] and able to extrapolate the sparse objects of interest in the synthetic aperture radar images. Meanwhile, the LRSD theory has also made some achievements in medical image biomarker segmentation task. Shi [24] developed an automatic segmentation method that leverages the LRSD techniques for accurate and robust detection of pathological organ from the CT images. To detect several specific types of biomarkers caused by various retinal diseases, the background of fundus image was modeled as a low-rank part, followed by the optimization algorithm and subtraction operation to achieve the final detection of biomarkers [25]. The application of the LRSD theory in the above tasks supplies us with a lot of inspiration for the task of accurate and rapid acquisition of CSCR biomarkers in this paper. The main contributions of our research are as follows: (1) we firstly introduce the multimodal fundus images into the CSCR biomarker segmentation task to avoid the interference of highlighted vessels on the location of biomarkers. (2) A simple yet effective semiautomatic localization technique is employed to reduce the search range of biomarkers, which is conducive to the improvement of segmentation efficiency. (3) To the best of our knowledge, the LRSD theory is integrated with the multimodal fundus images mentioned in (1) and the localization technique mentioned in (2) for the first time, which preliminarily realizes the construction of the baseline segmentation scheme in the CSCR biomarker segmentation task. (4) To further improve the segmentation performance of the above scheme, a joint segmentation framework consisting of the baseline scheme and RG method is designed, which is not only beneficial for the effective segmentation of CSCR biomarkers by RG, but also makes
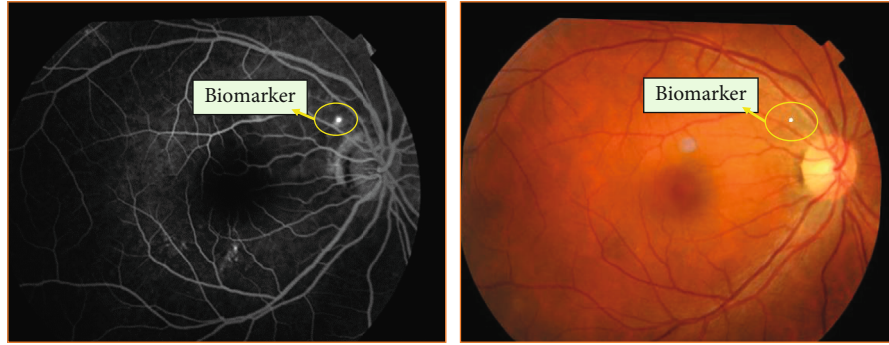
FIGURE 1: The biomarkers on the angiography and color fundus images.

up for the defect of undersegmentation of the baseline scheme. (5) The qualitative and quantitative ablation experiments are performed to verify the effectiveness of the proposed baseline segmentation scheme and the joint segmentation framework.

The rest of the paper is organized as follows. Section 2 presents the materials and detailed methods. Section 3 describes experimental results and discussion. Section 4 concludes this paper.

2. Materials and Methods

2.1. Materials. A total of 32 multimodal CSCR fundus image pairs are employed in the experiment of CSCR biomarker segmentation task, and the patient information involved in these images is processed to prevent the disclosure of privacy content. In addition, in order to utilize the multimodal information, we employ the method [26] to achieve the consistency of the spatial position between the angiography and color fundus images. Moreover, the ground truth of the CSCR biomarkers used in the experiment is annotated by three ophthalmologists to objectively test and evaluate the effectiveness of the proposed methods in the scene of CSCR biomarker segmentation.

2.2. Related Methods. This section focuses on the application and principle analysis of LRSD theory and RG method, which can lay the foundation for the segmentation task of CSCR biomarkers in this paper. To begin with, the LRSD-based method not only performs well in the task of target detection in natural scenes [22, 23, 27] but also has been successfully applied to the segmentation of lesions and organs in medical images [24, 25]. In general, target detection in natural scenes is realized by optimizing a paradigm in which the image background and the object to be detected are represented as L (i.e., low-rank matrix) and S (i.e., sparse matrix), respectively. In this way, target detection is cleverly transformed into the problem of solving low-rank matrix and sparse matrix in the mathematical field. The optimization problem can be expressed as follows:

$$(L, S) = \arg \min_{L,S} \ \text{rank}\,(L) + \lambda \|S\|_0, \text{ subject to } M = L + S, \quad (1)$$

where M is the observation matrix (i.e., the image matrix), and λ is the positive regularization parameter. $\|S\|_0$ represents the l_0-norm (i.e., the number of nonzero entries in S). However, the solution of Eq. (1) is a NP-hard problem due to the nonconvexity of the matrix rank and the l_0-norm. In this case, a relaxation scheme can replace (1), which can be written as follows:

$$(L, S) = \arg \min_{L,S} \ \|L\|_* + \lambda \|S\|_1, \text{ subject to } M = L + S, \quad (2)$$

where $\|L\|_*$ denotes the nuclear norm of the matrix L (i.e., the sum of singular values of L), and $\|S\|_1$ is the l_1-norm that represents the sum of the absolute values of S (i.e., $\|S\|_1 = \sum_{i,j} |S_{ij}|$). Under certain assumptions, L and S can be obtained based on the robust principal component analysis (RPCA) [28].

Furthermore, as a simple yet effective image segmentation technique, the RG method has been extensively utilized in the field of medical image processing and analysis, such as the segmentation of chondroblastoma in the X-ray image [29] and the brain segmentation in the CT and MRI images [30, 31]. The basic principles of the algorithms in the above applications are consistent, which divide the image into different regions according to the similarity between pixels, and the specific implementation steps involve the selection of seed points, the construction of growth rules, and the design of termination conditions. Although the RG method has a good performance in the medical image segmentation task, its accurate and fast seed point selection operation is still an issue to be overcome, which is of great significance to improve its segmentation quality and efficiency. In view of this situation, we propose a joint segmentation framework to make the RG method perform more remarkable in the segmentation task of CSCR biomarkers.

2.3. The Proposed Methodology. The successful application of the LRSD theory and RG method provides inspiration for us to carry out the CSCR biomarker segmentation task. On this basis, we further extend the above methods from the perspective of technique integration and apply the proposed methods to the segmentation of CSCR biomarkers. In general, a baseline segmentation scheme integrating multimodal fundus images, semiautomatic localization technique, and

LRSD theory is presented, which initially achieves the goal of rapid acquisition of biomarker location information. The specific steps are shown in Figure 2.

Step one: this step consists of the man-machine interactive and preprocessing operations. In order to speed up the location of biomarkers, the man-machine interactive operation (i.e., semiautomatic localization technique) is implemented on the angiography images, which is to initially lock the biomarker area through manual box selection mode and can thus avoid the mathematical operation on the whole image matrix. The location information of the box will be transferred to the color fundus image synchronously to ensure that the same area can be extracted. After that, the preprocessing operation composed of the green channel separation and contrast limited adaptive histogram equalization (CLAHE) is applied to the color fundus image block to obtain the preprocessed image block I_c for facilitating the subsequent vessel segmentation.

Step two: in this procedure, the vessel segmentation operation and the image inpainting operation are performed continuously. Firstly, the Laplacian of Gaussian (LoG) operation is performed on the preprocessed image block I_c in the previous step to obtain the blood vessels. The specific formulas can be expressed as follows:

$$\text{LoG}(r, c) = -\frac{1}{\pi\sigma^4}\left[1 - \frac{r^2 + c^2}{2\sigma^2}\right]e^{-\frac{r^2+c^2}{2\sigma^2}}, \quad (3)$$

$$G(x, y) = \sum_{r=-k}^{k}\sum_{c=-l}^{l}\text{LoG}(r, c)Ic(x + r, y + c), \quad (4)$$

where σ denotes the standard deviation with a value of 3, and (r, c) is the coordinate of the element in the LoG filter. k and l are the nonnegative integers that are both set to 3 in this paper. $G(x, y)$ represents the spatial filtering result of image I_c, and (x, y) is the coordinate of the corresponding element. Then, the final vessel mask can be acquired though a simple postprocessing mainly consisting of the binarization and small area removal processes. On this basis, the image inpainting technique [32] is adopted to weaken the highlighted vessel area in the angiography image block I_a and fill it with the surrounding background pixels.

Step three: after the image inpainting operation, the CSCR biomarker segmentation model is then established based on the LRSD theory and the inpainting image G_P. Considering that the fundus image is not absolutely pure, the noise in the image needs to be taken into account in the modeling process. Thus, the image G_P can be represented as Eq. (5).

$$Gp = L + S + N, \quad (5)$$

where N is the noise part of the image G_P (i.e., the observation matrix M) and is assumed to be independent and identically distributed(i.e., i.i.d.) in this paper. According to the conditions in [33], L and S can be achieved with the assumption $\|N\|_F \leq \delta$ for some $\delta > 0$, and then Eq. (2) can

be converted into the following relaxed version:

$$(L, S) = \arg\min_{L,S} \|L\|_* + \lambda\|S\|_1, \text{subject to } \|Gp - L - S\|_F \leq \delta. \quad (6)$$

The dual form of Eq. (6) can be expressed as follows:

$$(L, S, N) = \arg\min_{L,S,N} \|L\|_* + \lambda\|S\|_1 + \frac{1}{2\mu}\|N\|_F^2, \text{subject to } Gp$$
$$= L + S + N, \quad (7)$$

where $\|N\|_F$ denotes the Frobenius norm (i.e., $\|N\|_F = \sqrt{\sum_{i,j}N_{ij}^2}$). μ is a positive weight parameter. As usual, the Accelerated Proximal Gradient (APG) [34] is applied to recover L and S in this paper. Besides, in order to solve Eq. (7) more effectively, the patch-image model [22] is employ to reconstruct G_P, and the corresponding patch size and sliding step are set to 50×50 and 10, respectively. In view of the stability and accuracy of the APG method in the infrared target detection task, the experimental setup of this part is consistent with [22] in which the detailed parameters can be found. Then, the postprocessing operations mainly including the searching and sorting of connected regions are performed on S to promote the generation of the final CSCR biomarker block S_P.

Final step: although the semiautomatic localization technique accelerates the segmentation efficiency of CSCR biomarkers, it will cause the spatial positions of biomarkers obtained in the previous step to be inconsistent with their original positions. Therefore, in this step, the initial box position information is utilized to restore S_P to the original color fundus and angiography images, which is essential to provide effective position information of biomarkers for the ophthalmologists and automatic laser equipment.

In the above scheme, the introduction of multimodal fundus images weakens the interference of the highlighted vessels in the angiography image to the location of biomarkers, and the utilization of semiautomatic localization technique improves the efficiency of biomarker localization. Meanwhile, the LRSD theory transforms the task of biomarker segmentation into the problem of low-rank and sparse matrix decomposition, which is not only conducive to the effective location locking of biomarkers but also accelerates the efficiency of biomarker segmentation to a certain extent. Nevertheless, this scheme may cause the problem of undersegmentation, which leads to the inaccurate segmentation results, and thus stimulates the further design of a joint segmentation framework (refer to Figure 3 for the framework). Specifically, we combine the RG method with the above scheme. On the one hand, the LRSD theory is employed to provide the initial seed points for the RG method to ensure that it can obtain effective biomarkers. On the other hand, the segmentation results obtained by
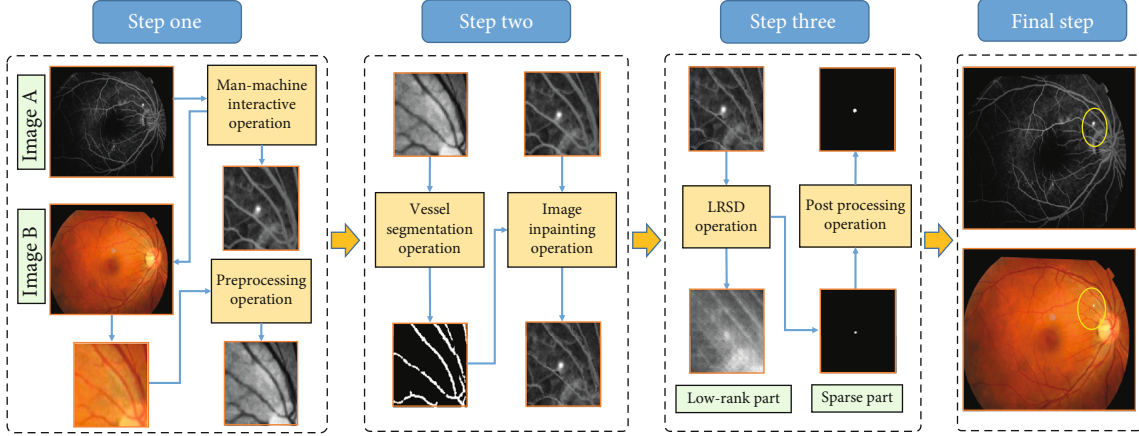
FIGURE 2: The schematic diagram of the baseline segmentation scheme.
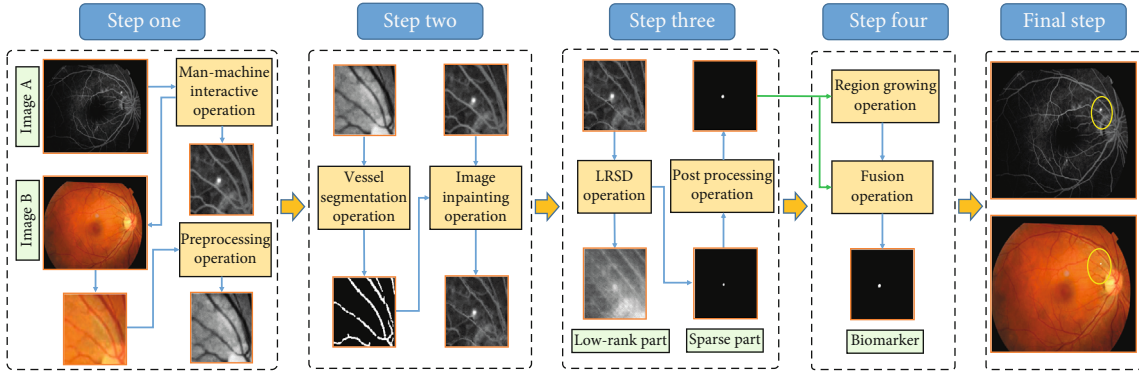
FIGURE 3: The schematic diagram of the joint segmentation framework.

RG and LRSD are fused to make up for the undersegmentation defect of the baseline segmentation scheme.

As shown in Figure 3, after the step three of baseline segmentation scheme, the step four is followed closely. Firstly, the position information of biomarkers in S_P is extracted to provide the initial region growing point for the RG method. Secondly, the biomarkers are automatically segmented based on the RG method under the condition of a given threshold. Then, the segmentation results of the two schemes are fused to get the final biomarkers. The process can be formulated as follows:

$$\left(S_d^x, S_d^y\right) = \arg \max_{S_d^x, S_d^y} Spd(1 : K1, 1 : K2), d \in [1, K], \quad (8)$$

$$Rpd = \mathrm{RG}\left(Ia, S_d^x, S_d^y, T\right), \quad (9)$$

$$FS = \sum_{d=1}^{K} (Spd + Rpd), \quad (10)$$

where K is the number of the biomarkers in the final CSCR biomarker block S_P, and S_{Pd} corresponds to the image block only containing the d-th biomarker. The size of S_P is $K_1 \times K_2$, and $\left(S_d^x, S_d^y\right)$ denotes the position information of the d-th biomarker in S_P. T is the threshold that is varied from 0.1 to 0.2 with a step size of 0.02. R_{pd} represents the segmented result of

the d-th biomarker by the RG method. F_S is the fusion result of the biomarkers acquired by the baseline segmentation scheme and RG method. Then, the operation in the final step of the baseline segmentation scheme is also performed on F_S to obtain the final CSCR biomarkers. The pseudocode of step four is as follows:

3. Results and Discussion

3.1. The Evaluating Indicators and Experimental Settings. In order to quantitatively evaluate the performance of baseline scheme and joint scheme in the CSCR biomarker segmentation task, sensitivity, F1-score, accuracy, and specificity are introduced as the evaluation indicators. The details are as follows:

$$\mathrm{Sensitivity} = \mathrm{TP}/(\mathrm{TP} + \mathrm{FN}), \quad (11)$$

$$\mathrm{F1\text{-}score} = 2\mathrm{TP}/(2\mathrm{TP} + \mathrm{FN} + \mathrm{FP}), \quad (12)$$

$$\mathrm{Accuracy} = (\mathrm{TP} + \mathrm{TN})/(\mathrm{TP} + \mathrm{FN} + \mathrm{TN} + \mathrm{FP}), \quad (13)$$

$$\mathrm{Specificity} = \mathrm{TN}/(\mathrm{TN} + \mathrm{FP}), \quad (14)$$

where the manually annotated biomarker pixels that are correctly segmented are defined as true positives (TP) and those that are wrongly segmented are false negatives(FN).
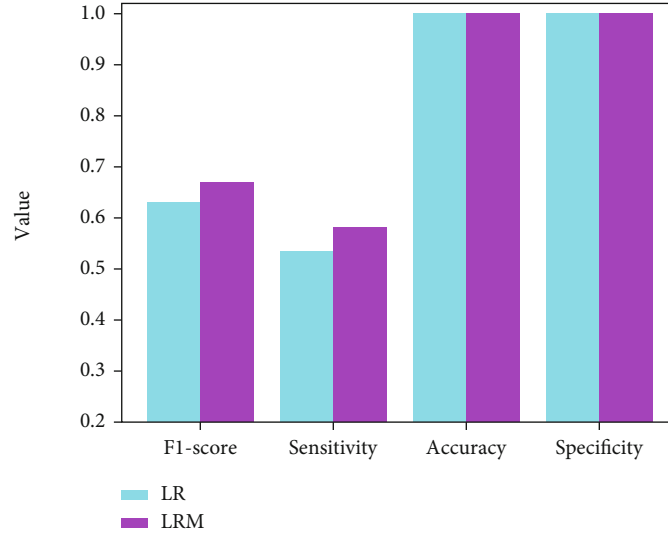
FIGURE 4: The comparison of LRM and LR.
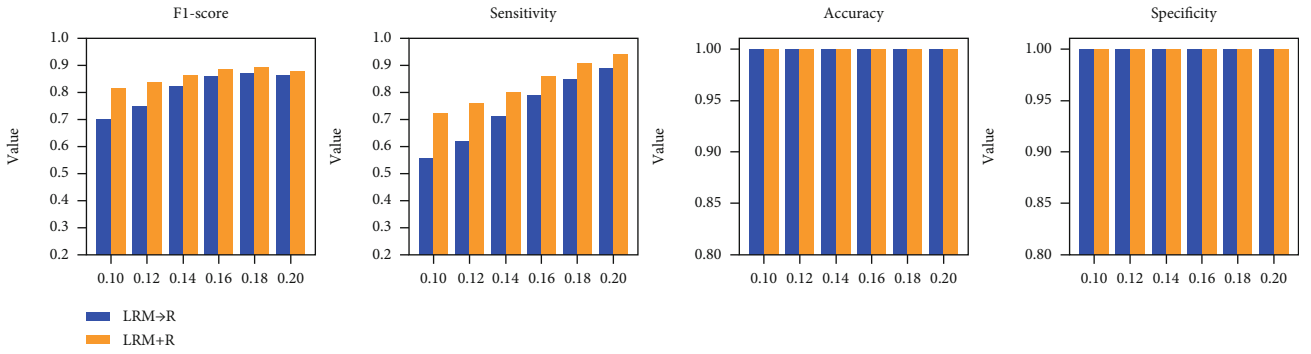
FIGURE 5: The comparison of LRM ⟶ R and LRM + R under the condition of various thresholds.
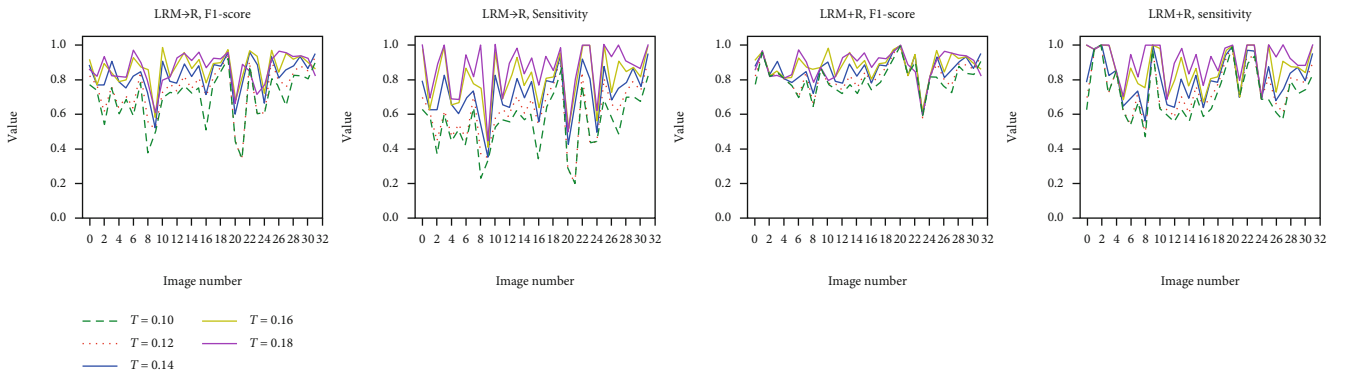
FIGURE 6: The comparison of LRM ⟶ R and LRM + R on each image with various thresholds.

Similarly, the manually annotated nonbiomarker pixels that are correctly identified are true negatives (TN), and the wrongly specified nonbiomarker pixels are false positives (FP). In addition, the ablation experiments are carried out carefully to show the rationality and effectiveness of the proposed schemes.

For convenience, the baseline segmentation scheme in this paper is represented by LRM, and the version of this scheme without the multimodal technique is marked as LR.

Meanwhile, the proposed joint segmentation framework is denoted by LRM + R, and its version without the fusion module is represented by LRM ⟶ R, which means that the LRSD is only applied to offer the initial seed points for the RG method.

3.2. The Discussion of Segmentation Results of Baseline Scheme. This section analyzes the performance of baseline segmentation scheme LRM. As shown in Figure 4, when
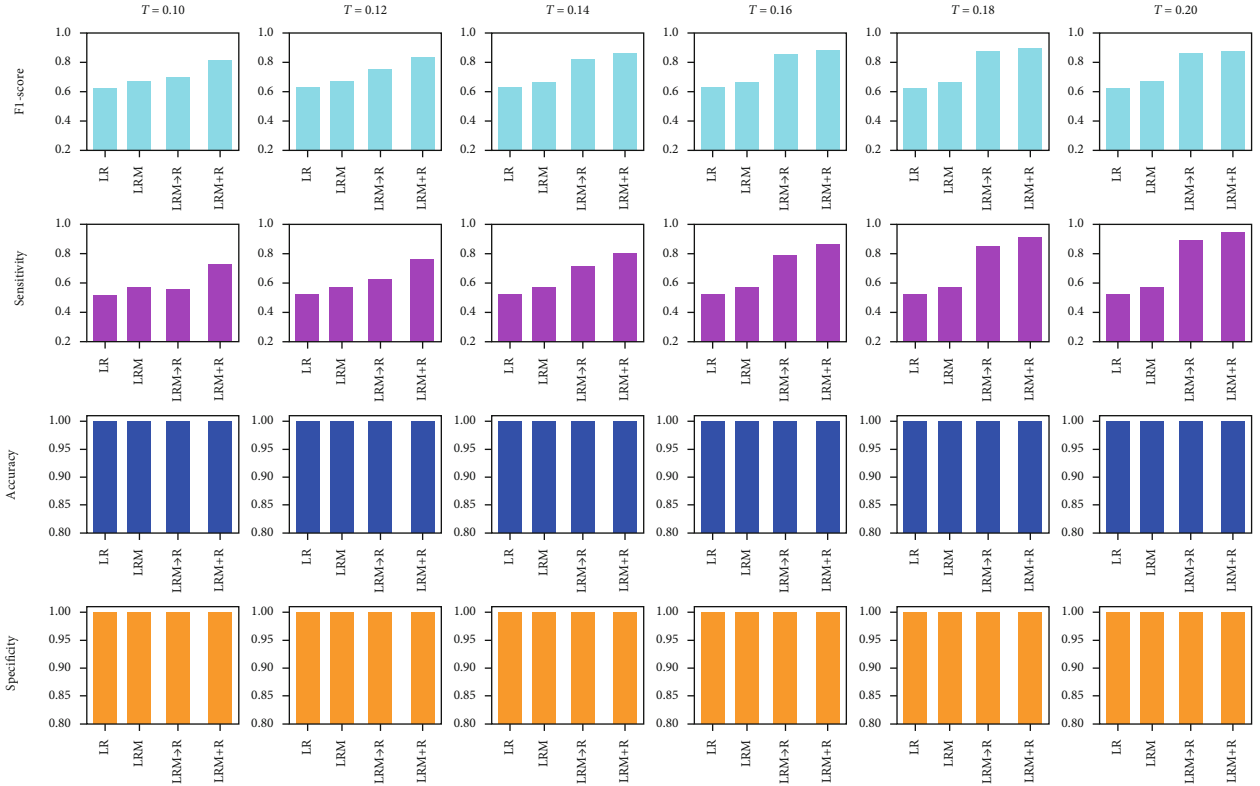
FIGURE 7: The overall comparison of the four schemes.
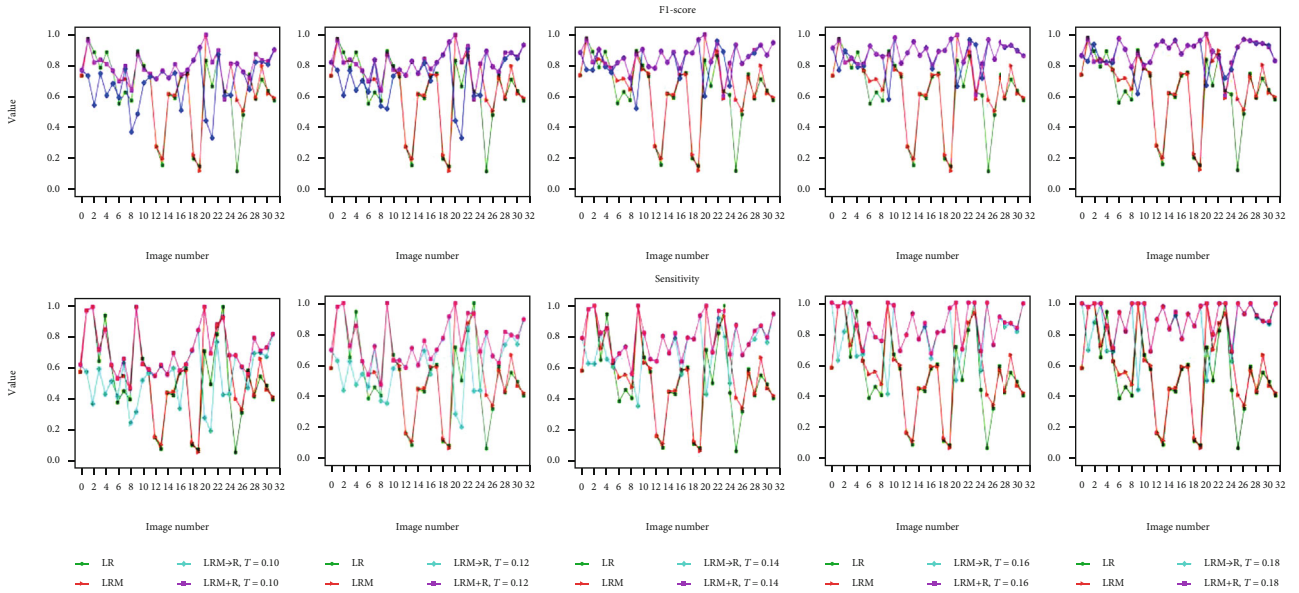
FIGURE 8: The performance of four schemes on each image.

the multimodal technique is not adopted, LR is significantly inferior to LRM in terms of F1-score and sensitivity indicators, which also implies the effectiveness and importance of introducing the multimodal fundus images into the CSCR biomarker segmentation task. Additionally, it can be clearly found that both LR and LRM have achieved more than 90% in the other two indicators, and the difference of the same indicators is not obvious.

This is mainly credited to the introduction of the semiautomatic location technique, which reduces the detection range of CSCR biomarkers and thus greatly decreases the false positives.

3.3. The Discussion of Segmentation Results of Joint Framework. Figure 5 shows the performance of LRM $\longrightarrow$ R and LRM + R in the CSCR biomarker segmentation scene.
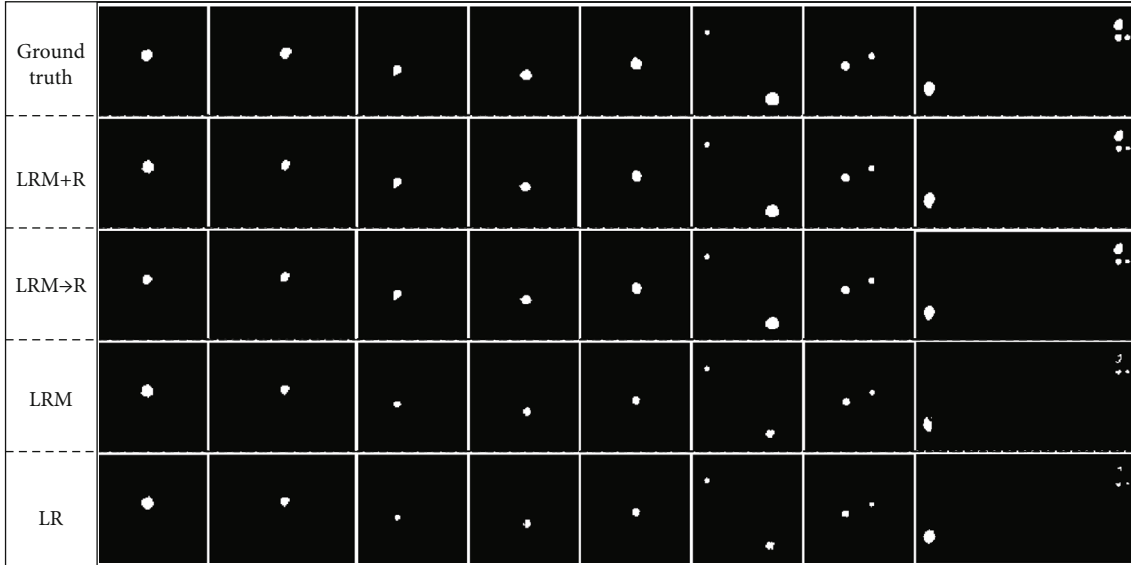
FIGURE 9: The segmentation results of CSCR biomarkers.

It should be noted that this figure is the overall performance of the two schemes on 29 image pairs. The reason is that the two schemes cannot work well on the other three image pairs when the threshold is set to 0.2, which also contributes to the threshold selection of the experiment from one of the perspectives. Further, with the threshold increasing from 0.1 to 0.18, the two schemes reveal an increasing trend in terms of F1-score and sensitivity indicators and obtain the best segmentation results at 0.18. Meanwhile, LRM + R is better than LRM $\longrightarrow$ R in these two indicators, which conveys the necessity of the fusion technique. For the other two indicators, the two schemes perform well, the reason of which is consistent with LR and LRM.

According to the above analysis, 0.2 is not an appropriate threshold for the CSCR biomarker segmentation task. In view of this, we observe the specific performance of the two schemes on 32 image pairs based on the other five thresholds. On the whole, it can be seen from Figure 6 that the performance of the two schemes is improved with the increase of threshold in terms of F1-score and sensitivity indicators. However, with the participation of the fusion technique, LRM + R can significantly create a smaller gap under different threshold conditions compared with LRM $\longrightarrow$ R, which reveals that the joint segmentation framework can lower the impact of threshold parameters on the segmentation performance of the model and thus alleviates the pressure of threshold selection to a certain extent. Moreover, the fluctuations of the two indicator values of each image pair based on the joint segmentation framework are less than those based on LRM $\longrightarrow$ R in most cases and show that LRM + R possesses better robustness in the biomarker segmentation task.

3.4. The Display and Discussion of Ablation Experiment Results. This section shows and discusses the overall performance of the four schemes. Figure 7 is the statistical results of four indicators of ablation experiment on 29

TABLE 1: The average values of F1-score and accuracy indicators.

Methods	T	F1-score/%	Sensitivity/%
LRM + R	0.10	80.2341	72.2436
	0.12	82.4836	75.5831
	0.14	85.7589	80.5158
	0.16	88.3595	86.9361
	0.18	88.3972	91.5447
LRM $\longrightarrow$ R	0.10	69.3491	54.8737
	0.12	74.0886	60.8251
	0.14	82.6932	71.8034
	0.16	86.6628	80.4348
	0.18	86.6598	86.0336
LRM		67.0231	58.0845
LR		62.9971	53.3516

images, in which the performance of four schemes can be clearly displayed. On the one hand, the introduction of semiautomatic localization technique promotes the four schemes to obtain higher accuracy and F1-score values. On the other hand, the segmentation ability of the joint segmentation framework designed on the basis of LRM is further enhanced under different thresholds, and the two indicator values of this framework exceed 80% when the threshold is greater than 0.12. Simultaneously, the independent performance (refer to Figure 8) of the four schemes on 32 images not only further demonstrates the effectiveness of the baseline segmentation scheme but also proves the necessity of further upgrading it to obtain LRM + R.

Furthermore, in order to convey the ablation experiment results more intuitively, some of the CSCR biomarker segmentation results achieved by the four schemes with the threshold of 0.18 are shown in Figure 9. It can be found that LRM is better than LR in most cases, but it has the defect of

---

Input: S_P, K, K_1, K_2, I_a, T;
    For $d = 1:K$
        Calculate the coordinate of seed point (S_d^x, S_d^y) by Eq. (8);
        Set the initial value of $\delta = 0$;
        Set the initial value of pixelnumber $Pn = 1$;
        Set the number of neighborhoods $Nd = 4$;
        Set the initial average gray value of the segmented region $Ra = I_a (S_d^x, S_d^y)$;
        While $Pn < K_1 \times K_2$.
            1: Calculate the δ value of each pixel in the neighborhood of the current seed point (S_d^x, S_d^y) by $\delta = |Ia(S_{di}^x, S_{di}^y) - Ra|$, $i = 1, 2, 3, Nd$ if $\delta < T$, add these pixels into R_{Pd};
            2: Calculate the average gray value Ra of the current segmentation region R_{Pd};
            3: $Pn = Pn++$; Update the seed point (S_d^x, S_d^y);
        End.
    End.
    Calculate F_S by Eq. (10).
Output F_S;

PSEUDOCODE 1: The pseudocode.

undersegmentation when compared with the ground truth. Although the LRM $\longrightarrow$ R scheme avoids the tedious matter of manually selecting seed points and almost exceeds the LRM in the actual segmentation task, the threshold factor makes it not always perform well. In this case, the proposed joint segmentation framework improves LRM $\longrightarrow$ R partly, in which the fusion technique based on the LRSD theory and RG method increases the true positives.

Finally, we discuss the CSCR biomarker segmentation results in the ablation experiments quantitatively. Table 1 records the average indicator values of 32 images segmentation results acquired by the four schemes under five thresholds (i.e., 0.1, 0.12, 0.14, 0.16 and 0.18). Of note, since the previous qualitative analysis has shown that the other two indicators of the four schemes are very high and lack of significant distinction, only the Accuracy and F1-score are taken into consideration here. As shown in Pseudocode 1, the proposed baseline segmentation scheme exceeds LR by 4.026% and 4.7329%, respectively, in the two indicators, which is an affirmation of the multimodal technique in weakening the interference of highlighted vessels to the location of CSCR biomarkers in the angiography images. On this basis, LRM $\rightarrow$ R works well under different thresholds and achieves more than 86% of the indicator value when the threshold is set to 0.18, which means that LRSD can provide an effective initial seed points for the RG method and then promote the segmentation of real CSCR biomarkers. However, this scheme may be limited by the thresholds, thus resulting in insufficient segmentation of the CSCR biomarkers. Fortunately, experiments show that the joint segmentation framework can alleviate this problem. It can be found that LRM + R has made significant progress, and the indicator values at the maximum threshold are 88.3972% and 91.5447%, respectively, which are 1.7374% and 5.5111% higher than those of LRM $\longrightarrow$ R and 21.3741% and 33.4602% higher than those of LRM. This demonstrates the superiority of the proposed joint segmentation framework.

4. Conclusions

In this paper, two CSCR biomarker segmentation methods are proposed to locate the leakage area efficiently and accurately, which can assist laser surgery in the treatment of chronic CSCR. Firstly, a baseline segmentation scheme integrating the multimodal fundus images, semiautomatic localization technique, and LRSD theory is proposed, which is not only the first attempt of LRSD in locating the CSCR leakage area, but also the preliminary realization of rapid acquisition of these biomarkers. Then, a joint segmentation framework is further designed to improve the above method, aiming at enabling the LRSD to supply the effective seed points to the RG method and making up for the defect of undersegmentation of baseline scheme. Qualitative and quantitative experiments demonstrate the feasibility of the baseline scheme to obtain the biomarkers and the effectiveness of the joint segmentation framework in improving the segmentation quality. In the future, the fully automatic CSCR biomarker segmentation method equipped with high segmentation quality and efficiency will be further explored based on the above research to fulfill the requirements of real-time locking CSCR biomarkers in automatic laser surgery.

Data Availability

The data used and analyzed in our research are available from the corresponding author upon request.

Conflicts of Interest

The authors declare that they have no conflict of interests regarding this paper.

Acknowledgments

References

[1] A. Daruich, A. Matet, A. Dirani et al., "Central serous chorioretinopathy: recent findings and new physiopathology hypothesis," *Progress in Retinal and Eye Research*, vol. 48, pp. 82–118, 2015.

[2] M. Gemenetzi, G. D. Salvo, and A. J. Lotery, "Central serous chorioretinopathy: an update on pathogenesis and treatment," *Eye*, vol. 24, no. 12, pp. 1743–1756, 2010.

[3] J. Yu, C. Jiang, and G. Xu, "Study of subretinal exudation and consequent changes in acute central serous chorioretinopathy by optical coherence tomography," *American Journal of Ophthalmology*, vol. 158, no. 4, pp. 752–756.e2, 2014.

[4] M. Wang, I. C. Munch, P. W. Hasler, C. Prünte, and M. Larsen, "Central serous chorioretinopathy," *Acta Ophthalmologica*, vol. 86, no. 2, pp. 126–145, 2008.

[5] A. Daruich, A. Matet, L. Marchionno et al., "Acute central serous chorioretinopathy," *Retina*, vol. 37, no. 10, pp. 1905–1915, 2017.

[6] L. A. Yannuzzi, "Central serous chorioretinopathy: a personal perspective," *American Journal of Ophthalmology*, vol. 149, no. 3, pp. 361–363.e1, 2010.

[7] C. A. Ferreira, S. Penas, J. Silva, and A. M. Mendonca, "Quantitative assessment of central serous chorioretinopathy in angiographic sequences of retinal images," in *2019 IEEE 6th Portuguese Meeting on Bioengineering (ENBENG)*, pp. 51–63, Lisbon, Portugal, 2019.

[8] H. Rabbani, M. J. Allingham, P. S. Mettu, S. W. Cousins, and S. Farsiu, "Fully automatic segmentation of fluorescein leakage in subjects with diabetic macular edema," *Investigative Ophthalmology & Visual Science*, vol. 56, no. 3, pp. 1482–1492, 2015.

[9] M. S. El-Shahawy, A. ElAntably, N. Fawzy, K. Samir, M. Hunter, and A. S. Fahmy, "Segmentation of diabetic macular edema in fluorescein angiograms," in *2011 IEEE International Symposium on Biomedical Imaging: From Nano to Macro*, pp. 661–664, Chicago, IL, USA, 2011.

[10] L. M. Costa, P. Marco, G. Ayala, E. de Ves, J. Domingo, and A. Simó, "Macular edema computer-aided evaluation in ocular vein occlusions," *Computers and Biomedical Research*, vol. 31, no. 5, pp. 374–384, 1998.

[11] J. Saito, S. T. D. Roxburgh, D. Sutton, and A. Ellingford, "A new method of image analysis of fluorescein angiography applied to age- related macular degeneration," *Eye*, vol. 9, no. 1, pp. 70–76, 1995.

[12] Y. Zhao, I. J. C. MacCormick, D. G. Parry et al., "Automated detection of leakage in fluorescein angiography images with application to malarial retinopathy," *Scientific Reports*, vol. 5, no. 1, article 10425, 2015.

[13] Y. Zhao, Y. Zheng, Y. Liu et al., "Intensity and compactness enabled saliency estimation for leakage detection in diabetic and malarial retinopathy," *IEEE Transactions on Medical Imaging*, vol. 36, no. 1, pp. 51–63, 2017.

[14] Y. Xie, W. Meng, R. Z. Li et al., "Early lung cancer diagnostic biomarker discovery by machine learning methods," *Translational Oncology*, vol. 14, no. 1, article 100907, 2021.

[15] K. Pieszko, J. Hiczkiewicz, P. Budzianowski et al., "Predicting long-term mortality after acute coronary syndrome using machine learning techniques and hematological markers," *Disease Markers*, vol. 2019, Article ID 9056402, 9 pages, 2019.

[16] V. J. Geraedts, M. Koch, M. F. Contarino et al., "Machine learning for automated EEG-based biomarkers of cognitive impairment during deep brain stimulation screening in patients with Parkinson's disease," *Clinical Neurophysiology*, vol. 132, no. 5, pp. 1041–1048, 2021.

[17] C. Cano-Espinosa, G. Gonzalez, G. R. Washko, M. Cazorla, and R. S. J. Estepar, "Biomarker localization from deep learning regression networks," *IEEE Transactions on Medical Imaging*, vol. 39, no. 6, pp. 2121–2132, 2020.

[18] S. Bhattacharyya, J. Epstein, and L. J. Suva, "Biomarkers that discriminate multiple myeloma patients with or without skeletal involvement detected using SELDI-TOF mass spectrometry and statistical and machine learning tools," *Disease Markers*, vol. 22, no. 4, p. 255, 2006.

[19] C.-L. Tsai, Y.-L. Yang, S.-J. Chen, C.-H. Chan, and W.-Y. Lin, "Automatic characterization and segmentation of classic choroidal neovascularization using Adaboost for supervised learning," in *IEEE Nuclear Science Symposuim & Medical Imaging Conference*, pp. 3610–3612, Knoxville, TN, USA, 2010.

[20] E. Trucco, C. R. Buchanan, T. Aslam, and B. Dhillon, "Contextual detection of ischemic regions in ultra-wide-field-of-view retinal fluorescein angiograms," in *2007 29th Annual International Conference of the IEEE Engineering in Medicine and Biology Society*, pp. 6739–6742, Lyon, France, 2007.

[21] B. Hassan, S. Qin, T. Hassan, R. Ahmed, and N. Werghi, "Joint Segmentation and Quantification of Chorioretinal Biomarkers in Optical Coherence Tomography Scans: A Deep Learning Approach," *IEEE Transactions on Instrumentation and Measurement*, vol. 70, pp. 1–17, 2021.

[22] C. Gao, D. Meng, Y. Yang, Y. Wang, X. Zhou, and A. G. Hauptmann, "Infrared patch-image model for small target detection in a single image," *IEEE Transactions on Image Processing*, vol. 22, no. 12, pp. 4996–5009, 2013.

[23] F. Biondi, "Low-Rank plus sparse decomposition and localized radon transform for ship-wake detection in synthetic aperture radar images," *IEEE Geoscience and Remote Sensing Letters*, vol. 15, no. 1, pp. 117–121, 2018.

[24] C. Shi, Y. Cheng, J. Wang, Y. Wang, K. Mori, and S. Tamura, "Low-rank and sparse decomposition based shape model and probabilistic atlas for automatic pathological organ segmentation," *Medical Image Analysis*, vol. 38, pp. 30–49, 2017.

[25] R. Wang, B. Chen, D. Meng, and L. Wang, "Weakly supervised lesion detection from fundus images," *IEEE Transactions on Medical Imaging*, vol. 38, no. 6, pp. 1501–1512, 2019.

[26] J. Wang, J. Chen, H. Xu et al., "Gaussian field estimator with manifold regularization for retinal image registration," *Signal Processing*, vol. 157, pp. 225–235, 2019.

[27] F. H. C. Tivive, A. Bouzerdoum, and C. Abeynayake, "GPR target detection by joint sparse and low-rank matrix decomposition," *IEEE Transactions on Geoscience and Remote Sensing*, vol. 57, no. 5, pp. 2583–2595, 2019.

[28] E. J. Candès, X. Li, Y. Ma, and J. Wright, "Robust principal component analysis?," *Journal of the ACM*, vol. 58, no. 1, pp. 1–37, 2009.

[29] P. Y. M. Anshad, S. S. Kumar, and S. Shahudheen, "Segmentation of chondroblastoma from medical images using modified

region growing algorithm," *Cluster Computing*, vol. 22, Supplement 6, pp. 13437–13444, 2019.

[30] X. Zhang, X. Li, and Y. Feng, "A medical image segmentation algorithm based on bi-directional region growing," *Optik*, vol. 126, no. 20, pp. 2398–2404, 2015.

[31] A. Kapoor and R. Aggarwal, "Image segmentation of MR images with multi-directional region growing algorithm," in *Innovations in Computational Intelligence and Computer Vision*, pp. 193–201, Springer, Singapore, 2021.

[32] A. Criminisi, P. Pérez, and K. Toyama, "Region filling and object removal by exemplar-based image Inpainting," *IEEE Transactions on Image Processing*, vol. 13, no. 9, pp. 1200–1212, 2004.

[33] Z. Zhou, X. Li, J. Wright, E. Candes, and Y. Ma, "Stable principal component pursuit," in *2010 IEEE international symposium on information theory*, pp. 1518–1522, Austin, TX, USA, 2010.

[34] Z. Lin, A. Ganesh, J. Wright, L. Wu, M. Chen, and Y. Ma, "Fast convex optimization algorithms for exact recovery of a corrupted low-rank matrix," in *Proc. CAMSAP*, pp. 1–18, Aruba, Netherland Antilles, 2009.

Retraction

Retracted: Development and Validation of Diagnostic Models for Hand-Foot-and-Mouth Disease in Children

Disease Markers

This article has been retracted by Hindawi following an investigation undertaken by the publisher [1]. This investigation has uncovered evidence of one or more of the following indicators of systematic manipulation of the publication process:

(1) Discrepancies in scope

(2) Discrepancies in the description of the research reported

(3) Discrepancies between the availability of data and the research described

(4) Inappropriate citations

(5) Incoherent, meaningless and/or irrelevant content included in the article

(6) Peer-review manipulation

The presence of these indicators undermines our confidence in the integrity of the article's content and we cannot, therefore, vouch for its reliability. Please note that this notice is intended solely to alert readers that the content of this article is unreliable. We have not investigated whether authors were aware of or involved in the systematic manipulation of the publication process.

Wiley and Hindawi regrets that the usual quality checks did not identify these issues before publication and have since put additional measures in place to safeguard research integrity.

We wish to credit our own Research Integrity and Research Publishing teams and anonymous and named external researchers and research integrity experts for contributing to this investigation.

The corresponding author, as the representative of all authors, has been given the opportunity to register their agreement or disagreement to this retraction. We have kept a record of any response received.

References

[1] F. Zhuo, M. Yu, Q. Chen et al., "Development and Validation of Diagnostic Models for Hand-Foot-and-Mouth Disease in Children," *Disease Markers*, vol. 2021, Article ID 1923636, 9 pages, 2021.

Hindawi

Research Article

Development and Validation of Diagnostic Models for Hand-Foot-and-Mouth Disease in Children

Feng Zhuo,[1] **Mengjie Yu,**[2] **Qiang Chen,**[3] **Nuoya Li,**[4] **Li Luo,**[3] **Meiying Hu,**[1] **Qi Dong,**[3] **Liang Hong,**[3] **Shouhua Zhang** (iD),[5] **and Qiang Tao** (iD)[4,5]

[1]*Pediatric Cardiology Center, Jiangxi Provincial Children's Hospital, Nanchang, Jiangxi 330006, China*
[2]*Key Laboratory of Drug Metabolism and Pharmacokinetics, China Pharmaceutical University, Nanjing, 210009 Jiangsu, China*
[3]*Department of Respiratory, Jiangxi Provincial Children's Hospital, Nanchang, Jiangxi 330006, China*
[4]*Department of General Surgery, Jiangxi Provincial Children's Hospital, Nanchang, Jiangxi 330006, China*
[5]*Department of General Surgery, The Affiliated Children's Hospital of Nanchang University, Nanchang, Jiangxi 330006, China*

Correspondence should be addressed to Shouhua Zhang; zshouhua416@163.com and Qiang Tao; taoqiang_2008@126.com

Objective. To find risk markers and develop new clinical predictive models for the differential diagnosis of hand-foot-and-mouth disease (HFMD) with varying degrees of disease. *Methods.* 19766 children with HFMD and 64 clinical indexes were included in this study. The patients included in this study were divided into the mild patients' group (mild) with 12292 cases, severe patients' group (severe) with 6508 cases, and severe patients with respiratory failure group (severe-RF) with 966 cases. Single-factor analysis was carried out on 64 indexes collected from patients when they were admitted to the hospital, and the indexes with statistical differences were selected as the prediction factors. Binary multivariate logistic regression analysis was used to construct the prediction models and calculate the adjusted odds ratio (OR). *Results.* SP, DP, NEUT#, NEUT%, RDW-SD, RDW-CV, GGT, CK/CK-MB, and Glu were risk markers in mild/severe, mild/severe-RF, and severe/severe-RF. Glu was a diagnostic marker for mild/severe-RF (AUROC = 0.80, 95% CI: 0.78-0.82); the predictive model constructed by temperature, SP, MOMO%, EO%, RDW-SD, GLB, CRP, Glu, BUN, and Cl could be used for the differential diagnosis of mild/severe (AUROC > 0.84); the predictive model constructed by SP, age, NEUT#, PCT, TBIL, GGT, Mb, β2MG, Glu, and Ca could be used for the differential diagnosis of severe/severe-RF (AUROC > 0.76). *Conclusion.* By analyzing clinical indicators, we have found the risk markers of HFMD and established suitable predictive models.

1. Introduction

Hand-foot-and-mouth disease (HFMD) is a common viral illness mainly caused by enterovirus 71 (EV71) and coxsackie A16 (CA16), which mainly affects children under 5 years of age [1, 2]. Most patients with HFMD have mild symptoms and can be cured in 7-10 days. However, a small number of patients will get worse and may have serious complications, such as nervous system damage and cardiopulmonary failure, which will lead to death [3, 4]. Early detection of severe HFMD with the worsening condition and timely appropriate treatment and nursing can significantly improve the treatment and prognosis of the children

[5, 6]. Therefore, it is particularly important to develop a clinical decision-making tool to predict and early identify HFMD patients with different degrees of disease to provide effective interventions.

Although many previous studies have focused on investigating the risk markers and exploring prediction models of HFMD [7–10], there are still few studies to find the risk factors of HFMD patients and establish a prediction model by using only various laboratory test indicators. In this study, retrospective case-control analysis was used to explore the risk factors of early recognition of progression from mild to severe and from common severe to severe-RF by analyzing various types of blood test indicators of HFMD patients

with different degrees of illness; to establish a suitable risk prediction model to objectively, systematically, and quantitatively evaluate the patient's condition; to explore the possibility of early progression of HFMD to severe and common severe to severe-RF; and to take early intervention measures, guide clinical treatment, and reduce the mortality of patients.

2. Methods

2.1. Participating Cohorts. From April 2009 to January 2020, patients with HFMD admitted to Jiangxi Children's Hospital were selected as the study objects, and the definition diagnosis of HFMD was based on the guidelines for the diagnosis and treatment of hand-foot-and-mouth disease (http://www.nhc.gov.cn/wjw/gfxwj/201304/4a5c8d7485c64d189afd5392a390bd84.shtml/; http://www.nhc.gov.cn/yzygj/wslgf/201306/6d935c0f43cd4a1fb46f8f71acf8e245.shtml/; http://www.nhc.gov.cn/yzygj/s3594q/201805/5db274d8697a41ea84e88eedd8bf8f63.shtml/). Inclusion criteria were positive enterovirus-specific nucleic acid test (CV-A16, EV-A71, etc.) or isolated enterovirus and identified as CV-A16, EV-A71, or other enterovirus causing HFMD. We also excluded several children with erupting diseases (e.g., papular urticaria, sandskin rash, chickenpox, atypical measles, infantile rash, shingles, rubella, and bullous rash caused by CV-A16 or EV-A71). The data used in this study were all detected at the first visit of patients. This retrospective study was approved by the ethics committee of Jiangxi Provincial Children's Hospital.

2.2. Outcomes. The categories of diagnosis results are mild, severe, and severe-RF, which mainly refer to the guidelines for the diagnosis and treatment of hand-foot-and-mouth disease. The main symptoms of mild patients are fever and rash of hands, feet, mouth, buttocks, and other parts, which can be accompanied by cough, runny nose, anorexia, and other symptoms. Some cases only present as rash or herpetic pharyngitis, and some cases may be without rash. Typical rashes are maculopapules, papules, and herpes. There is inflammatory redness around the rash, less fluidity in herpes, no pain, no itching, no scabs, and no scars when the rash recovers. Atypical rashes are usually small, thick, hard, and few, sometimes with ecchymosis. Some types of enteroviruses, such as CV-A6 and CV-A10, cause severe skin lesions, and the rash may present as bulla-like changes with pain and itching, not limited to the hands, feet, and mouth.

The main manifestations of severe patients are central nervous system damage, which usually occurs within 1-5 days of the course of the disease. The manifestations are mental illness, drowsiness, weakness of sucking, easily frightened, headache, vomiting, fidgety, limb shaking, myasthenia, neck rigidity, etc. Patients with severe respiratory failure were mainly characterized by increased heart rate and respiration, cold sweat, cold extremities, flowy skin, elevated blood pressure or tachycardia (bradycardia in some children), tachycardia, cyanosis of the mouth, coughing pink foaming sputum or bloody fluid, decreased blood pressure,

or shock. All data were collected independently of the evaluation of the study results.

2.3. Variables and Statistical Analysis. Gender, age, clinical blood test indicators, and other information collected at the first visit of HFMD patients were taken as potential predictive variables, and cases with blood test indicators missing more than 30% and variables with data missing more than 10% were eliminated. The processing method of missing values in the data was as follows: mode was used for interpolation of classified variables and mean was used for interpolation of continuous variables. For variables that do not conform to the normal distribution, the Mann–Whitney U test was used, and for variables that conform to the normal distribution, the independent-sample t-test was used. A P value < 0.05 was regarded as being statistically significant for all of the analyses. The adjusted odds ratio (OR) of each variable was obtained by logistic regression analysis. To estimate the ability to discriminate between patients with different diagnoses, we used the receiver operating characteristic (ROC) curve analysis for pairs of patients [11]. All analyses were performed using R software (version 4.0) and SPSS 26.0 (SPSS Inc., Chicago, IL, US).

3. Results

3.1. Study Population. Generally, 19766 children with HFMD met the inclusion criteria of this study, and 3091 children were excluded. The patients included in this study were divided into the mild patients' group (mild) with 12292 cases, severe patients' group (severe) with 6508 cases, and severe patients with respiratory failure group (severe-RF) with 966 cases. 64 predictive variables met the requirements and 24 variables were excluded. Some basic information and information on variables of subjects in each group are shown in Table 1.

3.2. Screening and Analysis of Difference Indexes. Through the statistical analysis of all the indicators included in the study, we found that 52, 44, and 51 indicators showed statistical differences between mild/severe, severe/severe-RF, and mild/severe-RF, respectively, and 30 indicators showed significant differences among the three groups (Table 2). With the aggravation of patients' condition, 23 indicators showed a significant trend of change (Table 2). The contents of 10 indicators including SP, DP, NEUT#, NEUT%, RDW-SD, RDW-CV, GGT, LDH, CK/CK-MB, and Glu showed an increasing trend in the blood of mild, severe, and severe-RF patients, while those of 13 indicators presented a decreasing trend, including LYMPH%, MONO%, EO#, EO%, BASO%, MCHC, ALB, ALB/GLB, β2MG, CRP, K, Na, and Cl.

3.3. Analysis of Risk Factors. Calculating the adjusted OR values between the mild/severe, mild/severe-RF, and severe/severe-RF groups, we found that a total of 19 indicators may be risk factors of mild development to severe (adjusted OR > 1.0), where temperature (adjusted OR = 2.76, 95% CI: 2.66-2.86) and Glu (adjusted OR = 1.60, 95% CI: 1.55-1.64) performed better (Figure 1(a)). A total of 17

TABLE 1: General characteristics of included populations.

TABLE 1: Continued.

Characteristics	Mild	Severe	Severe-RF
Num	12292	6508	966
Male	8152	4353	673
Age (days)	664.12 ± 4.66	670.56 ± 4.61	643.81 ± 10.99
Weight (kg)	11.34 ± 0.03	11.25 ± 0.03	11.40 ± 0.41
Temperature (°C)	37.41 ± 0.01	38.20 ± 0.01	38.18 ± 0.03
SP (mmHg)	90.91 ± 0.07	94.15 ± 0.12	100.29 ± 0.43
DP (mmHg)	54.01 ± 0.07	57.00 ± 0.11	60.50 ± 0.38
NEUT# ($\times 10^9$/L)	6.67 ± 0.04	7.11 ± 0.05	9.03 ± 0.16
NEUT% (%)	51.33 ± 0.15	57.19 ± 0.20	63.52 ± 0.51
LYMPH# ($\times 10^9$/L)	4.56 ± 0.02	4.09 ± 0.03	4.03 ± 0.10
LYMPH% (%)	38.17 ± 0.14	34.28 ± 0.17	29.36 ± 0.46
MONO# ($\times 10^9$/L)	1.16 ± 0.01	0.94 ± 0.01	0.90 ± 0.02
MONO% (%)	9.26 ± 0.03	7.80 ± 0.05	6.70 ± 0.11
EO# ($\times 10^9$/L)	0.12 ± 0.00	0.06 ± 0.00	0.04 ± 0.00
EO% (%)	1.12 ± 0.01	0.49 ± 0.01	0.29 ± 0.02
BASO# ($\times 10^9$/L)	0.02 ± 0.00	0.02 ± 0.00	0.01 ± 0.00
BASO% (%)	0.15 ± 0.00	0.13 ± 0.00	0.09 ± 0.01
WBC ($\times 10^9$/L)	12.54 ± 0.05	12.22 ± 0.05	14.05 ± 0.20
RBC ($\times 10^{12}$/L)	4.53 ± 0.00	4.56 ± 0.00	4.56 ± 0.01
HGB (g/L)	116.67 ± 0.09	116.67 ± 0.12	114.82 ± 0.36
MCH (pg)	25.89 ± 0.03	25.86 ± 0.03	25.62 ± 0.07
MCHC (g/L)	327.29 ± 0.27	325.32 ± 0.20	322.61 ± 0.49
RDW-SD (fL)	39.55 ± 0.03	40.34 ± 0.04	41.00 ± 0.11
HCT (%)	35.70 ± 0.03	35.90 ± 0.04	35.64 ± 0.11
MCV (fL)	79.11 ± 0.05	79.60 ± 0.07	79.40 ± 0.19
PLT ($\times 10^9$/L)	300.98 ± 0.86	301.81 ± 1.13	331.52 ± 3.36
P-LCR (%)	27.29 ± 0.07	25.96 ± 0.09	25.87 ± 0.23
MPV (fL)	10.31 ± 0.01	10.13 ± 0.01	10.11 ± 0.03
PDW (fL)	11.65 ± 0.02	11.35 ± 0.02	11.36 ± 0.06
PCT (%)	0.34 ± 0.01	0.31 ± 0.00	0.34 ± 0.00
RDW-CV (%)	14.13 ± 0.01	14.33 ± 0.02	14.62 ± 0.05
TP (g/L)	69.53 ± 0.05	71.35 ± 0.08	70.50 ± 0.26
ALB (g/L)	45.07 ± 0.03	44.88 ± 0.05	43.73 ± 0.16
GLB (g/L)	24.45 ± 0.04	26.47 ± 0.07	26.77 ± 0.22
ALB/GLB	1.92 ± 0.00	1.78 ± 0.01	1.73 ± 0.01
PA (mg/L)	154.07 ± 0.32	158.10 ± 0.43	154.12 ± 1.16
TBIL (μmol/L)	7.17 ± 0.04	7.41 ± 0.04	6.69 ± 0.10
DBIL (μmol/L)	2.48 ± 0.01	2.63 ± 0.02	2.43 ± 0.05
IDBL (μmol/L)	4.70 ± 0.04	4.79 ± 0.03	4.26 ± 0.07
ALT (U/L)	24.10 ± 0.29	22.93 ± 0.36	24.49 ± 1.14
AST (U/L)	47.20 ± 0.24	45.40 ± 0.28	49.48 ± 1.53
AST/ALT	2.38 ± 0.01	2.42 ± 0.01	2.50 ± 0.06
ALP (U/L)	217.48 ± 1.20	226.55 ± 1.96	214.66 ± 4.18
GGT (U/L)	12.50 ± 0.10	13.98 ± 0.14	15.33 ± 0.43

Characteristics	Mild	Severe	Severe-RF
5-NT (U/L)	5.31 ± 0.03	5.23 ± 0.04	5.04 ± 0.08
LDH (U/L)	426.74 ± 1.18	447.45 ± 1.69	463.15 ± 6.15
CK (U/L)	159.37 ± 3.22	154.94 ± 2.24	201.86 ± 11.10
CK-MB (U/L)	20.34 ± 0.13	17.02 ± 0.15	17.86 ± 0.39
CK/CK-MB	8.78 ± 0.08	10.80 ± 0.13	12.12 ± 0.43
CnTI (ng/mL)	0.49 ± 0.01	0.48 ± 0.01	0.49 ± 0.01
Mb (μg/L)	26.49 ± 0.28	22.04 ± 0.30	53.02 ± 3.22
β2MG (mg/L)	2.51 ± 0.01	2.31 ± 0.01	2.15 ± 0.02
CRP (mg/L)	19.50 ± 0.20	12.99 ± 0.21	10.82 ± 0.47
SAA (mg/L)	22.30 ± 0.08	23.48 ± 0.11	23.31 ± 0.29
Glu (mmol/L)	4.44 ± 0.01	5.08 ± 0.02	5.74 ± 0.07
BUN (mmol/L)	3.80 ± 0.01	3.58 ± 0.01	3.69 ± 0.05
CR (μmol/L)	27.57 ± 0.07	28.72 ± 0.15	29.40 ± 0.37
BUN/CR	0.15 ± 0.00	0.13 ± 0.00	0.13 ± 0.00
UA (μmol/L)	264.84 ± 0.78	263.40 ± 1.10	275.28 ± 4.01
K (mmol/L)	4.62 ± 0.01	4.57 ± 0.01	4.46 ± 0.02
Ca (mmol/L)	2.45 ± 0.00	2.45 ± 0.00	2.42 ± 0.00
Na (mmol/L)	139.23 ± 0.03	138.40 ± 0.04	137.93 ± 0.11
Mg (mmol/L)	0.97 ± 0.00	0.97 ± 0.00	0.97 ± 0.00
Cl (mmol/L)	104.79 ± 0.03	103.22 ± 0.04	102.51 ± 0.11
P (mmol/L)	1.64 ± 0.00	1.62 ± 0.00	1.62 ± 0.01

Note: values were presented with mean ± SEM. SP: systolic pressure; DP: diastolic pressure; NEUT#: neutrophil count; NEUT%: neutrophil ratio; LYMPH#: lymphocyte count; LYMPH%: lymphocyte ratio; MONO#: mononuclear cell; MONO%: mononuclear cell ratio; EO#: eosinophil; EO%: eosinophil ratio; BASO#: basophils; BASO%: basophil ratio; WBC: white blood cell; RBC: red blood cell; HGB: hemoglobin; MCH: mean corpuscular hemoglobin; MCHC: mean corpuscular hemoglobin concentration; RDW-SD: red blood cell distribution width; HCT: hematocrit; MCV: mean corpuscular volume; PLT: platelet; P-LCR: platelet-large cell ratio; MPV: mean platelet volume; PDW: platelet distribution width; PCT: thrombocytocrit; TP: total protein; ALB: albumin; GLB: globulin; PA: prealbumin; TBIL: total bilirubin; DBIL: direct bilirubin; IDBL: indirect bilirubin; ALT: glutamic-pyruvic transaminase; AST: glutamic oxalacetic transaminase; ALP: alkaline phosphatase; GGT: gamma-glutamyl transferase; 5-NT: $5'$-nucleotidase; LDH: lactate dehydrogenase; CK: creatine kinase; CK-MB: creatine kinase-myocardial band isoenzyme; CnTI: cardiac troponin; Mb: myohemoglobin; CRP: c-reaction protein; SAA: serum amyloid A; Glu: glucose; BUN: urea; CR: creatinine; UA: uric acid; K: potassium; Ca: calcium; Na: sodium; Mg: magnesium; Cl: chlorine; P: phosphorus.

indicators may be risk factors of mild development to severe-RF (adjusted OR > 1.0), among which temperature (adjusted OR = 2.67, 95% CI: 2.48-2.88) and Glu (adjusted OR = 1.75, 95% CI: 1.67-1.83) performed better (Figure 1(b)). A total of 13 indicators may be risk factors of severe development to severe-RF (adjusted OR > 1.0), of which Glu (adjusted OR = 1.22, 95% CI: 1.17-1.27) performed best (Figure 1(c)). We further analyzed and found that 9 indicators of SP, DP, NEUT#, NEUT%, RDW-SD, RDW-CV, GGT, CK/CK-MB, and Glu can be used as risk factors in mild/severe, mild/severe-RF, and severe/severe-RF. And with

Table 2: Difference indexes and fold change (FC) value.

Characteristics	Mild vs. severe		Mild vs. severe-RF		Severe vs. severe-RF	
	P	FC	P	FC	P	FC
SP	***	1.04	***	1.10	***	1.07
DP	***	1.06	***	1.12	***	1.06
NEUT#	***	1.07	***	1.35	***	1.27
NEUT%	***	1.11	***	1.24	***	1.11
RDW-SD	***	1.02	***	1.04	***	1.02
RDW-CV	***	1.01	***	1.03	***	1.02
GGT	***	1.12	***	1.23	**	1.10
LDH	***	1.05	***	1.09	*	1.04
CK/CK-MB	***	1.23	***	1.38	**	1.12
Glu	***	1.14	***	1.29	***	1.13
LYMPH%	***	0.90	***	0.77	***	0.86
MONO%	***	0.84	***	0.72	***	0.86
EO#	***	0.50	***	0.33	***	0.67
EO%	***	0.44	***	0.26	***	0.59
BASO%	***	0.87	***	0.60	***	0.69
MCHC	***	0.99	***	0.99	***	0.99
ALB/GLB	***	0.93	***	0.90	**	0.97
β2MG	***	0.92	***	0.86	***	0.93
CRP	***	0.67	***	0.55	***	0.83
K	***	0.99	***	0.97	***	0.98
Cl	***	0.99	***	0.98	***	0.99
Na	***	0.99	***	0.99	***	0.99
ALB	**	0.98	***	0.97	***	0.97
BASO#	***	1.00	***	0.50	**	0.50
WBC	***	0.97	***	1.12	***	1.15
TP	***	1.03	***	1.01	**	0.99
TBIL	**	1.03	**	0.93	***	0.90
CK-MB	***	0.84	***	0.88	*	1.05
Mb	***	0.83	***	2.00	***	2.41
BUN	***	0.94	*	0.97	*	1.03
Age	-	-	-	-	*	-
Gender	-	-	*	-	-	-
Temperature	***	1.02	***	1.02	-	-
LYMPH#	***	0.90	***	0.88	-	-
MONO#	***	0.81	***	0.78	-	-
RBC	***	1.01	*	1.01	-	-
HGB	-	-	***	0.98	***	0.98
MCH	-	-	**	0.99	**	0.99
HCT	***	1.01	-	-	*	0.99
MCV	***	1.01	-	-	-	-
PLT	-	-	***	1.10	***	1.10
P-LCR	***	0.95	***	0.95	-	-
MPV	***	0.98	***	0.98	-	-
PDW	***	0.97	***	0.98	-	-
PCT	***	0.91	-	-	***	1.10
GLB	***	1.08	***	1.09	-	-
PA	***	1.03	-	-	**	0.97
DBIL	***	1.06	-	-	***	0.92
IDBL	-	-	**	0.91	***	0.89
ALT	*	0.95	-	-	-	-
AST	***	0.96	-	-	**	1.09
AST/ALT	*	1.02	-	-	-	-
ALP	***	1.04	-	-	*	0.95
5-NT	-	-	**	0.95	-	-
CK	-	-	***	1.27	**	1.30
SAA	***	1.05	**	1.05	-	-
CR	***	1.04	***	1.07	-	-
BUN/CR	***	0.87	***	0.87	-	-
UA	-	-	*	1.04	**	1.05
Ca	-	-	***	0.99	***	0.99
P	***	0.99	*	0.99	-	-

***, **, and *: $P < 0.001$, 0.01, and 0.05, respectively; "-" represents the statistical significance of P values more than 0.05.

the aggravation of HFMD patients, the levels of these 9 indicators in the blood of mild, severe, and severe-RF patients all showed a significant increasing trend (Figure 2). Therefore, we speculate that these 9 indicators might be risk factors for HFMD and played an important role in suggesting the aggravation of patients' condition.

3.4. ROC Analysis of Difference Indexes. ROC curve analysis was used to investigate the diagnostic performance of each difference indicator. The top 10 indicators with good performance among each group are shown in Table 3. The results show that Glu (AUROC = 0.80, 95% CI: 0.78-0.82) can distinguish mild from severe-RF well. However, in mild/severe and severe/severe-RF, the single index does not differentiate well (AUROC < 0.75).

3.5. Development and Validation of Prediction Models. To improve the diagnostic distinction effect between mild/severe and severe/severe-RF, we further established prediction models. Two-thirds of the participants were randomly assigned to the model development data set, and one-third was kept as the independent validation data set. The variables with significant differences in mild/severe and severe/severe-RF were used as the prediction variables, and binary logistic regression analysis was used to establish the prediction models. The inclusion criterion of model variables was the Akaike Information Criterion (AIC) [12], and stepwise
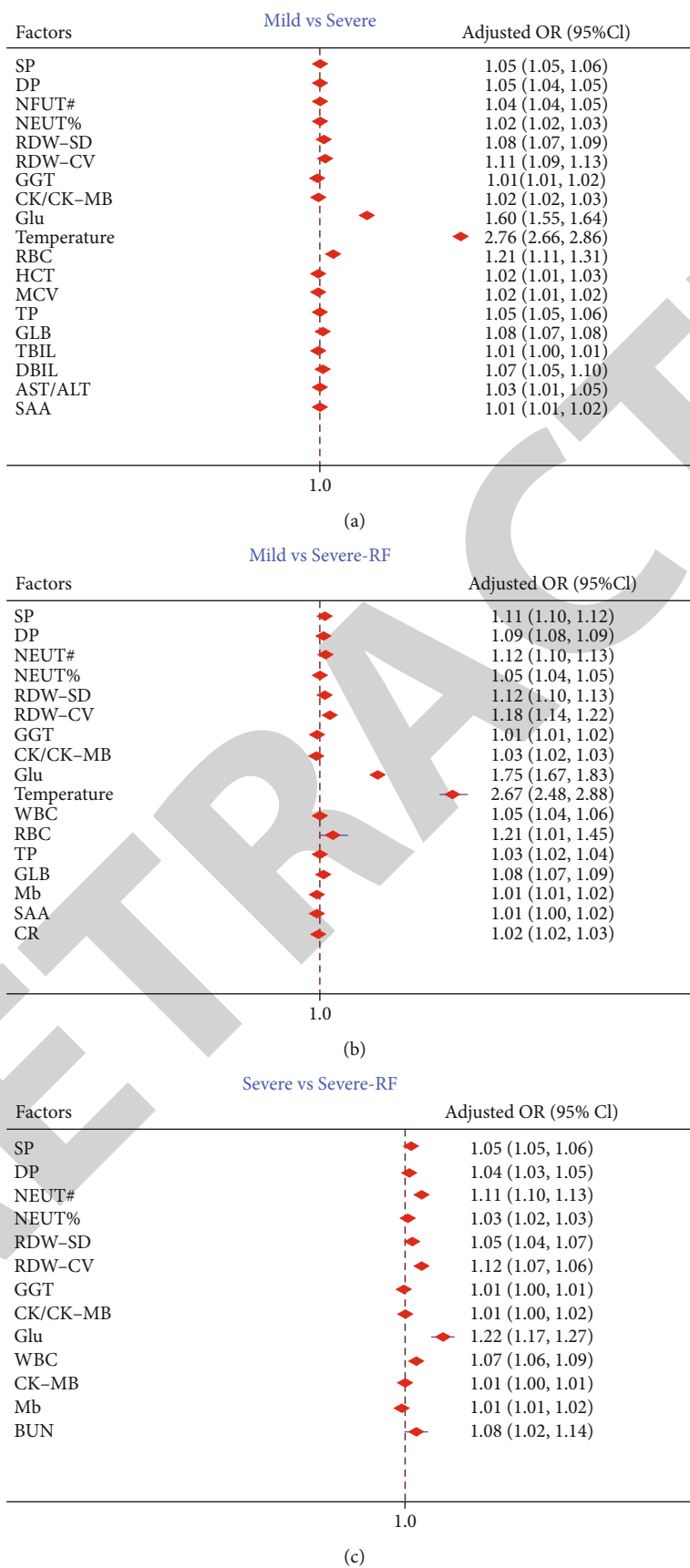
Figure 1: Risk factors of mild/severe, mild/severe-RF, and severe/severe-RF.
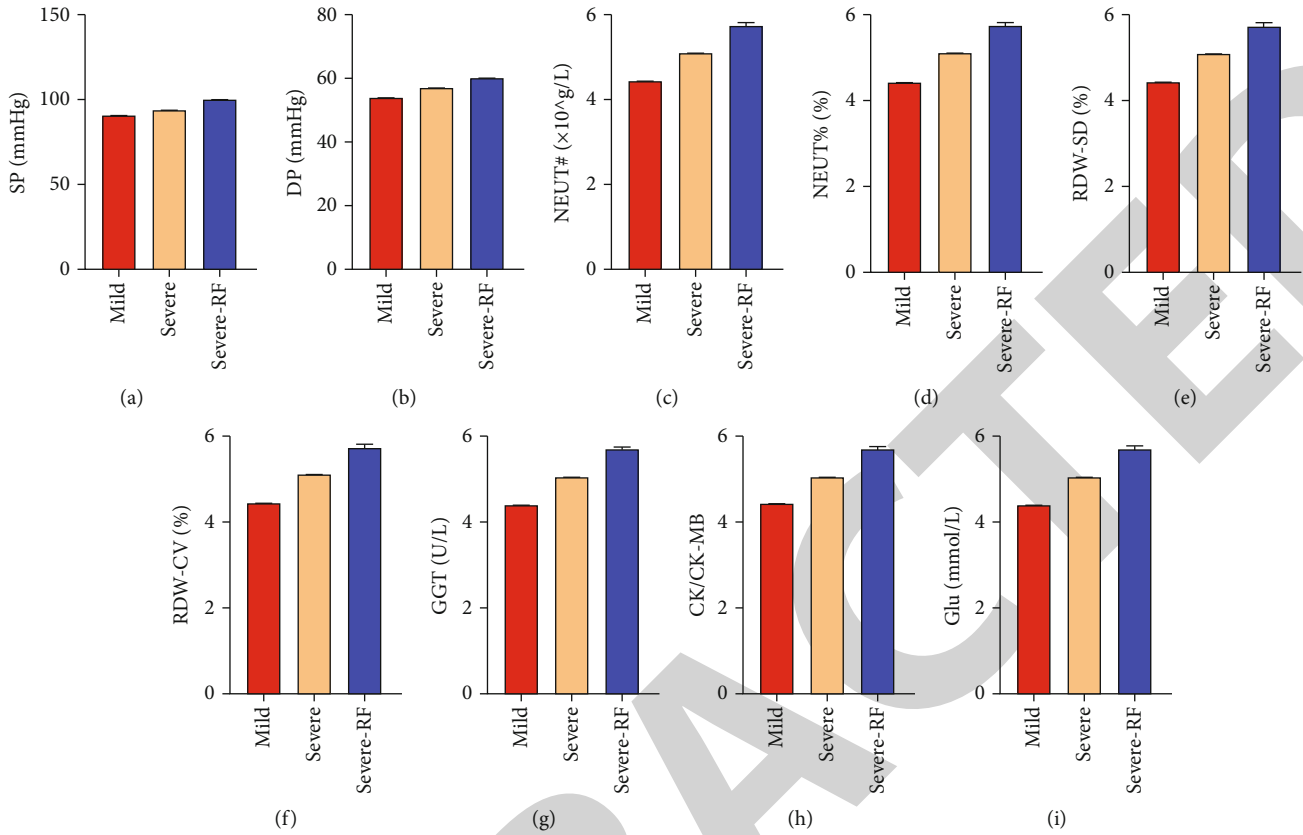
Figure 2: Changes in the content of 9 risk factors.

Table 3: Top 10 indicators of AUROC value in each group.

Mild vs. severe			Mild vs. severe-RF			Severe vs. severe-RF		
	AUROC	95% CI		AUROC	95% CI		AUROC	95% CI
Temperature	0.74	0.74-0.75	Glu	0.80	0.78-0.82	Glu	0.68	0.66-0.70
EO#	0.69	0.68-0.70	EO%	0.75	0.74-0.77	Ca	0.66	0.64-0.68
Glu	0.69	0.68-0.70	EO#	0.75	0.73-0.77	SP	0.65	0.63-0.67
EO%	0.68	0.68-0.69	SP	0.74	0.72-0.76	β2MG	0.65	0.63-0.66
Cl	0.65	0.65-0.66	Temperature	0.73	0.71-0.75	Mb	0.63	0.61-0.65
β2MG	0.64	0.63-0.65	Cl	0.71	0.69-0.73	NEUT#	0.62	0.60-0.64
MONO%	0.63	0.62-0.64	β2MG	0.71	0.69-0.72	NEUT%	0.61	0.59-0.63
SP	0.62	0.62-0.63	MONO%	0.70	0.69-0.72	LYMPH%	0.61	0.59-0.63
CK-MB	0.61	0.60-0.62	NEUT%	0.70	0.69-0.72	PCT	0.59	0.57-0.61
NEUT%	0.61	0.60-0.62	DP	0.68	0.66-0.70	DP	0.59	0.57-0.61

regression was used to fit the best logistic regression model. Because the variables with significant differences between mild/severe and severe/severe-RF were inconsistent, the prediction variables included in the final two models were different.

For the mild and severe groups, 10 indicators of temperature, SP, MOMO%, EO%, RDW-SD, GLB, CRP, Glu, BUN, and Cl were selected in this study to establish a prediction model, and the model equation was $P = \exp(K)/(1 + \exp(K))$ and $K = 0.987 \times$ temperature $+ 0.026 \times$ SP $- 0.073 \times$ MOMO% $- 0.291 \times$ EO% $+ 0.089 \times$ RDW $-$ SD $+ 0.061 \times$ GLB $- 0.020 \times$ CRP $+ 0.279 \times$ Glu $- 0.213 \times$ BUN $- 0.096 \times$ Cl $- 34.858$; $P > 0.5$ was identified as a severe patient. Finally, in the model development data set, the AUROC was 0.845 (95% CI: 0.838-0.852) and the sensitivity and specificity were 72.19% and 81.84%, respectively (Figure 3(a)), and in the validation data set, the AUROC was 0.839 (95% CI: 0.829-0.850) and the sensitivity and specificity were 72.00% and 81.52%, respectively (Figure 3(b)).

For the severe and severe-RF groups, SP, age, NEUT#, PCT, TBIL, GGT, Mb, β2MG, Glu, and Ca10 were selected
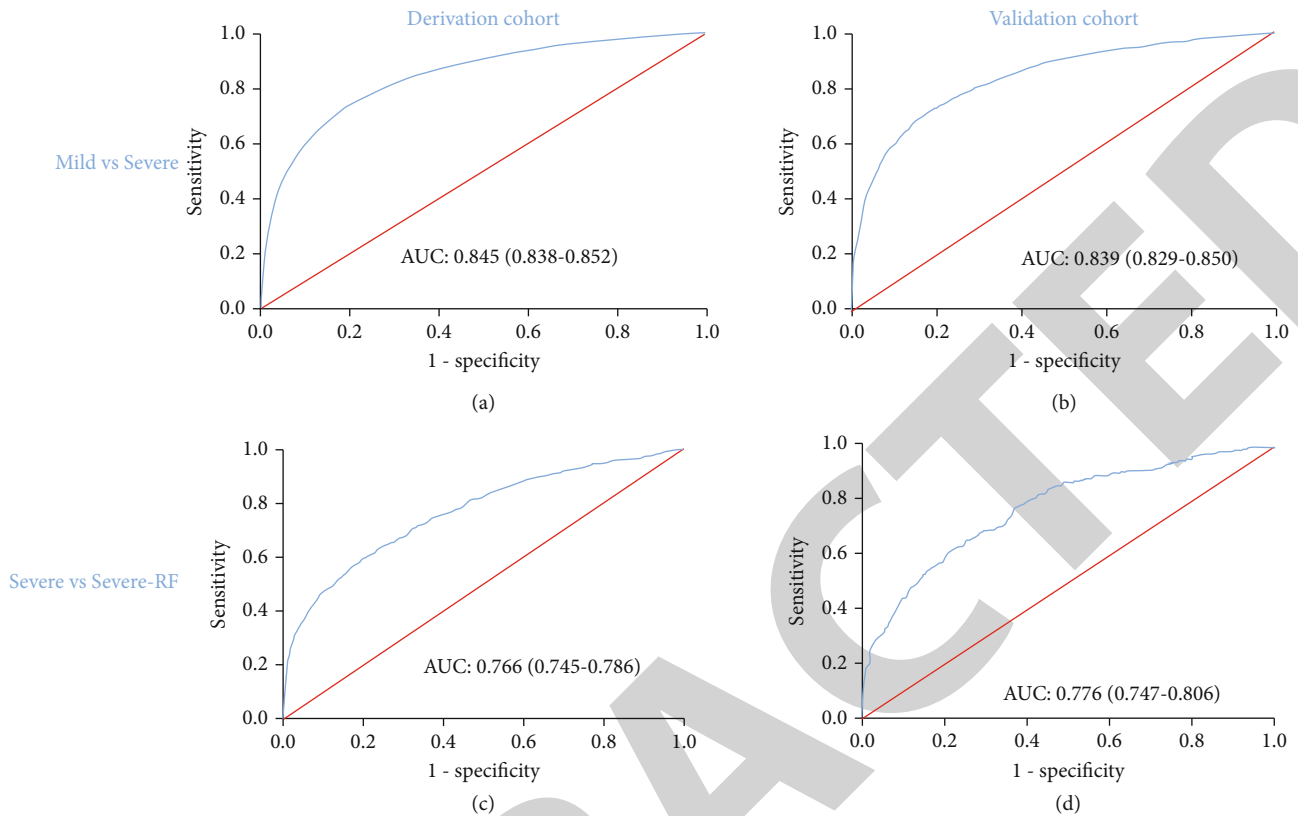
Figure 3: ROC curve of prediction model of mild/severe and severe/severe-RF in development queue and verification queue.

to establish the prediction model, and the model equation was $P = \exp(K)/(1 + \exp(K))$, $K = 0.047 \times SP - 0.001 \times age + 0.078 \times NEUT\# + 2.621 \times PCT - 0.068 \times TBIL + 0.013 \times GGT + 0.013 \times Mb - 0.705 \times \beta2MG + 0.154 \times Glu - 2.060 \times Ca - 1.790$; $P > 0.5$ was identified as severe-RF patients. Finally, in the model development data set, the AUROC was 0.766 (95% CI: 0.745-0.786) and the sensitivity and specificity were 59.08% and 80.70%, respectively (Figure 3(c)), and in the validation data set, the AUROC was 0.776 (95% CI: 0.747-0.806) and the sensitivity and specificity were 78.20% and 62.98%, respectively (Figure 3(d)).

4. Discussion

Severe HFMD patients have an acute onset and serious condition, often accompanied by serious complications (such as nervous system damage and cardiopulmonary failure), which will lead to death [3, 4]. Therefore, it is of great significance to find appropriate risk factors for early intervention and treatment of severe HFMD patients.

We analyzed the clinical data of patients with HFMD and found that temperature and Glu performed the best for warning of mild development into severe and severe-RF, and Glu performed the best for warning of severe development and severe-RF. Also, temperature and Glu as risk factors for HFMD have been reported in many pieces of literature [8, 13–15]. In the further analysis of the risk factors between each group, we found that the content of SP, DP, NEUT#, NEUT%, RDW-SD, RDW-CV, GGT, CK/CK-MB, and Glu 9 indicators in mild, severe, and severe-RF patients all showed a significant increasing trend and can be used as risk factors in mild/severe, mild/severe-RF, and severe/severe-RF. Peng et al. found that in patients with severe HFMD, hyperglycemia, hypertension, and tachycardia are risk factors for neurogenic pulmonary edema [14]. Fang et al. also found that increased neutrophil count and increased EV71 infection are risk factors for severe HFMD [15]. Therefore, we speculate that these 9 indicators are closely related to the progression of HFMD patients and are potential risk predictors of HFMD. In the follow-up study, we will use these indicators as predictors to build a risk prediction model and subdivide and quantify the risks of each type of HFMD.

Although China has issued diagnosis and treatment guidelines for HFMD, scholars have established various prediction models based on local climate conditions, seasons, and other information [16–18], using the clinical prediction rules (CPRs) [19], machine learning system [20], and other conditions, but no relevant reports have been reported on the diagnosis of mild, severe, and severe-RF by clinical detection. In this study, we found that Glu performs better in the differential diagnosis of mild/severe-RF, and then, we developed and validated clinical prediction models for mild/severe and severe/severe-RF, respectively. The ROC curve showed that the models had good discrimination and accuracy, which could be used to diagnose HFMD patients with different conditions. Compared with the

prediction models, CPRs [19], machine learning system [20], and nomogram [7] developed based on information such as climatic conditions and seasons, the indicators used in our model are all derived from patients and are more closely related to HFMD patients. It is more suitable for clinical diagnosis.

During the development of the model, we tried to build a model with the indicators of significant differences between the mild/severe and severe/severe-RF groups as the predictive variables to differentiate and diagnose the mild/severe and severe/severe-RF at the same time, but the discrimination was not good. For example, the temperature has a significant difference in mild/severe, but no difference in severe/severe-RF. However, when developing the prediction model of mild/-severe, there is a large difference in the AUROC of whether to include temperature in the model built for prediction variables (included/excluded = 0.845/0.802). Temperature is not included here, and the modeling data is only obtained during model development and no detailed data is provided in this paper. The severity of disease of mild, severe, and severe-RF is different, and the importance of different predictive variables in establishing the prediction model of mild/severe and severe/severe-RF is different. Therefore, we chose different prediction factors for mild/severe and severe/severe-RF to build two different prediction models.

5. Strengths and Limitations of This Study

The advantage of our study is that, compared with the existing literature reports, the number of cases included in this study is more (19766 cases), covering mild, severe, and severe-RF patients, and for the first time, blood test indicators are used to establish the prediction model of severe and severe-RF. The limitations of this study, the lack of virus types in the data leading to HFMD, may lead to bias and limit clinical practice. Moreover, this study is a single-center retrospective study conducted in Jiangxi Province, China. We are not sure whether our results can show similar results in other ethnic groups in other regions. Finally, some qualitative indicators (such as lethargy, hyperglycemia, and vomiting) also play a certain role in the diagnosis of HFMD with different conditions, but this study is not included. In the follow-up study, we will investigate whether combining these indicators will optimize our model.

6. Conclusion

For the HFMD patients with mild, severe, and severe-RF, we have found appropriate risk factors and developed appropriate predictive models to help clinicians diagnose severe and severe-RF HFMD patients early.

Data Availability

The data used to support the findings of this study are included within the article.

Conflicts of Interest

The authors declare that they have no conflict of interest.

Acknowledgments

References

[1] L. Qin, D. Dang, X. Wang et al., "Identification of immune and metabolic predictors of severe hand-foot-mouth disease," *PLoS One*, vol. 14, no. 5, article e0216993, 2019.

[2] R. Dolin, "Enterovirus 71 — Emerging infections and emerging questions," *The New England Journal of Medicine*, vol. 341, no. 13, pp. 984-985, 1999.

[3] S. Y. Zhang, M. Y. Xu, H. M. Xu et al., "Immunologic characterization of cytokine responses to enterovirus 71 and coxsackievirus A16 infection in children," *Medicine (Baltimore)*, vol. 94, no. 27, article e1137, 2015.

[4] G. M. Leung, W. J. Xing, J. T. Wu, and H. Yu, "Hand, foot, and mouth disease in mainland China-Authors' reply," *Lancet Infectious Diseases*, vol. 14, no. 11, pp. 1042–1042, 2014.

[5] K. T. Van Voorhis and T. S. Willis, "Implementing a pediatric rapid response system to improve quality and patient safety," *Pediatric Clinics of North America*, vol. 56, no. 4, pp. 919–933, 2009.

[6] A. Monaghan, "Detecting and managing deterioration in children," *Paediatric Nursing*, vol. 17, no. 1, pp. 32–35, 2005.

[7] B. Wang, H. Feng, P. Huang et al., "Developing a nomogram for risk prediction of severe hand-foot-and-mouth disease in children," *Indian Journal of Pediatrics*, vol. 86, no. 4, pp. 365–370, 2019.

[8] C. Liu, K. Wang, N. Lin, J. Cai, B. Cui, and B. Wu, "Risk factors of severe hand, foot and mouth disease in Shantou, China: a case-control study," *Journal of Infection in Developing Countries*, vol. 12, no. 5, pp. 359–364, 2018.

[9] X. F. Ni, X. Li, C. Xu et al., "Risk factors for death from hand-foot-mouth disease: a meta-analysis," *Epidemiology and Infection*, vol. 148, article e44, 2020.

[10] L. Mei, X. Song, Y. Kong, and G. Yu, "An assessment of a pediatric early warning system score in severe hand-foot-and-mouth disease children: to detect clinical deterioration in hospitalized children," *Medicine (Baltimore)*, vol. 97, no. 26, article e11355, 2018.

[11] E. F. Schisterman, D. Faraggi, B. Reiser, and M. Trevisan, "Statistical inference for the area under the receiver operating characteristic curve in the presence of random measurement error," *American Journal of Epidemiology*, vol. 154, no. 2, pp. 174–179, 2001.

[12] H. Bozdogan, "Akaike's Information Criterion and Recent Developments in Information Complexity," *Journal of Mathematical Psychology*, vol. 44, no. 1, pp. 62–91, 2000.

[13] B. J. Sun, H. J. Chen, Y. Chen, X. D. An, and B. S. Zhou, "The Risk Factors of Acquiring Severe Hand, Foot, and Mouth Disease: A Meta- Analysis," *Canadian Journal of Infectious Diseases and Medical Microbiology,*, vol. 2018, article 2751457, pp. 1–12, 2018.

Research Article

Identification of Six Autophagy-Related-lncRNA Prognostic Biomarkers in Uveal Melanoma

Yao Chen ⓘ**, Lu Chen** ⓘ**, Jinwei Wang** ⓘ**, Jia Tan, and Sha Wang** ⓘ

Hunan Key Laboratory of Ophthalmology, Eye Center of Xiangya Hospital, Central South University, China

Correspondence should be addressed to Sha Wang; wangsha_1982@csu.edu.cn

Currently, no autophagy-related long noncoding RNA (lncRNA) has been reported to predict the prognosis of uveal melanoma patients. Our study screened for autophagy-related lncRNAs in 80 samples downloaded from The Cancer Genome Atlas (TCGA) database through lncRNA-mRNA coexpression. We used univariate Cox to further filter the lncRNAs. Multivariate Cox regression and LASSO regression were applied to construct an autophagy-associated lncRNA predictive model and calculate the risk score. Clinical risk factors were validated using Cox regression to determine whether they were independent prognostic indicators. Functional enrichment was performed using Gene Ontology and Kyoto Encyclopedia of Genes and Genomes. The model was built with six predictive autophagy-associated lncRNAs and clustered uveal melanoma patients into high- and low-risk groups. The risk score of our model was a significant independent prognostic factor (hazard ratio = 1.0; $p < 0.001$). Moreover, these six lncRNAs were significantly concentrated in the biological pathways of cytoplasmic component recycling, energy metabolism, and apoptosis. Thus, the six autophagy-associated lncRNAs are potential molecular biomarkers and treatment targets for uveal melanoma patients.

1. Introduction

Uveal melanoma is the most common intraocular malignancy in adults; the 10-year mortality rate of uveal melanoma is approximately 40%. Metastasis occurs in almost half of uveal melanoma patients, primarily in the liver. The survival time decreases to less than 1 year once metastasis is discovered [1]. Researchers have identified biomolecular abnormalities associated with a poor prognosis in uveal melanoma, such as the presence of monosomy 3 and gain of chromosome 8 [2]. Gene expression profiling divided the cancer into Class 1 and Class 2 based on the risk of metastasis [3] and revealed metastasis-related genetic mutations in BAP1, GNAQ/GNA11, EIF1AX, and SF3B1 [4, 5]. Despite the progress in understanding genetic regulation in uveal melanoma, current treatment modalities for this disease, such as brachytherapy, charged-particle radiotherapy, proton beam therapy, photodynamic therapy, and surgical excision, are still not beneficial to overall survival [6]. New strategies and potential targets are imperative to treat uveal melanoma.

Autophagy is a catabolic process involving the multistep degradation of proteins and organelles; it participates in maintaining cellular homeostasis, which is associated with heart disease, senescence, neurodegeneration, and cancer development [7]. Current studies of autophagy in uveal melanoma, though few, expose a new frontier to understand its carcinogenic and metastatic molecular mechanisms. Upregulated autophagy in uveal melanoma through intensified hypoxia is associated with metastasis and a poor prognosis [8]. However, enhanced autophagy in other studies inhibits cell proliferation and tumor growth [9]. Recently, Li et al. found that lncRNA ZNMT1 inhibited the tumorigenesis of uveal melanoma by inducing autophagy [10]. However, no other autophagy-associated lncRNA was reported [10].

Long noncoding RNAs (lncRNAs) are RNAs with a transcript length longer than 200 nucleotides that do not encode proteins; they play pivotal roles in epigenetic modification, chromatin remodeling, and genetic imprinting [11]. Gene sequencing of cancer has identified several protein-encoding genes as potential antitumor targets, with 98% of the sequence in noncoding regions, which indicates that most

mechanisms of lncRNAs remain unclarified in cancer research [12]. Current studies have unraveled a close relationship between lncRNAs and uveal melanoma [13–15]. lncRNA interacts with microRNA (miRNA) and promotes uveal melanoma cell proliferation, tumor initiation, and metastasis by targeting EZH2 or through the p53 signaling pathway [13]. lncRNA such as SNHG15 indicates a poor prognosis in uveal melanoma, while TCONS_00004101, RP11-551L14.4, and TCONS_00004845 are metastasis-associated lncRNAs of uveal melanoma [16]. Autophagy-related lncRNAs have been studied extensively in several biological pathways and represent a new frontier for cancer study [17]. However, autophagy-associated lncRNAs in uveal melanoma have been rarely studied. This study was aimed at building an autophagy-associated lncRNA profile using TCGA database, investigating new lncRNA predictive biomarkers, and identifying potential molecular targets for uveal melanoma.

2. Materials and Methods

2.1. Data Extraction. The transcriptome RNA sequencing and clinical data of 80 uveal melanoma samples were downloaded from The Cancer Genome Atlas (TCGA) data portal (https://portal.gdc.cancer.gov/). The study excluded samples with a follow-up time of less than 30 days because these patients might have died of unpredictable factors. The raw data were collected, standardized by log2 transformation, and merged into a matrix file. The lncRNA profiling data was acquired from the RNA-seq dataset using Perl language. The Ensembl ID numbers of the genes were transformed to gene symbols using Perl language based on the Ensembl database.

2.2. Identification of Autophagy-Related Genes and lncRNA/mRNA Coexpression Network. The autophagy-related genes were downloaded from the Human Autophagy Database (HADb, http://www.autophagy.lu/) and gene set enrichment analysis (GSEA, https://www.gsea-msigdb.org/gsea/index.jsp). Pearson's correlation analysis was conducted using R software 3.6.2 to calculate the correlation of lncRNAs and autophagy-related genes. lncRNAs with squared correlation coefficient $R^2 > 0.3$ and $p < 0.001$ were considered correlated with autophagy. Visualization of lncRNA/mRNA coexpression network was performed by Cytoscape software 3.6.1.

2.3. Establishment of Autophagy-Related lncRNA Biomarkers. Univariate Cox regression was applied to identify the prognostic value of autophagy-related lncRNAs, in which p value < 0.05 was incorporated into the least absolute shrinkage and selection operator (LASSO) regression [18] with the glmnet R package. Multivariate Cox regression analysis based on the results of LASSO regression was performed to establish a risk score and identify the prognostic lncRNA biomarkers. The risk score was established from the expression levels multiplied by the Cox regression coefficients: risk score $= (0.34184 * SOS1 - IT1) + (1.14771 * AC016747.1) + (0.55510 * AC100791.3) - (2.78048 * AC$ 104825.1) $- (1.59941 * AC090617.5) + (0.33215 * AC$ 018904.1). Patients with survival data were divided into high-risk and low-risk groups according to the median risk score. Kaplan–Meier survival analysis was applied to evaluate the predictive ability of the autophagy-related lncRNA biomarkers. Moreover, the relationship between the prognostic biomarkers and clinical features such as gender, age, tumor stage, and T stage from the TNM staging method (a method to describe the tumor status) was evaluated using univariate and multivariate Cox proportional hazard regression analyses.

2.4. Construction of a Predictive Nomogram [19]. We constructed a nomogram to predict the survival of uveal melanoma patients (1-, 3-, and 5-year survival). The concordance index (*C*-index), calibration plot, and receiver operating characteristic (ROC) analysis were used to validate the biomarkers.

2.5. Gene Ontology (GO) and Kyoto Encyclopedia of Genes and Genomes (KEGG) Enrichment Analysis. We used GSEA v3.0 software [20, 21] to identify the top 10 KEGG signaling pathways and functionally enriched GO terms regulated by the autophagy-related biomarkers.

2.6. Cell Culture. Normal human uveal melanocytes (UM-U-95) were donated while uveal melanoma cell line MP46 (CRL-3298) was purchased from ATCC. The cells were cultured in DMEM with 10% heat-inactivated fetal bovine serum at 37°C incubator and 5% CO_2 in air atmosphere.

2.7. qRT-PCR. We utilized the qRT-PCR to validate the expression of these lncRNA biomarkers between normal human uveal melanocytes and uveal melanoma. cDNA of each sample was converted for qPCR. The primers were designed by Primer3 targeting each lncRNA biomarker. U6 was utilized for the housekeeping gene. The cycling condition was conducted as follows: 94°C for denaturation, 60°C for annealing, and 72°C for extension. All PCR was performed in LightCycler 480 (Roche). Primers are listed in supplementary table 2.

2.8. Statistical Analysis. Differences between groups were compared using R software (Wilcoxon test). LASSO regression analysis and univariate and multivariate Cox regression analyses were applied to identify prognostic lncRNA biomarkers for uveal melanoma patients. Kaplan–Meier analysis was used to build survival curves, and the significance of the differences in survival time was calculated using the log-rank test. $p < 0.05$ was considered statistically significant.

3. Results

3.1. Screening for Autophagy-Associated lncRNAs in Uveal Melanoma Patients. We identified 14142 lncRNAs from the RNA sequencing data of TCGA-UVM. In total, 516 autophagy-associated genes were obtained from GSEA and the HADb database (Supplementary table 1). We constructed a lncRNA-mRNA coexpression network to

(a)

(b)
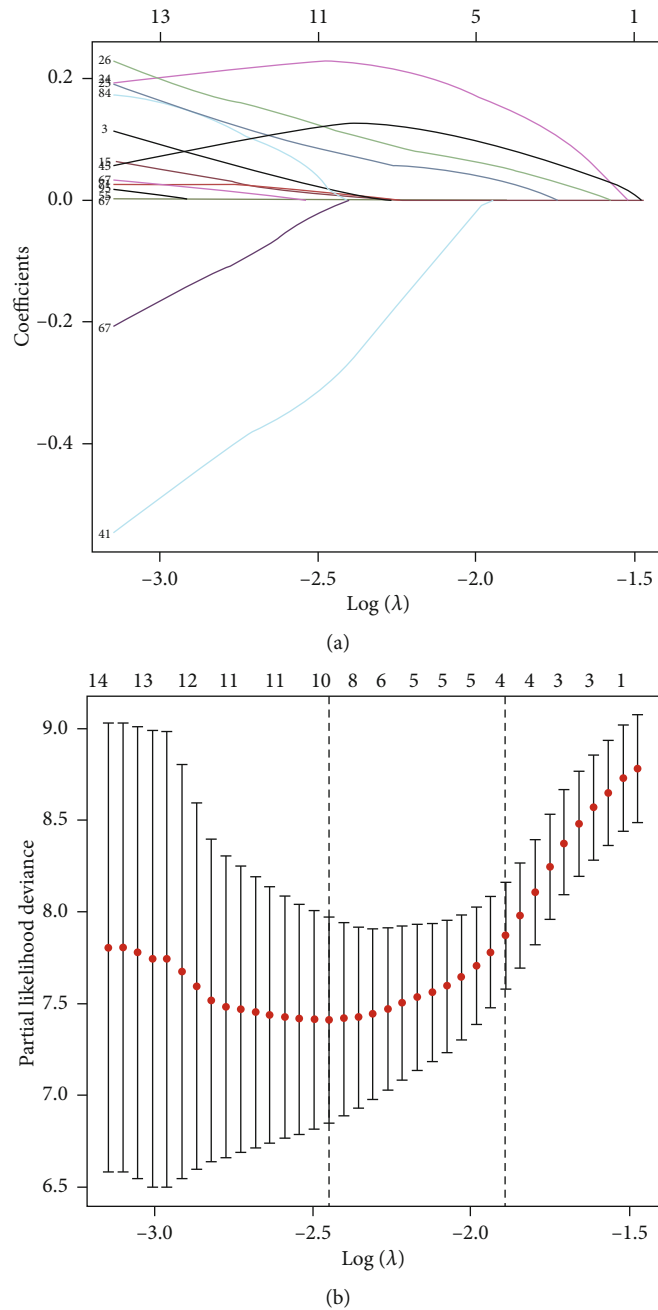
FIGURE 1: LASSO model. Autophagy-related lncRNA selection using the LASSO model. (a) Shows the profiles of LASSO coefficients. (b) Shows the LASSO coefficient values of the 6 autophagy-related lncRNAs in uveal melanoma. The vertical dashed lines are the optimal log (λ) values.

screen for autophagy-associated lncRNAs. 730 lncRNAs were selected through Pearson's correlation analysis with the criteria of $|R^2| > 0.3$ and $p < 0.001$.

3.2. Coexpression of lncRNA/mRNA and Construction of the Autophagy-Associated lncRNA Model in Uveal Melanoma. We identified 105 autophagy-associated lncRNAs with a prognostic value in uveal melanoma patients based on the results of Cox univariate analysis ($p < 0.05$) and then selected six prognosis-related lncRNAs by LASSO regression analysis (Figure 1). A coexpression network of lncRNAs and mRNAs

was constructed (Supplementary Fig. 2B). As shown in the Sankey diagram (Supplementary Fig. 2A), among these lncRNAs, SOS1-IT1, AC016747.1, AC100791.3, and AC018904.1 are risky prognostic lncRNAs, whereas AC104825.1 and AC090617.5 are protective prognostic lncRNAs. The risk score was calculated with the following formula: risk score $= (0.34184 * SOS1 - IT1) + (1.14771 * AC016747.1) + (0.55510 * AC100791.3) - (2.78048 * AC 104825.1) - (1.59941 * AC090617.5) + (0.33215 * AC 018904.1)$. The relationship between the selected lncRNAs and prognosis is shown in the forest map (Figure 2(a)).

(a)

(b)
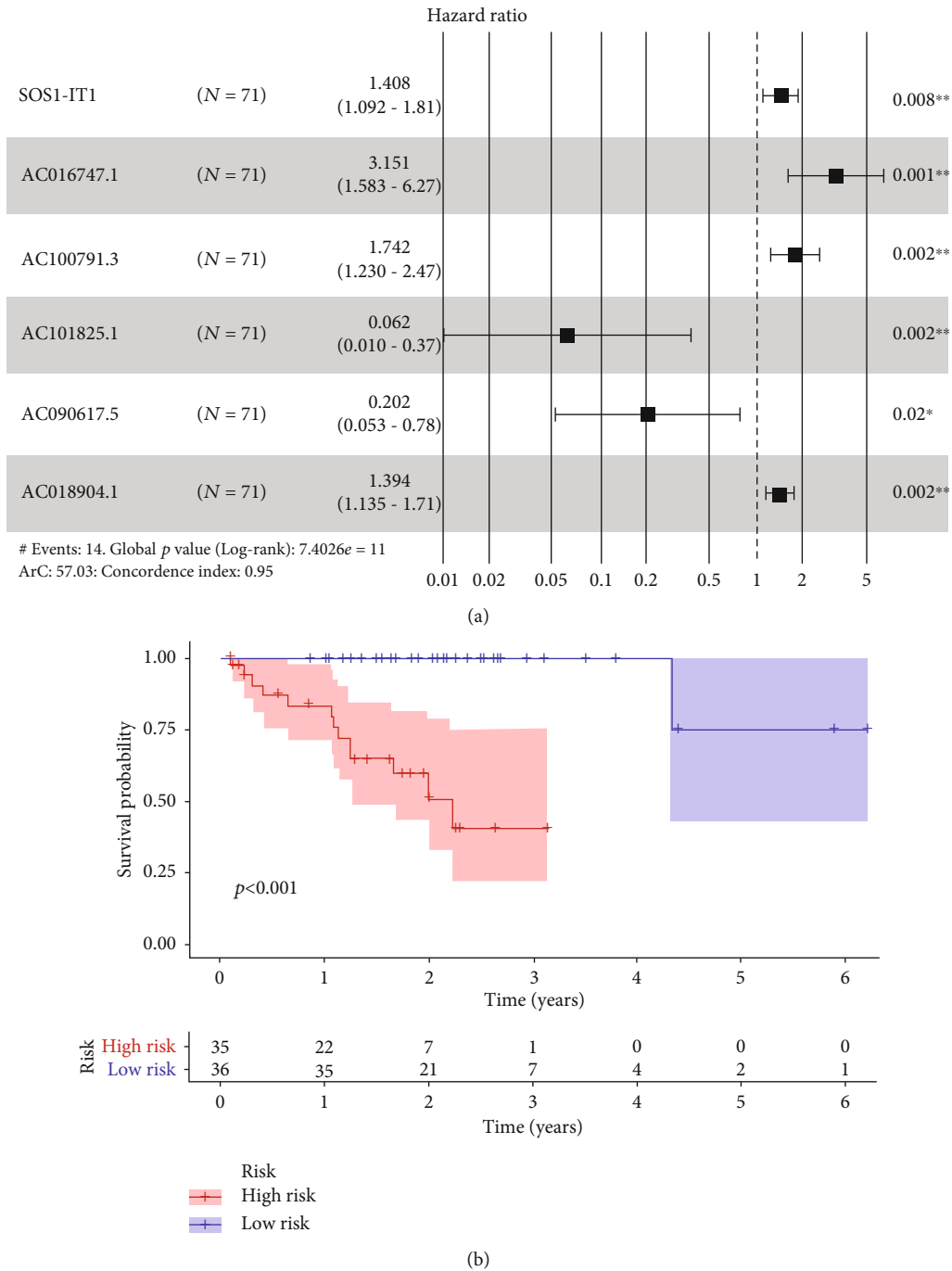
FIGURE 2: The selected biomarkers and prognosis: (a) forest map of the relationships among the six autophagy-associated lncRNAs and prognosis in uveal melanoma patients; (b) overall survival of the six-lncRNA signatures in uveal melanoma patients.

3.3. Evaluation of the Prognostic Biomarkers. To evaluate the aforementioned autophagy-lncRNA prognostic model, we divided the uveal melanoma patients into high- and low-risk groups according to the median risk score of the selected six autophagy-related lncRNAs. The number of patient deaths increased with increasing risk score (Figure 3(b)). The overall survival was longer in the low-risk group than in the high-risk group ($p < 0.001$) (Figure 3(c)). Regarding individual lncRNAs of the prognostic signature, the survival rate was also significantly associated with the expression of

each lncRNA (patients were divided into high- and low-expression groups based on the median expression of lncRNA) (Figure 4).

3.4. Prognostic Associations of the Selected lncRNA Biomarkers for Clinicopathological Features. We studied the relationship between the risk score of autophagy-associated lncRNA biomarkers and clinicopathological characteristics of the uveal melanoma patients, such as age, gender, and tumor stage. The risk score was significantly increased if the

(a)

(b)

(c)
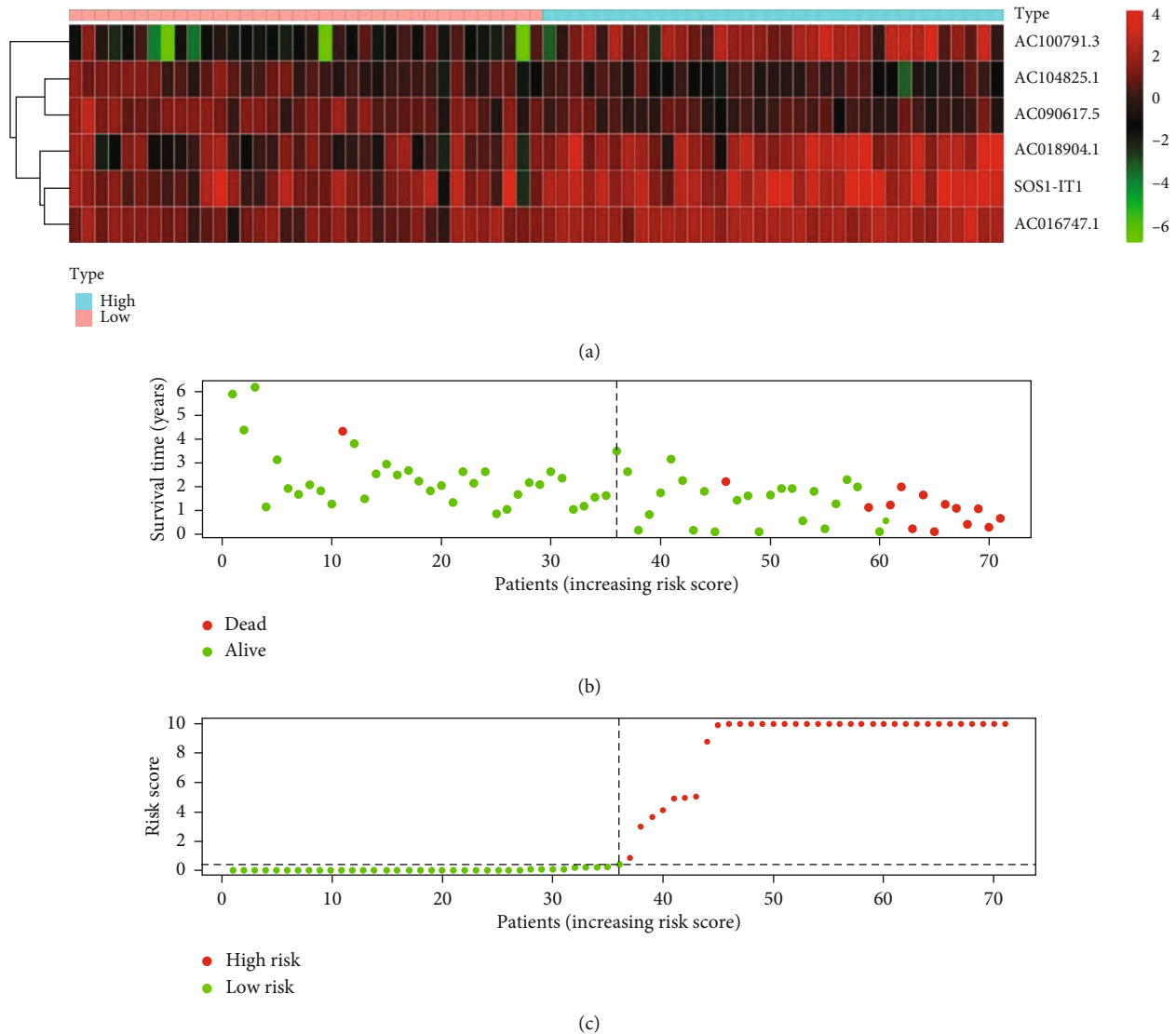
FIGURE 3: Risk score: (a) heatmap of the expression of the six lncRNAs in uveal melanoma patients; (b) distribution of the survival time and status in relation to risk score; (c) distribution of high- and low-risk patients according to the risk score.

patient was older than 60 years. Univariate Cox regression was performed to identify three independent prognostic indicators (age, stage, and risk score) (Figure 5(a)). Multivariate Cox regression revealed that risk score was a strong independent prognostic factor for uveal melanoma survival (Figure 5(b)). The subsequent calculated AUCs for risk score, age, gender, stage, and stage T of the ROC curves were 0.905, 0.637, 0.519, 0.860, and 0.688, respectively, which demonstrates that the risk score and stage were two influential indicators (Figure 5(f)). The nomogram for overall survival prediction at 1, 3, and 5 years was constructed by integrating these clinicopathological features, and calibration plots of the nomogram suggested consistency between observation and prediction (Figure 6). The C-index was 0.912 for the nomogram. ROC analysis showed that the AUCs of the nomogram at 1-, 3-, and 5-year survival were 1.003, 1.076, and 0.896, respectively, which indicates a favourable predictive capability of our model.

3.5. Gene Set Enrichment Analysis of the lncRNA Biomarkers. Gene set enrichment analysis of the autophagy-associated lncRNA biomarkers was performed using gene sets in GO and KEGG. GO analysis showed that the autophagy-associated lncRNAs were mostly enriched in cellular ATP metabolic process, protein metabolic process, and proton transporting activity (Figure 7(a)). KEGG analysis indicated that the autophagy-associated lncRNAs were concentrated in molecular signaling pathways such as amino sugar and nucleotide sugar metabolism, proteasome, apoptosis, and oxidative phosphorylation (Figure 7(b)). To further verify the six lncRNA biomarkers, we tested these six autophagy-associated lncRNAs' expression between normal uveal melanocyte and uveal melanoma. Our qRT-PCR results demonstrated that the expression of SOS1-IT1, AC016747.1, AC100791.3, and AC018904.1 was higher in uveal melanoma cell line; in contrast, uveal melanoma cell lines had a significantly lower expression of AC104825.1 and AC090617.5
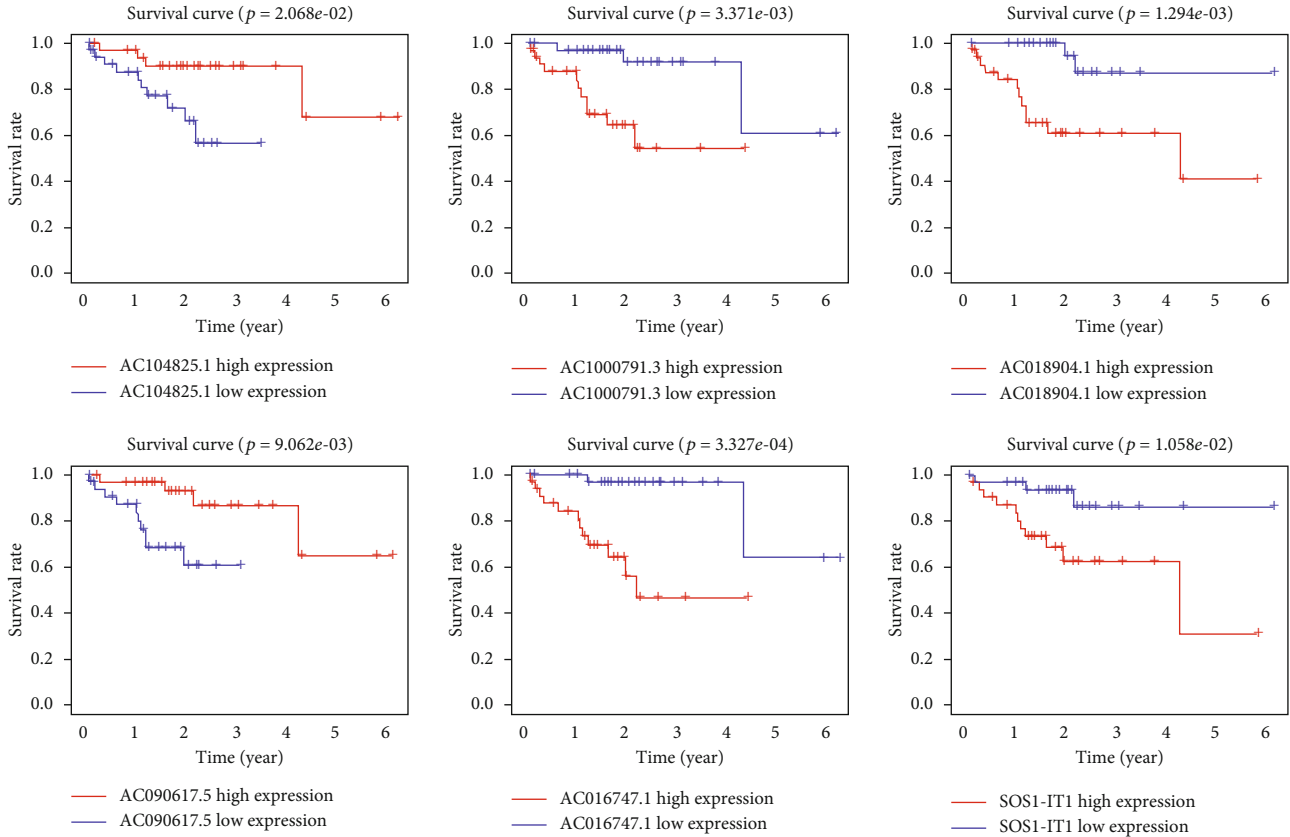
FIGURE 4: The association between the selected lncRNAs and survival. Expression of the selected six lncRNAs and their relationship to the survival rate of uveal melanoma patients.

(Figure 8) with p value < 0.05. These results confirmed the clinical utility of six autophagy-associated lncRNAs as biomarkers for uveal melanoma.

4. Discussion

Uveal melanoma is the most common primary intraocular tumor in adults, and progress has been made in genetic prognostic testing, with gene expression profiling clustering the tumor into Class 1 (high metastatic potential) and Class 2 (low metastatic potential) tumors [3]. Additionally, researchers have reported miRNA signatures to predict uveal melanoma prognosis based on bioinformatics analysis [22, 23]. However, studies using real-world samples of uveal melanoma reported no association between the miRNAs and overall survival or metastasis [24]. Therefore, more effective biomarkers must be investigated.

Autophagy is a highly conversed cellular process that maintains the energy level to recycle amino acid and other nutrients, as well as renew cytoplasmic constituents [25]. Autophagy has dual functions in tumorigenesis: in normal cells, autophagy plays a pivotal role in surveilling damaged organelles, purging congregated proteins, and reducing abnormal DNA and reactive oxygen compounds, preventing somatic cells from transforming into cancer cells [26–28]. Conversely, in tumor cells, the aforementioned functions of autophagy inversely accelerate the metabolism rate, enhance

the cellular capability of taking up nutrients, resist apoptosis, and develop multidrug resistance, which subsequently propels cancer development [29, 30]. In uveal melanoma patients, autophagy-associated proteins MAP1LC3A and BECN1 are commonly upregulated and are related to tumor development which resulted in poor prognosis [8]. In uveal melanoma cell lines, increased autophagy helps tumor cell survive stressed conditions [9], which indicates the vital role of autophagy in uveal melanoma progression.

In recent years, several bioinformatics studies have been performed on uveal melanoma with the development of high-throughput sequencing to identify useful indicators for prognosis or therapeutic targets, including genome-wide predictors, methylation biomarkers, and prognostic lncRNAs [31–33]. In particular, since the discovery of lncRNAs' function as important regulators in multiple cellular processes, lncRNAs have become a hotspot in cancer studies. However, autophagy-associated lncRNAs have been less reported in uveal melanoma and a detailed and thorough analysis of the associations between lncRNA expression and autophagy in uveal melanoma prognosis remains poorly understood.

We identified six autophagy-associated lncRNAs to predict the prognosis of uveal melanoma by screening lncRNAs from 80 tumor samples from TCGA database. Clinical features such as age older than 60 years and stage were independent risk factors. Furthermore, the functions of these
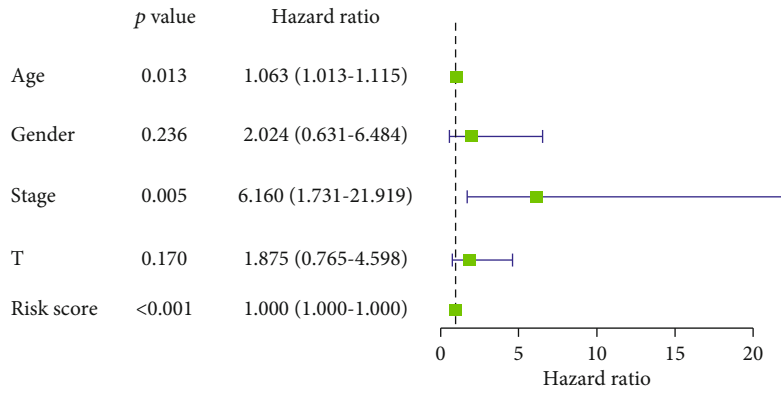
(a)
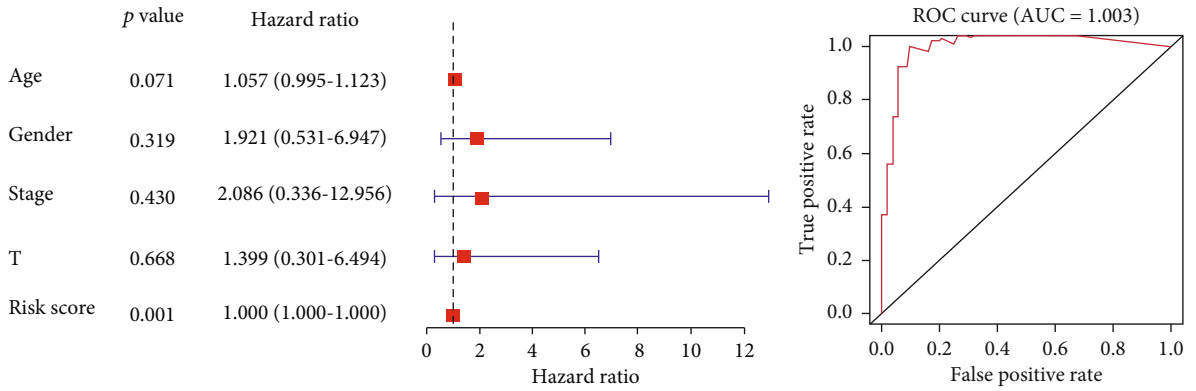
(b)

(c)
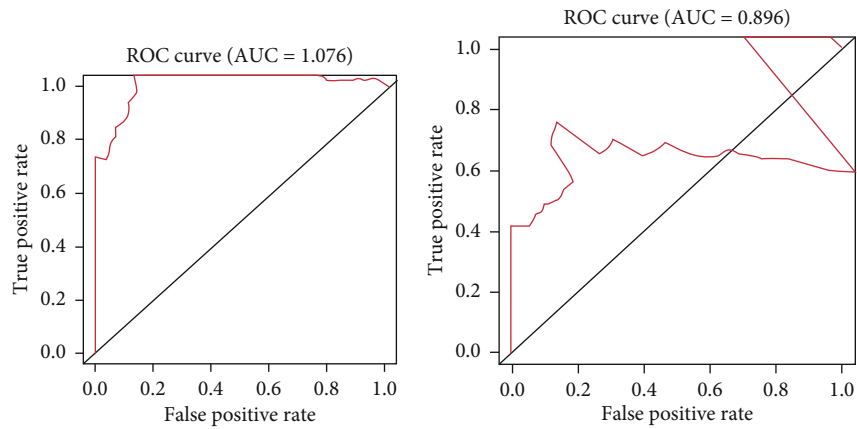
(d)

(e)

FIGURE 5: Continued.

(f)
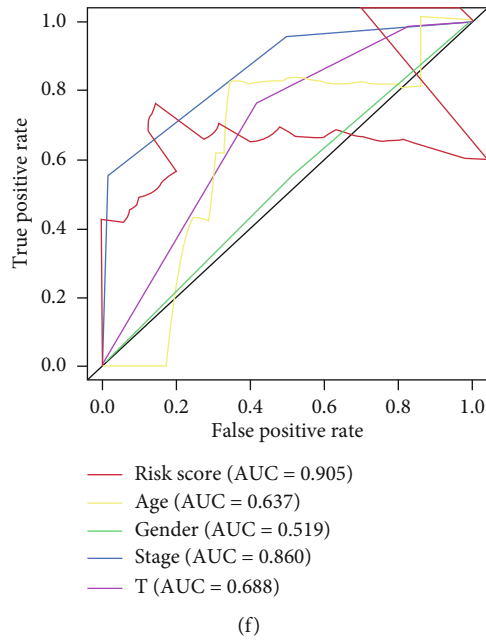
FIGURE 5: Risk factors. Univariate (a) and multivariate (b) Cox regression analyses of clinical features, such as age, gender, stage, T stage, and risk score. The 1-year (c), 3-year (d), and 5-year (e) ROC curves of the risk scores and ROC curves of the clinical features (f).

(a)

(b)
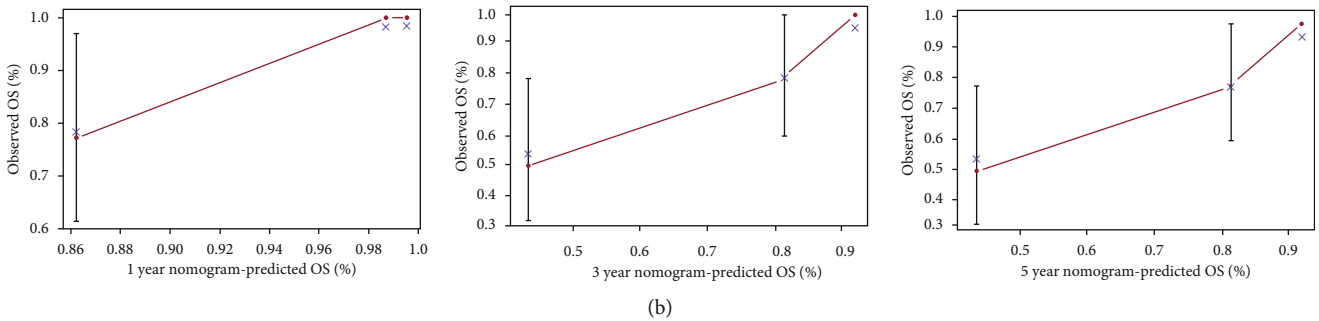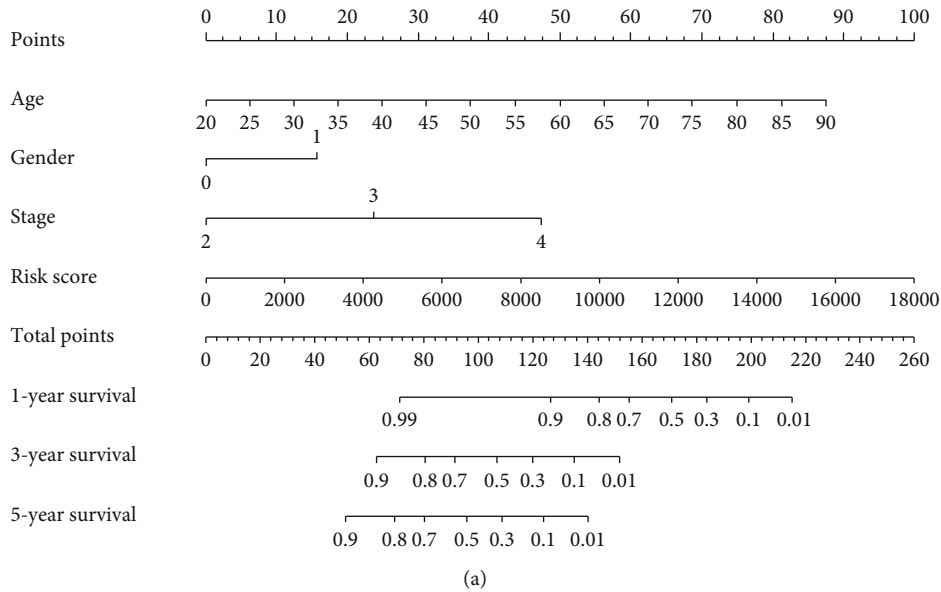
FIGURE 6: Overall survival. Nomogram for the overall survival prediction at 1, 3, and 5 years (a) and calibration plots of the nomogram at 1, 3, and 5 years (b).

High expression ◄ - - - - - - - ► Low expression

— KEGG_Amino_sugar_and_nucleotide_sugar_metabolism
— KEGG_Apoptosis
— KEGG_Oxidative_phosphorylation
— KEGG_Proteasome
— KEGG_Pyrimidine_metabolism

(a)

High expression ◄ - - - - - - ► Low expression

— GO_ATP_metabolic_process
— GO_Glycine_metabolic_process
— GO_Proton_transmembrane_transporter_activity
— GO_Proton_tranporting_two_sector_atpase_complex_catalytic_domain
— GO_Regulation_of_cellular_amino_acid_metabolic_process

(b)

Figure 7: Gene set enrichment analysis of the lncRNA biomarkers. The top five enriched gene sets are shown from gene set enrichment analysis of the autophagy-associated lncRNA biomarkers performed using gene sets of GO (a) and KEGG (b).
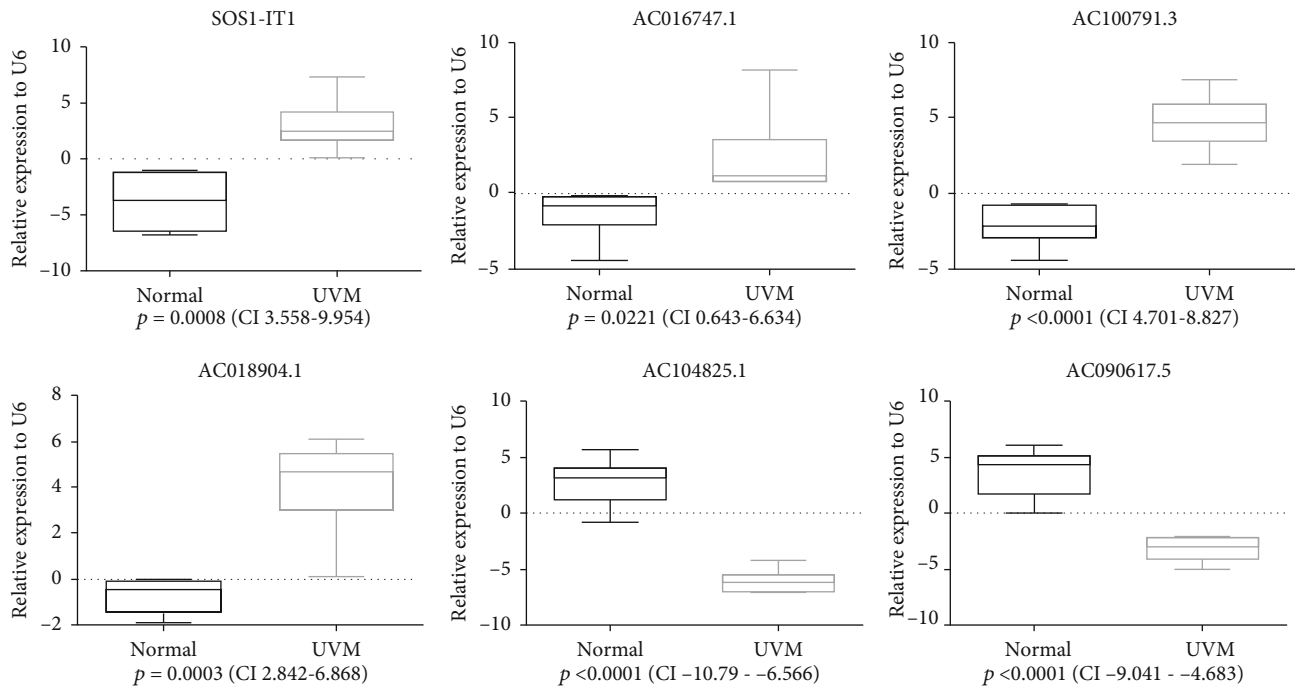
FIGURE 8: RT-PCR results. The expression of six lncRNAs in uveal melanoma and normal uveal melanocyte. Normal; human uveal melanocytes; UVM: human uveal melanoma cells: *P*: *p* value; CI: confidence interval.

lncRNAs are concentrated on cellular energy and nutrient metabolism and protease activity based on GO and KEGG analyses, consistent with the functions of autophagy.

Among these six lncRNAs, SOS1-IT1, AC016747.1, AC100791.3, and AC018904.1 are hazardous indicators, while AC104825.1 and AC090617.5 are protective factors. SOS1-IT1 was also reported as a risk factor in an ivermectin-related three-lncRNA prognostic model of ovarian cancer [34]. According to the description on GeneCards (https://www.genecards.org/), it is sense intronic to MAP4K3, which is a serine/threonine kinase leading to T-cell activation, cellular autophagy inhibition, cancer recurrence, and metastasis [35]. AC016747.1, also known as LOC339803, acts as a ceRNA of miR-30a-5p and promotes the migration and invasion of hepatocellular carcinoma [36]. Additionally, it is highly expressed in human atherosclerotic lesions to enhance transcription factors in abnormal endothelial metabolism when subjected to hypoxia [37]. AC100791.3 is antisense to TBC1D16 according to Gene-Cards, with the protein TBC1D16 playing a critical role in the progression of cutaneous melanoma [38]. AC018904.1, although its function is unclear, is described as antisense to ADAM10 on GeneCards. ADAM10, as a disintegrin and metalloproteinase 10, participates in multiple catalytic activities, including apoptosis, autoimmunity, cell adhesion and metabolism, cancer proliferation, and metastasis [39]. Increased ADAM10 impairs autophagy and aggravates inflammatory activities in fibroblasts. However, in Alzheimer's disease, ADAM10 facilitates autophagy in cleaving and removing abnormal proteins, demonstrating a neuroprotective effect [40]. These facts imply a potential effect of AC018904.1 on autophagy. No data have been reported for

the remaining two lncRNAs AC104825.1 and AC090617.5 or their aliases on GeneCards. Further study is warranted on the above six lncRNAs to unravel the underlying mechanisms between autophagy and uveal melanoma, and they could also be used as possible biologic targets.

However, this study has some limitations. First, the 80 samples in TCGA database were relatively small compared with the patient number of other cancer types, leading to deviation in the analysis. Second, because most of the clinical data of the M and N stages of uveal melanoma patients are not available, whether they are independent risk factors is unclear. Third, the prognostic value of our model should be further validated and confirmed by other cohorts. Fourth, other prognostic features, such as ciliary body involvement, tumor height, epithelioid cell type, and chromosomal status, were not included in our study because some of the information was not available.

5. Conclusions

Our study filtered six autophagy-related lncRNAs through TCGA database. The risk model based on these six lncRNAs could cluster the prognosis of uveal melanoma into high- and low-risk groups. More importantly, the risk score could be used as an independent risk factor for the prediction of overall survival and provide evidence for potential biomarkers in uveal melanoma treatment.

Data Availability

The data used during the study are available online (TCGA database, https://portal.gdc.cancer.gov/; HADb database,

http://www.autophagy.lu/; and GSEA database, https://www.gsea-msigdb.org/gsea/index.jsp).

Conflicts of Interest

The authors declare that there is no conflict of interest regarding the publication of this paper.

Acknowledgments

Supplementary Materials

Supplementary 1. Supplementary Table 1: a total of 516 autophagy-associated genes obtained from GSEA and the HADb database.

Supplementary 2. Supplementary Table 2: primers for rtPCR.

Supplementary 3. Supplementary Figure: coexpression. Coexpression of lncRNA/mRNA shown with a Sankey diagram (A) and Cytoscape (B).

References

[1] M. Bande, D. Fernandez-Diaz, B. Fernandez-Marta et al., "The role of non-coding RNAs in uveal melanoma," *Cancers*, vol. 12, no. 10, p. 2944, 2020.

[2] F. Hamadeh, C. A. Medina, A. D. Singh, J. P. Reynolds, and C. V. Biscotti, "Uveal melanoma: an analysis of cellular features and comparison to monosomy 3 status," *Diagnostic Cytopathology*, vol. 44, no. 5, pp. 377–383, 2016.

[3] J. W. Harbour, "The genetics of uveal melanoma: an emerging framework for targeted therapy," *Pigment Cell & Melanoma Research*, vol. 25, no. 2, pp. 171–181, 2012.

[4] C. Chattopadhyay, D. W. Kim, D. S. Gombos et al., "Uveal melanoma: from diagnosis to treatment and the science in between," *Cancer*, vol. 122, no. 15, pp. 2299–2312, 2016.

[5] K. M. Staby, K. Gravdal, S. J. Mork, S. Heegaard, O. K. Vintermyr, and J. Krohn, "Prognostic impact of chromosomal aberrations and GNAQ, GNA11 and BAP1 mutations in uveal melanoma," *Acta Ophthalmologica*, vol. 96, no. 1, pp. 31–38, 2018.

[6] B. Tarlan and H. Kiratli, "Uveal melanoma: current trends in diagnosis and management," *Turkish Journal of Ophthalmology*, vol. 46, no. 3, pp. 123–137, 2016.

[7] B. Levine and G. Kroemer, "Autophagy in the pathogenesis of disease," *Cell*, vol. 132, no. 1, pp. 27–42, 2008.

[8] A. N. Giatromanolaki, G. St Charitoudis, N. E. Bechrakis et al., "Autophagy patterns and prognosis in uveal melanomas," *Modern Pathology*, vol. 24, no. 8, pp. 1036–1045, 2011.

[9] Y. Zhao, W. Wang, I. Min et al., "BRAF V600E-dependent role of autophagy in uveal melanoma," *Journal of Cancer Research and Clinical Oncology*, vol. 143, no. 3, pp. 447–455, 2017.

[10] P. Li, J. He, Z. Yang et al., "ZNNT1 long noncoding RNA induces autophagy to inhibit tumorigenesis of uveal melanoma by regulating key autophagy gene expression," *Autophagy*, vol. 16, no. 7, pp. 1186–1199, 2020.

[11] J. R. Prensner and A. M. Chinnaiyan, "The emergence of lncRNAs in cancer biology," *Cancer Discovery*, vol. 1, no. 5, pp. 391–407, 2011.

[12] E. Guzel, T. M. Okyay, B. Yalcinkaya, S. Karacaoglu, M. Gocmen, and M. H. Akcakuyu, "Tumor suppressor and oncogenic role of long non-coding RNAs in cancer," *Northern Clinics of Istanbul*, vol. 7, no. 1, pp. 81–86, 2020.

[13] X. M. Huang, S. S. Shi, T. M. Jian, D. R. Tang, T. Wu, and F. Y. Sun, "LncRNA PVT1 knockdown affects proliferation and apoptosis of uveal melanoma cells by inhibiting EZH2," *European Review for Medical and Pharmacological Sciences*, vol. 23, no. 7, pp. 2880–2887, 2019.

[14] Q. Lu, N. Zhao, G. Zha, H. Wang, Q. Tong, and S. Xin, "LncRNA HOXA11-AS exerts oncogenic functions by repressing p21 and miR-124 in uveal melanoma," *DNA and Cell Biology*, vol. 36, no. 10, pp. 837–844, 2017.

[15] H. Xu, J. Gong, and H. Liu, "High expression of lncRNA PVT1 independently predicts poor overall survival in patients with primary uveal melanoma," *PLoS One*, vol. 12, no. 12, article e0189675, 2017.

[16] X. Wu, X. F. Li, Q. Wu, R. Q. Ma, J. Qian, and R. Zhang, "LncRNA SNHG15 predicts poor prognosis in uveal melanoma and its potential pathways," *International Journal of Ophthalmology*, vol. 13, no. 8, pp. 1195–1201, 2020.

[17] L. B. Frankel, M. Lubas, and A. H. Lund, "Emerging connections between RNA and autophagy," *Autophagy*, vol. 13, no. 1, pp. 3–23, 2017.

[18] R. Tibshirani, "The lasso method for variable selection in the Cox model," *Statistics in Medicine*, vol. 16, no. 4, pp. 385–395, 1997.

[19] A. Iasonos, D. Schrag, G. V. Raj, and K. S. Panageas, "How to build and interpret a nomogram for cancer prognosis," *Journal of Clinical Oncology: Official Journal of the American Society of Clinical Oncology*, vol. 26, no. 8, pp. 1364–1370, 2008.

[20] A. Subramanian, P. Tamayo, V. K. Mootha et al., "Gene set enrichment analysis: a knowledge-based approach for interpreting genome-wide expression profiles," *Proceedings of the National Academy of Sciences of the United States of America*, vol. 102, no. 43, pp. 15545–15550, 2005.

[21] V. K. Mootha, C. M. Lindgren, K. F. Eriksson et al., "PGC-1α-responsive genes involved in oxidative phosphorylation are coordinately downregulated in human diabetes," *Nature Genetics*, vol. 34, no. 3, pp. 267–273, 2003.

[22] L. Falzone, G. L. Romano, R. Salemi et al., "Prognostic significance of deregulated microRNAs in uveal melanomas," *Molecular Medicine Reports*, vol. 19, no. 4, pp. 2599–2610, 2019.

[23] X. Xin, Y. Zhang, F. Ling et al., "Identification of a nine-miRNA signature for the prognosis of uveal melanoma," *Experimental Eye Research*, vol. 180, pp. 242–249, 2019.

[24] A. C. Larsen, L. Holst, B. Kaczkowski et al., "MicroRNA expression analysis and multiplex ligation-dependent probe amplification in metastatic and non-metastatic uveal melanoma," *Acta Ophthalmologica*, vol. 92, no. 6, pp. 541–549, 2014.

[25] R. C. Russell, H. X. Yuan, and K. L. Guan, "Autophagy regulation by nutrient signaling," *Cell Research*, vol. 24, no. 1, pp. 42–57, 2014.

[26] S. Rao, L. Tortola, T. Perlot et al., "A dual role for autophagy in a murine model of lung cancer," *Nature Communications*, vol. 5, no. 1, p. 3056, 2014.

[27] A. Takamura, M. Komatsu, T. Hara et al., "Autophagy-deficient mice develop multiple liver tumors," *Genes & Development*, vol. 25, no. 8, pp. 795–800, 2011.

[28] J. Y. Guo, G. Karsli-Uzunbas, R. Mathew et al., "Autophagy suppresses progression of K-ras-induced lung tumors to oncocytomas and maintains lipid homeostasis," *Genes & Development*, vol. 27, no. 13, pp. 1447–1461, 2013.

[29] Y. J. Li, Y. H. Lei, N. Yao et al., "Autophagy and multidrug resistance in cancer," *Chinese Journal of Cancer*, vol. 36, no. 1, p. 52, 2017.

[30] R. K. Amaravadi, A. C. Kimmelman, and J. Debnath, "Targeting autophagy in cancer: recent advances and future directions," *Cancer Discovery*, vol. 9, no. 9, pp. 1167–1181, 2019.

[31] B. Xu, R. Ma, H. Ren, and J. Qian, "Genome-wide analysis of uveal melanoma metastasis-associated LncRNAs and their functional network," *DNA and Cell Biology*, vol. 37, no. 2, pp. 99–108, 2018.

[32] M. F. Bakhoum and B. Esmaeli, "Molecular characteristics of uveal melanoma: insights from The Cancer Genome Atlas (TCGA) project," *Cancers*, vol. 11, no. 8, p. 1061, 2019.

[33] Y. Ni, Z. Zhang, G. Chen, W. Long, L. Tong, and J. Zeng, "Integrated analyses identify potential prognostic markers for uveal melanoma," *Experimental Eye Research*, vol. 187, p. 107780, 2019.

[34] N. Li and X. Zhan, "Anti-parasite drug ivermectin can suppress ovarian cancer by regulating lncRNA-EIF4A3-mRNA axes," *The EPMA Journal*, vol. 11, no. 2, pp. 289–309, 2020.

[35] H. C. Chuang and T. H. Tan, "MAP4K3/GLK in autoimmune disease, cancer and aging," *Journal of Biomedical Science*, vol. 26, no. 1, p. 82, 2019.

[36] C. Xue, X. Zhang, P. Gao, X. Cui, C. Zhu, and X. Qin, "LncRNA loc339803 acts as CeRNA of miR-30a-5p to promote the migration and invasion of hepatocellular carcinoma cells," *Journal of Cancer*, vol. 12, no. 4, pp. 1061–1072, 2021.

[37] P. R. Moreau, T. Ord, N. L. Downes et al., "Transcriptional profiling of hypoxia-regulated non-coding RNAs in human primary endothelial cells," *Frontiers in Cardiovascular Medicine*, vol. 5, p. 159, 2018.

[38] J. Wouters, M. Vizoso, A. Martinez-Cardus et al., "Comprehensive DNA methylation study identifies novel progression-related and prognostic markers for cutaneous melanoma," *BMC Medicine*, vol. 15, no. 1, p. 101, 2017.

[39] T. M. Smith Jr., A. Tharakan, and R. K. Martin, "Targeting ADAM10 in cancer and autoimmunity," *Frontiers in Immunology*, vol. 11, p. 499, 2020.

[40] D. Puigoriol-Illamola, C. Grinan-Ferre, F. Vasilopoulou, R. Leiva, S. Vazquez, and M. Pallas, "11β-HSD1 inhibition by RL-118 promotes autophagy and correlates with reduced oxidative stress and inflammation, enhancing cognitive performance in SAMP8 mouse model," *Molecular Neurobiology*, vol. 55, no. 12, pp. 8904–8915, 2018.

Review Article

A Review of Novel Cardiac Biomarkers in Acute or Chronic Cardiovascular Diseases: The Role of Soluble ST2 (sST2), Lipoprotein-Associated Phospholipase A2 (Lp-PLA2), Myeloperoxidase (MPO), and Procalcitonin (PCT)

Junpei Li,[1] Tianyu Cao,[2] Yaping Wei,[3] Nan Zhang,[4] Ziyi Zhou,[5] Zhuo Wang,[3] Jingyi Li,[6] Yue Zhang,[6] Sijia Wang,[7] Ping Wang,[7] Nannan Cheng,[6] Lijing Ye,[6] Minghui Li,[1] Yu Yu [1] Congcong Ding,[1] Ziheng Tan,[1] Biming Zhan,[1] Qiangqiang He,[3] Huihui Bao,[1] Yanqing Wu,[1] Lishun Liu,[5,8] Jianping Li,[4] Xiping Xu,[3,8,9] Xiaoshu Cheng [1] and Xiao Huang [1]

[1]Department of Cardiology, Nanchang University Second Affiliated Hospital, Nanchang, China
[2]University of California, Santa Barbara, CA, USA
[3]Beijing Advanced Innovation Center for Food Nutrition and Human Health, College of Food Science and Nutritional Engineering, China Agricultural University, Beijing, China
[4]Department of Cardiology, Peking University First Hospital, Beijing, China
[5]Graduate School at Shenzhen, Tsinghua University, Shenzhen, China
[6]State Key Laboratory of Natural Medicines, Research Center of Biostatistics and Computational Pharmacy, China Pharmaceutical University, Nanjing, China
[7]Public Health College, Sun Yat-Sen University, Guangzhou, China
[8]Shenzhen Evergreen Medical Institute, Shenzhen, China
[9]National Clinical Research Center for Kidney Disease, State Key Laboratory for Organ Failure Research, Guangdong Provincial Institute of Nephrology, Division of Nephrology, Nanfang Hospital, Southern Medical University, Guangzhou, China

Correspondence should be addressed to Xiao Huang; drxiaohuang@163.com

While the received traditional predictors are still the mainstay in the diagnosis and prognosis of CVD events, increasing studies have focused on exploring the ancillary effect of biomarkers for the aspiring of precision. Under which circumstances, soluble ST2 (sST2), lipoprotein-associated phospholipase A2 (Lp-PLA2), myeloperoxidase (MPO), and procalcitonin (PCT) have recently emerged as promising markers in the field of both acute and chronic cardiovascular diseases. Existent clinical studies have demonstrated the significant associations between these markers with various CVD outcomes, which further verified the potentiality of markers in helping risk stratification and diagnostic and therapeutic work-up of patients. The current review article is aimed at illuminating the applicability of these four novels and often neglected cardiac biomarkers in common clinical scenarios, including acute myocardial infarction, acute heart failure, and chronic heart failure, especially in the emergency department. By thorough classification, combination, and discussion of biomarkers with clinical and instrumental evaluation, we hope the current study can provide insights into biomarkers and draw more attention to their importance.

1. Introduction

Cardiovascular disease (CVD), a major global disease burden, is the leading cause of death and disability worldwide [1]. Among these, acute myocardial infarction, acute heart failure, and chronic heart failure are the most common manifestations. There are validated biomarkers used at present, for example, troponin which possesses high specificity and

sensitivity when diagnosing acute myocardial infarction and BNP/NT-proBNP which is used to assess the severity of heart failure. Although the treatment of CVD has made gratifying progress, traditional biomarkers inevitably have the problem of residual risk omission in the screening of high-risk groups and accurate diagnosis, management, and prognosis of the disease. For this reason, the studies of novel biomarkers are becoming the main task. The search for novel biomarkers with a long half-life and good stability of myocardium has a wide range of applications and values in clinical diagnosis. In the pursuing of precision, the study of biomarkers has become one of the main tasks in CVD. This article reviews four novel cardiac biomarkers which are very significant but have not been used routinely in clinical practice. These biomarkers can be expected for future application in clinical practice.

2. Biological Metabolism of Myocardial Markers

Soluble suppression of tumorigenicity 2 (sST2) is a member of the IL-1 receptor family, which contains two subtypes, soluble ST2 (sST2) and transmembrane ST2 (ST2L), mainly expressed in cardiomyocytes, reflecting the stress of the ventricular wall and is associated with inflammation and immune response [2]. The interaction of ST2L and IL-33 can mitigate cardiac hypertrophy and myocardial fibrosis, thereby exerting protection on the myocardium. On the contrary, sST2 removes IL-33 from the circulation, promoting cardiac hypertrophy, fibrosis, and ventricular dysfunction [3].

The expression of sST2 was upregulated with myocardial ischemia or mechanical stress, which plays an important role in myocardial remodeling after ischemic injury. It is a promising prognostic biomarker for predicting future clinical heart failure and death in myocardial ischemia patients and has synergy with established heart biomarkers in predicting value [4].

Lipoprotein-associated phospholipase A2 (Lp-PLA2) belongs to group VII of the PLA2 superfamily, currently composed of six types and divided into 16 distinct groups [5]. This enzyme is secreted mainly by macrophages and circulates in the blood as a compound of low-density lipoprotein (LDL) and high-density lipoprotein (HDL). Lp-PLA2 most often combines with LDL (>80%) and HDL (round 10%), whereas it rarely interacts with VLDL or Lp (a) [5]. Lp-PLA2 can hydrolyze oxidized LDL to two biologically active products, named lysophosphatidylcholine (lysoPC) and oxidized nonesterified fatty acids (oxNEFAs). LysoPC appears to stand for most of Lp-PLA2-caused inflammation responses. It has a strong proinflammatory and proatherosclerosis effect [5]. The high upregulation of Lp-PLA2 in atherosclerosis plaques is associated with plaque rupture and may therefore represent underlying vascular inflammation and plaque rupture [6]. Results based on available basic and epidemiological studies suggest that lowering Lp-PLA2 reduces the risk of cardiovascular disease, which grants Lp-PLA2 potential to become an important diagnostic index for the risk prediction and prognosis of CVDs.

Myeloperoxidase (MPO) is a key element of the innate immune system. It is found in the aniline blue granules of myeloid cells (mainly neutrophils and monocytes) and is a specific marker of myeloid cells. During neutrophil activation, lysosomal-phagosome fusion leads to the release of MPO, while the assembly of NADPH oxidase complex on the inner surface of the membrane leads to the production of superoxide anions (O_2^-), which rapidly decompose to hydrogen peroxide (H_2O_2). MPO catalyzes the reaction of H_2O_2 with chloride ions (Cl^-) to form hypochlorous acid (HOCl), which helps to destroy microorganisms in the phagocytic lysosome. However, some MPO were released extracellularly, where HOCL is produced to promote the development of host tissue damage and disease [7]. Although the development of HOCl has a crucial effect on removing pathogens, HOCl and other reactive species derived from MPO cause oxidative tissue damage and cell dysfunction, which further promote disease outcomes [8]. In addition, MPO plays an important role in atherosclerosis and cardiovascular and cerebrovascular diseases [9]. It involves the formation of atherosclerosis that is modified by LDL, reduces the antiatherosclerotic properties of HDL [10, 11], contains bioavailability of nitric oxide and leads to endothelial dysfunction [12, 13], and promotes endothelial cell apoptosis and thrombosis.

Procalcitonin (PCT) is a propeptide substance of no hormone activity calcitonin (CT). This glycoprotein is composed of 116 amino acids and has a molecular weight of 13,000. During normal metabolism, PCT, generated from thyroid C cell secretion, can rarely be detected in serum or cerebrospinal fluid in a healthy population (<0.05 μg/l) [14]. However, PCT releasement upsurges due to the upregulation of endotoxins and other mediators (such as interleukin- (IL-) 1B, tumor necrosis factor- (TNF-) a, and IL-6) [15]. These characteristics made PCT preferable to markers such as white blood cell (WBC) or CRP to possess more specificity for bacterial infections and may allow PCT to be used to distinguish bacterial from viral infections and other noncommunicable diseases [16, 17]. Until now, a growing number of researchers have supported PCT testing in patients with CVDs, including patients with shortness of breath, possible heart failure, suspected endocarditis, and acute coronary syndrome [18].

3. Clinical Impact of Cardiac Markers

3.1. sST2. The American heart failure cohort study (PRIDE study) [19] which analyzed 593 patients from the emergency department with acute dyspnea (with or without HF) found that sST2 concentrations were significantly higher in ADHF patients than in non-HF patients. Although NT-proBNP was significantly superior to sST2 in diagnosing ADHF, sST2 has more important value when it comes to prognosis since the ADHF-induced mortality population, within one year, has significantly higher sST2 concentration than survivals (1.08 vs. 0.18 ng/ml, $P < 0.001$). It is noteworthy that the prognostic value of both sST2 and NT-proBNP is additive; that is, patients with increased NT-proBNP and sST2 have the highest mortality rate in 1 year, which is about

40%; the prognostic value of sST2 combined with NT-proBNP maintained 4 years after the disease onset.

The PRIDE research [20] also shown that, compared to survivors, patients who died in 1 year (67.4 vs. 35.8 ng/ml; $P < 0.001$) and 4 years (47.4 vs. 35.6 ng/ml, $P = 0.01$) have a higher sST2 level. Thus, sST2 ≥ 35 ng/ml was recommended as a predictor threshold for a poor prognosis, and the risk of death is significantly increased once beyond this threshold value. In 2014, a total of 1528 ADHF patients were enrolled in the Heart Failure Center of Beijing Fuwai Hospital for sST2 measurement, a prospective study [21]. The result has shown that the population with the highest sST2 concentration quartile (55.6 ng/ml) has a significantly higher rate of adverse outcomes (all-cause mortality or heart transplantation) than patients with the lowest sST2 concentration quartile (25.2 ng/ml).

sST2 concentration correlates with left ventricular ejection fraction. Most patients with reducing LVEF contain higher sST2 concentration, with threshold value dependent on different studies. Results from a global multicenter ADHF cohort study which contains 11 countries [22] show that sST2 concentration has incremental value on traditional clinical variables in predicting 30-day and 1-year mortality at risk stratification. The ASCEND Heart Failure Trial, a multi-country, multicenter prospective randomized controlled trial in ADFF patients [23], conducted marker research for 858 patients from most North American subjects. With a mean LVEF level of $31.6 \pm 15\%$, the ASCEND study found that a higher sST2 concentration is positively associated with the risk of mortality within 180 days with a quarterly sST2 level. However, the prognostic value of baseline sST2 was reduced after adjustment for clinical covariates and NT-proBNP. Also, patients with increasing sST2 concentration (>60 ng/ml) were reported to have higher 180-day mortality than patients with lower sST2 during the follow-up period. Pascual-Figal et al. [24] conducted a prospective study on 107 ADHF inpatients (LVEF $47 \pm 15\%$), and results show that sST2 concentration > 65 ng/ml has a strong predictive value on risk of mortality.

sST2 (reflecting myocardial fibrosis and remodeling), hsTnT (indicating myocardial necrosis), and NT-proBNP (identifying myocardial stretch) concentration provide additional prognostic information for patients with ADHF, respectively. When used together, these markers further provide better risk stratification. sST2 concentration changed rapidly in HF circumstance, especially after diagnosis treatment. When baseline sST2 was validated to have the prognostic effect, more current studies claim that continuous measurements greatly increase the amount of available prognostic information, and the use of sST2 as a monitoring tool appears to be particularly advantageous [25]. In ADHF patients, sST2 concentration tends to decrease after the start of treatment and presents itself as an important prognostic factor both at admission and during hospitalization. Therefore, for ADHF patients, sST2 concentration should be assessed at baseline (for initial risk assessment and shunt) and also measured posttreatment to reflect treatment effectiveness and help decision-making for further treatment.

sST2 also has important prognostic assessment value for CHF patients to help with targeted treatment and follow-up, which potentially improve quality of life and long-term outcomes. The association between sST2 levels and risk of death was determined at the University of Pennsylvania Hospital in a multicenter prospective cohort study (PHFS) which included 1141 CHF outpatients. According to tertiles of sST2 levels, sST2 > 36.3 ng/ml contains higher risk of negative outcomes compared to sST2 ≤ 22.3 ng/ml. sST2 is a powerful biomarker for CHF patients' prognostic assessment, and the interaction between sST2 and NT-proBNP further improves the assessment of the prognosis on top of clinical risk assessment [26]. A German study of 891 outpatients who received treatment for HF showed that in a multivariate Cox proportional risk model, sST2 and NT-proBNP could both significantly predict the risk of mortality [27]. Based on the results of the CORONA study of 1449 patients aged over 60 years with ischemic etiology of CHF (LVEF 40%) [28], the mean sST2 level is 17.8 (IQR: 0.2-400.0 ng/ml). According to COX regression analysis, sST2 > 28.8 ng/ml was found to be associated with CVD mortality, nonfatal MI, and stroke. In 2331 CHF patients (left ventricular ejection fraction < 35%) in the US HF-ACTION study with a median baseline sST2 level of 23.7 ng/ml (IQR: 18.6-31.8) [29], the sST2 level was found to be independently associated with HF patients' prognosis in the multivariate model after adjustment for covariates and NT-proBNP. A doubling of the baseline sST2 level significantly increased the risk of CVD mortality, all-cause mortality, or hospitalization. However, sST2 did not significantly increase the reclassification of risk through the change of C statistic, improvement of the net weight classification, and comprehensive discrimination. Despite robust relationships in traditional multivariate modeling, the effect of sST2 on identification and risk prediction is not significant. Further studies are required to illustrate the role of sST2 in CHF risk stratification.

Information about the aforementioned studies about sST2 is recapitulated in Table 1. Despite limited value in diagnosing ADHF and CHF, sST2 have shown vital significance regarding the prognostic process. Increasing studies not only have shown that higher baseline sST2 concentration is frequently associated with a higher risk of adverse event outcomes and mortality but also revealed an additive value of sST2 in the prognosis of ADFH and CHF to traditional predictors; we therefore believe that such markers have great potential and should gain more attention in the clinical practice.

3.2. Lp-PLA2. Studies related to Lp-PLA2 have focused on cardiovascular and cerebrovascular diseases due to the proinflammatory and proatherosclerotic effects of Lp-PLA2. Total plasma Lp-PLA2 was found to be predictive in cardiac death in 524 Athens patients with continuous stable coronary artery disease (CAD) who were followed for an average of 34 months [30]. Among 224 African Americans and 336 Caucasians who underwent coronary angiography, Lp-PLA2 activity and index (a comprehensive measure of mass and activity) were determined to be associated with the presence of coronary heart disease (CAD). The findings

TABLE 1: Summary of clinical studies on the relationship between sST2 and adverse outcomes.

Study	Country	Patients	Outcome	sST2 measurement method	sST2 concentration for higher risk
PRIDE study [20]	USA	593 patients with acute dyspnea	1-year mortality	Enzyme-linked immunosorbent assay	67.4 vs. 35.8 ng/ml
			4-year mortality	Enzyme-linked immunosorbent assay	47.4 vs. 35.6 ng/ml
Heart Failure Center of Beijing Fuwai Hospital [21]	China	1528 ADHF patients	Adverse outcomes (all-cause mortality or heart transplantation)		≥55.6 ng/ml vs. <25.2 ng/ml
MOCA study [22]	11 countries*	5306 patients hospitalized for ADHF	30-day and 1-year mortality	—	—
ASCEND Heart Failure Trial [23]	USA	858 acute HF subjects with a mean LVEF level of 31.6 ± 15%	180-day mortality	The presage ST2 assay	>60 ng/ml
University Hospital Virgen de la Arrixaca [24]	Spain	107 consecutive ADHF patients	All-cause mortality	High-sensitivity sandwich immunoassay	>65 ng/ml
Penn Heart Failure Study (PHFS) [26]	USA	1141 CHF outpatients	All-cause mortality or cardiac transplantation	Highly sensitive sandwich monoclonal immunoassay	>36.3 ng/ml vs. ≤22.3 ng/ml
A German study by Bayes-Genis et al. [27]	Spain	891 ambulatory patients	All-cause mortality	High-sensitivity sandwich monoclonal immunoassay	>50 ng/ml
CORONA study [28]	Multicountry	1449 patients aged over 60 years with ischemic etiology of CHF (LVEF 40%)	CVD mortality, nonfatal MI, and stroke	Presage® ST2 assay	>28.8 ng/ml
HF-ACTION study [29]	Greece	2331 CHF patients (LVEF < 35%)	All-cause mortality or hospitalization, cardiovascular mortality or heart failure hospitalization, and all-cause mortality	Dual monoclonal antibody immunoassay	>35 ng/ml

*Austria ($n = 137$), Czech Republic ($n = 1917$), Finland ($n = 620$), France ($n = 199$), Netherlands ($n = 367$), Italy ($n = 213$), Japan ($n = 144$), Spain ($n = 107$), Switzerland ($n = 609$), Tunisia ($n = 187$), and the United States ($n = 597$ for Cleveland, $n = 209$ for Boston).

suggested an independent influence of vascular inflammation in African Americans as a cause of CAD risk and underscored the importance of Lp-PLA2 as a cardiovascular risk factor [31]. Similarly, Lp-PLA2 was found to corelate with CVD events in a nested case-control study based on people with high insulin resistance and diabetes from American Indians [32]. In addition, this study found that the quality of Lp-PLA2 is negatively associated with CVDs. Another study involving 25 isolated patients with isolated coronary artery ectasia (CAE) without stenosis and 25 control groups with normal coronary angiography in the Turkish population found that the Lp-PLA2 level was significantly higher in isolated CAE patients compared with patients with normal angiographic coronary arteries, which suggested that Lp-PLA2 may also be involved in the pathogenesis of CAE [33]. In 4537 US individuals without baseline peripheral artery disease (PAD), higher Lp-PLA2 quality and activity were associated with the occurrence of clinical PAD events [34]. Lp-PLA2 activity was significantly and positively associated with carotid intima-media thickness (IMT) and plaques in 929 Japanese men aged 50-79 years, but the Mendelian randomized study did not support Lp-PLA2 as a cause of subclinical atherosclerosis [35]. Increased Lp-PLA2 activity was found to be associated with significantly fast progression of aortic stenosis (AS) in 183 patients with mild AS from Quebec, Canada, but no corelationship was found in patients with moderate or severe AS [36]. The Lp-PLA2 activity level was significantly associated with coronary heart disease in men and women with type 2 diabetes [37]. However, there are studies that showed opposite results. No significant association between microcerebral hemorrhage (CMB) and Lp-PLA2 measurements was observed in 819 Framingham

Offspring participants with an average age of 73 years [38]. A cross-sectional study of 921 nonstroke patients in Barcelona found that although Lp-PLA2 was independently associated with silent cerebral infarction in women, the addition of Lp-PLA2 to clinical variables did not improve its predictive ability [39]. The inconsistent result was observed in studies with the Chinese population as well. Most studies showed that Lp-PLA2 is a risk factor associated with cardiovascular and cerebrovascular diseases. The quality of Lp-PLA2 is positively associated with subclinical atherosclerosis determined by asymptomatic cerebral artery stenosis (ACAS), intracranial artery stenosis (ICAS), and extracranial artery stenosis (ECAS) in north China regions, especially for male gender and older population, which substantiated that Lp-PLA2 quality may be a potential biomarker for the detection of adult ACAS [40]. A prospective study examined Lp-PLA2 quality in 3401 participants from the Chinese Acute Ischemic Stroke Blood Pressure Reduction Trial and found that the accumulated incidence rate for all-cause mortality increased in the quarters of Lp-PLA2 quality [41]. In a multicenter, randomized control clinical trial, Lp-PLA2 activity was not found to increase in patients who were without intracranial artery stenosis, which suggests a better response to dual antiplatelet therapy in patients with mild stroke or high-risk transient ischemic attack to prevent dual stroke and concurrent vascular events [42]. From another Chinese RCT study, a higher level of Lp-PLA2 activity in the onset of the acute phase was associated with an increased risk of short-term recurrent vascular events [43]. However, opposite results have been observed as well. In a 7-year follow-up study that included 90,000 Chinese population, reduction in Lp-PLA2 activity was not associated with a major risk of vascular or nonvascular disease in adults [44]. To sum up, controversy about the role of Lp-PLA2 in cardiovascular and cerebrovascular diseases does exist because of inconsistent and limited studies. More researches with diverse data characteristics and huge data sizes should be developed to validate the practicability of Lp-PLA2.

3.3. MPO.

There is elevated evidence shown that circulation MPO protein concentration is not only associated with the rate of coronary artery disease (CAD) but also related to the severity of the disease. A case-control study including 874 angiographically proven CAD patients has shown an advanced MPO level in CAD patients and elevated MPO level in the progress of non-ST segment elevation of the acute coronary syndrome and acute myocardial infarction from stable CAD [45]. The study by Samsamshariat et al. included 50 cases of stable CAD patients, unstable CAD patients, and the control group, respectively. Its results showed that unstable CAD patients had a higher level of plasma MPO level $(71.2 \pm 19.6 \, \text{ng/ml})$ than both stable CAD patients $(34.5 \pm 6.8 \, \text{ng/ml})$ and control groups $(23.0 \pm 3.6 \, \text{ng/ml})$ $(P < 0.001)$ [46]. Study from Pawlus et al. and Tretjakovs et al. reported that serum MPO concentration increased with the development of CAD, and patients with unstable CAD and myocardial infarction have a significantly elevated level of MPO compared to healthy subjects and stable angina pectoris patients [47, 48].

Furthermore, in patients who are diagnosed with acute myocardial infarction, the MPO level is higher than patients with angina pectoris [49, 50] or stable CAD [51]; meanwhile, there is a significant association between MPO concentration and angiographically detected coronary artery stenosis [52, 53]. Rebeiz et al. reported that elevation in plasma MPO could be used to identify coronary artery stenosis in 398 cases of negative chest pain with troponin patients, in which elevated quartiles of MPO concentration are closely associated with coronary artery stenosis, coronary thrombosis, and plaque ulcers [54]. It is noteworthy that, for patients who suffered from fatal or nonfatal CAD, the aforementioned relationship is much stronger, which confirmed the idea that the MPO level is associated with the severity of CAD. Overall, a large body of studies has supported the association between elevated MPO levels with CAD and a dose-response relationship between MPO levels and the severity of CAD.

Some studies revealed the predictive ability of MPO on major adverse cardiovascular events (MACE). In 604 chest pain patients collected by Brennan et al., an increase in the MPO level was independently associated with advanced risk of MACE at 30 days and 6 months of follow-up after adjustment for risk factors [55]. More specifically, at 30 days, cardiac troponin alone can predict 58% of MACE, while baseline MPO is able to predict 84.5% of MACE. MPO remained a strong and independent predictor of MACE at 30 days and 6 months in the patients who were consistently troponin-negative. This suggested that MPO is not only an inflammatory marker of myocardial necrosis response but also a predictor of the presence of susceptible plaques. Brennan et al.'s study showed that plasma MPO could independently predict the early stage of acute myocardial infarction and the risk of MACE in the period of 30 days and 6 months, meanwhile also forehead its potential practicability on the risk stratification of chest pain patients [55]. Similarly, the CAPTURE trial, which involved 547 patients with resting recurrent chest pain, observed that MPO serum levels of >350 ng/ml were highly predictive of nonfatal acute myocardial infarction within 72 hours [56]. Such corelationship remained robust even in patients who are troponin-negative. At the same time, Morrow et al. claimed that elevated baseline MPO in patients with non-ST-elevation ACS was associated with a higher risk of nonfatal MI or recurrent ACS within 30 days, and the addition of B-type natriuretic peptides and cardiac troponin to the MPO can improve short-term risk assessment and patient stratification [57].

Some studies also found that such predictive value may persist over a long period of time. In a research with a mean follow-up time of 25 ± 16 months, 73 patients diagnosed as ST segment elevation myocardial infarction subjects and 46 health control groups and patients with plasma MPO concentration > 68 ng/ml have tripled the incident rate of MACE compared to patients with low MPO [58]. Among 885 stable severe angiography CAD patients, mortality is positively associated with MPO tertiles. After 13 years of follow-up and covariate analysis, patients with the highest MPO have as much as three times greater CVD mortality than those with the lowest MPO level [53]. During 9 years of angiographic CAD studies, patients with the highest

MPO quartile were 1.5 times more likely to die of cardiovascular causes than patients with the lowest MPO quartile after fully adjusting for variables [59]. These findings suggested that from a mid- to long-term perspective, MPO is highly associated with cardiovascular events.

A prospective population-based Atherosclerosis Risk in Communities (ARIC) cohort study, after 9.6 years of the follow-up study, found that no significant association between intracellular monocyte MPO level and incident of cardiovascular events was found among 1465 patients without a history of PAD, myocardial infarction, or heart failure [60].

The MPO level is independently associated with cardiovascular events, and the dose-dependent relationship between MPO level and CAD severity also has great potential in guiding the diagnostic and treatment process in clinical practice. However, the prediction value of MPO on MACE in asymptomatic patients has remained uncertain and needs to be explored in more and larger studies.

3.4. PCT. It is difficult to distinguish acute heart failure (AHF) from respiratory infection for patients with HF with acute respiratory symptoms (e.g., cough, sputum, tachypnea, or pleural pain) [61] due to the overlapping clinical and radiological examination [62, 63]. Delayed symptomatic treatment [64] or inadequate treatment [65] can increase the risk of adverse outcomes, so on-time and accurate differential diagnosis is crucial in which field.

In a study consisting of 4698 patients with congestive heart failure, PCT value was found about 4 times higher in patients with HF with the presence of respiratory infections [66]. Similar results have been found in biomarkers for heart failure research in a different country [65]. At present, most studies have shown that serum PCT has certain clinical significance in the diagnosis of patients with heart failure complicated with infection. Berge et al. believed that PCT is superior to CRP and WBC when it comes to the diagnosis of AHF patients for concomitant pneumonia [67]. A large multicenter study in China was conducted with patients with congestive HF, and the results showed that the critical value of PCT for the diagnosis of infection increased significantly with the increase of the severity of HF, and the threshold value of PCT for the diagnosis of concomitant infection in patients with grades II, III, and IV congestive HF is 0.086 μg/l, 0.0192 μg/l, and 0.657 μg/l [66]. Alba et al.'s research claims that the cutoff PCT value for pneumonia excluding heart failure is 0.1 ng/ml (sensitivity 97%, specificity 69%) and for HF with pneumonia is 0.4 ng/ml (specificity 97%) and believed that the combined use of PCT and NT-proBNP can more effectively distinguish AHF and pneumonia [68]. In short, it can be seen that PCT can be helpful in determining respiratory tract infection, but the inconsistency in threshold value suggested further researchers.

Some studies have observed the correlation between PCT and bacteremia, which is the primary diagnostic criterion for endocarditis in emergency department patients with fever [69, 70]. In an observational study involving 1083 patients with suspected infection, PCT was strongly associated with positive blood culture (AUC 0.803) and has a negative predictive value of 99.6% in bacteriaemia exclusion [70]. A prospective cohort study which consisted of 67 consecutive admissions with suspected endocarditis and 21 patients with an infection found a strong association between PCT levels with endocarditis and significantly higher procalcitonin levels in patients with endocarditis (median 6.56 ng/ml vs. 0.44 ng/ml, $P < 0.001$, AUC 0.856 (95% CI 0.750-0.962)). In this study, the sensitivity and predictive value of PCT also outperformed the CRP, with the optima PCT cutoff value of 2.3 ng/ml, sensitivity 81%, specificity 85%, negative predictive value 92%, and positive predictive value 72% [71]. A recent meta-analysis reviewed six studies, including more than 1000 suspected cases of infection, of which about 20% were confirmed as infective endocarditis, showing a slightly lower diagnostic effect of PCT (AUC 0.71) [72]. Meanwhile, this meta-analysis suggested the use of a low PCT threshold to exclude endocarditis in routine clinical practice, and PCT is recommended in the diagnosis of infective endocarditis, but the specific threshold value needs to be further explored.

In order to study the clinical significance of PCT in the prognosis of AHF patients, Demissei et al. included 1781 patients with acute decompensated heart failure (ADHF) excluding those with infection from the PROTECT research to investigate the corelationship between outcomes during hospitalization and after discharge with the serum PCT level [73]. In this study, an elevated PCT level was found to be associated with an increased rate of treatment failure in ADHF patients during hospitalization (OR 1.2, 95% CI, 0.8-2.2). When the PCT level > 0.2 ng/ml, cardiovascular, renal mortality, or readmission rate at 30 days after discharge and all-cause mortality at 180 days after discharge both significantly increased. However, after adjusting for prognostic factors including age, albumin, sodium, renal function, previous HF hospitalization, history of edema, and systolic blood pressure, the PCT level in ADHF patients with the exclusion of infection is only associated with 30-day all-cause mortality (HR 2.3, 95% CI, 1.3-4.2).

In Villanueva et al.'s research on 261 AHF patients with the exclusion of active infection, after a mean follow-up time of 2 years, logPCT was found to be linearly associated with all-cause mortality in COX regression analysis (HR 1.43, 95% CI, 1.12-1.82, $P = 0.0004$). LogPct was found to be positively correlated with the incidence of all-cause readmissions (IRR = 1.22, 95% CI, 1.02-1.44, $P = 0.025$), except for patients who were lost during follow-up (died during admission), and also associated with AHF-induced readmission (IRR = 1.28, 95% CI, 1.02-1.61, $P = 0.032$). This study concluded that the serum PCT level in AHF patients with infection excluded was independently positively associated with the risk of long-term death and rehospitalization.

In addition to its predictive value in the prognosis of patients with heart failure, there is growing evidence linking PCT with the degree and prognosis of atherosclerosis in patients with coronary heart disease. More studies have shown that in patients with acute coronary syndrome, especially in complex cases, the PCT level is elevated [74, 75]. Research conducted on 2131 cases of CAD patients found that PCT has a strong prognostic value after 3.6 years of

follow-up [74]. PCT concentration was significantly higher in patients who died of cardiovascular diseases, as well as in patients with acute coronary syndromes, compared with patients with stable angina. In the COX regression model, elevated PCT concentration is associated with cardiovascular mortality (OR 1.34, 95% CI, 1.08-1.65, $P = 0.007$). In another research that included 400 cases of CAD patients with the SX scoring algorithm system, the high SX group have elevated serum PCT levels compared to the low SX group ($P < 0.001$) [76]. The cutoff value for PCT in the aforementioned study is 0.0335 ng/ml.

The detection of PCT will be helpful in the diagnosis and treatment of patients with bacterial infection and endocarditis. Moreover, for patients without infection, a high PCT level is an independent risk factor for poor prognosis.

4. Conclusion

Increasing studies have focused on exploring the synergy value or independent value of biomarkers, while the limitations of currently widely used blood markers have been regularly reported in clinical practice. The current study reviewed some frequently overlooked biomarkers that have shown significance in both diagnostic and prognostic processes. Despite accumulating evidence suggesting their association with CVDs and their predictive ability on diseases' prognostic process, more research is needed to establish the clinical role of biomarkers.

Data Availability

The data supporting this review are from previously reported studies and datasets, which have been cited at relevant places within the text as References [1–75].

Conflicts of Interest

All authors declare that there is no conflict of interest regarding the publication of this paper.

Authors' Contributions

Junpei Li and Tianyu Cao contributed equally to this work.

Acknowledgments

References

[1] GBD 2013 DALYs and HALE Collaborators, C. J. L. Murray, R. M. Barber et al., "Global, regional, and national disability-adjusted life years (DALYs) for 306 diseases and injuries and healthy life expectancy (HALE) for 188 countries, 1990-2013: quantifying the epidemiological transition," *Lancet*, vol. 386, no. 10009, pp. 2145–2191, 2015.

[2] H. Iwahana, K. Yanagisawa, A. Ito-Kosaka et al., "Different promoter usage and multiple transcription initiation sites of the interleukin-1 receptor-related human ST2 gene in UT-7 and TM12 cells," *European Journal of Biochemistry*, vol. 264, no. 2, pp. 397–406, 1999.

[3] R. Kakkar and R. T. Lee, "The IL-33/ST2 pathway: therapeutic target and novel biomarker," *Nature Reviews. Drug Discovery*, vol. 7, pp. 827–840, 2008.

[4] E. O. Weinberg, M. Shimpo, G. W. de Keulenaer et al., "Expression and regulation of ST2, an interleukin-1 receptor family member, in cardiomyocytes and myocardial infarction," *Circulation*, vol. 106, no. 23, pp. 2961–2966, 2002.

[5] F. Huang, K. Wang, and J. Shen, "Lipoprotein-associated phospholipase A2: the story continues," *Medicinal Research Reviews*, vol. 40, pp. 79–134, 2020.

[6] M. K. Jensen, M. L. Bertoia, L. E. Cahill, I. Agarwal, E. B. Rimm, and K. J. Mukamal, "Novel metabolic biomarkers of cardiovascular disease," *Nature Reviews. Endocrinology*, vol. 10, pp. 659–672, 2014.

[7] M. J. Davies and C. L. Hawkins, "The role of myeloperoxidase in biomolecule modification, chronic inflammation, and disease," *Antioxidants & Redox Signaling*, vol. 32, pp. 957–981, 2020.

[8] A. J. Kettle, R. F. Anderson, M. B. Hampton, and C. C. Winterbourn, "Reactions of superoxide with myeloperoxidase," *Biochemistry*, vol. 46, pp. 4888–4897, 2007.

[9] N. Teng, G. J. Maghzal, J. Talib, I. Rashid, A. K. Lau, and R. Stocker, "The roles of myeloperoxidase in coronary artery disease and its potential implication in plaque rupture," *Redox Report*, vol. 22, pp. 51–73, 2017.

[10] Emerging Risk Factors Collaboration, E. di Angelantonio, N. Sarwar et al., "Major lipids, apolipoproteins, and risk of vascular disease," *JAMA*, vol. 302, no. 18, pp. 1993–2000, 2009.

[11] W. Q. Liu, Y. Z. Zhang, Y. Wu et al., "Myeloperoxidase-derived hypochlorous acid promotes ox-LDL-induced senescence of endothelial cells through a mechanism involving β-catenin signaling in hyperlipidemia," *Biochemical and Biophysical Research Communications*, vol. 467, no. 4, pp. 859–865, 2015.

[12] R. A. Koeth, V. Haselden, and W. H. Tang, "Myeloperoxidase in cardiovascular disease," *Advances in Clinical Chemistry*, vol. 62, pp. 1–32, 2013.

[13] R. Stocker, A. Huang, E. Jeranian et al., "Hypochlorous acid impairs endothelium-derived nitric oxide bioactivity through a superoxide-dependent mechanism," *Arteriosclerosis, Thrombosis, and Vascular Biology*, vol. 24, no. 11, pp. 2028–2033, 2004.

[14] C. Picariello, C. Lazzeri, S. Valente, M. Chiostri, and G. F. Gensini, "Procalcitonin in acute cardiac patients," *Internal and Emergency Medicine*, vol. 6, pp. 245–252, 2011.

[15] B. Muller, J. C. White, E. S. Nylen, R. H. Snider, K. L. Becker, and J. F. Habener, "Ubiquitous expression of the calcitonin-i gene in multiple tissues in response to sepsis," *The Journal of Clinical Endocrinology and Metabolism*, vol. 86, pp. 396–404, 2001.

[16] P. Linscheid, D. Seboek, H. Zulewski, U. Keller, and B. Muller, "Autocrine/paracrine role of inflammation-mediated calcitonin gene-related peptide and adrenomedullin expression in

human adipose tissue," *Endocrinology*, vol. 146, pp. 2699–2708, 2005.

[17] M. Christ-Crain and B. Muller, "Procalcitonin in bacterial infections–hype, hope, more or less?," *Swiss Medical Weekly*, vol. 135, pp. 451–460, 2005.

[18] P. Schuetz, L. B. Daniels, P. Kulkarni, S. D. Anker, and B. Mueller, "Procalcitonin: a new biomarker for the cardiologist," *International Journal of Cardiology*, vol. 223, pp. 390–397, 2016.

[19] J. L. Januzzi Jr., W. F. Peacock, A. S. Maisel et al., "Measurement of the interleukin family member ST2 in patients with acute dyspnea: results from the PRIDE (Pro-Brain Natriuretic Peptide Investigation of Dyspnea in the Emergency Department) study," *Journal of the American College of Cardiology*, vol. 50, no. 7, pp. 607–613, 2007.

[20] J. L. Januzzi, A. Mebazaa, and S. Di Somma, "ST2 and prognosis in acutely decompensated heart failure: the International ST2 Consensus Panel," *The American Journal of Cardiology*, vol. 115, pp. 26B–31B, 2015.

[21] R. Zhang, Y. Zhang, J. Zhang et al., "The prognostic value of plasma soluble ST2 in hospitalized Chinese patients with heart failure," *PLoS One*, vol. 9, no. 10, article e110976, 2014.

[22] J. Lassus, E. Gayat, C. Mueller et al., "Incremental value of biomarkers to clinical variables for mortality prediction in acutely decompensated heart failure: the Multinational Observational Cohort on Acute Heart Failure (MOCA) study," *International Journal of Cardiology*, vol. 168, no. 3, pp. 2186–2194, 2013.

[23] W. H. Tang, Y. Wu, J. L. Grodin et al., "Prognostic value of baseline and changes in circulating soluble ST2 levels and the effects of nesiritide in acute decompensated heart failure," *JACC Heart Fail*, vol. 4, no. 1, pp. 68–77, 2016.

[24] D. A. Pascual-Figal, S. Manzano-Fernández, M. Boronat et al., "Soluble ST2, high-sensitivity troponin T- and N-terminal pro-B-type natriuretic peptide: complementary role for risk stratification in acutely decompensated heart failure," *European Journal of Heart Failure*, vol. 13, no. 7, pp. 718–725, 2011.

[25] S. Manzano-Fernández, J. L. Januzzi, F. J. Pastor-Pérez et al., "Serial monitoring of soluble interleukin family member ST2 in patients with acutely decompensated heart failure," *Cardiology*, vol. 122, no. 3, pp. 158–166, 2012.

[26] B. Ky, B. French, K. McCloskey et al., "High-sensitivity ST2 for prediction of adverse outcomes in chronic heart failure," *Circulation. Heart Failure*, vol. 4, no. 2, pp. 180–187, 2011.

[27] A. Bayes-Genis, M. de Antonio, A. Galán et al., "Combined use of high-sensitivity ST2 and NTproBNP to improve the prediction of death in heart failure," *European Journal of Heart Failure*, vol. 14, no. 1, pp. 32–38, 2012.

[28] K. Broch, T. Ueland, S. H. Nymo et al., "Soluble ST2 is associated with adverse outcome in patients with heart failure of ischaemic aetiology," *European Journal of Heart Failure*, vol. 14, no. 3, pp. 268–277, 2012.

[29] G. M. Felker, M. Fiuzat, V. Thompson et al., "Soluble ST2 in ambulatory patients with heart failure: association with functional capacity and long-term outcomes," *Circulation. Heart Failure*, vol. 6, no. 6, pp. 1172–1179, 2013.

[30] L. S. Rallidis, C. C. Tellis, J. Lekakis et al., "Lipoprotein-Associated Phospholipase A$_2$ Bound on High- Density Lipoprotein Is Associated With Lower Risk for Cardiac Death in Stable Coronary Artery Disease Patients: A 3-Year Follow-Up," *Journal of the American College of Cardiology*, vol. 60, no. 20, pp. 2053–2060, 2012.

[31] E. Anuurad, Z. Ozturk, B. Enkhmaa, T. A. Pearson, and L. Berglund, "Association of lipoprotein-associated phospholipase A2 with coronary artery disease in African-Americans and Caucasians," *The Journal of Clinical Endocrinology and Metabolism*, vol. 95, pp. 2376–2383, 2010.

[32] J. R. Kizer, J. G. Umans, J. Zhu et al., "Lipoprotein-associated phospholipase A(2) mass and activity and risk of cardiovascular disease in a population with high prevalences of obesity and diabetes: the Strong Heart Study," *Diabetes Care*, vol. 35, no. 4, pp. 840–847, 2012.

[33] L. Korkmaz, E. Erkuş, A. Kırış et al., "Lipoprotein phospholipase A2 in patients with isolated coronary artery ectasia," *Clinical Research in Cardiology*, vol. 100, no. 6, pp. 511–514, 2011.

[34] P. K. Garg, A. M. Arnold, K. D. Hinckley Stukovsky et al., "Lipoprotein-associated phospholipase A2 and incident peripheral arterial disease in older adults: the Cardiovascular Health Study," *Arteriosclerosis, Thrombosis, and Vascular Biology*, vol. 36, no. 4, pp. 750–756, 2016.

[35] H. Ueshima, T. Kadowaki, T. Hisamatsu et al., "Lipoprotein-associated phospholipase A$_2$ is related to risk of subclinical atherosclerosis but is not supported by Mendelian randomization analysis in a general Japanese population," *Atherosclerosis*, vol. 246, pp. 141–147, 2016.

[36] R. Capoulade, A. Mahmut, L. Tastet et al., "Impact of plasma Lp-PLA2 activity on the progression of aortic stenosis: the PROGRESSA study," *JACC: Cardiovascular Imaging*, vol. 8, no. 1, pp. 26–33, 2015.

[37] I. J. Hatoum, F. B. Hu, J. J. Nelson, and E. B. Rimm, "Lipoprotein-associated phospholipase A2 activity and incident coronary heart disease among men and women with type 2 diabetes," *Diabetes*, vol. 59, pp. 1239–1243, 2010.

[38] J. R. Romero, S. R. Preis, A. S. Beiser et al., "Lipoprotein phospholipase A2 and cerebral microbleeds in the Framingham Heart Study," *Stroke*, vol. 43, no. 11, pp. 3091–3094, 2012.

[39] I. Riba-Llena, A. Penalba, D. Pelegrí et al., "Role of lipoprotein-associated phospholipase A$_2$ activity for the prediction of silent brain infarcts in women," *Atherosclerosis*, vol. 237, no. 2, pp. 811–815, 2014.

[40] P. Nazerian, C. Mueller, A. M. Soeiro et al., "Diagnostic accuracy of the aortic dissection detection risk score plus D-dimer for acute aortic syndromes: the ADvISED prospective multicenter study," *Circulation*, vol. 137, no. 3, pp. 250–258, 2018.

[41] L. Han, C. Zhong, X. Bu et al., "Prognostic value of lipoprotein-associated phospholipase A$_2$ mass for all-cause mortality and vascular events within one year after acute ischemic stroke," *Atherosclerosis*, vol. 266, pp. 1–7, 2017.

[42] M. Yang, A. Wang, J. Li et al., "Lp-PLA2and dual antiplatelet agents in intracranial arterial stenosis," *Neurology*, vol. 94, no. 2, pp. e181–e189, 2020.

[43] J. Lin, H. Zheng, B. L. Cucchiara et al., "Association of Lp-PLA2-A and early recurrence of vascular events after TIA and minor stroke," *Neurology*, vol. 85, no. 18, pp. 1585–1591, 2015.

[44] I. Y. Millwood, D. A. Bennett, R. G. Walters et al., "A phenome-wide association study of a lipoprotein-associated phospholipase A2 loss-of-function variant in 90 000 Chinese adults," *International Journal of Epidemiology*, vol. 45, no. 5, pp. 1588–1599, 2016.

[45] G. Ndrepepa, S. Braun, J. Mehilli, N. von Beckerath, A. Schomig, and A. Kastrati, "Myeloperoxidase level in patients with stable coronary artery disease and acute coronary

syndromes," *European Journal of Clinical Investigation*, vol. 38, pp. 90–96, 2008.

[46] S. Z. Samsamshariat, G. Basati, A. Movahedian, M. Pourfarzam, and N. Sarrafzadegan, "Elevated plasma myeloperoxidase levels in relation to circulating inflammatory markers in coronary artery disease," *Biomarkers in Medicine*, vol. 5, pp. 377–385, 2011.

[47] J. Pawlus, M. Holub, M. Kozuch, M. Dabrowska, and S. Dobrzycki, "Serum myeloperoxidase levels and platelet activation parameters as diagnostic and prognostic markers in the course of coronary disease," *International Journal of Laboratory Hematology*, vol. 32, pp. 320–328, 2010.

[48] P. Tretjakovs, A. Jurka, I. Bormane et al., "Circulating adhesion molecules, matrix metalloproteinase-9, plasminogen activator inhibitor-1, and myeloperoxidase in coronary artery disease patients with stable and unstable angina," *Clinica Chimica Acta*, vol. 413, no. 1-2, pp. 25–29, 2012.

[49] D. A. Khan, M. S. Sharif, and F. A. Khan, "Diagnostic performance of high-sensitivity troponin T, myeloperoxidase, and pregnancy-associated plasma protein A assays for triage of patients with acute myocardial infarction," *The Korean Journal of Laboratory Medicine*, vol. 31, pp. 172–178, 2011.

[50] A. Trentini, V. Rosta, S. Spadaro et al., "Development, optimization and validation of an absolute specific assay for active myeloperoxidase (MPO) and its application in a clinical context: role of MPO specific activity in coronary artery disease," *Clinical Chemistry and Laboratory Medicine*, vol. 58, no. 10, pp. 1749–1758, 2020.

[51] B. U. Goldmann, V. Rudolph, T. K. Rudolph et al., "Neutrophil activation precedes myocardial injury in patients with acute myocardial infarction," *Free Radical Biology & Medicine*, vol. 47, no. 1, pp. 79–83, 2009.

[52] M. Baseri, R. Heidari, B. Mahaki, Y. Hajizadeh, A. Momenizadeh, and M. Sadeghi, "Myeloperoxidase levels predicts angiographic severity of coronary artery disease in patients with chronic stable angina," *Advanced Biomedical Research*, vol. 3, p. 139, 2014.

[53] C. L. Heslop, J. J. Frohlich, and J. S. Hill, "Myeloperoxidase and C-reactive protein have combined utility for long-term prediction of cardiovascular mortality after coronary angiography," *Journal of the American College of Cardiology*, vol. 55, pp. 1102–1109, 2010.

[54] A. G. Rebeiz, H. M. Tamim, R. M. Sleiman et al., "Plasma myeloperoxidase concentration predicts the presence and severity of coronary disease in patients with chest pain and negative troponin-T," *Coronary Artery Disease*, vol. 22, no. 8, pp. 553–558, 2011.

[55] M. L. Brennan, M. S. Penn, F. van Lente et al., "Prognostic value of myeloperoxidase in patients with chest pain," *The New England Journal of Medicine*, vol. 349, no. 17, pp. 1595–1604, 2003.

[56] S. Baldus, C. Heeschen, T. Meinertz et al., "Myeloperoxidase serum levels predict risk in patients with acute coronary syndromes," *Circulation*, vol. 108, no. 12, pp. 1440–1445, 2003.

[57] D. A. Morrow, M. S. Sabatine, M. L. Brennan et al., "Concurrent evaluation of novel cardiac biomarkers in acute coronary syndrome: myeloperoxidase and soluble CD40 ligand and the risk of recurrent ischaemic events in TACTICS-TIMI 18," *European Heart Journal*, vol. 29, no. 9, pp. 1096–1102, 2008.

[58] M. G. Kaya, R. Yalcin, K. Okyay et al., "Potential role of plasma myeloperoxidase level in predicting long-term outcome of

[59] H. Scharnagl, M. E. Kleber, B. Genser et al., "Association of myeloperoxidase with total and cardiovascular mortality in individuals undergoing coronary angiography–the LURIC study," *International Journal of Cardiology*, vol. 174, no. 1, pp. 96–105, 2014.

[60] A. O. Oyenuga, D. Couper, K. Matsushita, E. Boerwinkle, and A. R. Folsom, "Association of monocyte myeloperoxidase with incident cardiovascular disease: the Atherosclerosis Risk in Communities Study," *PLoS One*, vol. 13, article e0205310, 2018.

[61] A. Maisel, C. Mueller, R. Nowak et al., "Mid-region pro-hormone markers for diagnosis and prognosis in acute dyspnea: results from the BACH (Biomarkers in Acute Heart Failure) trial," *Journal of the American College of Cardiology*, vol. 55, no. 19, pp. 2062–2076, 2010.

[62] T. Nanbu, I. Satou, H. Nishijima, and A. Kitabatake, "Differentiation of vasospastic angina from noncardiac chest pain by history and coronary risk factors in patients with chest pain at rest," *Internal Medicine*, vol. 36, pp. 676–679, 1997.

[63] R. T. Tsuyuki, R. S. McKelvie, J. M. Arnold et al., "Acute precipitants of congestive heart failure exacerbations," *Archives of Internal Medicine*, vol. 161, no. 19, pp. 2337–2342, 2001.

[64] R. C. Wuerz and S. A. Meador, "Effects of prehospital medications on mortality and length of stay in congestive heart failure," *Annals of Emergency Medicine*, vol. 21, pp. 669–674, 1992.

[65] A. Maisel, S. X. Neath, J. Landsberg et al., "Use of procalcitonin for the diagnosis of pneumonia in patients presenting with a chief complaint of dyspnoea: results from the BACH (Biomarkers in Acute Heart Failure) trial," *European Journal of Heart Failure*, vol. 14, no. 3, pp. 278–286, 2012.

[66] W. Wang, X. Zhang, N. Ge et al., "Procalcitonin testing for diagnosis and short-term prognosis in bacterial infection complicated by congestive heart failure: a multicenter analysis of 4,698 cases," *Critical Care*, vol. 18, no. 1, p. R4, 2014.

[67] K. Berge, M. N. Lyngbakken, G. Einvik et al., "Diagnostic and prognostic properties of procalcitonin in patients with acute dyspnea: data from the ACE 2 study," *Clinical Biochemistry*, vol. 59, pp. 62–68, 2018.

[68] G. A. Alba, Q. A. Truong, H. K. Gaggin et al., "Diagnostic and prognostic utility of procalcitonin in patients presenting to the emergency department with dyspnea," *The American Journal of Medicine*, vol. 129, no. 1, pp. 96–104.e7, 2016, e107.

[69] A. C. Rast, A. Kutz, S. Felder et al., "Procalcitonin improves the Glasgow prognostic score for outcome prediction in emergency patients with cancer: a cohort study," *Disease Markers*, vol. 2015, 2015.

[70] S. Laukemann, N. Kasper, P. Kulkarni et al., "Can we reduce negative blood cultures with clinical scores and blood markers? Results from an observational cohort study," *Medicine (Baltimore)*, vol. 94, no. 49, article e2264, 2015.

[71] C. Mueller, P. Huber, G. Laifer, B. Mueller, and A. P. Perruchoud, "Procalcitonin and the early diagnosis of infective endocarditis," *Circulation*, vol. 109, pp. 1707–1710, 2004.

[72] C. W. Yu, L. I. Juan, S. C. Hsu et al., "Role of procalcitonin in the diagnosis of infective endocarditis: a meta- analysis," *The American Journal of Emergency Medicine*, vol. 31, no. 6, pp. 935–941, 2013.

[73] B. G. Demissei, J. G. Cleland, C. M. O'Connor et al., "Procalcitonin-based indication of bacterial infection identifies high risk acute heart failure patients," *International Journal of Cardiology*, vol. 204, pp. 164–171, 2016.

[74] C. R. Sinning, J. M. Sinning, A. Schulz et al., "Association of serum procalcitonin with cardiovascular prognosis in coronary artery disease," *Circulation Journal*, vol. 75, no. 5, pp. 1184–1191, 2011.

[75] M. Remskar, M. Horvat, S. Hojker, and M. Noc, "Procalcitonin in patients with acute myocardial infarction," *Wiener Klinische Wochenschrift*, vol. 114, pp. 205–210, 2002.

[76] A. Kurtul and D. Elcik, "Procalcitonin is an independent predictor for coronary atherosclerotic burden in patients with stable coronary artery disease," *International Journal of Cardiology*, vol. 236, pp. 61–64, 2017.

Research Article

Perineural Invasion Should Be Regarded as an Intermediate-Risk Factor for Recurrence in Surgically Treated Cervical Cancer: A Propensity Score Matching Study

Ting Wan [iD],[1] **Hua Tu** [iD],[1] **Lili Liu** [iD],[2] **He Huang** [iD],[1] **Yanling Feng** [iD],[1] and **Jihong Liu** [iD][1]

[1]*Department of Gynecologic Oncology, Sun Yat-sen University Cancer Center, State Key Laboratory of Oncology in South China, Collaborative Innovation, Center for Cancer Medicine, Guangzhou, China*
[2]*Department of Pathology, Sun Yat-sen University Cancer Center, State Key Laboratory of Oncology in South China, Collaborative Innovation, Center for Cancer Medicine, Guangzhou, China*

Correspondence should be addressed to Jihong Liu; liujh@sysucc.org.cn

Background. Perineural invasion (PNI) is considered as a poor prognostic factor in cervical cancer, but there has been no postoperative adjuvant therapy for it, because whether it belongs to high- or intermediate-risk factors has not been determined, this study intends to provide evidences to solve this problem. *Methods.* We conducted a retrospective analysis of cervical cancer patients who underwent radical surgery and be reported PNI from January 2012 to June 2017 at the Sun Yat-sen University Cancer Center. After 1 : 1 propensity score matching (PSM), a group of patients without PNI was matched according to the clinical pathological features. Postoperative pathological parameters and prognosis were evaluated between the PNI and the matched groups. *Results.* 1836 patients were screened, of which 162 (8.8%) diagnosed as stages IB1 to IIB reported PNI. Comparing to the matched group, more PNI (+) patients had deep outer cervix stromal invasion, cervical tunica adventitia invasion, positive lymph nodes, and positive margins. Among patients without high-risk factors, PNI (+) patients had worse 3-year overall survival (90.8% vs. 98.1%, $P = 0.02$), PNI (+) patients with single intermediate-risk factor and PNI (-) patients who meet with SEDLIS criteria had similar progress free survival ($P = 0.63$) and overall survival ($P = 0.63$), even similar survival curves. *Conclusion.* PNI is related to a worse overall survival among cervical cancer patients without high-risk factors and play the role as an intermediate-risk factor.

1. Introduction

Perineural invasion (PNI) is the neoplastic invasion of nerves by cancer cells and is an important prognostic factor related to poor outcomes in many malignancies such as head and neck and digestive tract carcinomas [1–4]. Numerous studies have explored the mechanism of PNI, and suggested that it could be the fourth route of cancer spread [5–7]. Nevertheless, the roles of PNI in cervical cancer have not been paid enough attention by gynaecologists, although many pathology centers have made routine reports about PNI in postoperative pathological results. A few studies have discussed the prognostic value of PNI in cervical cancer, but came to contradictory conclusions [8–13]. In 2015, a systematic review and meta-analysis suggested that PNI is a poor prognostic factor for cervical cancer, but only three small sample retrospective cohorts were included in the study and failed to distinguish whether PNI is a high- or intermediate-risk factor.

According to the clinical practice guidelines of the National Comprehensive Cancer Network (NCCN), there are definite recommendations that patients should receive adjuvant radiation if they have any of the following high-risk factors after radical surgery: lymph node metastasis, parametrial invasion, or resection margin involvement. Intermediate-risk factors have also been defined as lymphovascular space invasion (LVSI), stromal invasion, and tumour size according to the Sedlis criteria [14]. However,

PNI has not been recognized as an intermediate- or high-risk factor in cervical cancer. While postoperative pathology reports of many patients illustrate PNI conditions, there are currently no treatment recommendations for PNI.

Therefore, we conducted this retrospective and matched cohort study with the largest sample size in the literature and intent to demonstrate that PNI is a high-risk factor or intermediate-risk factor for cervical cancer.

2. Material and Methods

This study has been approved by the appropriate Ethics Committee and Institutional Review Board (IRB) of the Sun Yat-sun University Cancer Center (SYSUCC, Guangzhou, China) in 2020, and the requirement for written informed consent was waived by the IRB because no specific privacy of the patients was involved. Since 2012, PNI was gradually recognized and thus reported at SYSUCC as part of the patient's pathological results. Diagnosis of PNI was defined: surgically resected cervical cancer tissues were fixed in 10% neutral buffered formaldehyde fixative and embedded in paraffin, and the specimens were cut into $4\,\mu m$ thick sections and stained with hematoxylin and eosin. When microscopic examination revealed that cancer cells infiltrated any layer of nerve fibers (including epineurium, perineurium, and endoneurium) or surrounded nerve circumference $\geq 33\%$, it was judged as PNI positive. When the pathologist fails to confirm whether the tissue was an invaded nerve bundle, the immunohistochemical staining specific marker S100 was used to help determine [15]. Data from all patients who underwent radical hysterectomy and pelvic lymphadenectomy at SYSUCC between January 2012 and June 2017 were assessed. Patients were screened if PNI has been reported in the postoperative pathological results and were diagnosed according to the International Federation of Gynaecology and Obstetrics (FIGO, 2009) as stage IA2 to IIB squamous cell carcinoma, adenocarcinoma, or adenosquamous carcinoma of the cervix. Other subtypes such as neuroendocrine or clear cell carcinoma was excluded in this study. Patients who had a cone biopsy or definite radiation before radical surgery were also excluded because of the possibility of missed diagnosis of PNI. Neoadjuvant chemotherapy with 2-3 cycles of the paclitaxel and cispaltin regimen could apply in patients with stage IB2, IIA2, or IIB prior to radical surgery.

After surgery, patients with any of the high-risk factors such as lymph node metastasis, parametrial invasion, and resection margin involvement would undergo adjuvant concurrent chemoradiation with weekly cisplatin, whereas patients with any two of the following intermediate factors would receive adjuvant radiation (modified Sedlis criteria): pathological tumour size larger than 4 cm, deep stromal invasion, and lymphovascular space invasion (LVSI). The volume of adjuvant radiation included parametrium, vaginal margin, presacral nodes, the entirety of the common iliac, external iliac, internal iliac, and obturator nodes. In patients with common iliac and/or para-aortic nodal involvement, extended field pelvic and para-aortic radiotherapy up to the level of renal vessels was delivered. The dose was approximately 50 Greys (Gy) with conventional fractionation of 1.8 to 2.0 Gy daily; additional brachytherapy with a dose of 18 to 21 Gy was given to patients who had positive vaginal stump. Finally, patients with one intermediate-risk factor received 2-3 cycles adjuvant chemotherapy of paclitaxel and cisplatin or underwent observation, which is according to the will of patients.

The clinical and pathological characteristics of the patients were recorded, including age, FIGO stage, tumour size, histological type, tumour differentiation, preoperative treatment, surgical approach, postoperative adjuvant therapy, LVSI, ovarian invasion, lower uterine segment invasion, deep stromal invasion of the cervical canal, deep stromal invasion of the cervix, lymph node invasion, parametrium invasion, positive margins, and PNI.

The follow-up data were also recorded. Follow-up procedures included physical examination, abdominal and pelvic ultrasonic examination, serum squamous carcinoma cell antigen level (for squamous carcinoma and adenosquamous carcinoma), and CA125 (for adenocarcinoma and adenosquamous carcinoma). These were performed in SYSUCC every three months for two years and then every six months until the fifth year. Computed tomography (CT) or magnetic resonance imaging (MRI) scans were performed when doctors suspected recurrence.

According to the literature, if the pathological slides are not reread with special staining, the real incidence of PNI may be underestimated [11]. The PNI situation we collected from the pathological record may not represent the real PNI population, while the workload of rereading all the cervical cancer pathological slides from 2012 to 2017 is very huge. In order to avoid this bias, we matched a group of PNI (-) patients according to baseline clinical characteristics, including tumour size, pathological type, FIGO stage, tumour differentiation, and preoperative treatment in the same period by using 1:1 propensity score matching (PSM), and the pathological slides of matched group were reread by the pathologist to confirm there was no PNI. The match tolerance of PSM was set to 0.01. Propensity scores of individuals were calculated using logistic regression analysis (SPSS version 23.0, Chicago, IL, USA), baseline characteristics were analysed using Chi-square statistics or Fisher's exact test in the case of categorical variables, and the t-test or analysis of variance (ANOVA) for continuous variables. The flow diagram of recruitment and exclusion is shown in Figure 1S (Supplementary materials).

The comparisons of characteristics between two groups were performed using nonparametric statistics. Numerical parameters were expressed as the median and range, and the Mann-Whitney U test was used to examine the differences. Fisher's exact test and the Chi-square test were used to compare rates between two groups, as appropriate. Survival curves were constructed according to the Kaplan-Meier estimator, and differences were compared using the log-rank test. A two-tailed P value < 0.05 was considered statistically significant. All statistical analyses were performed using the SPSS software version 23.0 (SPSS Inc, Chicago, IL, USA).

3. Results

3.1. Patients Characteristics.
Between January 2012 and June 2017, 1836 patients staged from IA2 to IIB received radical hysterectomy and pelvic lymphadenectomy with or without para-aortic lymph node dissection. Of them, 162 patients (8.8%) reported PNI after surgery, and the FIGO stage of these patients ranged from IB1 to IIB. No patients with stage IA were reported PNI. Table 1 summarizes the patients' demographics and tumour features assessed before and after PSM. Most PNI were found in the cervix, 10 patients had PNI in the parametrium or surgical margin, and two patients had found PNI in the metastatic ovaries.

The mean age of patients with PNI was 51.5 ± 9.0 years old. The average tumour size was 3.9 ± 1.3 cm. The histological type was mostly squamous cell carcinoma, but adenocarcinoma or adenosquamous cell carcinoma accounted for 28.4%, which was larger than that in the normal cervical cancer population. 95.1% of patients had tumours with moderate or poor differentiation. Furthermore, 92.6% of patients underwent open radical hysterectomy, whereas only 7.4% received minimally invasive surgery.

After 1 : 1 PSM, there were no significant differences in pathological type, tumour differentiation, FIGO stage, primary therapy, NACT courses, and surgical approach between two groups. However, patients in the matched group were younger (50.8 vs. 51.5 years, $P = 0.05$), and more patients had pathological complete remission or complete remission after NACT (20.3% vs. 0%, $P = 0.01$).

3.2. Postoperative Characteristics and Adjuvant Therapy.
Table 2 demonstrates the postoperative characteristics of patients with PNI and its matched group. No significant differences were observed between two groups in terms of LVSI, ovarian invasion, and invasion of the lower uterine segment. However, more patients with PNI had deep cervical canal stromal invasion (66% vs. 39.5%, $P = 0.01$), deep outer cervix stromal invasion (90.7% vs. 61.1%, $P = 0.01$), cervical tunica adventitia invasion (45.1% vs. 10.5%, $P = 0.01$), positive lymph nodes (35.2% vs. 18.3%, $P = 0.01$), and positive margins (37% vs. 14.8%, $P = 0.01$).

Since the patients with PNI had more risk factors than patients in the matched group, instances of postoperative adjuvant therapy were also higher: 80.2% of PNI patients underwent adjuvant radiation with or without chemotherapy, whereas the ratio in the matched group was 69.1%.

3.3. Survival Outcomes

3.3.1. Progression-Free Survival and Overall Survival of All Patients.
The last follow-up date was 1st October 2020, and the median follow-up period was 55 months (range, 2-100 months). Recurrence was observed in 40 patients with PNI, with a median time for recurrence at 12 months. For the matched group, there were 22 patients and 12 months, respectively. Moreover, 27 patients with PNI (27/40, 67.5%) and 10 patients in the matched group (45.5%) had distant recurrence with or without local recurrence, which means larger ratio of patients in PNI group had distant recurrence ($P = 0.03$). After treatment for recurrence, 36 patients (90%) with PNI and 11 patients (50%) in the matched group eventually died ($P = 0.01$).

The 3-year progression-free survival (PFS) rate for patients with PNI and those in the matched group was 76.4% (95% confidence interval (CI): 72.9%-79.9%) and 87.8% (95% CI: 72.2%-90.4%) ($P = 0.01$), whereas the 3-year overall survival (OS) rate was 78.6% (95% CI: 75.2%-82.0%) and 93.9% (95% CI: 91.9%-95.9%) ($P = 0.01$), respectively. The PFS and OS survival curves for these two groups are represented in Figure 1.

3.3.2. PFS and OS of Patients Stratified by High-Risk Factors.
In order to understand the exact impact of PNI in different risk subgroup, we stratified the patients by the high-risk factors (with any of these three factors: positive lymph nodes, parametrium, or margin) and observed their PFS and OS. In the PNI and matched groups, 89 (54.9%) and 43 (26.5%) patients had one or more high-risk factors, respectively. Among patients with high-risk factors, we could see a worse trend in patients with PNI, the 3-year PFS for patients with PNI and those in the matched group was 67.9% (95% CI: 62.7%-77.4%) and 76.2% (95% CI: 69.6%-82.8%) ($P = 0.19$), and the 3-year OS was 68.3% (95% CI: 63.0%-73.6%) and 82.4% (95% CI: 76.4%-88.4%) ($P = 0.08$), respectively. On the other hand, among patients without high-risk factors, the 3-year PFS for patients with PNI and those in the matched group was 86.6% (95% CI: 82.4%-90.8%) and 92.1% (95% CI: 89.6%-94.6%) ($P = 0.14$), and the 3-year OS was 90.8% (95% CI: 87.2%-94.4%) and 98.1% (95% CI: 96.7%-99.5%) ($P = 0.02$), respectively (Figure 2), indicating that PNI play an important role on poor prognosis in patients without high-risk factors.

3.3.3. PNI (+) Patients with One Moderate-Risk Factor vs. PNI (-) Patients Who Met with Sedlis Criteria.
To further confirm whether PNI is an intermediate-risk factor, we picked out the PNI (+) patients who combined with single intermediate-risk factor (any of the following factors: tumor size large than 4 cm, deep stromal invasion, or LVSI) and those PNI (-) patients who met with Sedlis criteria (intermediate-risk factors from NCCN guideline). There were 34 PNI (+) patients combining with single intermediate-risk factor, three of them recurred and two died; 50 PNI (-) patients met with the Sedlis criteria, seven of them recurred, and two died. The survival curve of these patients is shown in Figure 3, indicating a similar PFS ($P = 0.63$) and OS ($P = 0.63$), even the similar survival curves (Figure 3). We proved that PNI might be a new intermediate-risk factor who play a similar role in cervical cancer like large tumor size, deep stromal invasion, or LVSI.

4. Discussion

PNI is an important prognostic factor in many malignancies, which is also the indication for adjuvant therapy. However, in cervical cancer, there is still controversy about whether PNI is an independent prognostic factor. In the studies reported by Elsahwi et al. [11] (192 patients included; 24 had PNI) and Cho et al. [12] (185 patients included; 13 had

TABLE 1: Patient characteristics.

Patient characteristics		Before PSM			After PSM		
		PNI (+), $n = 162$	PNI (-), $n = 1674$	P	PNI (+), $n = 162$	PNI (-), $n = 162$	P
Mean age (yr)		51.5 ± 9.0	50.3 ± 9.6	0.03	51.5 ± 9.0	50.8 ± 9.1	0.05
Average tumor size (cm)		3.9 ± 1.3	2.6 ± 1.6	0.01	3.9 ± 1.3	3.9 ± 1.2	0.93
Pathological type	Squamous carcinoma	116 (71.6%)	1462 (87.3%)	0.02	116 (71.6%)	118 (72.8%)	0.89
	Adenocarcinoma	31 (19.1%)	153 (9.1%)		31 (19.1%)	28 (17.3%)	
	Adenosquamous carcinoma	15 (9.3%)	59 (3.5%)		15 (9.3%)	16 (9.9%)	
Tumor differentiation	Well	8 (4.9%)	235 (14.0%)	0.01	8 (4.9%)	6 (3.7%)	0.93
	Moderate	63 (38.9%)	724 (43.3%)		63 (38.9%)	63 (38.9%)	
	Poor	91 (56.2%)	715 (42.7%)		91 (56.2%)	93 (57.4%)	
FIGO stage	IA2	0	63 (3.8%)	0.01	0	0	0.96
	IB1	41 (25.3%)	752 (44.9%)		41 (25.3%)	38 (23.5%)	
	IB2	13 (8.0%)	209 (12.5%)		13 (8.0%)	14 (8.6%)	
	IIA1	59 (36.4%)	204 (12.2%)		59 (36.4%)	60 (37.0%)	
	IIA2	26 (16.1%)	136 (8.1%)		26 (16.0%)	27 (16.7%)	
	IIB	23 (14.2%)	98 (5.9%)		23 (14.2%)	23 (14.2%)	
Primary therapy	Radical surgery	111 (68.5%)	1284 (76.7%)	0.01	111 (68.5%)	98 (60.5%)	0.12
	NACT	51 (31.5%)	390 (23.3%)		51 (31.5%)	64 (39.5%)	
NACT courses		2.3	2	0.36	2.3	2.2	0.78
Response to NACT	pCR	0	41 (10.5%)	0.01	0	6 (9.4%)	0.01
	CR	0	52 (13.3%)		0	7 (10.9%)	
	PR	39 (76.5%)	245 (62.8%)		39 (76.5%)	42 (65.6%)	
	SD	11 (21.6%)	40 (10.3%)		11 (21.6%)	9 (14.1%)	
	PD	1 (2.0%)	12 (3.1%)		1 (2.0%)	0	
Surgical approach	Minimally invasive surgery	12 (7.4%)	136 (8.1%)	0.46	12 (7.4%)	20 (12.3%)	0.14
	Laparotomy	150 (92.6%)	1538 (91.9%)		150 (92.6%)	142 (87.7%)	

PNI: perineural invasion; FIGO: International Federation of Gynecology and Obstetrics; NACT: neoadjuvant chemotherapy; pCR: pathological complete remission; CR: complete remission; PR: partial remission; SD: stable disease; PD: progress disease.

PNI), PNI was not associated with worse prognosis in early cervical cancer. By contrast, in the study reported by Tang et al. [16] (larger cohort, 406 patients included; 43 had PNI), PNI were identified as independent risk factors for OS and DFS. None of past studies has been able to state with certainty whether PNI is a high- or intermediate-risk factor. In our matched case study, we firstly proved that PNI was an intermediate-risk factor systematically. As the original finding of intermediate-risk factors for cervical cancer, any single intermediate-risk factor has not been definitely proved an independent poor prognostic factor, but pairwise combinations of the intermediate-risk factors can be shown to clearly affect prognosis.

The factors associated with PNI are clear enough in the literature, which were LVSI, deep stromal invasion, tumour size ≥ 4 cm, and parametrium invasion [8–13, 17]; we also found these common features in our cohort. What is interesting is that we specifically found a relatively higher proportion of patients who had adenocarcinoma or adenosquamous cell carcinoma with the moderate or poor differentiation, and these findings were seldom reported in the past studies. In

2019, Wang et al. conducted a multi-institutional Chinese cohort to explore the reproducibility and prognostic significance of Silva pattern system in adenocarcinoma of cervical cancer, which is still a new pattern for the pathology of adenocarcinoma. They found perineural invasion was significantly correlated with the Silva pattern system and appeared in most Silva C tumors ($P = 0.001$), and they suggested revising the Silva C criteria by adding perineural invasion as a factor [18]. These characteristics can help us better understand and predict PNI.

Tumour metastasis along nerve has been proven by clinical researches. Capek et al. reviewed 17 cases of bladder, rectal, and cervical cancers and concluded that as tumour spreads, with parts of the nerve invasion confirmed by biopsy, the L5-S1 spinal nerves and the sciatic nerve were most frequently involved, and tumour cells could use the splanchnic nerves as conduits and spread from the end organ to the lumbosacral plexus [19]. In our study, we found that PNI could present in the ovaries or the surgical margin, away from the local tumour of the cervix. According to the recommendations of NCCN guidelines, for patients with FIGO

TABLE 2: Postoperative characteristics and adjuvant therapy.

Parameters		PNI (+), $n = 162$	PNI (-), $n = 162$	P
LVSI	Yes	54 (33.3%)	51 (31.5%)	0.72
	No	108 (66.7%)	111 (68.5%)	
Ovarian invasion	Yes	8 (5.0%)	3 (1.9%)	
	No	137 (84.6%)	143 (88.3%)	0.30
	Ovary Preserved	17 (10.4%)	16 (9.8%)	
The lower segment of uterine invasion	Yes	38 (23.5%)	26 (16.1%)	0.09
	No	124 (76.5%)	136 (83.9%)	
Deep stromal of cervical canal invasion	Yes	107 (66.1%)	64 (39.5%)	0.01
	No	55 (33.9%)	98 (60.5%)	
Deep stromal of outer cervix invasion	Yes	147 (90.7%)	99 (61.1%)	0.01
	No	15 (9.3%)	63 (38.9%)	
Tunica adventitia of cervix invasion	Yes	73 (45.1%)	17 (10.5%)	0.01
	No	89 (54.9%)	145 (89.5%)	
Lymph node invasion	Yes	57 (35.2%)	28 (17.3%)	0.01
	No	105 (64.8%)	134 (82.7%)	
Positive margin	Yes	60 (37.0%)	24 (14.8%)	0.01
	No	102 (63.0%)	138 (85.2%)	
Postoperative adjuvant therapy	Radiation with or without chemotherapy	130 (80.2%)	112 (69.1%)	
	Chemotherapy Alone	17 (10.5%)	26 (16.1)	0.03
	Observation	15 (9.3%)	24 (14.8%)	

LVSI: lymphovascular space invasion.
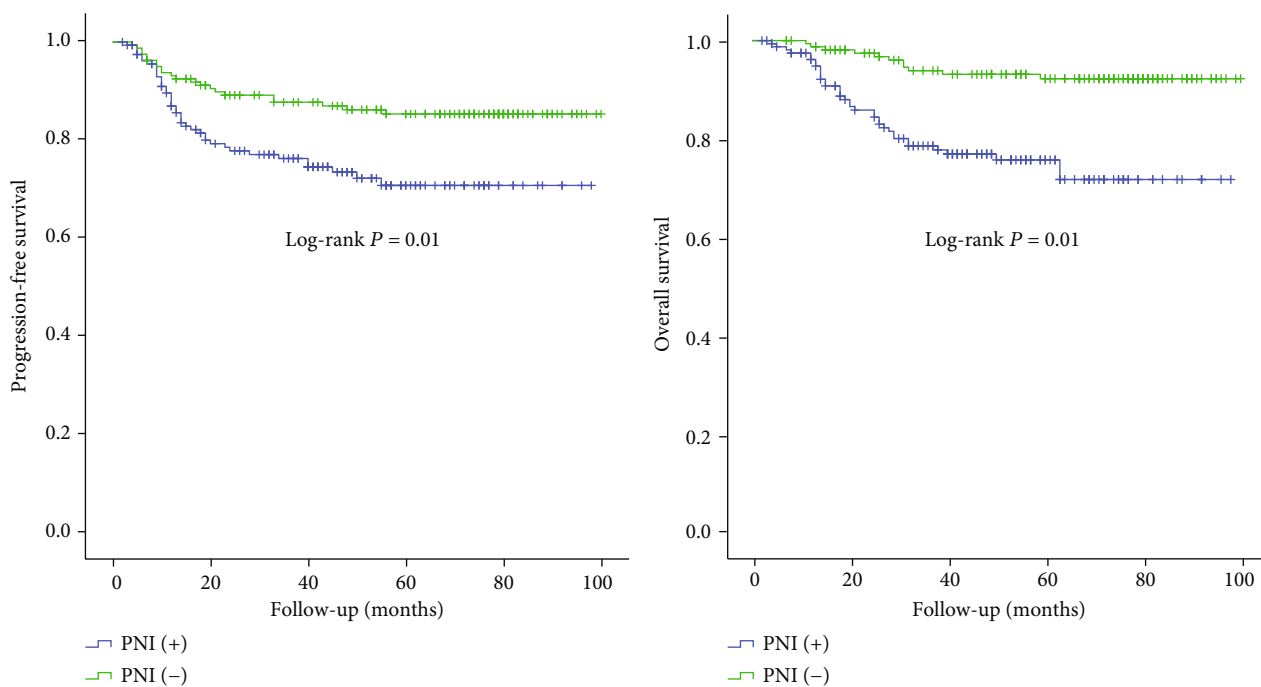
FIGURE 1: Progression-free survival and overall survival of patients in group PNI (+) and PNI (-).

stage IB1-IIA2 cervical cancer, the recommended surgical procedure is type C radical hysterectomy (Querleu-Morrow classification system), involving two subtypes: type C1 and type C2, of which type C1 is also known as Nerve-Sparing Radical Hysterectomy (NSRH). However, the detail indication for NSRH has not been established, which may not be
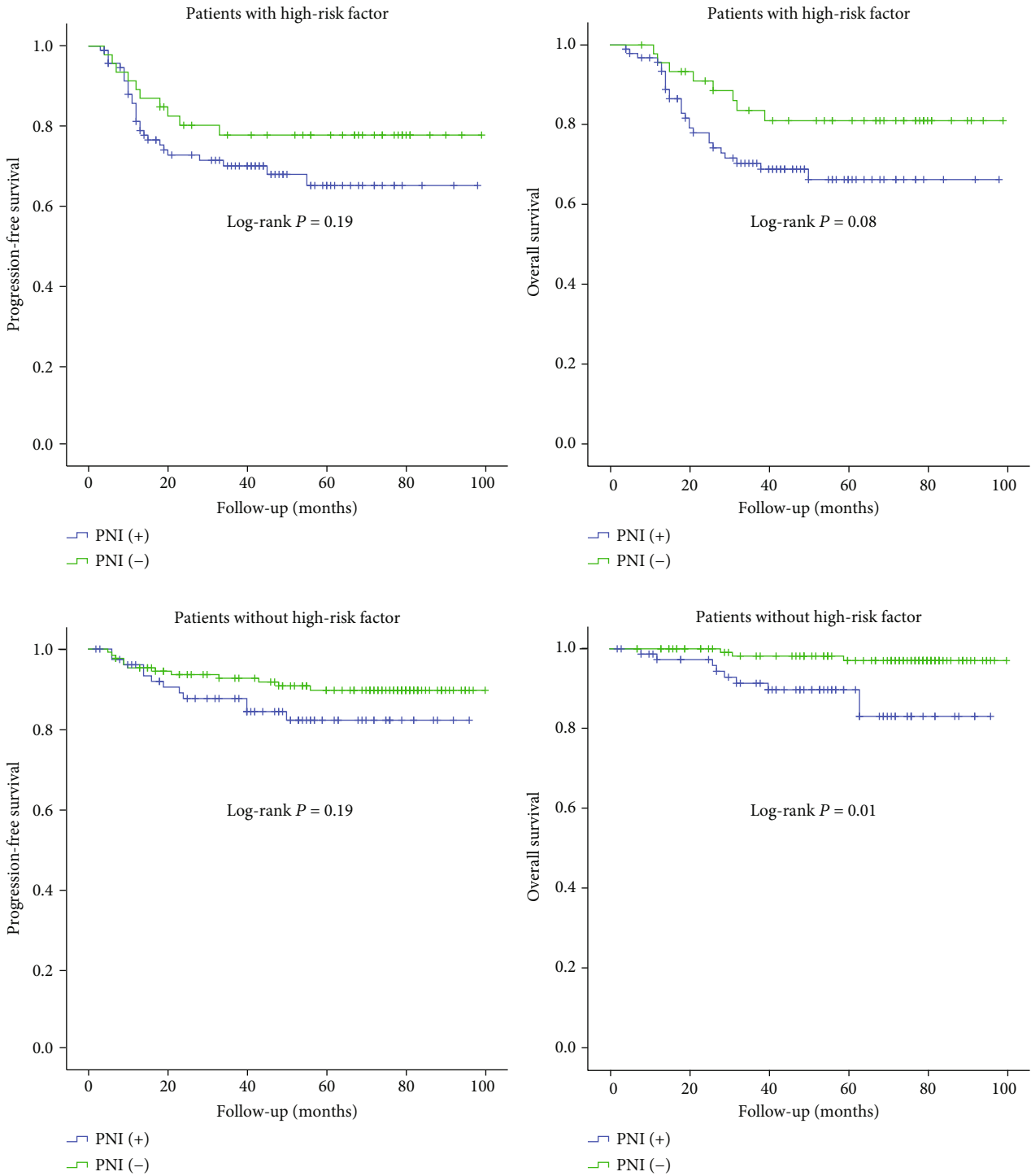
FIGURE 2: Progression-free survival and overall survival of patients in PNI (+) and PNI (-) patients stratified by high-risk factors (any of the following factors: positive lymph node, positive parametrium, or positive surgical margin).

suitable for patients prone to PNI according to the existed evidences. Concurrent chemoradiotherapy might be the proper treatment for the patients prone to PNI rather than NSRH, and clinical trials should be carried out to verify these considerations.

Our study possibly has the largest sample size of cervical cancer patients with PNI (among English language published data); we provide meaningful information about the new clinical characteristics, exact prognostic value, and further treatment for patients with PNI which were all seldom mentioned in the past studies. Nevertheless, our study may have two possible weaknesses. First, we did not review all the pathological slides of the 1836 patients to identify the actual incidence rate of PNI, and this may leave out a small number
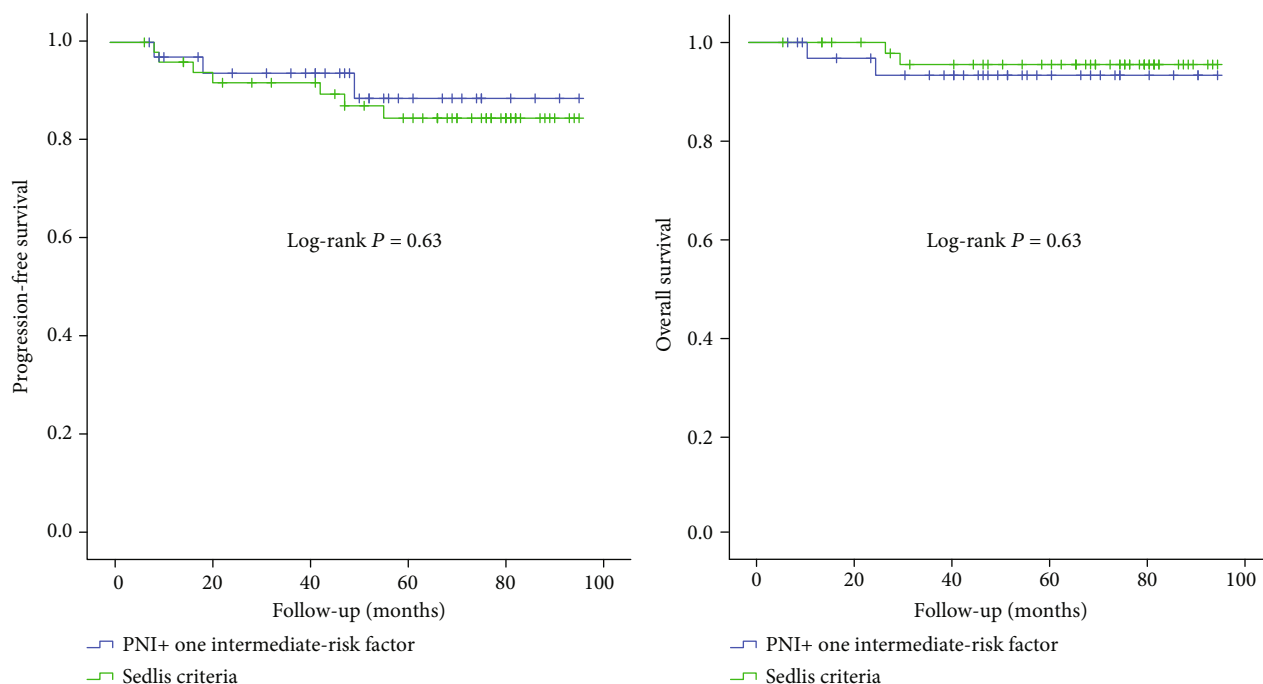
FIGURE 3: Progression-free survival and overall survival in patients with PNI + one intermediate-risk factor and patients who meet with Sedlis criteria but without PNI.

of patients with insignificant PNI. The review of all the slides was an enormous workload that we could not realistically finish; nevertheless, the data we used were based on the reported pathological results and were in accordance with the actual clinical situation. Second, the matched cases may not entirely represent the population of PNI (-) cases. However, we evaluated the clinical characteristics and prognosis of the patients in matched group, and concluded that these patients were in line with our general clinical cognition of normal population in the same FIGO stages.

5. Conclusions

PNI is likely to occur in cervical cancer patients with risk factors. Our study firstly proved that PNI play the role as an intermediate-risk factor when without high-risk factors, further studies should explore the adjuvant therapy for PNI.

Data Availability

All the original data of this study have been uploaded to the database specified by the Ethics Committee of Sun Yat-sen University Cancer Center, RDD Management Committee, http://www.researchdata.org.cn/. Data are available upon reasonable request.

Additional Points

Precis. (i) PNI is likely to occur in cervical cancer patients with risk factors for recurrence. (ii) PNI is related to worse overall survival among cervical cancer patients without

high-risk factors. (iii) We prove PNI plays the role as an intermediate-risk factor in cervical cancer patients.

Conflicts of Interest

The authors have no conflicts of interest to declare.

Authors' Contributions

Ting Wan is responsible for the study design, data curation, writing original draft, writing—review, and editing; Hua Tu for the study design and statistics analysis; Lili Liu for the pathological review, writing—review, and editing; He Huang for the study design, writing—review, and editing; Yanling Feng for the data curation and methodology; and Jihong Liu for the manuscript editing, supervision, and project administration. Ting Wan and Hua Tu contributed equally to the manuscript. Hua Tu is co-first author.

Supplementary Materials

Figure 1S: flow diagram of recruitment and propensity score matching *(Supplementary Materials)*

References

[1] H. Ozaki, T. Hiraoka, R. Mizumoto et al., "The prognostic significance of lymph node metastasis and intrapancreatic perineural invasion in pancreatic cancer after curative resection," *Surgery Today*, vol. 29, no. 1, pp. 16–22, 1999.

[2] W. L. Law and K. W. Chu, "Anterior resection for rectal cancer with mesorectal excision: a prospective evaluation of 622 patients," *Annals of Surgery*, vol. 240, no. 2, pp. 260–268, 2004.

[3] C. H. Su, S. H. Tsay, C. C. Wu et al., "Factors influencing postoperative morbidity, mortality, and survival after resection for hilar cholangiocarcinoma," *Annals of Surgery*, vol. 223, no. 4, pp. 384–394, 1996.

[4] N. Duraker, S. Sisman, and G. Can, "The significance of perineural invasion as a prognostic factor in patients with gastric carcinoma," *Surgery Today*, vol. 33, no. 2, pp. 95–100, 2003.

[5] Y. L. Bunimovich, A. A. Keskinov, G. V. Shurin, and M. R. Shurin, "Schwann cells: a new player in the tumor microenvironment," *Cancer Immunology, Immunotherapy*, vol. 66, no. 8, pp. 959–968, 2017.

[6] Y. Long, D. S. Yao, Y. S. Wei, and G. T. Wu, "Effects of nerve growth factor expression on perineural invasion and worse prognosis in early-stage cervical cancer," *Chinese Medical Journal*, vol. 131, no. 19, pp. 2360–2363, 2018.

[7] S. Deborde and R. J. Wong, "How Schwann cells facilitate cancer progression in nerves," *Cellular and Molecular Life Sciences*, vol. 74, no. 24, pp. 4405–4420, 2017.

[8] S. Memarzadeh, S. Natarajan, D. P. Dandade et al., "Lymphovascular and perineural invasion in the parametria: a prognostic factor for early-stage cervical cancer," *Obstetrics and Gynecology*, vol. 102, no. 3, pp. 612–619, 2003.

[9] H. Ozan, S. Ozuysal, and B. Ediz, "Perineural invasion in early-stage cervical carcinoma," *European Journal of Gynaecological Oncology*, vol. 30, no. 4, pp. 379–383, 2009.

[10] L. C. Horn, A. Meinel, U. Fischer, K. Bilek, and B. Hentschel, "Perineural invasion in carcinoma of the cervix uteri–prognostic impact," *Journal of Cancer Research and Clinical Oncology*, vol. 136, no. 10, pp. 1557–1562, 2010.

[11] K. S. ElSahwi, E. Barber, J. Illuzzi et al., "The significance of perineural invasion in early-stage cervical cancer," *Gynecologic Oncology*, vol. 123, no. 3, pp. 561–564, 2011.

[12] H. C. Cho, H. Kim, H. Y. Cho, K. Kim, J. H. No, and Y. B. Kim, "Prognostic significance of perineural invasion in cervical cancer," *International Journal of Gynecological Pathology : official journal of the International Society of Gynecological Pathologists.*, vol. 32, no. 2, pp. 228–233, 2013.

[13] Y. Zhu, G. Zhang, Y. Yang et al., "Perineural invasion in early-stage cervical cancer and its relevance following surgery," *Oncology Letters*, vol. 15, no. 5, pp. 6555–6561, 2018.

[14] A. Sedlis, B. N. Bundy, M. Z. Rotman, S. S. Lentz, L. I. Muderspach, and R. J. Zaino, "A randomized trial of pelvic radiation therapy versus no further therapy in selected patients with stage IB carcinoma of the cervix after radical hysterectomy and pelvic lymphadenectomy: a gynecologic oncology group study," *Gynecologic Oncology*, vol. 73, no. 2, pp. 177–183, 1999.

[15] Z. H. Zhou, G. F. Xu, W. J. Zhang, H. B. Zhao, and Y. Y. Wu, "Reevaluating significance of perineural invasion in gastric cancer based on double immunohistochemical staining," *Archives of Pathology & Laboratory Medicine*, vol. 138, no. 2, pp. 229–234, 2014.

[16] M. Tang, Q. Liu, X. Yang et al., "Perineural invasion as a prognostic risk factor in patients with early cervical cancer," *Oncology Letters*, vol. 17, no. 1, pp. 1101–1107, 2019.

[17] J. E. Skret-Magierlo, P. J. Soja, A. Skret, A. Kruczek, E. Kaznowska, and L. Wicherek, "Perineural space invasion in cervical cancer (FIGO IB1-IIB) accompanied by high-risk factors for recurrence," *Journal of Cancer Research and Therapeutics*, vol. 10, no. 4, pp. 957–961, 2014.

[18] W. Wang, G. Song, J. Lin et al., "Study of the revisited, revised, and expanded Silva pattern system for Chinese endocervical adenocarcinoma patients," *Human Pathology*, vol. 84, pp. 35–43, 2019.

[19] S. Capek, B. M. Howe, K. K. Amrami, and R. J. Spinner, "Perineural spread of pelvic malignancies to the lumbosacral plexus and beyond: clinical and imaging patterns," *Neurosurgical Focus*, vol. 39, no. 3, article E14, 2015.

Hindawi

Retraction

Retracted: Identification of Ferroptosis-Related Long Noncoding RNA and Construction of a Novel Prognostic Signature for Gastric Cancer

Disease Markers

This article has been retracted by Hindawi following an investigation undertaken by the publisher [1]. This investigation has uncovered evidence of one or more of the following indicators of systematic manipulation of the publication process:

(1) Discrepancies in scope

(2) Discrepancies in the description of the research reported

(3) Discrepancies between the availability of data and the research described

(4) Inappropriate citations

(5) Incoherent, meaningless and/or irrelevant content included in the article

(6) Peer-review manipulation

The presence of these indicators undermines our confidence in the integrity of the article's content and we cannot, therefore, vouch for its reliability. Please note that this notice is intended solely to alert readers that the content of this article is unreliable. We have not investigated whether authors were aware of or involved in the systematic manipulation of the publication process.

In addition, our investigation has also shown that one or more of the following human-subject reporting requirements has not been met in this article: ethical approval by an Institutional Review Board (IRB) committee or equivalent, patient/participant consent to participate, and/or agreement to publish patient/participant details (where relevant).

Wiley and Hindawi regrets that the usual quality checks did not identify these issues before publication and have since put additional measures in place to safeguard research integrity.

We wish to credit our own Research Integrity and Research Publishing teams and anonymous and named external researchers and research integrity experts for contributing to this investigation.

The corresponding author, as the representative of all authors, has been given the opportunity to register their agreement or disagreement to this retraction. We have kept a record of any response received.

References

[1] W. Chen, Z. Feng, J. Huang et al., "Identification of Ferroptosis-Related Long Noncoding RNA and Construction of a Novel Prognostic Signature for Gastric Cancer," *Disease Markers*, vol. 2021, Article ID 7724997, 2021.

Hindawi

Research Article

Identification of Ferroptosis-Related Long Noncoding RNA and Construction of a Novel Prognostic Signature for Gastric Cancer

WenZheng Chen [ID],[1,2] **ZongFeng Feng** [ID],[3] **JianFeng Huang** [ID],[3] **PengCheng Fu** [ID],[3] **JianBo Xiong** [ID],[1] **Yi Cao** [ID],[1] **Yi Liu** [ID],[1] **Yi Tu** [ID],[4] **ZhengRong Li** [ID],[1] **ZhiGang Jie** [ID],[1] **and Tao Xiao** [ID][1]

[1]Department of Gastrointestinal Surgery, The First Affiliated Hospital of Nanchang University, China
[2]Department of Second Abdominal Surgery, Jiangxi Province Cancer Hospital, China
[3]Medical College of Nanchang University, China
[4]Department of Pathology, The First Affiliated Hospital of Nanchang University, China

Correspondence should be addressed to ZhiGang Jie; jiezg123@126.com and Tao Xiao; xcz258@163.com

Background. Gastric cancer is the most common malignant tumor of the digestive system. It has a poor prognosis and is clinically challenging to treat. Ferroptosis is a newly defined mode of programmed cell death. The roles and prognostic value of ferroptosis-related long noncoding RNAs (lncRNAs) in gastric cancer remain unknown. *Results*. In the current study, 20 ferroptosis-related lncRNAs were identified via univariate Cox analysis, least absolute shrinkage, and selection operator Cox regression analysis and used to construct a prognostic signature and classify gastric cancer patients into high-risk and low-risk groups. The signature was validated using TCGA training and testing cohorts. The risk signature was an independent prognostic indicator of survival and accurately predicted the prognoses of patients with gastric cancer. It was also associated with immune cell infiltration. Gene set enrichment analysis was used to investigate underlying mechanisms that the 20 ferroptosis-related lncRNAs were involved in. Chemosensitivity and immune checkpoint inhibitor analyses indicated that high-risk patients were more sensitive to the immune checkpoint inhibitor programmed cell death protein 1. *Conclusions*. The important role of ferroptosis-related lncRNAs in immune infiltration identified in the current study may assist the determination of personalized prognoses and treatments in patients with gastric cancer. These 20 lncRNAs can be used as the diagnostic and prognostic markers for gastric cancer.

1. Introduction

Gastric cancer is the most common malignant tumor of the digestive system, ranking fifth in incidence and fourth in mortality globally. In 2020, more than one million new cases of gastric cancer and 769,000 deaths were reported worldwide [1]. Because of the increasing incidence of autoimmune gastritis and dysbiosis of the gastric flora, the incidence of gastric cancer is also gradually increasing in young people [2, 3]. To date, the precise mechanisms underlying the initiation and progression of gastric cancer remain unknown.

Ferroptosis is a newly defined mode of cell death that is iron dependent and is triggered by lipid peroxidation and lethal reactive oxygen species (ROS). It is distinct from necrosis, apoptosis, and autophagy [4]. Long noncoding RNAs (lncRNAs) are noncoding RNA molecules of approximately 200 nucleotides in length that induce the occurrence, development, and metastasis of tumors by mediating chromosome modification, transcriptional activation, and interference [5, 6]. Recent reports suggest that ferroptosis-related lncRNAs play important roles in tumorigenesis, progression, and metastasis via multiple mechanisms. Wu et al. [7] reported that lncRNA NEAT1 promoted ferroptosis and ferroptosis sensitivity in non-small-cell lung cancer by regulating the expression of ACSL4. Qi et al. [8] reported that lncRNA GABPB1-AS1 could induce ferroptosis in
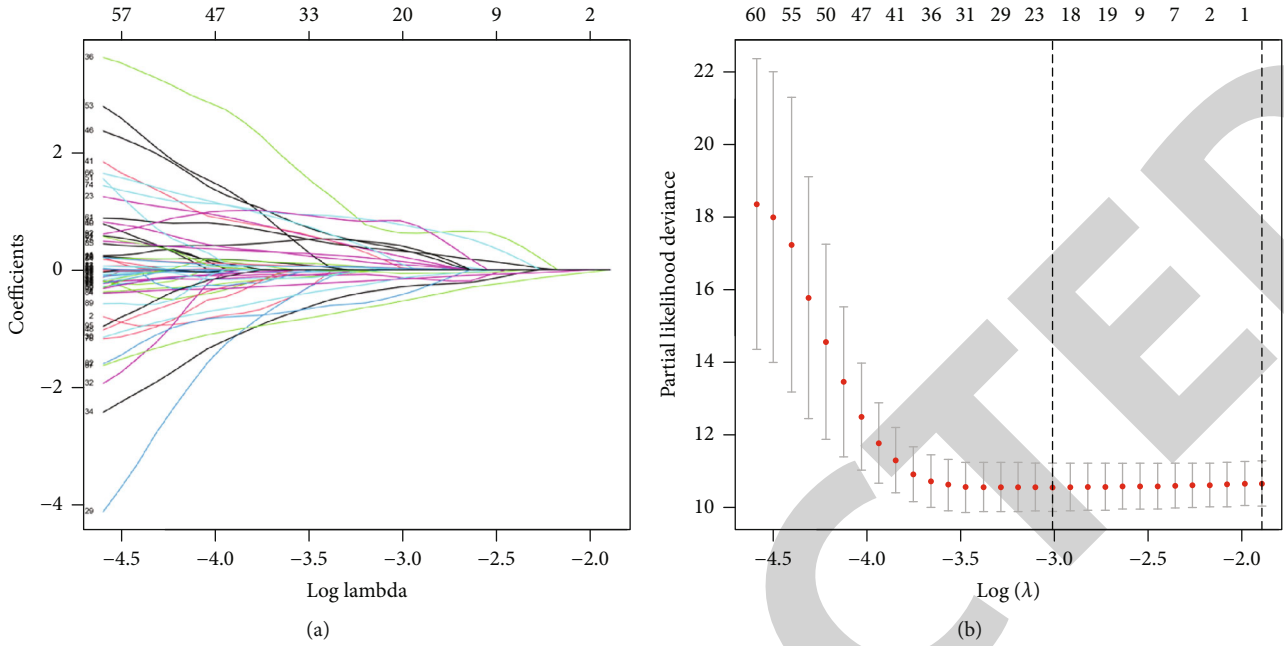
FIGURE 1: Twenty ferroptosis-related lncRNAs were identified via LASSO regression analysis. (a) LASSO coefficient profiles of the ferroptosis-related lncRNAs. (b) Partial likelihood deviance of different numbers of variables calculated via the LASSO regression model.

hepatocellular carcinoma cells by inhibiting the translation of GABPB1. Wang et al. [9] reported that LINC00336 regulated the expression of cystathionine-β-synthase to promote lung cancer cell ferroptosis by serving as an endogenous micro-RNA 6852 "sponge." Gai et al. [10] proposed that MT1DP regulates the miR-365a-3p/NRF2 signaling pathway, resulting in the sensitization of non-small-cell lung cancer cells to erastin-induced ferroptosis.

The roles and prognostic value of ferroptosis-related lncRNAs in gastric cancer remain unclear. In the current study, ferroptosis-related lncRNAs potentially involved in gastric cancer were screened to construct a prognostic signature, and the potential mechanisms involved were investigated. To the best of our knowledge, the study is the first to construct and validate a ferroptosis-related lncRNA prognostic signature for used in gastric cancer patients. Functional enrichment, immune cell infiltration, chemosensitivity, and immune checkpoint inhibitors were also analyzed. The study resulted in the development of an effective, practical, and quantitative approach for clinicians to use to predict survival and formulate individualized treatments in gastric cancer patients.

2. Materials and Methods

2.1. Data Collection and Differential Ferroptosis-Related lncRNAs.
Raw counts from RNA-seq transcriptome data and corresponding clinical data derived from gastric cancer tissues were extracted from the TCGA database. Ferroptosis-related genes were downloaded from the FerrDb database [11]. Differentially expressed ferroptosis-related lncRNAs were screened via Pearson's correlational analyses ($p < 0.01$, Spearman correlation coefficient > 0.3).

2.2. Construction and Validation of the Prognostic Ferroptosis-Related lncRNA Signature.
Ferroptosis-related lncRNAs associated with survival were evaluated via univariate Cox regression analysis. Gastric cancer samples were randomly divided into a training set and a testing set at a 1 : 1 ratio. A prognostic signature was then constructed in patients with gastric cancer based on LASSO Cox regression. The formula used to calculate prognostic signature risk scores was

$$\text{risk score} = \sum \left(\text{Exp}[\text{lncRNA}] \times \text{coef}[\text{lncRNA}] \right) \quad (1)$$

where Exp [lncRNA] is the corresponding expression of the included lncRNA, and coef [lncRNA] represents the regression coefficient. The risk score of each patient was calculated, and each patient was assigned to a low-risk group or a high-risk group based on the median risk score in the training and testing cohorts. Kaplan-Meier analysis and areas under ROC curves were used to evaluate the performance of the prognostic signature.

2.3. Correlations with Clinicopathological Characteristics and the Establishment of a Nomogram.
Univariate and multivariate Cox regression analyses were conducted to investigate whether risk scores and relevant clinicopathological characteristics were associated with overall survival in gastric cancer patients. Nomograms that included age, sex, grade, stage, TNM classifications, and risk score were used to calculate the total score and predict 1, 3, and 5-year survival probabilities. Resulting 1, 3, and 5-year-dependent ROC curves were used to evaluate nomogram performance.

2.4. Tumor-Infiltrating Immune Cells and Functional Enrichment Analysis.
Infiltration levels of distinct immune

(a)

(b)

(c)

(d)

(e)

(f)
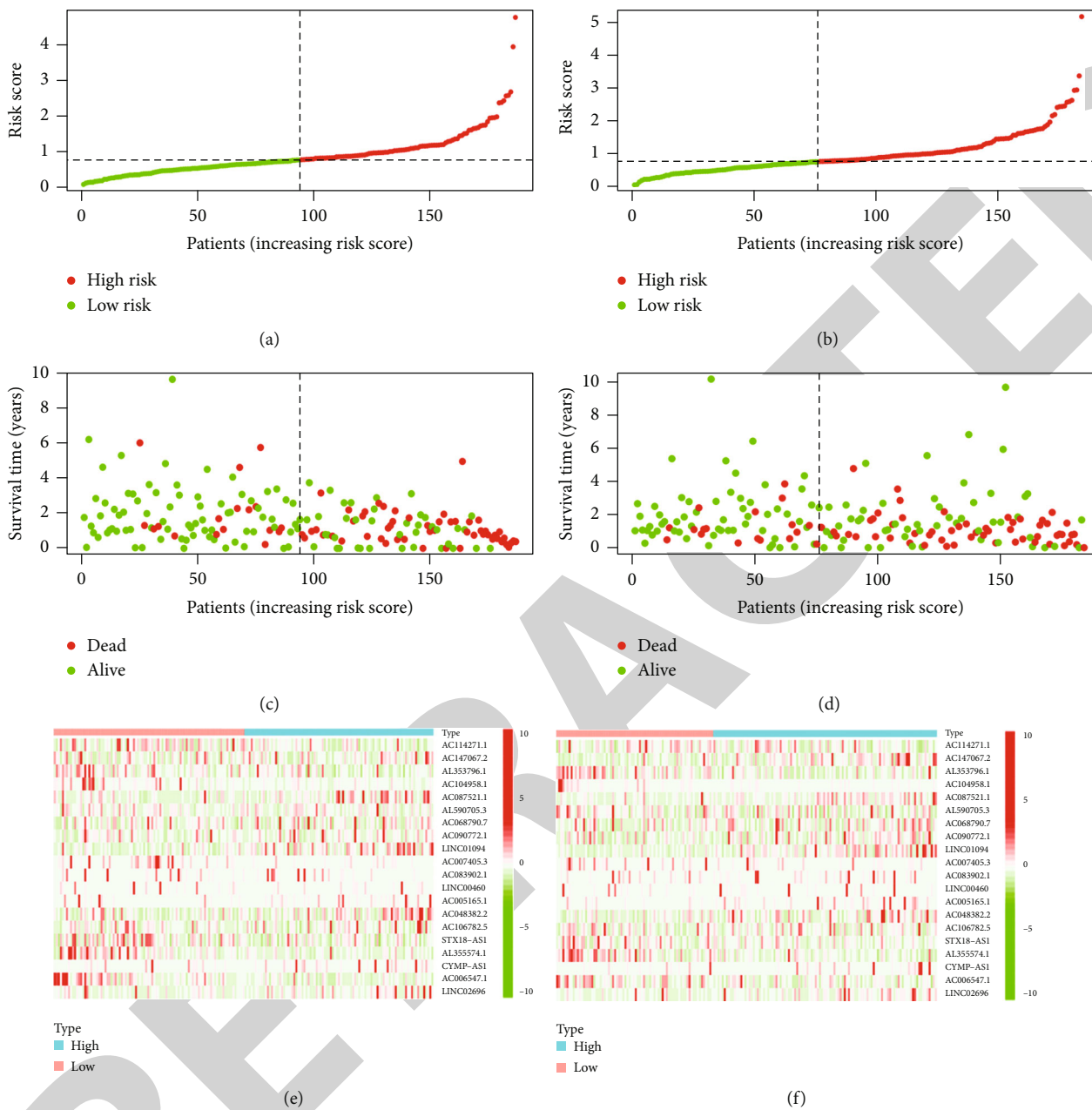
Figure 2: Continued.
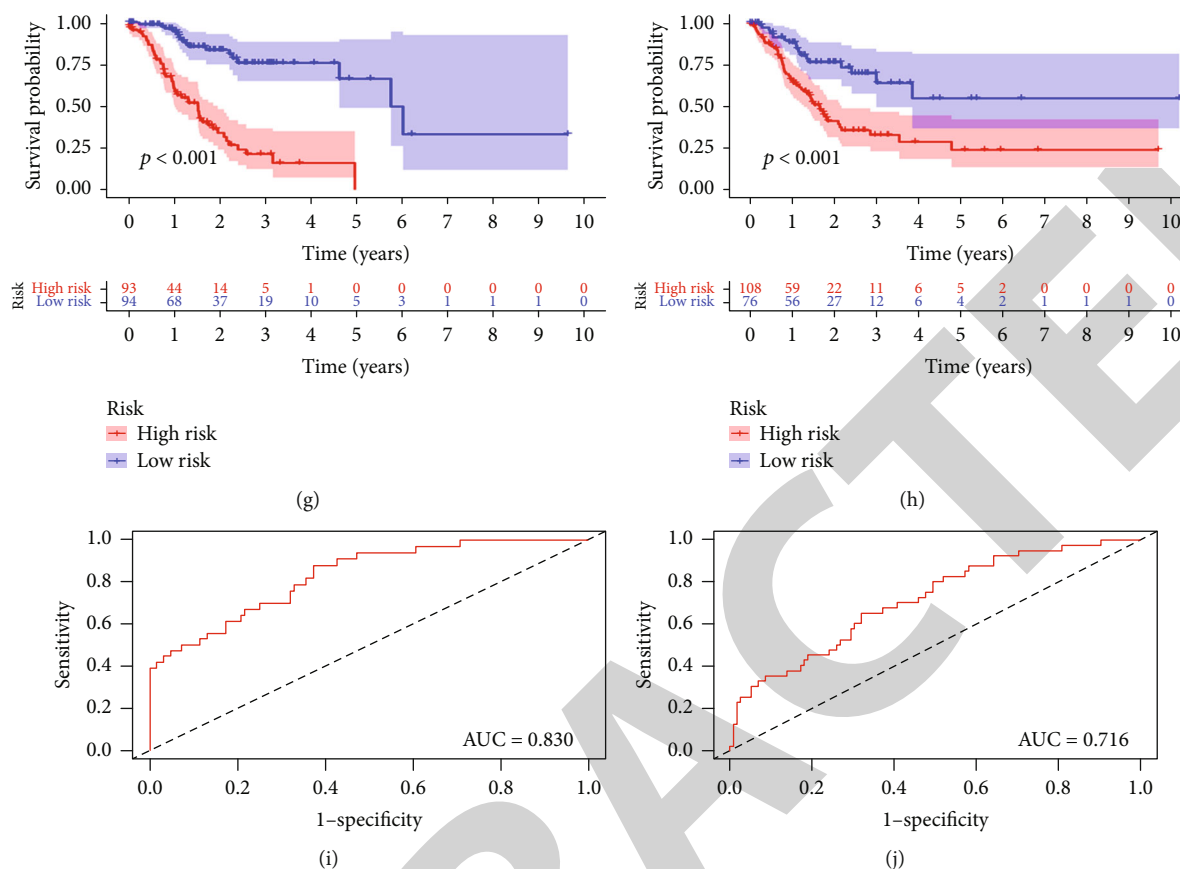
FIGURE 2: Construction and validation of a prognostic signature derived from 20 ferroptosis-related lncRNAs in the training set and the testing set. (a, b) Risk score distribution. (c, d) Overall survival status. (e, f) Heatmaps. (g, h) Kaplan-Meier curves for overall survival. (i, j) AUC values.

cells were quantified and evaluated in the low-risk group and the high-risk group using the "CIBERSORT" R package [12]. KEGG by gene set enrichment analyses was performed to explore different molecular mechanisms in high-risk and low-risk patients. A false discovery rate q value of <0.05 was considered statistically significant.

2.5. Prediction of Responses to Chemotherapy and Immunotherapy.
IC50s of common chemotherapeutics were calculated to evaluate clinical responses to gastric cancer treatment using pRRophetic [13] and ggplot2 packages in R . The Wilcoxon signed rank test was conducted. Relationships between risk score and expression levels of genes related to immune checkpoints were investigated, including PD1, PDL1, and CTLA4.

2.6. Statistical Analysis.
All statistical analyses were conducted using R statistical software version 4.0.4 and strawberry-perl-5.32.0.1. Differentially expressed lncRNAs were identified using the Benjamini-Hochberg method. Hazard ratios and a 95% confidence intervals were evaluated via univariate and multivariate Cox regression models. $p < 0.05$ was considered to indicate statistical significance.

3. Results

3.1. Identification of Prognostic Ferroptosis-Related lncRNAs in Gastric Cancer.
RNA-seq transcriptome data and matched clinical data for 32 normal gastric tissues and 371 gastric cancer tissues were downloaded from the TCGA database. A total of 259 ferroptosis-related genes were obtained from the FerrDb database (Table S1). A total of 1,378 differentially expressed ferroptosis-related lncRNAs were identified via Pearson's correlational analyses ($p < 0.01$, Spearman correlation coefficient > 0.3). Preliminary screening via univariate Cox analysis identified 95 ferroptosis-related lncRNAs that were significantly correlated with survival (Table S2).

3.2. Construction and Validation of a Ferroptosis-Related lncRNA Prognostic Signature.
A total of 371 gastric cancer samples were randomly allocated to a training set ($n = 186$) or a testing set ($n = 185$). Twenty lncRNAs were identified and used to construct a prognostic signature via least absolute contraction and selection operator (LASSO) Cox regression analysis: AC114271.1, AC147067.2, AL353796.1, AC104958.1, AC087521.1, AL590705.3, AC068790.7, AC090772.1, LINC01094, AC007405.3, AC083902.1, LINC00460, AC005165.1, AC048382.2, AC106782.5,
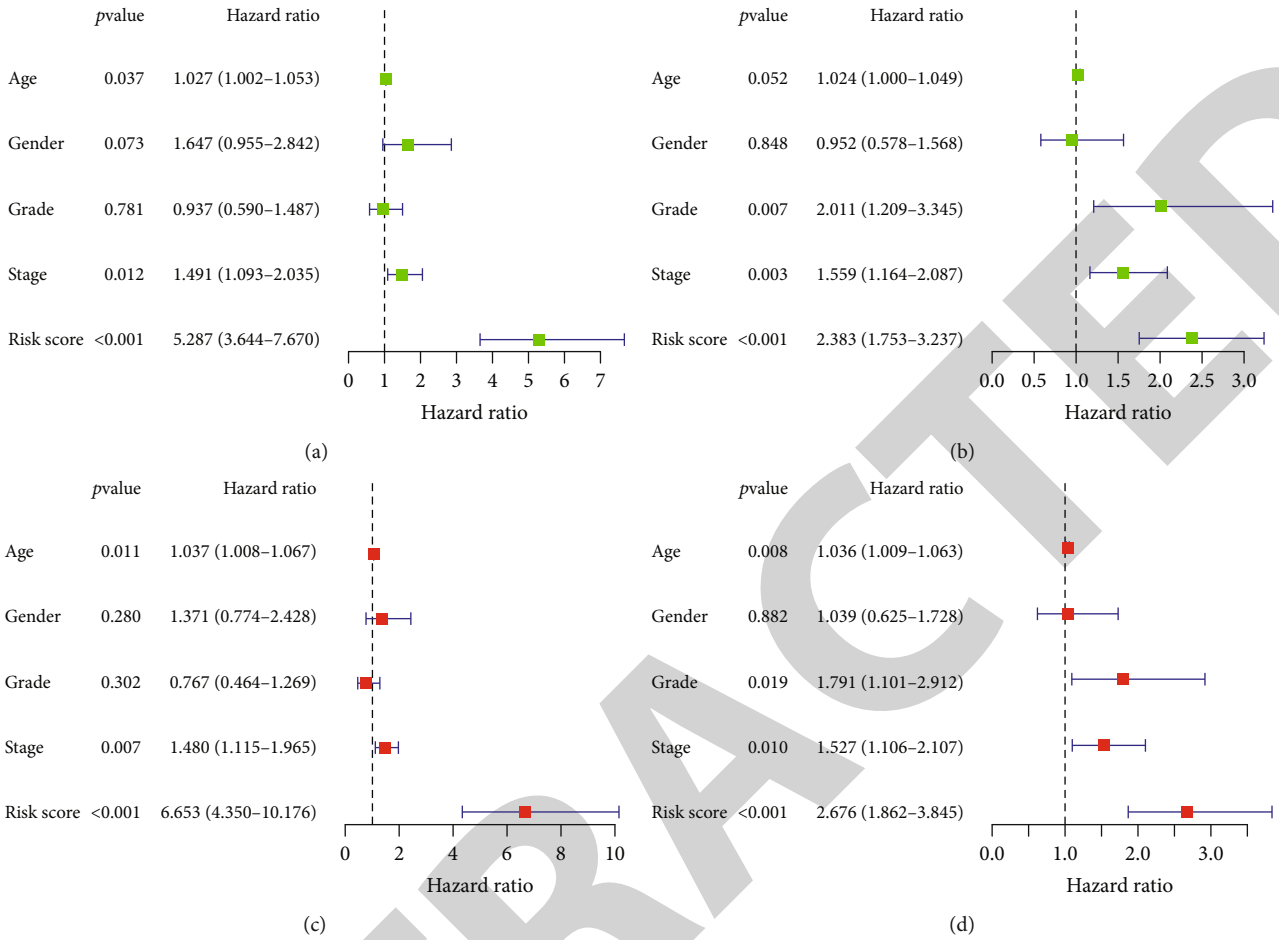
FIGURE 3: Univariate and multivariate Cox regression of prognostic factors in the training set and the testing set. (a, b) Univariate Cox regression analysis of prognostic factors. (c, d) Multivariate Cox regression analysis of prognostic factors.

STX18-AS1, AL355574.1, CYMP-AS1, AC006547.1, and LINC02696 (Figures 1(a) and 1(b)). Compared with normal gastric tissues, seven of these lncRNAs (AC114271.1, AL353796.1, AC104958.1, AC007405.3, STX18-AS1, AL355574.1, AC006547.1) were downregulated in cancer tissues, whereas the other thirteen were upregulated. The following risk score was calculated:

$-0.1331 \times \mathrm{Exp}\,(\mathrm{AC114271.1}) + 0.2263 \times \mathrm{Exp}\,(\mathrm{AC147067.2}) + -0.1447 \times \mathrm{Exp}\,(\mathrm{AL353796.1}) + -0.2940 \times \mathrm{Exp}\,(\mathrm{AC104958.1}) + 0.6273 \times \mathrm{Exp}\,(\mathrm{AC087521.1}) + 0.0391 \times \mathrm{Exp}\,(\mathrm{AL590705.3}) + 0.0877 \times \mathrm{Exp}\,(\mathrm{AC068790.7}) + 0.3460 \times \mathrm{Exp}\,(\mathrm{AC090772.1}) + 0.3227 \times \mathrm{Exp}\,(\mathrm{LINC01094}) + -0.0630 \times \mathrm{Exp}\,(\mathrm{AC007405.3}) + 0.1053 \times \mathrm{Exp}\,(\mathrm{AC083902.1}) + 0.0299 \times \mathrm{Exp}\,(\mathrm{LINC00460}) + 0.0246 \times \mathrm{Exp}\,(\mathrm{AC005165.1}) + 0.7701 \times \mathrm{Exp}\,(\mathrm{AC048382.2}) + 0.1408 \times \mathrm{Exp}\,(\mathrm{AC106782.5}) + -0.4244 \times \mathrm{Exp}\,(\mathrm{STX18-AS1}) + -0.1582 \times \mathrm{Exp}\,(\mathrm{AL355574.1}) + 0.4122 \times \mathrm{Exp}\,(\mathrm{CYMP-AS1}) + -0.5316 \times \mathrm{Exp}\,(\mathrm{AC006547.1}) + 0.8347 \times \mathrm{Exp}\,(\mathrm{LINC02696}).$

Using the median risk score as the cut-off value, patients in the training set and the testing set were divided into high-risk and low-risk groups. Distribution patterns of risk scores and survival status are shown in Figures 2(a)–2(d). The changing trends in expression levels of the 20 ferroptosis-

related lncRNAs as determined via heatmapping were concordant with their risk scores in the prognostic signature (Figures 2(e) and 2(f)). In Kaplan–Meier survival analysis, the high-risk group exhibited worse overall survival than the low-risk group in both the training set and the testing set (Figures 2(g) and 2(h)). Receiver operating characteristic (ROC) curves were plotted, and the area under the curve (AUC) values were 0.830 in the training set and 0.716 in the testing set (Figures 2(i) and 2(j)).

3.3. Associations between Prognostic Risk Score and Clinicopathological Characteristics. Univariate and multivariate Cox regression analyses were conducted in the training set and the testing set to investigate whether risk score independently predicted the prognoses of patients with gastric cancer. Univariate Cox regression stage and risk score were significantly associated with overall survival in both cohorts (Figures 3(a) and 3(b)). Multivariate Cox regression age, stage, and risk score were significant prognostic indicators in both cohorts (Figures 3(c) and 3(d)).

Associations between risk score and clinicopathological features were assessed. Overall survival was significantly longer in the low-risk group than in the high-risk group in

(a)

(b)

(c)

(d)

(e)

(f)
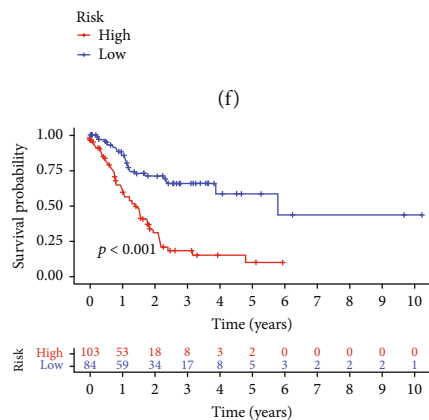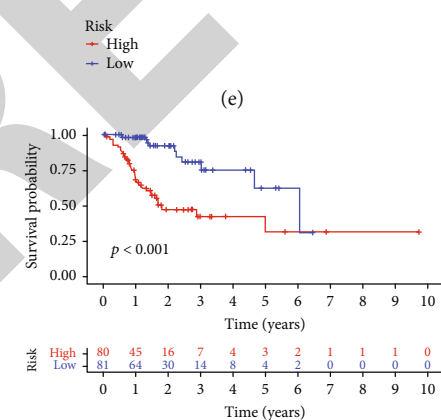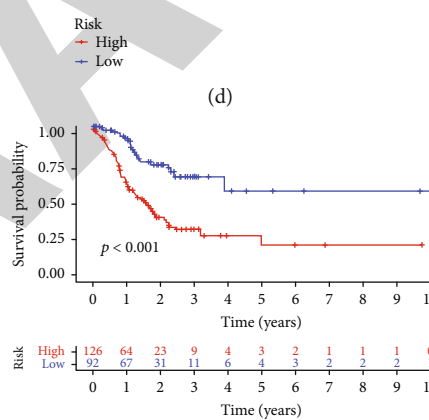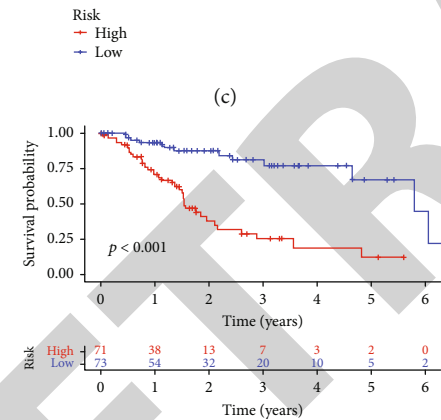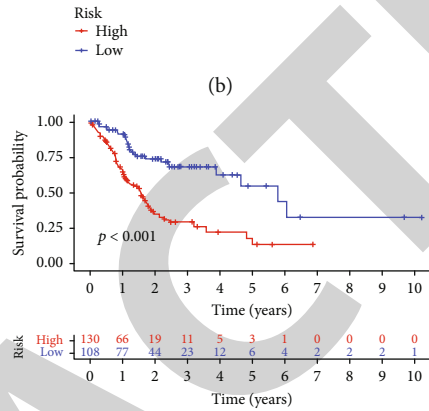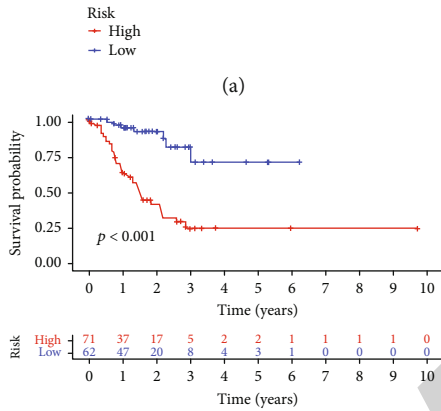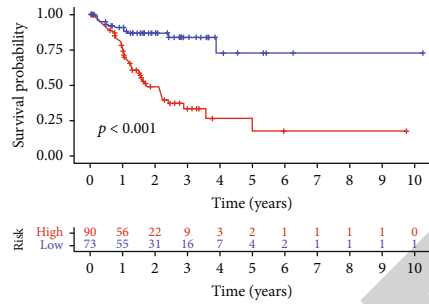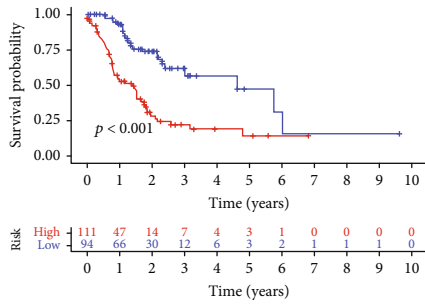
(g)

(h)

Figure 4: Continued.
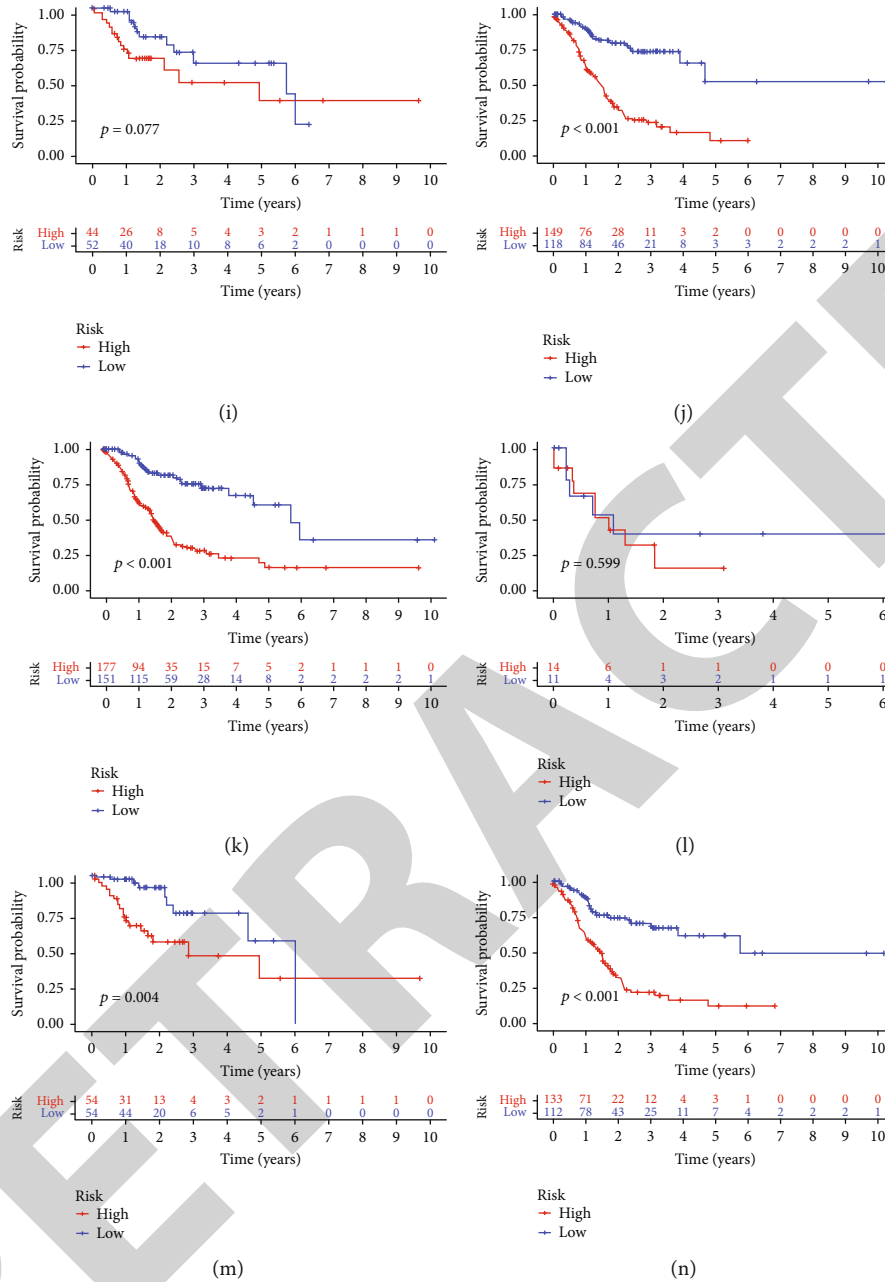
Figure 4: Kaplan-Meier plots depicting subgroup survival predicted by the prognostic signature derived from 20 ferroptosis-related lncRNAs stratified by clinical characteristics. (a, b) Patients aged >65 years and ≤65 years. (c, d) Female and male patients. (e, f) Grades 1-2 and grade 3. (g, h) Stages I-II and III-IV. (i, j) T1-2 and T3-4. (k, l) M0 and M1. (m, n) N0 and N1–3.

patients aged both >65 years and ≤65 years, in both sexes, in grades 1-2 and grade 3, in stages I-II and III-IV, and in T1-2, T3-4, M0, M1, N0, and N1–3 classifications (Figures 4(a)–4(n)). Prognostic nomograms derived from both cohorts composed of clinicopathological characteristics and risk scores were established as a quantitative and visual method for predicting 1, 3, and 5-year overall survival probability in gastric cancer patients (Figures 5(a) and 5(b)). In the training set, the respective AUC values for 1, 3, and 5-year overall survival were 0.830, 0.852, and 0.947, and in the testing set, they were 0.716, 0.724, and 0.684 (Figures 5(c) and 5(d)).

3.4. Risk Scores and Immune Cell Infiltration. To further investigate the reasons for the different prognoses in the high-risk and low-risk groups, differences in immune cell infiltration and correlations between immune cell infiltration and risk score were analyzed. Resting dendritic cells, eosinophils, monocytes, and M2 macrophages were significantly more prevalent in the high-risk group. Plasma cells and follicular helper T cells were significantly more prevalent in the low-risk group (Figure 6(a)). Numbers of resting dendritic cells, eosinophils, M2 macrophages, monocytes, and resting CD4 memory T cells were positively correlated with risk score, and numbers of follicular helper T cells were negatively correlated with risk score

(a)

(b)

(c)

(d)
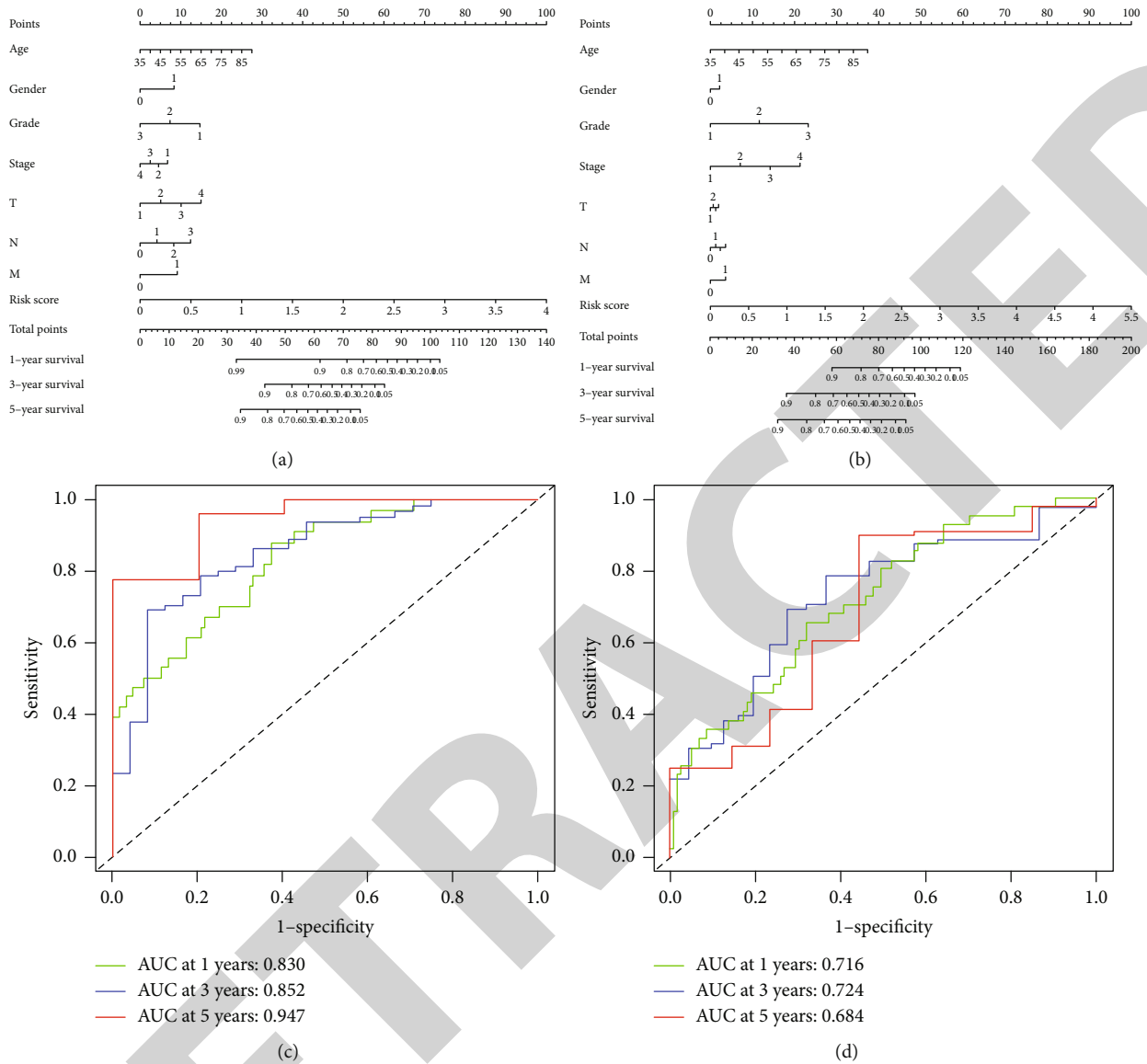
Figure 5: Nomograms and AUC values for the prognostic signature. (a, b) Nomograms based on clinical factors and risk scores in the training set and the testing set (c, d) Nomograms of AUC values for 1, 3, and 5-year survival rates in the training set and the testing set.

(Figure 6(b)). Numbers of resting dendritic cells, eosinophils, monocytes, M2 macrophages, and follicular helper T cells were strongly correlated with risk score (Figure 6(c)).

3.5. Functional Enrichment Analysis. Kyoto Encyclopedia of Genes and Genomes (KEGG) functional enrichment analyses of 20 ferroptosis-related lncRNAs were conducted to investigate differences in biological functions between the high-risk and low-risk groups (Table S3). The top five pathways enriched in the high-risk group were the hypertrophic cardiomyopathy signaling pathway, dilated cardiomyopathy signaling pathway, focal adhesion signaling pathway, extracellular matrix receptor interaction signaling pathway, and calcium signaling pathway (Figures 7(a)–7(e)). The top five pathways enriched in the low-risk group were the spliceosome signaling pathway, homologous recombination signaling pathway, oxidative phosphorylation signaling

pathway, Huntington's disease signaling pathway, and RNA polymerase signaling pathway (Figures 7(f)–7(j)).

3.6. Responses to Chemotherapy and Immunotherapy in High-Risk and Low-Risk Patients. The pRRophetic algorithm was used to predict the IC50s of cisplatin, docetaxel, and paclitaxel, which are common chemotherapeutic agents used in gastric cancer patients. There were no differences in sensitivity to the three chemotherapeutics based on risk score (Figures 8(a)–8(c)). Potential susceptibility to immune checkpoint inhibitors targeting the immune checkpoint proteins programmed cell death protein 1 (PD1), programmed death ligand 1 (PDL1), and cytotoxic T-lymphocyte-associated protein 4 (CTLA4) was also investigated in both groups. Samples from the high-risk group had higher expression of PD1 (Figure 8(d)), suggesting that high-risk patients may respond better to immune checkpoint inhibitors targeting PD1.
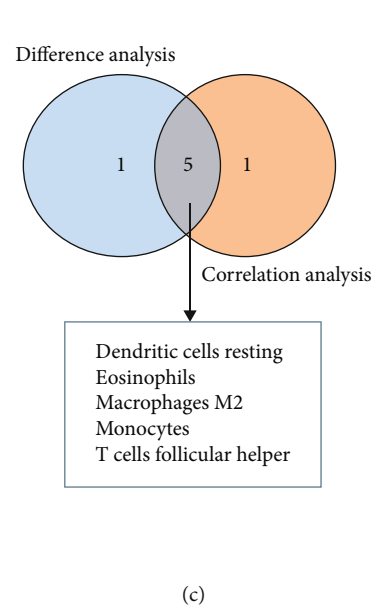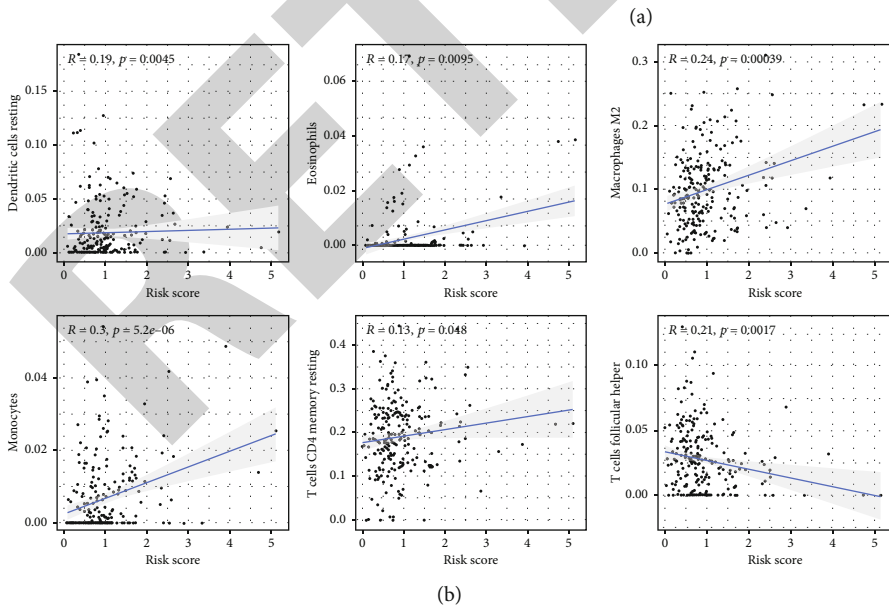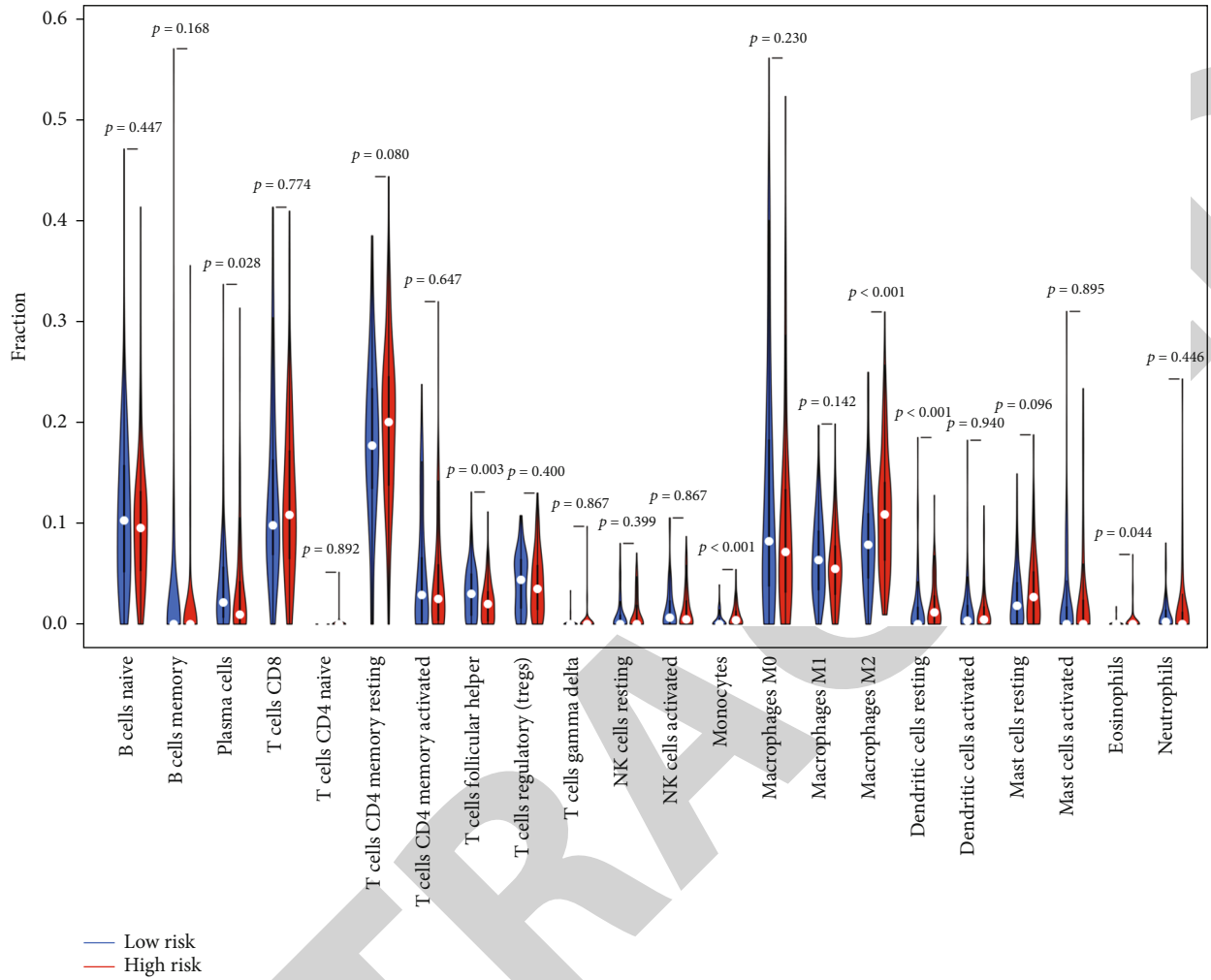
FIGURE 6: Differences in immune cell infiltration and correlations between immune cell infiltration and risk scores. (a) Differences in infiltration levels of 22 immune cell types in the high-risk and low-risk groups. (b) Correlations between risk scores and the levels of infiltration of 22 immune cell types (only significant correlations were plotted). (c) Venn diagram of immune cells based on the results of violin plots and scatter plots.
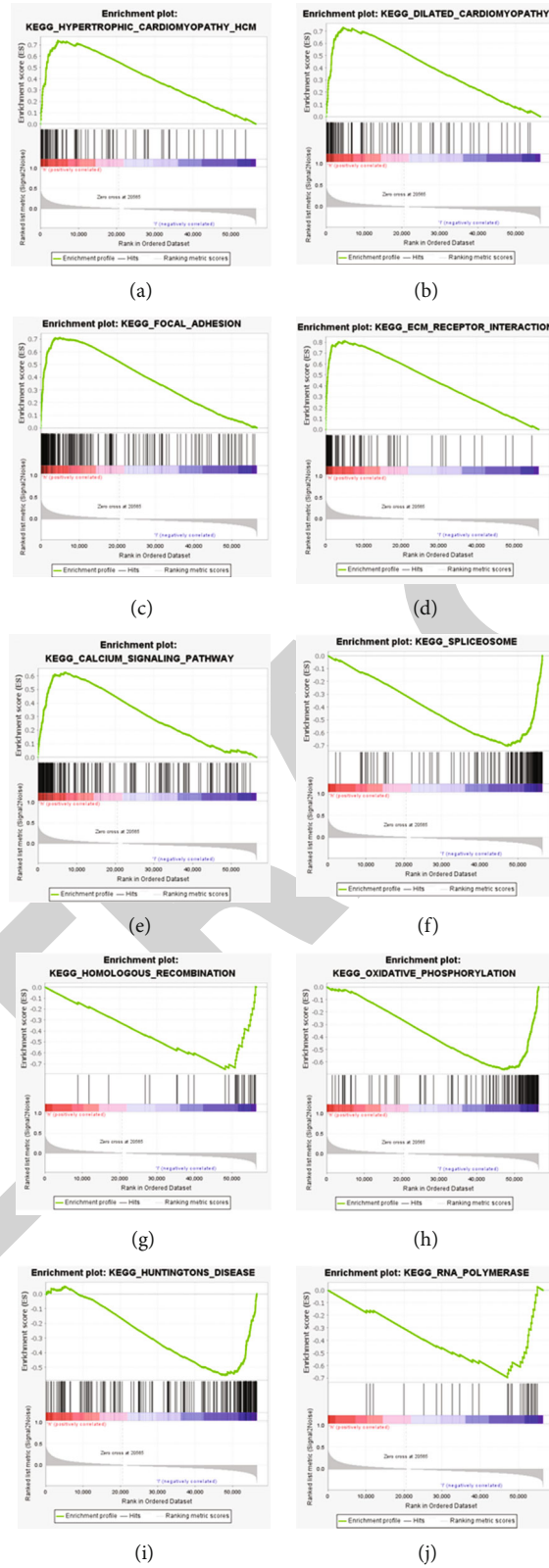
Figure 7: Distinct pathways enriched in the high-risk and low-risk groups. (a–e) Top five pathways enriched in the high-risk group. (f–j) Top five pathways enriched in the low-risk group.
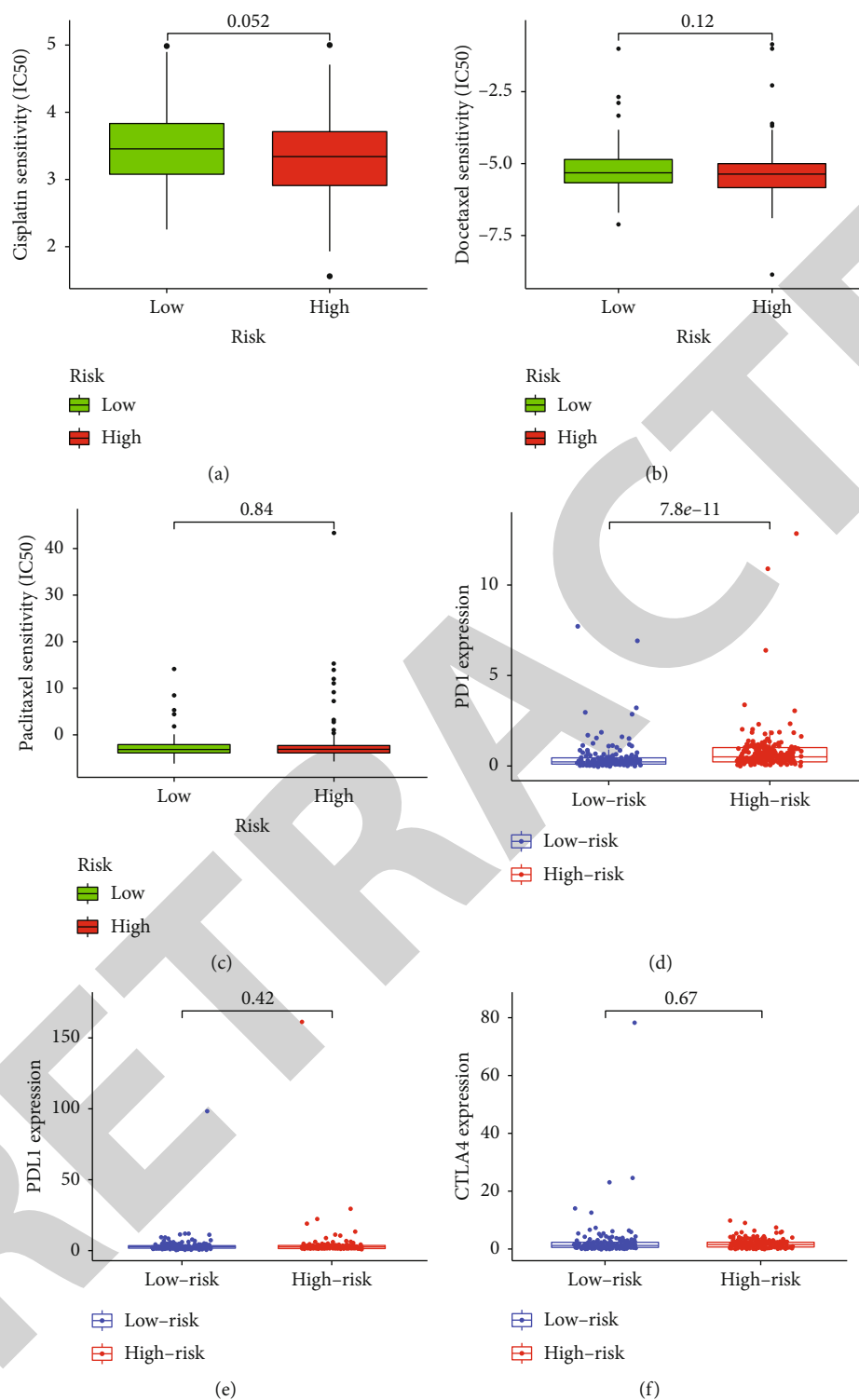
Figure 8: Correlations between risk scores and chemotherapeutic drugs and immune checkpoint inhibitors. (a) Cisplatin. (b) Docetaxel. (c) Paclitaxel. (d) PD1. (e) PDL1. (f) CTLA4.

4. Discussion

Studies indicate that ferroptosis plays important roles in biological processes associated with gastric cancer [14–19]. The circ-0008035/miR-599/EIF4A1 axis can reportedly promote gastric cancer cell proliferation and suppress apoptosis and ferroptosis [14]. Exosomal miR-522 secreted by cancer-associated fibroblasts targets ALOX15 and blocks lipid-ROS accumulation, inhibiting ferroptosis in gastric cancer cells [15]. C-Myb regulates CDO1, inhibiting erastin-induced ferroptosis in gastric cancer cells by upregulating the GPX4 expression [16]. The polyunsaturated fatty acid biosynthesis

pathway reportedly plays an essential role in ferroptosis and determines ferroptosis sensitivity in gastric cancer [17]. Guan et al. [18] reported that tanshinone IIA could induce p53 to upregulate gastric cancer cell ferroptosis. Niu et al. [19] confirmed that physcion 8-O-β-glucopyranoside stimulated gastric cancer cell ferroptosis by regulating the miR-103a-3p/GLS2 axis. Notably however, studies investigating ferroptosis-related lncRNA and the development of a prognostic tool for gastric cancer based on it are lacking.

In the current study, prognostic ferroptosis-related lncRNAs were screened via univariate Cox regression analyses, and 20 ferroptosis-related lncRNAs were identified via LASSO regression. A ferroptosis-related lncRNA prognostic signature for application in gastric cancer patients was then constructed and validated in two independent cohorts. In univariate and multivariate Cox regression analyses, the risk score was an independent prognostic indicator in gastric cancer patients. In survival and clinicopathological analyses, the signature accurately predicted prognoses and was an independent prognostic indicator in gastric cancer patients. Nomograms provided a quantitative and visual method for predicting 1, 3, and 5-year overall survival probabilities in gastric cancer patients. ROC curves indicated that the ferroptosis-related lncRNA prognostic signature was highly accurate and reliable. The roles of immune cells infiltrating the tumor microenvironment and responses to common chemotherapeutic agents and immune checkpoint inhibitors in gastric cancer patients were also investigated. The results of the study highlighted a novel biomarker and potential therapeutic target in gastric cancer.

The prognostic signature proposed in the present study was derived from 20 lncRNAs. Some of them reportedly participate in the development and occurrence of various tumors by regulating drug resistance. Meng et al. [20] demonstrated that the LINC00460-miR-149-5p/miR-150-5p-mutant p53 feedback loop could induce oxaliplatin resistance in colorectal cancer. LINC00460 promotes gefitinib resistance in non-small-cell lung cancer by targeting epidermal growth factor receptor by sponging miR-769-5p [21]. In clear cell renal cell carcinoma, LINC01094 can reportedly target the miR 577/CHEK2/FOXM1 axis, promoting radio resistance [22]. KEGG functional enrichment analyses elucidated the probable mechanisms of the high-risk group and low-risk group, but the specific mechanisms of ferroptosis-related lncRNAs in gastric cancer are fiendishly complex and still unclear, and this will be one focus of our future work. In the current study, correlations between the prognostic signature and chemotherapeutics and immune checkpoint inhibitors were analyzed. The model suggested that high risk scores were associated with sensitivity to immunotherapies such as PD1, but not associated with sensitivity to the common chemotherapeutic agent cisplatin, docetaxel, and paclitaxel. We surmised that immunotherapy is of greater benefit than chemotherapy in patients with high risk scores.

Immune cells that infiltrate tumors have diverse effects on tumor progression. In the present study, numbers of resting dendritic cells, eosinophils, monocytes, M2 macrophages, and follicular helper T cells were strongly correlated with risk score, indicating that these immune cells may play important

roles in the occurrence and progression of gastric cancer. The roles of immune cell infiltration in gastric cancer are gradually being determined. Tumor-associated macrophages reportedly participate in the progression of gastric cancer via the TGFβ2/NF-κB/Kindlin-2 axis [23]. Macrophage-derived exosomal miR-21 mediates cisplatin resistance in gastric cancer cells by downregulating PTEN, resulting in activation of the PI3K/AKT signaling pathway [24]. Eosinophils may represent a T helper 2-biased response preventing cancer development, or they may promote a T helper 1-type response leading to the progression of precancerous lesions [25]. Melanoma antigen gene-1 may regulate CCL3 and CCL20, causing recruited dendritic cells to stimulate antitumor immunity specific to gastric cancer in vivo or in vitro [26].

To the best of our knowledge, the current study is the first to construct a ferroptosis-related lncRNA-based gastric cancer prognostic signature and validate it in gastric cancer patients. Functional enrichment, immune cell infiltration, immune checkpoint inhibitors, and chemosensitivity were also analyzed. Investigating the effects of ferroptosis-related lncRNAs on tumor immune cell infiltration will contribute to a better understanding of how the tumor microenvironment is modulated and facilitate better predictions of prognoses and treatment outcomes in patients with gastric cancer. Despite its strengths, the present study had some limitations. The main datasets in the study were obtained from the TCGA database, and other datasets should be investigated using the prognostic ferroptosis-related lncRNA signature, to reduce selection bias. Additionally, the function of the signature must be validated in clinical research with larger samples.

5. Conclusions

Twenty ferroptosis-related lncRNAs associated with prognoses in gastric cancer patients were identified, the role of immune cell infiltration was systematically explored, and correlations between chemosensitivity and immune checkpoint inhibitors were assessed. The signature developed has many potential prognostic applications and may contribute to determining individual therapeutic strategies and expanding insights into therapeutic approaches in gastric cancer patients. These 20 lncRNAs can be used as the diagnostic and prognostic markers for gastric cancer.

Data Availability

All data used in the study can be downloaded from the TCGA data repository (https://gdac.broadinstitute.org/; accessed 26 February 2021) and the FerrDb database (http://www.zhounan.org/ferrdb; accessed 26 February 2021).

Conflicts of Interest

The authors declare no conflicts of interest.

Authors' Contributions

Acknowledgments

Supplementary Materials

Table S1: ferroptosis-related genes downloaded from the FerrDb database. Table S2: univariate Cox regression analysis of ferroptosis-related genes. Table S3: detailed results of gene set enrichment analyses in the high-risk group and the low-risk group. (Supplementary Materials)

References

[1] H. Sung, J. Ferlay, R. L. Siegel et al., "Global Cancer Statistics 2020: GLOBOCAN Estimates of Incidence and Mortality Worldwide for 36 Cancers in 185 Countries," *CA: A Cancer Journal for Clinicians*, vol. 71, no. 3, pp. 209–249, 2021.

[2] W. F. Anderson, C. S. Rabkin, N. Turner, J. F. Fraumeni Jr., P. S. Rosenberg, and M. C. Camargo, "The face of cancer among US Non-Hispanic Whites," *Journal of the National Cancer Institute*, vol. 110, no. 6, pp. 608–615, 2018.

[3] M. C. Camargo, W. F. Anderson, J. B. King et al., "Divergent trends for gastric cancer incidence by anatomical subsite in US adults," *Gut*, vol. 60, no. 12, pp. 1644–1649, 2011.

[4] S. J. Dixon, K. M. Lemberg, M. R. Lamprecht et al., "Ferroptosis: an iron-dependent form of nonapoptotic cell death," *Cell*, vol. 149, no. 5, pp. 1060–1072, 2012.

[5] N. Gao, Y. Li, J. Li et al., "Long non-coding RNAs: the regulatory mechanisms, research strategies, and future directions in cancers," *Frontiers in Oncology*, vol. 10, 2012.

[6] L. Statello, C. J. Guo, L. L. Chen, and M. Huarte, "Gene regulation by long non-coding RNAs and its biological functions," *Nature Reviews Molecular Cell Biology*, vol. 22, no. 2, pp. 96–118, 2021.

[7] H. Wu and A. Liu, "Long non-coding RNA NEAT1 regulates ferroptosis sensitivity in non-small-cell lung cancer," *The Journal of International Medical Research*, vol. 49, no. 3, 2021.

[8] W. Qi, Z. Li, L. Xia et al., "LncRNA GABPB1-AS1 and GABPB1 regulate oxidative stress during erastin-induced ferroptosis in HepG2 hepatocellular carcinoma cells," *Scientific Reports*, vol. 9, 2019.

[9] M. Wang, C. Mao, L. Ouyang et al., "Long noncoding RNA LINC00336 inhibits ferroptosis in lung cancer by functioning as a competing endogenous RNA," *Cell Death and Differentiation*, vol. 26, no. 11, pp. 2329–2343, 2019.

[10] C. Gai, C. Liu, X. Wu et al., "_MT1DP_ loaded by folate-modified liposomes sensitizes erastin-induced ferroptosis via regulating miR-365a-3p/NRF2 axis in non-small cell lung cancer cells," *Cell Death & Disease*, vol. 11, no. 9, p. 751, 2020.

[11] N. Zhou and J. Bao, "FerrDb: a manually curated resource for regulators and markers of ferroptosis and ferroptosis-disease associations," *Database*, vol. 2020, 2020.

[12] A. M. Newman, C. L. Liu, M. R. Green et al., "Robust enumeration of cell subsets from tissue expression profiles," *Nature Methods*, vol. 12, no. 5, pp. 453–457, 2015.

[13] P. Geeleher, N. Cox, and R. S. Huang, "pRRophetic: an R package for prediction of clinical chemotherapeutic response from tumor gene expression levels," *PLoS One*, vol. 9, no. 9, 2014.

[14] C. Li, Y. Tian, Y. Liang, and Q. Li, "Circ_0008035 contributes to cell proliferation and inhibits apoptosis and ferroptosis in gastric cancer via miR-599/EIF4A1 axis," *Cancer cell international*, vol. 20, 2020.

[15] H. Zhang, T. Deng, R. Liu et al., "CAF secreted miR-522 suppresses ferroptosis and promotes acquired chemo-resistance in gastric cancer," *Molecular cancer*, vol. 19, 2020.

[16] S. Hao, J. Yu, W. He et al., "Cysteine dioxygenase 1 mediates erastin-induced ferroptosis in human gastric cancer cells," *Neoplasia*, vol. 19, no. 12, pp. 1022–1032, 2017.

[17] J. Y. Lee, M. Nam, H. Y. Son et al., "Polyunsaturated fatty acid biosynthesis pathway determines ferroptosis sensitivity in gastric cancer," *Proceedings of the National Academy of Sciences of the United States of America*, vol. 117, no. 51, pp. 32433–32442, 2020.

[18] Z. Guan, J. Chen, X. Li, and N. Dong, "Tanshinone IIA induces ferroptosis in gastric cancer cells through p53-mediated SLC7A11 down-regulation," *Bioscience Reports*, vol. 40, no. 8, 2020.

[19] Y. Niu, J. Zhang, Y. Tong, J. Li, and B. Liu, "Physcion 8-O-β-glucopyranoside induced ferroptosis via regulating miR-103a-3p/GLS2 axis in gastric cancer," *Life sciences*, vol. 237, 2019.

[20] X. Meng, W. Sun, J. Yu et al., "LINC00460-miR-149-5p/miR-150-5p-mutant p53 feedback loop promotes oxaliplatin resistance in colorectal cancer," *Molecular Therapy Nucleic Acids*, vol. 22, pp. 1004–1015, 2020.

[21] G. Ma, J. Zhu, F. Liu, and Y. Yang, "Long noncoding RNA LINC00460 promotes the gefitinib resistance of nonsmall cell lung cancer through epidermal growth factor receptor by sponging miR-769-5p," *DNA and Cell Biology*, vol. 38, no. 2, pp. 176–183, 2018.

[22] Y. Jiang, W. Li, Y. Yan, X. Yao, W. Gu, and H. Zhang, "LINC01094 triggers radio-resistance in clear cell renal cell carcinoma via miR-577/CHEK2/FOXM1 axis," *Cancer cell international*, vol. 20, 2020.

[23] Z. Wang, Department of Gastroenterological Surgery, Peking University People's Hospital, Y. Yang et al., "Tumor-associated macrophages regulate gastric cancer cell invasion and metastasis through TGFβ2/NF-κB/Kindlin-2 axis," *Chinese Journal of Cancer Research*, vol. 32, no. 1, pp. 72–88, 2020.

[24] P. Zheng, L. Chen, X. Yuan et al., "Exosomal transfer of tumor-associated macrophage-derived miR-21 confers cisplatin

Research Article

Research on an Intelligent Lightweight-Assisted Pterygium Diagnosis Model Based on Anterior Segment Images

Bo Zheng,[1,2] **Yunfang Liu,**[3] **Kai He,**[1] **Maonian Wu,**[1,2] **Ling Jin,**[4] **Qin Jiang,**[4] **Shaojun Zhu,**[1,2] **Xiulan Hao,**[1,2] **Chenghu Wang** ⓘ**,**[4] **and Weihua Yang** ⓘ[4]

[1]*School of Information Engineering, Huzhou University, Huzhou 313000, China*
[2]*Zhejiang Province Key Laboratory of Smart Management & Application of Modern Agricultural Resources, Huzhou University, Huzhou 313000, China*
[3]*The First People's Hospital of Huzhou, Huzhou313000, China*
[4]*The Affiliated Eye Hospital of Nanjing Medical University, Nanjing 210029, China*

Correspondence should be addressed to Chenghu Wang; wangchenghu1226@163.com and Weihua Yang; benben0606@139.com

Aims. The lack of primary ophthalmologists in China results in the inability of basic-level hospitals to diagnose pterygium patients. To solve this problem, an intelligent-assisted lightweight pterygium diagnosis model based on anterior segment images is proposed in this study. *Methods*. Pterygium is a common and frequently occurring disease in ophthalmology, and fibrous tissue hyperplasia is both a diagnostic biomarker and a surgical biomarker. The model diagnosed pterygium based on biomarkers of pterygium. First, a total of 436 anterior segment images were collected; then, two intelligent-assisted lightweight pterygium diagnosis models (MobileNet 1 and MobileNet 2) based on raw data and augmented data were trained via transfer learning. The results of the lightweight models were compared with the clinical results. The classic models (AlexNet, VGG16 and ResNet18) were also used for training and testing, and their results were compared with the lightweight models. A total of 188 anterior segment images were used for testing. Sensitivity, specificity, F1-score, accuracy, kappa, area under the concentration-time curve (AUC), 95% CI, size, and parameters are the evaluation indicators in this study. *Results*. There are 188 anterior segment images that were used for testing the five intelligent-assisted pterygium diagnosis models. The overall evaluation index for the MobileNet2 model was the best. The sensitivity, specificity, F1-score, and AUC of the MobileNet2 model for the normal anterior segment image diagnosis were 96.72%, 98.43%, 96.72%, and 0976, respectively; for the pterygium observation period anterior segment image diagnosis, the sensitivity, specificity, F1-score, and AUC were 83.7%, 90.48%, 82.54%, and 0.872, respectively; for the surgery period anterior segment image diagnosis, the sensitivity, specificity, F1-score, and AUC were 84.62%, 93.50%, 85.94%, and 0.891, respectively. The kappa value of the MobileNet2 model was 77.64%, the accuracy was 85.11%, the model size was 13.5 M, and the parameter size was 4.2 M. *Conclusion*. This study used deep learning methods to propose a three-category intelligent lightweight-assisted pterygium diagnosis model. The developed model can be used to screen patients for pterygium problems initially, provide reasonable suggestions, and provide timely referrals. It can help primary doctors improve pterygium diagnoses, confer social benefits, and lay the foundation for future models to be embedded in mobile devices.

1. Introduction

Pterygium is a common and frequently occurring disease in ophthalmology. It is the degeneration and growth of conjunctival fibrovascular tissue on the cornea, which usually leads to astigmatism and dry eyes. Covering the pupil area can cause a significant decrease in vision. The main treat-ment is surgical resection [1]. Pterygium can usually be diagnosed by anterior segment images [1]. Anterior segment images are taken with a slit lamp digital microscope and obtained by the diffuse illumination method at a magnification of 10x. Professional ophthalmologists often diagnose ocular surface diseases by viewing the anterior segment images. At present, the incidence of pterygium disease in

China is 9.84% [2], and there are few professional ophthalmologists in county-level and lower hospitals and community hospitals and other basic-level hospitals. Therefore, it is difficult for the basic-level hospitals to meet the needs of the huge number of pterygium patients. The problem was to be solved; an intelligent lightweight-assisted diagnosis model based on anterior segment images is proposed in the study. The model can help nonprofessional ophthalmologists in the primary hospital to make preliminary diagnoses of pterygium patients and help them obtain pterygium grading (three types of normal, observation, and surgery) to get an accurate referral. The model can also be embedded in mobile phones to assist users in self-screening. Some primary doctors may not provide effective services to pterygium patients, and this model can help to solve the problem.

The combination of ophthalmology and artificial intelligence (AI) has become closer with the development of AI [3–9]. In 2016, a deep learning model was proposed by the Google team; it can diagnose DR automatically through fundus images [10]. Deep learning models have been used by lots of researchers to diagnose DR [11–14] since then. In addition to DR, researchers have used deep learning methods to detect common fundus diseases, including glaucoma [15–17], retinal vein occlusion [18, 19], age-related macular degeneration [20–22], and even research on the classification of multiple common fundus diseases [23]. These studies obtained good results.

There are many studies on the diagnosis of fundus-related diseases using deep learning methods but relatively few studies on ocular surface diseases. Pterygium is a common disease on the ocular surface. AI research on pterygium is mainly pterygium detection. Traditional learning methods mainly extract the pterygium characteristics in anterior segment images to detect pterygium. Related researchers have used the adaptive nonlinear enhancement method, SVM, to segment pterygium tissue to detect pterygium [24–26]. In recent years, researchers such as Mohd Asyraf Zulkifley have used neural networks, DeepLab V2, and other deep learning methods to detect and segment pterygium [27–29]; researchers such as Zamani et al. have used a variety of deep learning models to perform two-class detection of pterygium [30]. Existing research on pterygium detection is mostly based on the two-class detection of pterygium based on anterior segment images. It has not been further determined whether the pterygium is operated on, which cannot meet the needs of precision medicine. The deep learning models used for detecting pterygium are currently mostly classic; the excessive number of parameters requires considerable space and cannot be used on mobile terminals or low-configuration devices.

An intelligent lightweight-assisted pterygium diagnosis model is designed by using transfer learning in this study. The model detects normal images, pterygium observation periods, and pterygium surgery periods from anterior segment images. Comparative research with classic models is carried out simultaneously and reported as follows.

2. Materials and Methods

2.1. Data Source.
The Affiliated Eye Hospital of Nanjing Medical University provided anterior segment images for this study. The images were obtained from two models of slit lamp digital microscopy. In this study, 436 anterior segment images were used to train an intelligent lightweight-assisted pterygium diagnosis model. The dataset consists of 142, 144, and 150 anterior segment images for the normal, pterygium observation period, and pterygium surgery period, respectively. There were 188 images for model testing, which consisted of 61, 62, and 65 anterior segment images for the normal condition, pterygium observation period, and pterygium surgery period, respectively. The patients' gender and age were not restricted when selecting the images. The personal information of patient-related was all removed from the images to avoid infringing on patient privacy.

In this study, the images selected had high quality. Thus, ophthalmologists can easily diagnose whether the image shows a normal anterior segment or pterygium. The anterior segment images were either normal or showed pterygium. The image selected was diagnosed only as normal, pterygium observation period, or pterygium surgery period. The marking standard was [31] as follows. The normal anterior segment image is characterized by no obvious conjunctival hyperemia or proliferation, and the cornea is transparent; the anterior segment image of the pterygium observation period is characterized by the horizontal length of the pterygium head tissue invading the limbus of the cornea <3 mm; the anterior segment image of the pterygium surgery period is characterized by the horizontal length of the pterygium head tissue invading the limbus of the cornea ≥3 mm. The three types of anterior segment images were shown in Figure 1. There were two professional ophthalmologists who diagnosed the anterior segment images independently. If the diagnostic results of two ophthalmologists were identical, the final clinical diagnosis result was achieved. If the diagnostic results of two ophthalmologists were different, the final clinical diagnostic result was given by an expert ophthalmologist.

Figure 1(a) is the normal anterior segment image; Figure 1(b) is the pterygium observation period anterior segment image; Figure 1(c) is the pterygium surgery period anterior segment image.

2.2. Data Augmentation.
The quantity of training data was too small. Therefore, the original images were augmented by flipping and rotating the original image. First, the original image was flipped horizontally, and then, the original image and the horizontally flipped image were rotated clockwise and counterclockwise by 1° and 2°, respectively, so that the augmented image maintained the original medical characteristics. An original image and its augmented image are shown in Figure 2.

2.3. Lightweight Model Training.
The study uses a MobileNet [32] model; the initial parameters used in the model were pretrained on the ImageNet Large Scale Visual Recognition Challenge (ILSVRC) [33] dataset. A total of 436 original anterior segment images and 4,360 augmented anterior segment images were used to train two intelligent lightweight assisted diagnosis models for detecting pterygium grading.
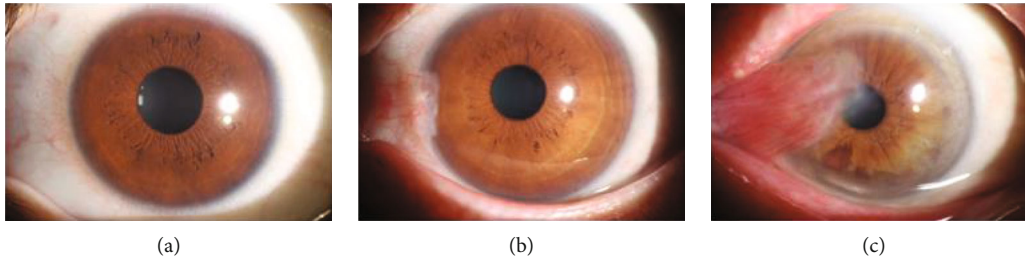
FIGURE 1: Three types of anterior segment images.

The network structure is not changed, and only the final output is changed to 3 categories in the transfer learning process.

MobileNet is a lightweight model designed specifically for mobile and embedded terminals. This study focuses on the transfer learning of the MobileNet model with an inverted residual structure. Its basic network structure mainly includes convolutional layers, bottleneck layers, and an average pooling layer. The structure of the bottleneck layers is shown in Figure 3 [32], it usually includes pointwise convolution and depthwise convolution; when the stride is 1, the input is added to the output. The structure of MobileNet 2 is shown in [32].

In this study, a total of 436 original anterior segment images and 4,360 augmented anterior segment images were selected to train the two lightweight models. The images input to the two lightweight models were 224×224. Intelligent lightweight-assisted diagnosis models were obtained after training.

2.4. Classic Model Training. AlexNet [34], VGG16 [35], and ResNet18 [36] are three classic deep learning classification models. This study used 4,360 augmented anterior segment images to train three intelligent classic-assisted diagnosis models for detecting pterygium grading. The network structure of the three models with their initial parameters pretrained on the ILSVRC [33] dataset was used. The network structure is not changed, and only the final output is changed to 3 categories in the transfer learning process. The images input to the three models were 224×224. Intelligent-assisted diagnosis models were obtained after training. The results of the three models were compared to the lightweight models.

The server was used to train and test the five models. A computer was also used to test the five models because the basic hospitals usually do not have servers. The hardware configuration of the server used in this study is Intel (R) Xeon (R) Gold 5118 CPU, the main frequency is 2.3 GHz, the graphics card is Tesla V100, the video memory is 32 GB, and the operating system is Ubuntu 18.04. The hardware configuration of the computer used in this study is Intel (R) Core (TM) i5-4200M CPU, the main frequency is 2.5, the augmentation method is GHz, NVIDIA GeForce GT 720M x, the video memory is 1 GB, and the operating system is windows10.

2.5. Statistical Analysis. The SPSS 22.0 statistical software was used to analyze the results. The accuracy, size and parameters

Original image | Horizontally flipped image

Rotated counterclockwise by 1° of a | Rotated counterclockwise by 1° of b

Rotated clockwise by 1° of a | Rotated clockwise by 1° of b

Rotated counterclockwise by 2° of b | Rotated counterclockwise by 2° of b

Rotated clockwise by 2° of a | Rotated clockwise by 2° of b

(a) (b)
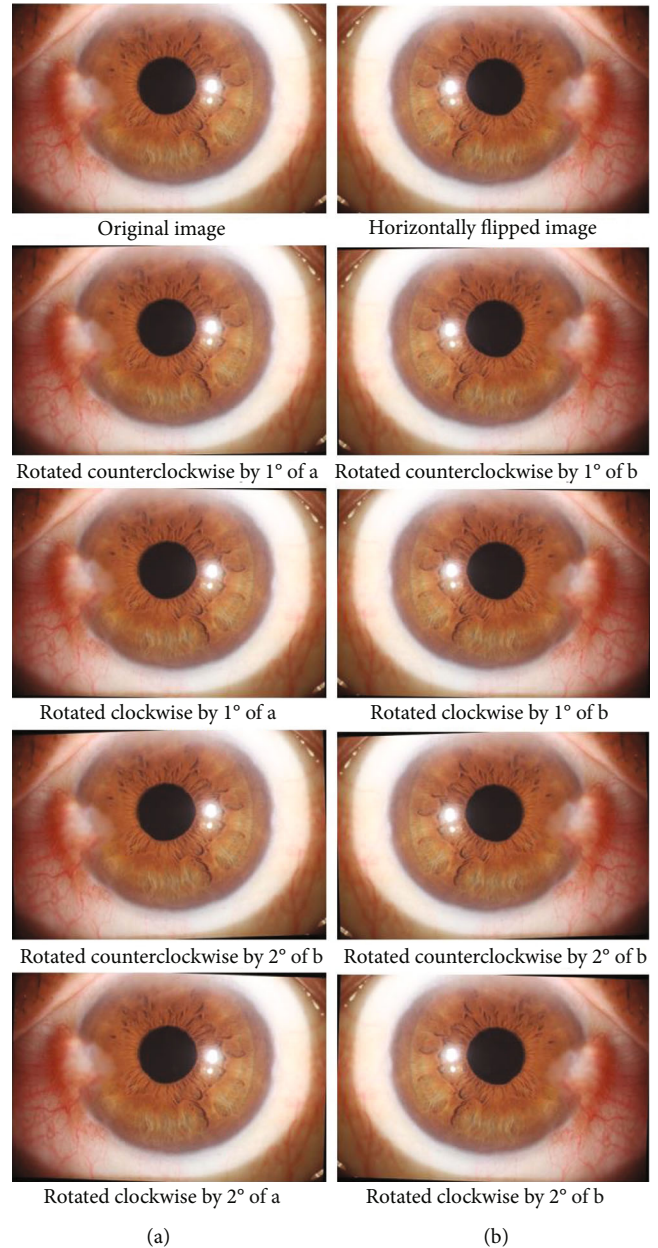
FIGURE 2: Original image and its augmented images.

of models, time, sensitivity, specificity, F1-score, and AUC for the pterygium diagnostic models were calculated for the normal anterior segment image, pterygium observation
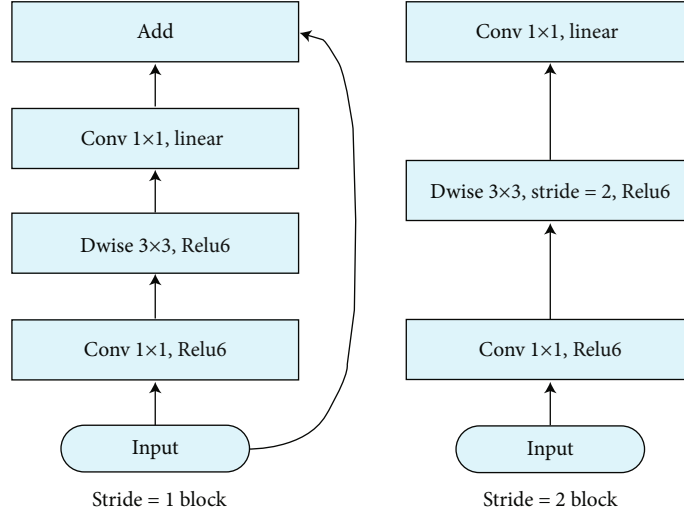
FIGURE 3: Bottleneck structure.

TABLE 1: Diagnostic results of MobileNet 1 (original data).

Clinical	MobileNet diagnosis (original data)			
	Normal	Observe	Surgery	Total
Normal	59	2	0	61
Observe	4	45	13	62
Surgery	1	8	56	65
Total	64	55	69	188

TABLE 2: Diagnostic results of MobileNet 1 (augmented data).

Clinical	MobileNet diagnosis (augmented data)			
	Normal	Observe	Surgery	Total
Normal	59	2	0	61
Observe	2	52	8	62
Surgery	0	10	55	65
Total	61	64	63	188

period anterior segment image, and surgery period anterior segment image; then, ROC curves were plotted. The consistency between the expert and the model was evaluated by kappa value.

3. Results

A total of 188 anterior segment images were used to test the intelligent lightweight-assisted pterygium diagnosis models based on original data (MobileNet 1) and augmented data (MobileNet 2) for pterygium. The expert diagnosed 61 images as normal anterior segment, 62 as pterygium observation period, and 65 as pterygium surgery period. MobileNet 1 diagnosed 64 images as normal anterior segment, 55 as pterygium observation period, and 69 as pterygium surgery period. MobileNet 2 diagnosed 61 images as normal anterior segment, 64 as pterygium observation period, and 63 as pterygium surgery period. The two models' diagnostic results are shown in Tables 1 and 2.

A total of 188 anterior segment images were used to test the three classic intelligent-assisted pterygium diagnosis models (AlexNet, VGG16, ResNet18) based on augmented data (MobileNet 2) for pterygium. The three models' diagnostic results were compared with MobileNet 1 and MobileNet 2. Compared with the results of expert diagnosed, except for ResNet18, the sensitivity of the other four models for diagnosing the anterior segment image as normal was above 90%, the sensitivity of diagnosing the anterior segment image

as pterygium observation period was up to 83.87% (AlexNet and MobileNet2), and the highest sensitivity of diagnosing the anterior segment image as pterygium surgery period was 86.15% (MobileNet1). The specificities of the five models for diagnosing anterior segment images as normal, pterygium observation period, and pterygium surgery period were mostly above 85%. Among them, the specificities of MobileNet 2 for diagnosing anterior segment images as the three grades were all above 90%, which showed that the models' misdiagnosis rates were low. The AUC values of MobileNet 2 for diagnosing anterior segment images as normal, pterygium observation period, and pterygium surgery period were the highest among the five models, which were 0.976, 0.872, and 0.891, respectively. The five models' evaluation results are compared in Table 3.

In Table 3, the sizes and parameters of the five models are compared. MobileNet 1 and MobileNet 2 had the smallest sizes and parameters among them, 13.5 M and 4.2 M, respectively. VGG16 had the largest size and parameters, 527 M and 138 M, respectively. As shown in Table 3, MobileNet 2 had the smallest space and the least number of parameters, and the evaluation indicators, such as sensitivity, specificity, F1-score, AUC, kappa value, and accuracy rate, still had good results. The AUC, kappa value, accuracy, and test time were the best among the 5 models. The five models' ROC curves of diagnosing the anterior segment image as normal, pterygium observation period, and pterygium surgery period are compared in Figure 4.

Table 3: The five models' evaluation results.

Model	Evaluation indicators	Normal	Observe	Surgery
	Sensitivity	96.72%	72.58%	86.15%
	Specificity	96.06%	92.06%	89.43%
	F1-score	94.40%	76.92%	83.58%
	AUC	0.964	0.823	0.878
	95% CI	0.931-0.996	0.751-0.895	0.820-0.936
MobileNet (original data)	Kappa		77.64%	
	Accuracy		85.11%	
	Size (MB)		13.5	
	Parameters (million)		4.2	
	Time-S (ms)		5.86	
	Time-C (ms)		473.37	
	Sensitivity	96.72%	83.87%	84.62%
	Specificity	98.43%	90.48%	93.50%
	F1-score	96.72%	82.54%	85.94%
	AUC	0.976	0.872	0.891
	95% CI	0.947-1	0.811-0.933	0.833-0.948
MobileNet (augmented data)	Kappa		82.44%	
	Accuracy		88.30%	
	Size (MB)		13.5	
	Parameters (million)		4.2	
	Time-S (ms)		5.75	
	Time-C (ms)		465.53	
	Sensitivity	91.80%	83.87%	84.62%
	Specificity	98.43%	88.10%	77.61%
	F1-score	94.12%	80.62%	85.94%
	AUC	0.951	0.860	0.891
	95% CI	0.909-0.993	0.797-0.922	0.833-0.948
AlexNet	Kappa		80.05%	
	Accuracy		86.70%	
	Size (MB)		233	
	Parameters (million)		60	
	Time-S (ms)		1.06	
	Time-C (ms)		64.63	
	Sensitivity	96.72%	79.03%	67.69%
	Specificity	92.13%	81.75%	97.56%
	F1-score	90.77%	73.13%	78.57%
	AUC	0.944	0.804	0.826
	95% CI	0.907-0.982	0.733-0.874	0.754-0.899
VGG16	Kappa		71.34%	
	Accuracy		80.85%	
	Size (MB)		527	
	Parameters (million)		138	
	Time-S (ms)		1.72	
	Time-C (ms)		1020.11	

TABLE 3: Continued.

Model	Evaluation indicators	Normal	Observe	Surgery
	Sensitivity	81.97%	66.13%	75.38%
	Specificity	95.28%	81.75%	84.55%
	F1-score	85.47%	65.08%	73.68%
	AUC	0.886	0.739	0.800
	95% CI	0.825-0.947	0.660-0.819	0.728-0.871
ResNet18	Kappa		61.67%	
	Accuracy		74.47%	
	Size (MB)		44.6	
	Parameters (million)		33	
	Time-S (ms)		2.53	
	Time-C (ms)		170.88	
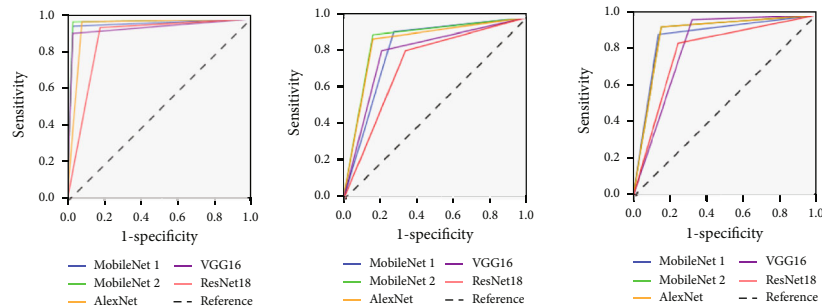
FIGURE 4: ROC of the five models for normal, pterygium observation period, and surgery period.

Time-S means the time of testing one image based on server; time-C means the time of testing one image based on the computer.

4. Discussion

Pterygium is a common ocular surface disease that can cause vision loss and affect appearance. It has a higher incidence among people working outdoors in rural and remote areas (such as fishermen and farmers). For vast rural and remote areas that lack professional medical resources for ophthalmology, the intelligent-assisted diagnosis model can provide a convenient method for screening pterygium for local patients. It can avoid the rush of patients to go to county hospitals or prefectural hospitals and reduce their financial burden. Additionally, the model further provides treatment suggestions to facilitate the referral of patients in need of surgery at the basic-level hospital; it can also reasonably allocate medical resources.

In 2012, the AlexNet model [34] won the championship of the classification in the ILSVRC competition. The network structure of the AlexNet model has 7 layers, while the network structure of the VGG model [35] has up to 19 layers and researchers often use VGG 16, which has 16 layers. The ResNet model [36] has up to 152 layers, but researchers often use ResNet 18 and ResNet 50. The network structures of the models almost are deep, so it is suitable for the extraction of more complex image features. The above models are classic and occupy a large amount of space and have many parameters. The MobileNet model is a lightweight model. The depth of the separable convolution kernel and linear bottleneck was used to reduce the number of parameters so that the model occupies a small space. The complexity of the anterior segment image is relatively low, so AlexNet obtained better results than the three classic models. MobileNet is further simplified based on the classic model and obtained the best diagnosis results among these models.

MobileNet2 had the best overall diagnosis results among the 5 models, but its sensitivity for diagnosing the pterygium observation period and pterygium surgery period was only 83.87% and 84.62%, respectively. The sensitivity was low because the number of the training samples was only 436. Although the images were augmented by 10 times, the augmented images were more similar to the original image. The effect improved, but the improvement was small.

As shown in Table 2, the MobileNet 2 model did not diagnose the pterygium surgery period images as normal images. Only pterygium observation periods were diagnosed as normal images. Most of the other errors were diagnosed between the pterygium observation period and pterygium surgery period. Patients diagnosed during the pterygium observation period and pterygium surgery period were recommended to go to the superior hospital for further confirmation, and the correct diagnosis was obtained after referral. Since the pterygium observation period images were diagnosed as normal anterior segment images, the model

asked the user to diagnose again after obtaining the diagnosis result of the normal anterior segment image or asked the user whether to upload the image to the doctor. If the user had doubts about the diagnosis result, the user could upload the image, and a doctor confirmed the diagnosis result.

In this study, the parameters of the MobileNet lightweight model were only 4.2 M, and the model size was 13.5 M, which was suitable for embedding in mobile devices and offline operation of embedded devices. Users of basic-level medical institutions can take photos of the anterior segment through the camera so that the device and the local medical computer can be simultaneously diagnosed. Therefore, pterygium screening can be performed at the basic-level hospital. The training images of the MobileNet2 model were obtained from the slit lamp digital microscope, which has a certain gap with the anterior segment images taken by the mobile device camera. In the future, more images of the anterior segment taken by the mobile device camera will be collected to improve the model and make the model more suitable for mobile applications. People in the vast rural areas and remote mountainous areas of China have difficulty seeing a doctor. Mobile devices can realize self-screening, which is convenient for users to pay attention to their ocular surface health at any time.

5. Conclusion

This study used deep learning methods to propose a three-category intelligent lightweight-assisted pterygium diagnosis model, MobileNet, based on amplified data. Its results were compared with three classic deep learning models (AlexNet, VGG16, and ResNet18). The MobileNet 2 model had the fewest parameters, and its overall evaluation index results were the best. This model can be used on low-configuration computers at basic-level hospitals, and it can help primary doctors preliminarily screen pterygium problems in patients through anterior segment images. It can also provide suitable recommendations and timely referrals, improve the diagnosis level of primary ophthalmology, and obtain good social benefits. Additionally, the small size and few parameters of the lightweight model lay the foundation for future models to be embedded in mobile devices so that it is convenient for mobile users to screen themselves for pterygium problems.

Data Availability

The datasets used and/or analysed during the present study are available from the corresponding author on reasonable request.

Conflicts of Interest

All the authors declare that there is no conflict of interest about the publication of this article.

Authors' Contributions

Bo Zheng and Yunfang Liu contributed equally to this study.

Acknowledgments

References

[1] X. Wu, M. Li, and F. Xu, "Research progress of treatment techniques for pterygium," *Recent Advances in Ophthalmology*, vol. 41, no. 3, pp. 296–300, 2021.

[2] H. Ren, X. Li, and Y. Cai, "Current status and prospect of individualized clinical treatment of pterygium," *Yan Ke Xue Bao*, vol. 35, no. 4, pp. 255–261, 2020.

[3] R. Poplin, A. V. Varadarajan, K. Blumer et al., "Prediction of cardiovascular risk factors from retinal fundus photographs via deep learning," *Nature Biomedical Engineering*, vol. 2, no. 3, pp. 158–164, 2018.

[4] Y. Peng, S. Dharssi, Q. Chen et al., "DeepSeeNet: A Deep Learning Model for Automated Classification of Patient-based Age-related Macular Degeneration Severity from Color Fundus Photographs," *Ophthalmology*, vol. 126, no. 4, 2019.

[5] M. Rohm, V. Tresp, M. Müller et al., "Predicting visual acuity by using machine learning in patients treated for neovascular age-related macular degeneration," *Ophthalmology*, vol. 125, no. 7, pp. 1028–1036, 2018.

[6] W. H. Yang, B. Zheng, M. N. Wu et al., "An evaluation system of fundus photograph-based intelligent diagnostic technology for diabetic retinopathy and applicability for research," *Diabetes Therapy*, vol. 10, no. 5, pp. 1811–1822, 2019.

[7] J. Xu, C. Wan, W. Yang et al., "A novel multi-modal fundus image fusion method for guiding the laser surgery of central serous chorioretinopathy," *Mathematical Biosciences and Engineering*, vol. 18, no. 4, pp. 4797–4816, 2021.

[8] Q. Dai, X. Liu, X. Lin et al., "A novel meibomian gland morphology analytic system based on a convolutional neural network," *IEEE Access*, vol. 9, no. 1, pp. 23083–23094, 2021.

[9] H. Zhang, K. Niu, Y. Xiong, W. Yang, Z. Q. He, and H. Song, "Automatic cataract grading methods based on deep learning," *Computer methods and programs in biomedicine*, vol. 182, p. 104978, 2019.

[10] V. Gulshan, L. Peng, M. Coram et al., "Development and validation of a deep learning algorithm for detection of diabetic retinopathy in retinal fundus photographs," *JAMA*, vol. 316, no. 22, pp. 2402–2410, 2016.

[11] R. Raman, S. Srinivasan, S. Virmani, S. Sivaprasad, C. Rao, and R. Rajalakshmi, "Fundus photograph-based deep learning algorithms in detecting diabetic retinopathy," *Eye (London, England)*, vol. 33, no. 1, pp. 97–109, 2019.

[12] S. Kermany, M. Goldbaum, W. Cai et al., "Identifying medical diagnoses and treatable diseases by image-based deep learning," *Cell*, vol. 172, no. 5, pp. 1122–1131.e9, 2018.

[13] M. Raju, V. Pagidimarri, R. Barreto, A. Kadam, V. Kasivajjala, and A. Aswath, "Development of a deep learning algorithm for automatic diagnosis of diabetic retinopathy," *Studies in Health Technology and Informatics*, vol. 245, no. 1, pp. 559–563, 2017.

[14] U. Schmidt-Erfurth, A. Sadeghipour, B. S. Gerendas, S. M. Waldstein, and H. Bogunović, "Artificial intelligence in

retina," *Progress in Retinal and Eye Research*, vol. 67, pp. 1–29, 2018.

[15] M. Christopher, A. Belghith, C. Bowd et al., "Performance of deep learning architectures and transfer learning for detecting glaucomatous optic neuropathy in fundus photographs," *Scientific Reports*, vol. 8, no. 1, p. 16685, 2018.

[16] Z. Li, Y. He, S. Keel, W. Meng, R. T. Chang, and M. He, "Efficacy of a deep learning system for detecting glaucomatous optic neuropathy based on color fundus photographs," *Ophthalmology*, vol. 125, no. 8, pp. 1199–1206, 2018.

[17] F. A. Medeiros, A. A. Jammal, and E. B. Mariottoni, "Detection of progressive glaucomatous optic nerve damage on fundus photographs with deep learning," *Ophthalmology*, vol. 128, no. 3, pp. 383–392, 2021.

[18] D. Nagasato, H. Tabuchi, H. Ohsugi et al., "Deep neural network-based method for detecting central retinal vein occlusion using ultrawide-field fundus ophthalmoscopy," *Journal of Ophthalmology*, vol. 2018, Article ID 1875431, 6 pages, 2018.

[19] D. Nagasato, H. Tabuchi, H. Ohsugi et al., "Deep-learning classifier with ultrawide-field fundus ophthalmoscopy for detecting branch retinal vein occlusion," *International Journal of Ophthalmology*, vol. 12, no. 1, pp. 98–103, 2019.

[20] P. Burlina, N. Joshi, K. D. Pacheco, D. E. Freund, J. Kong, and N. M. Bressler, "Utility of deep learning methods for referability classification of age-related macular degeneration," *JAMA Ophthalmology*, vol. 136, no. 11, pp. 1305–1307, 2018.

[21] J. Yim, R. Chopra, T. Spitz et al., "Predicting conversion to wet age-related macular degeneration using deep learning," *Nature Medicine*, vol. 26, no. 6, pp. 892–899, 2020.

[22] Q. Yan, D. E. Weeks, H. Xin et al., "Deep-learning-based prediction of late age-related macular degeneration progression," *Nature Machine Intelligence*, vol. 2, no. 2, pp. 141–150, 2020.

[23] B. Zheng, Q. iang, B. Lu et al., "Five-category intelligent auxiliary diagnosis model of common fundus diseases based on fundus images," *Translational Vision Science & Technology*, vol. 10, no. 7, 2021.

[24] S. R. Abdani, W. M. D. W. Zaki, A. Mustapha, and A. Hussain, "Iris segmentation method of pterygium anterior segment photographed image," in *2015 IEEE Symposium on Computer Applications & Industrial Electronics (ISCAIE)*, pp. 69–72, Langkawi, Malaysia, 2015.

[25] S. R. Abdani, W. M. D. W. Zaki, A. Hussain, and A. Mustapha, "An adaptive nonlinear enhancement method using sigmoid function for iris segmentation in pterygium cases," in *2015 International Electronics Symposium (IES)*, pp. 53–57, Surabaya, Indonesia, 2015.

[26] W. M. D. W. Zaki, M. M. Daud, S. R. Abdani, A. Hussain, and H. A. Mutalib, "Automated pterygium detection method of anterior segment photographed images," *Computer Methods and Programs in Biomedicine*, vol. 154, pp. 71–78, 2018.

[27] S. R. Abdani, M. A. Zulkifley, and A. Hussain, "Compact convolutional neural networks for pterygium classification using transfer learning," in *2019 IEEE International Conference on Signal and Image Processing Applications (ICSIPA)*, pp. 140–143, Kuala Lumpur, Malaysia, 2019.

[28] M. A. Zulkifley, S. R. Abdani, and N. H. Zulkifley, "Pterygium-Net: a deep learning approach to pterygium detection and localization," *Multimedia Tools and Applications*, vol. 78, no. 24, pp. 34563–34584, 2019.

[29] S. R. Abdani, M. A. Zulkifley, and A. M. Moubark, "Pterygium tissues segmentation using densely connected deeplab," in

[30] N. S. M. Zamani, W. M. D. W. Zaki, A. B. Huddin, A. Hussain, H. A. Mutalib, and A. Ali, "Automated pterygium detection using deep neural network," *IEEE Access*, vol. 8, pp. 191659–191672, 2020.

[31] K. Gumus, K. Erkilic, D. Topaktas, and J. Colin, "Effect of pterygia on refractive indices, corneal topography, and ocular aberrations," *Cornea*, vol. 30, no. 1, pp. 24–29, 2011.

[32] M. Sandler, A. Howard, M. Zhu, A. Zhmoginov, and L.-C. Chen, "Mobile Net V2: inverted residuals and linear bottlenecks," in *2018 IEEE/CVF Conference on Computer Vision and Pattern Recognition*, pp. 4510–4520, Salt Lake City, UT, USA, 2018.

[33] J. Deng, W. Dong, R. Socher, L.-J. Li, K. Li, and L. Fei-Fei, "Image Net: A Large-Scale Image Database," in *2009 IEEE Conference on Computer Vision and Pattern Recognition*, pp. 248–255, Miami, FL, USA, 2009.

[34] A. Krizhevsky, I. Sutskever, and G. Hinton, "Imagenet classification with deep convolutional neural networks," in *Proceedings of the 25th International Conference on Neural Information Processing Systems (NIPS)*, pp. 1097–1105, Lake Tahoe, Nevada, US, 2012.

[35] K. Simonyan and A. Zisserman, "Very deep convolutional networks for large-scale image recognition," https://arxiv.org/abs/1409.1556.pdf.

[36] K. He, X. Zhang, S. Ren, and J. Sun, "Deep residual learning for image recognition," in *2016 IEEE Conference on Computer Vision and Pattern Recognition (CVPR)*, pp. 770–778, Las Vegas, NV, USA, 2016.

2020 IEEE 10th Symposium on Computer Applications & Industrial Electronics (ISCAIE), pp. 229–232, Malaysia, 2020.

Research Article

Optical Coherence Tomography Angiography as a Noninvasive Assessment of Cerebral Microcirculatory Disorders Caused by Carotid Artery Stenosis

Xinyue Li [iD],[1,2] **Shiyi Zhu,**[3] **Sujun Zhou,**[1,2] **Yanwei Zhang,**[3] **Yiheng Ding,**[1,2] **Bingjie Zheng,**[3] **Pei Wu** [iD],[3] **Yan Shi,**[1,2] **Hong Zhang** [iD],[1,2] **and Huaizhang Shi** [iD][3]

[1]*Eye Hospital, First Affiliated Hospital of Harbin Medical University, China*
[2]*Key Laboratory of Basic and Clinical Research of Heilongjiang Province, China*
[3]*Department of Neurosurgery, First Affiliated Hospital of Harbin Medical University, China*

Correspondence should be addressed to Hong Zhang; zhanghong@hrbmu.edu.cn
and Huaizhang Shi; shihuaizhang@hrbmu.edu.cn

Purpose. Using retinal optical coherence tomography angiography (OCTA), we aimed to investigate the changes in important indicators of cerebral microcirculatory disorders, such as the properties of the radial peripapillary capillaries, vascular complexes, and the retinal nerve fiber layer, caused by carotid stenosis and postoperative reperfusion. *Methods*. In this prospective longitudinal cohort study, we recruited 40 carotid stenosis patients and 89 healthy volunteers in the First Affiliated Hospital of Harbin Medical University (Harbin, China). Eyes with ipsilateral carotid stenosis constituted the experimental group, while the fellow eyes constituted the contralateral eye group. Digital subtraction angiography, CT perfusion imaging (CTP), and OCTA examinations were performed in all subjects. The vessel density of the radial peripapillary capillaries (RPC), superficial retinal vascular complexes (SVC), deep vascular complexes (DVC), choriocapillaris (CC), and the thickness of the retinal nerve fiber layer (RNFL) were assessed. Propensity-matched analysis was undertaken to adjust for covariate imbalances. Intergroup comparative analysis was conducted, and the paired sample t-test was used to evaluate the preoperative and postoperative changes in OCTA variables. *Results*. The ocular vessel density in the experimental group was significantly lower than that in the control group (RPC: 55.95 vs. 57.24, $P = 0.0161$; SVC: 48.65 vs. 52.22, $P = 0.0006$; DVC: 49.65 vs. 57.50, $P < 0.0001$). Participants with severe carotid stenosis have reduced contralateral ocular vessel density (RPC 54.30; SVC 48.50; DVC 50.80). Unilateral stenosis removal resulted in an increase in vessel density on both sides, which was detected by OCTA on the 4th day (RPC, $P < 0.0001$; SVC, $P = 0.0104$; DVC, $P = 0.0104$). Moreover, the ocular perfusion was consistent with that established by CTP. *Conclusion*. OCTA can be used for sensitive detection and accurate evaluation of decreased ocular perfusion caused by carotid stenosis and may thus have the potential for application in noninvasive detection of cerebral microcirculation disorders. This trial is registered with NCT04326842.

1. Introduction

Carotid artery stenosis (CAS) is one of the major causes of cerebral ischemic stroke, and its early detection is of considerable significance for stroke prevention [1, 2]. Overall, the prevalence of asymptomatic carotid stenosis in the general population ranges from 1.6% to 5.7% [3]. Delays in timely diagnosis and treatment aggravate patients' cognitive decline and substantially increase the risk of falling [4]. Due to the high CAS-inflicted disability rates and the great economic burden imposed on society, screening for abnormalities preceding the occurrence of such severe complications is of critical global importance.

Despite the rapid evolution of magnetic resonance imaging (MRI) perfusion techniques and the wide availability of perfusion single-photon emission computed tomography

(SPECT), PET perfusion imaging with radiolabeled water is still considered the gold standard in cerebral perfusion evaluation with imaging [5]. Due to its high price and radiation risk, this approach cannot be used for large-scale early screening of cerebral ischemia. Thus, CT perfusion imaging (CTP) is commonly used in the clinic. However, most carotid artery stenosis patients are unable to tolerate CTP because of their poor systemic vascular condition. Therefore, a simple, noninvasive, and inexpensive screening tool for carotid artery stenosis is crucial.

The ophthalmic artery is an important branch of the internal carotid artery. The retinal and cerebral arterioles originate from the same germ layer and have common anatomical and physiological characteristics [6]. Therefore, retinal microvascular abnormalities are considered to reflect the degree of cerebral microvascular disease [7]. Several studies [8–11] have confirmed that ocular manifestations can reflect the changes of carotid vessels; however, the potential of previously employed examination methods is limited. For example, a risk of allergy to contrast media exists in retinal angiography [12]. Moreover, other methods, such as retinal thickness [11] and fundus photography [10], do not possess adequate accuracy for the observation of tiny blood vessels. Optical coherence tomography angiography (OCTA) is a new technology that provides high-resolution retinal vascular images suitable for direct observation of $5\,\mu m$ capillaries. Although this noninvasive, rapid, and accurate technique can automatically and quantitatively measure the ocular vessel density, no published reports exist on the use of OCTA for cerebral perfusion prediction. The purpose of this study was to establish the relationship between retinal blood perfusion detected by OCTA and cerebral perfusion.

2. Methods

2.1. Study Design and Participants.
This single-institutional, prospective, cohort, exploratory, observational clinical trial was designed in compliance with the Declaration of Helsinki. The study protocol was approved by the Ethics Committee of the First Affiliated Hospital of Harbin Medical University (Harbin, China) and was registered at the International Clinical Trials Register (http://www.clinicaltrials.gov. NCT04326842). All subjects signed informed consent forms prior to their inclusion in the study.

We recruited patients with carotid artery stenosis from the neurosurgical ward and healthy controls from physical examination centers between April 2020 and July 2020.

The following eye examinations had to be completed in all participants: visual acuity (VA), diopter measurement using automated optometry, intraocular pressure (IOP) measurement by a noncontact tonometer, slit-lamp biomicroscope, fundus examination, and OCTA. All subjects were examined by ultrasound to determine whether the bilateral carotid arteries were stenosed. Controls were confirmed without carotid artery stenosis. Patients with stenosis were further preoperatively examined by digital subtraction angiography (DSA) to determine the degree of carotid artery stenosis. The grade of carotid stenosis was evaluated using DSA in accordance with the North America Symptomatic Carotid

Endarterectomy Trial (NASCET) criteria [13]. The degree of carotid artery stenosis was graded as moderate (50%–70%) and severe (≥70%). The system medical history and family history of each subject were also recorded.

2.2. Exclusion Criteria.
Subjects were excluded if the following criteria were met: (1) age < 18 years; (2) IOP > 21 mmHg; (3) VA > logMAR 1.0; (4) spherical equivalent (SE) > −6.00 D; (5) other serious eye diseases which may affect OCTA results, including diabetic retinopathy, hypertensive retinopathy, retinal vascular occlusion, age-related macular degeneration, and uveitis; (6) major intraocular surgery performed in the past six months or a history of laser photocoagulation or intravitreal injection; (7) glaucoma or first-degree relatives with a history of glaucoma; and (8) any disease that might cause poor scan quality (image quality < 6).

2.3. OCTA: Technique and Clinical Applications.
The same experienced examiner used AngioVue® OCTA (Optovue, Inc., Fremont, CA, USA) to scan all eyes with 6×6 mm of macular area and 4.5×4.5 mm of optic nerve area without mydriasis to obtain microvascular images of the eyes. Each scan was repeated three times to obtain an optimal image quality. The instrument was operated at a central wavelength of 840 nm and a speed of 68,000 A-scans per second, with each B-scan having 245 A-scans in both the horizontal and vertical directions. The microangiography composite algorithm analyzes the changes of the complex signal (the intensity and phase changes are included in the continuous B-scan at the same position) and then generates the microvascular image. As can be seen in Figure 1, based on the distribution and shape of the retinal blood vessels, the retinal microvascular system was divided into radial peripapillary capillaries (RPC), superficial vascular complexes (SVC), deep vascular complexes (DVC), and choriocapillaris (CC). OCTA can also measure the thickness of the retinal nerve fiber layer (RNFL). The image analysis software of OCTA equipment was used for automatic analysis of the image, and a series of parameters such as vessel density (VD) and retinal thickness were calculated (Supplementary Figure 1). This version of AngioVue® software (RTVue XR version 2018.1.0.43, Optovue, Inc., Fremont, CA, USA) can remove the projection artifacts on the deep retina through 3D projection artifact removal (3D PAR) technology, facilitating clearer visualization at all depths of the vascular structures in the enface images and B-scans. VD was defined as the proportion of the blood flow signal detected by OCTA to the corresponding area. The numerical value was calculated automatically by the OCTA software.

2.4. CTP: Technique and Clinical Applications.
All patients were examined pre- and postoperatively by CTP to determine the cerebral blood flow perfusion of patients with carotid artery stenosis. CTP imaging was performed on a Philips 256-slice CT scanner (Philips Brilliance iCT). Cerebral perfusion scan mode was employed with a tube voltage of 120 kV and a tube current of 150 mA. The scanning time was 50 s, the layer thickness was 5 mm, and the coverage was 12 cm. Lobitridol injection (350 mg/mL) was used as
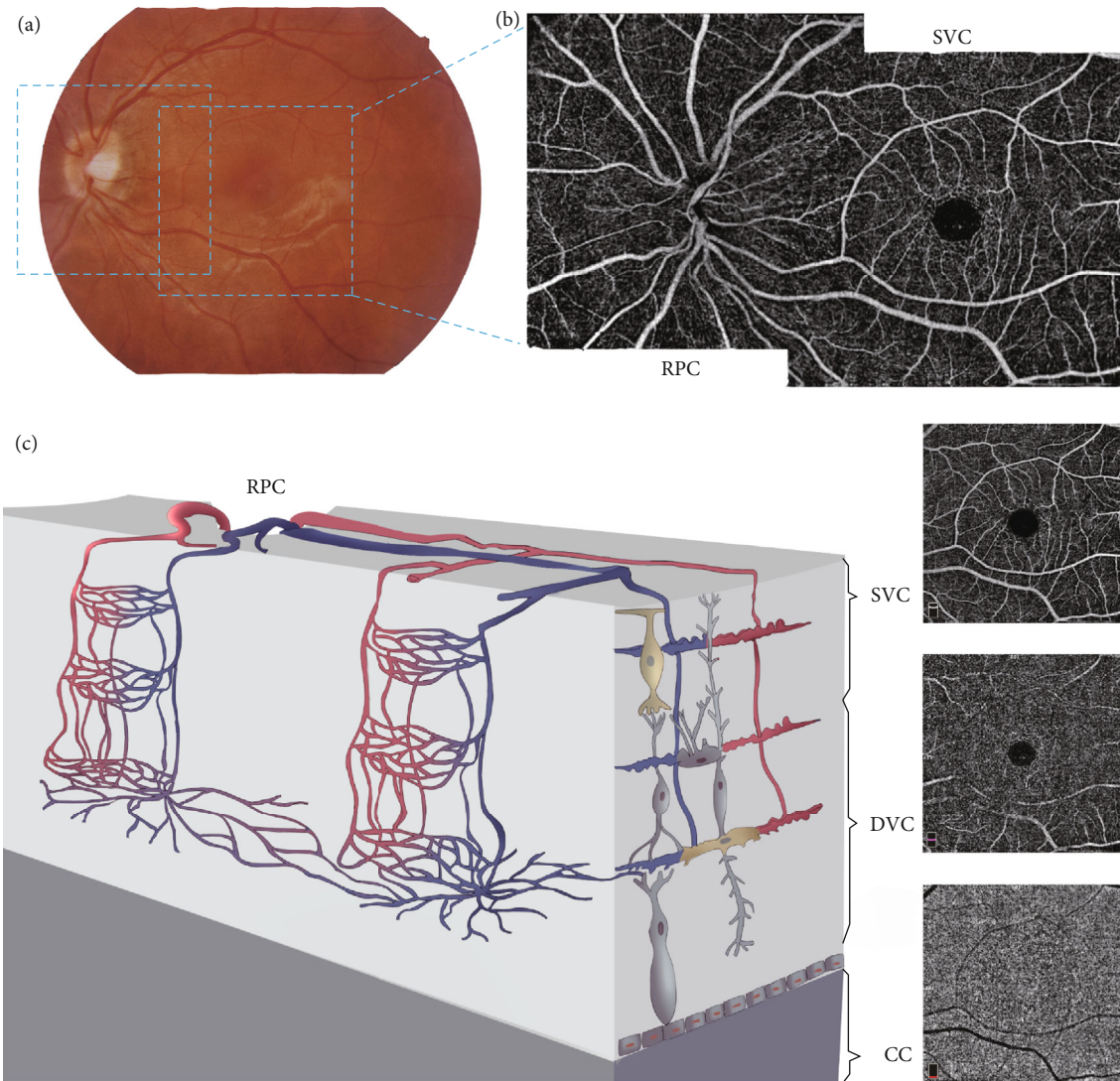
FIGURE 1: Retinal vascular plexuses and interconnecting layers. (a) Color fundus photograph demonstrates two 6×6 mm regions of scan (blue square); (b) the OCTA en face images are arrayed from the most superficial on top to the deepest at the bottom; (c) the cartoon depicts the anatomical relationships between arterial and venous systems in the two vascular plexuses and the interconnecting layers. RPC: radical peripapillary capillaries; SVC: superficial vascular complexes; DVC: deep vascular complexes; CC: choriocapillaris.

the contrast medium. The total amount was 100 mL, and the applied injection flow rate was 5 mL/min. We obtained 400 CTP images by scanning, which were then transferred into a special postprocessing workstation. Postprocessing of the CTP scans was performed using commercially available software with an Extended Brilliance Workspace (version 4.5.4, Philips Healthcare). The images were analyzed by two experienced neuroimaging diagnostics. In the perfusion image, the central layer of the semioval center layer, the body of the lateral ventricle layer, and the basal ganglia layer were considered as the region of interest (ROI) to avoid the inclusion of calcifications and old infarcted tissues as far as possible. The frontal, temporal, and parietal lobes of the middle cerebral artery were drawn by hand in the same area as the ROI. The cerebral blood flow (CBF), cerebral blood volume (CBV), mean transit time (MTT), and peak time (TTP) of the lesion side and the contralateral corresponding area were

measured by mirror symmetry with the midline. The pre- and postoperative data obtained were quantitatively and qualitatively analyzed and compared. Each level was measured three times; finally, the average value was taken to ensure that the final selected ROI data were reliable and consistent.

2.5. Interventional Procedure. The patients in the experimental group were treated with carotid endarterectomy (CEA) or carotid artery stenting (CAS). Their surgical indications, surgical procedures, and surgical norms were performed in compliance with the AHA guidelines [14] and "Rutherford's Vascular Surgery." [15].

2.6. Follow-Up Assessments. Before discharge, OCTA and CTP examinations were repeated in all patients on the 4th day after the operation. This information was also collected
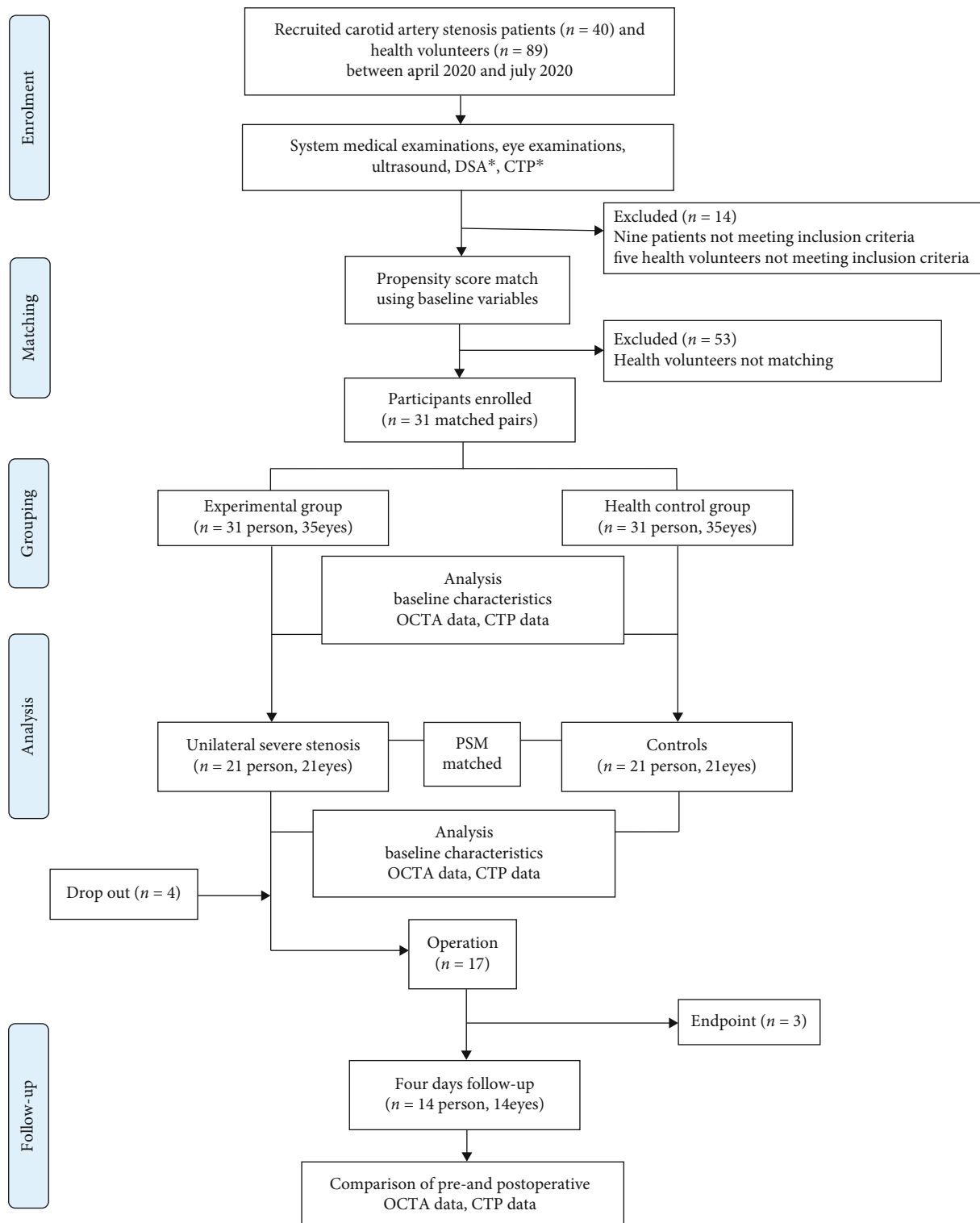
Figure 2: Flow chart of patient recruitment into the study. *DSA CTP only for patients.

and recorded. The hypothesis of blinding was considered during the study design: technicians were blinded to the patient's condition before and after surgery.

2.7. Statistical Analysis. This study was purely exploratory; thus, no prospective sample size calculation was conducted.

Categorical variables are presented as percentages, continuous variables as mean ± SD, and skewed variables as median (boundaries of interquartile range, IQR). Propensity score-matched (PSM) analysis was performed using a multivariable logistic regression model based on age, gender, tobacco use, alcohol intake, and diabetes mellitus status.

TABLE 1: Characteristics of the study participants.

Characteristic	Experimental group	Control group	$\chi^2/W/Z$	P
Age, median (y)	63	63	249.5	0.1495
Male, n (%)	27 (87.1%)	23 (74.2%)	-2.1082	0.0719
Tobacco, n (%)	15 (48.4%)	14 (45.2%)	0.0648	0.7991
Alcohol, n (%)	11 (35.5%)	6 (19.4%)	2.0261	0.1546
Hypertension, n (%)	28 (90.3%)	21 (67.7%)	4.7692	0.0586[a]
Diabetes, n (%)	6 (19.4%)	9 (29.0%)	0.7915	0.3737
OCTA characteristic				
RPC VD (%) Median (IQR)	55.95 (53.30-58.10)	57.24 (56.00-59.20)	5.7924	0.0161
SVC VD (%) Median (IQR)	48.65 (45.50-51.10)	52.22 (50.14-53.53)	11.785	0.0006
DVC VD (%) Median (IQR)	49.65 (46.50-53.70)	57.50 (53.80-59.85)	20.152	<.0001
CC VD (%) Median (IQR)	67.41 (62.90-69.92)	68.74 (65.91-71.11)	1.560365	0.1320

VD: vessel density; RPC: radical peripapillary capillaries; SVC: superficial vascular complexes; DVC: deep vascular complexes; CC: choriocapillaris. [a]The P value was verified by Fisher's exact probability test.
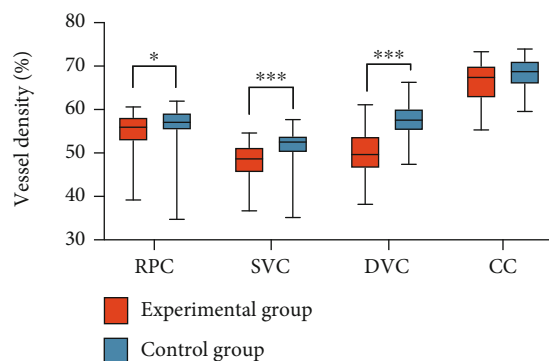
FIGURE 3: Vessel density of the stenotic side of the eye. The vessel density of the stenotic side of the eye in the experimental group was lower than that in the control group. RPC: radical peripapillary capillaries; SVC: superficial vascular complexes; DVC: deep vascular complexes; CC: choriocapillaris.

Participants were matched in pairs using 1 : 1 greedy nearest neighbor matching, resulting in the formation of 31 matched pairs in each group.

The clinical characteristics of the groups were compared using the χ^2 test for categorical variables, paired t-test for normally distributed continuous variables, and Wilcoxon rank-sum tests for nonnormally distributed continuous variables. Paired sample t-tests were employed to assess and compare the preoperative and postoperative changes in OCTA variables.

Fisher's exact probability test was applied to verify the P value when 25% of the theoretical frequency was lower than 5. All tests were bilateral, with statistical significance at $P < 0.05$. All statistical analyses were performed using SPSS software (v25, IBM, Armonk, NY, USA), and Prism 7 (v7.02, GraphPad, La Jolla, CA, USA) was employed for graph generation.

3. Results

3.1. Characteristics of the Participants. A total number of 129 participants (40 patients and 89 healthy volunteers) were recruited between April 2020 and July 2020 (Figure 2). Fourteen participants were excluded for not meeting the inclusion criteria. After PSM analysis, 31 matched pairs were obtained (31 in the experimental group and 31 in the healthy control group). Of the 31 patients in the experimental group, 14 cases of unilateral severe stenosis or occlusion were followed up on the 4th day postoperatively.

After 1 : 1 PSM adjustment, baseline demographic and clinical variables were well balanced between the two groups (Table 1).

3.2. RPC, SVC, DVC, and CC Vessel Densities. The RPC, SVC, and DVC vessel densities in the patients were significantly lower than those in the healthy controls, with statistically significant differences ($P = 0.0161$; 0.0006; <0.0001, Table 1). Although no statistical difference was available in CC between the two groups, the choriocapillaris VD of the diseased side was generally lower than that of the control group (Figure 3).

3.3. Bilateral Changes Caused by Unilateral Carotid Stenosis. Of the 31 patients in the experimental group, 21 had unilateral severe stenosis or occlusion. Twenty-one controls that matched the general condition of the control group were selected by the PSM tendency score. The retina vessel densities of the two groups were then compared. The results showed that although the contralateral carotid artery had no stenosis in patients with severe unilateral carotid artery stenosis and occlusion, the blood supply of the contralateral eyes was reduced, and the SVC and DVC vessel densities were significantly lower than those of the control eyes, with statistically significant differences ($P = 0.0123$; 0.0007, Table 2). As can be

TABLE 2: Ocular conditions of contralateral eyes with severe unilateral carotid artery stenosis and occlusion and healthy control eyes.

OCTA characteristic	Contralateral eyes	Control eyes	Z	P
RPC VD (%) Median (IQR)	54.30 (51.90-57.60)	57.07 (55.13-59.16)	2.7747	0.0958
SVC VD (%) Median (IQR)	48.50 (45.80-52.00)	52.22 (50.14-53.21)	6.2650	0.0123
DVC VD (%) Median (IQR)	50.80 (47.10-53.80)	56.13 (53.07-58.63)	11.621	0.0007
CC VD (%) Median (IQR)	65.50 (61.90-68.76)	67.02 (65.88-71.11)	1.5597	0.1188

VD: vessel density; RPC: radical peripapillary capillaries; SVC: superficial vascular complexes; DVC: deep vascular complexes; CC: choriocapillaris.
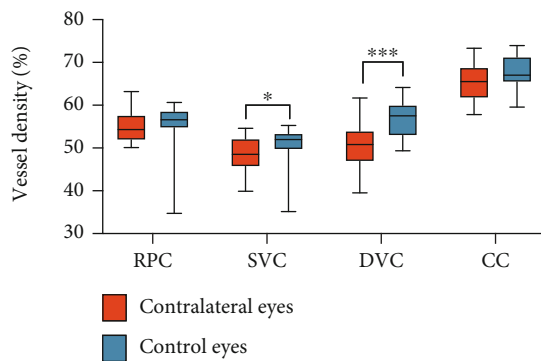
FIGURE 4: Vessel density of the contralateral eyes with severe unilateral carotid artery stenosis. The vessel density of the contralateral eyes with severe unilateral carotid artery stenosis in the experimental group was lower than that of the control eyes. RPC: radical peripapillary capillaries; SVC: superficial vascular complexes; DVC: deep vascular complexes; CC: choriocapillaris.

seen in Figure 4, the RPC and CC vessel densities of the contralateral eyes were generally slightly lower than those of the control eyes.

3.4. OCTA and Relationship with CTP. In this study, we found that patients with poor cerebral perfusion caused by severe carotid artery stenosis or occlusion also had poorer retinal vessel density than patients with moderate carotid artery stenosis (Figure 5).

3.5. Comparison of Pre- and Postoperative OCTA and CTP. Of the 21 patients with unilateral severe stenosis, 14 were followed up on the 4th day after the operation. The characteristics of their condition are presented in Table 3. After the operation, with the improvement of cerebral perfusion, the ocular blood supply of the operated side was significantly improved (PRC, $P < 0.0001$; SVC, $P = 0.0104$; DVC, $P = 0.0104$; RNFL, $P < 0.0001$). Meanwhile, the condition of the contralateral eye had also improved. This significant change is visible in Figure 6.

4. Discussion

Our study confirmed and explained the mechanism by which carotid artery stenosis or occlusion affects the ocular blood supply. OCTA can sensitively detect subtle changes in the ocular blood supply in the early stage of carotid artery stenosis and after CEA or CAS surgery. We confirmed the relationship between ocular microcirculation and cerebral perfusion. Therefore, OCTA may be used as a noninvasive quantitative screening method for carotid artery stenosis or occlusion.

Atherosclerosis is a systemic vascular disorder involving multiple arterial beds, including carotid and coronary arteries [16]. Detection of atheroma plaque by noninvasive techniques in the easily accessible carotid artery emerged as a surrogate marker for advanced atherosclerosis in other vascular beds, including coronary arteries [17]. The carotid artery is the earliest involved blood vessel in the development of atherosclerosis [18]. Carotid artery stenosis is defined by the narrowing of the carotid arteries and commonly caused by atherosclerosis, potentially leading to ischemic disease. All ocular vessels receive their blood supply from the ophthalmic artery, a branch of the internal carotid artery. On the other hand, systemic diseases such as diabetes and hypertension can cause chronic damage to vessels, including carotid arteries and ocular vessels. Therefore, from the anatomical point, stenosis or occlusion of the proximal vessel can naturally affect the blood supply of the distal branch. From the pathological point, carotid artery and ocular vascular density damage also have many similarities.

Increasingly more scientific attention has been paid to microvessel damage in cerebrovascular disease research. However, microvascular lesions cannot be directly observed using traditional examination methods. Moreover, due to the radiation trauma caused by the examination, it is not feasible to check repeatedly and monitor the disease. Previous studies have shown that carotid artery stenosis causes morphological changes in certain eye characteristics, including an abnormal diameter of the retinal vessels [10], thinning of RNFL [19], and thinning of the choroid [20]. Several investigations have revealed that retinal vessels can be used as a noninvasive observation object for reliable evaluation of the cerebral microvascular system [12, 21, 22]. The birth of the OCTA technology has enabled the observations not only of the small blood vessels with an approximate size of $250\,\mu$m but also of capillaries with a size of $5\,\mu$m. This increased visibility facilitates the implementation of accurate observations of the microvascular system of the brain. OCTA is not only simple and fast to operate but also radiation-free. Furthermore, this approach does not require the
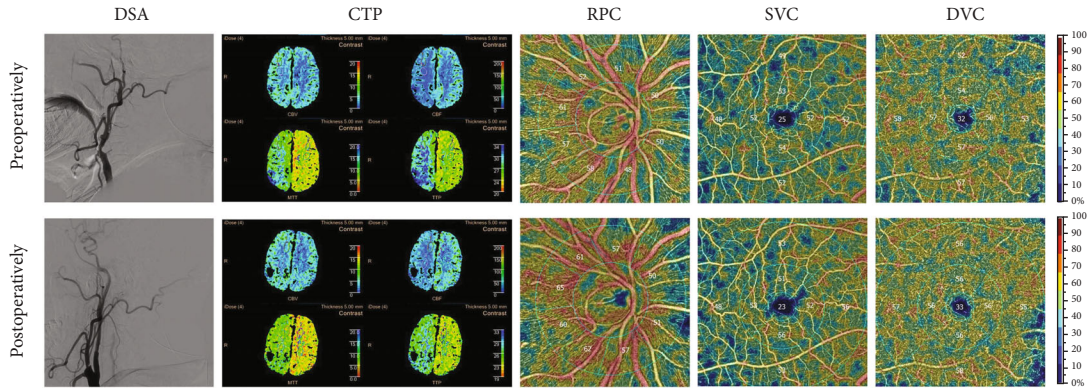
FIGURE 5: Brain and eye perfusion in the patients with moderate and severe carotid stenosis. Color bars represent vessel density; brighter colors indicate higher values. RPC: radical peripapillary capillaries; SVC: superficial vascular complexes; DVC: deep vascular complexes; CC: choriocapillaris; RPC: radical peripapillary capillaries; SVC: superficial vascular complexes; DVC: deep vascular complexes; CC: choriocapillaris.

TABLE 3: Changes of blood supply to the eyes and brain before and after the operation.

OCTA characteristic	Operated side median (IQR)	P	Nonoperated side median (IQR)	P
RPC VD (%) Median (IQR)	1.55 (0.40-2.60)	<0.0001	0.65 (-1.65-2.20)	0.4332
SVC VD (%) Median (IQR)	1.70 (0.40-2.80)	0.0104	0.00 (-2.10-4.60)	1.0000
DVC VD (%) Median (IQR)	4.00 (0.70-6.50)	0.0104	-1.55 (-3.60-4.30)	0.1691
RNFL (μm) Median (IQR)	2.50 (2.00-11.00)	<0.0001	4.00 (0.50-6.50)	0.005
rCBF	0.19 (0.02-0.31)	0.0011	—	—
$\triangle$MTT	-0.22 (-0.46–0.16)	<0.0001	—	—

VD: vessel density; RPC: radical peripapillary capillaries; SVC: superficial vascular complexes; DVC: deep vascular complexes; RNFL: retinal nerve fiber layer; rCBF: the ratio of the values measured in the symptomatic hemisphere to those in the asymptomatic hemisphere for cerebral blood flow; $\triangle$MTT: the absolute difference in mean transit time values between the symptomatic and the asymptomatic hemispheres.
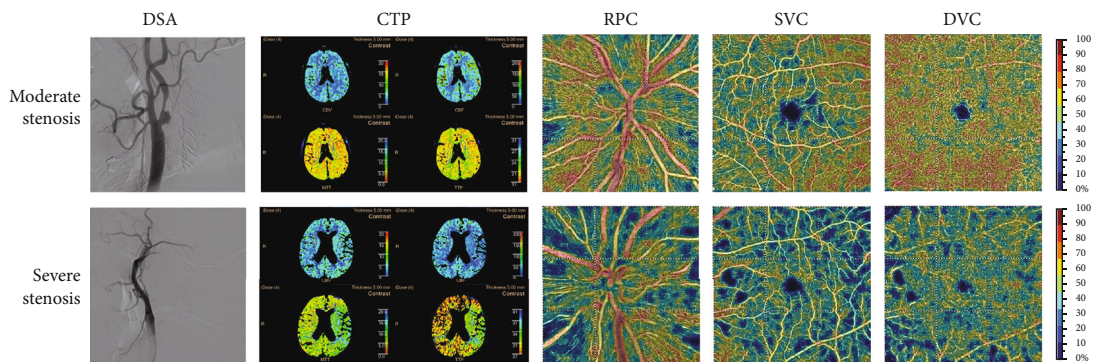
FIGURE 6: Preoperative (top row) and postoperative (bottom row) images of a patient with carotid artery occlusion. Compared with the preoperative OCTA image, there were more brightly colored areas (suggesting an increase in the blood flow density in this area), and the value of VD on the image was also higher. These changes were not observed in the CTP's image. RPC: radical peripapillary capillaries; SVC: superficial vascular complexes; DVC: deep vascular complexes; CC: choriocapillaris.

administration of intravenous dye injection, and thus, it is suitable for early detection of ischemia and follow-up detection. The automatic blood flow measurement function of

Optovue has been certified by FDA, and its objectivity has been widely recognized. In normal people, macular vessel density is extremely stable and can reflect the amount of

circulatory perfusion. Hence, macular vessel density has become an excellent tool to measure the impact of various retinopathies and even systemic microcirculation diseases, such as diabetes [23], hypertension [24], cerebral small vessel disease [25], Alzheimer's disease [26], and migraine [27].

Our first major finding was that the ocular vessel density on the diseased side in unilateral moderate carotid artery stenosis was lower than that in normal controls (Table 1, Figure 3). This result is in line with the findings of previous studies showing worse retinal vascular parameters in subjects with carotid artery stenosis. For example, thinner retinal vessel caliber, lower venous responses to flicker stimulation, and decreased central retinal arteriolar equivalent [10] were reported to be associated with carotid artery stenosis. However, manually measured retinal vasculature measurements were employed in these previous studies, which are subjective. Using OCTA, we easily examined the microvasculature down to the capillary level. In a previous study, the OCTA results showed that the flow density in the superficial retinal OCT angiogram of the macula in patients with CAS was significantly lower than that in healthy controls (study group: 48.52 ± 4.46; control group: 51.88 ± 2.70; $P = 0.003$) [28]. This finding is consistent with our research results.

Carotid artery stenosis exceeding 70% not only affected the ocular blood supply of the ipsilateral side but also reduced the ocular vessel density of the contralateral side (Table 2, Figure 4). After CEA or CAS operation, the ocular vessel densities on both operated and nonoperated sides increased. Previous studies obtained similar results, in which unilateral carotid revascularization improved the cerebral perfusion and metabolism not only of the ipsilateral cerebral hemisphere but also of the contralateral cerebral hemisphere [4, 29, 30]. In an earlier examination, Lee et al. recruited 20 patients with severe carotid stenosis, and OCTA was performed before CAS and one month after that. The vessel density on the operated side of the DVC increased significantly after stent implantation ($P = 0.010$). Interestingly, the vessel densities in the SVC ($P = 0.028$) and DVC ($P = 0.034$) were significantly higher after stent implantation on the nonoperated side as well. Evidence shows that the bilateral ocular blood flow [31] and the retinal electrophysiological response [32] were improved postoperatively. Unfortunately, this phenomenon has not been well explained to date. Here, we present two hypotheses concerning its possible mechanism. First, from a physiological point of view, when the blood supply to one side of the cerebral hemisphere is decreased, the body establishes a contralateral collateral circulation to balance the global cerebral perfusion. Liu et al. measured the direction of the ophthalmic artery flow and bilaterally in the internal carotid arteries in a group of 116 patients with unilateral carotid artery stenosis and found that the direction was reversed in 36% of the patients [33]. In another study, Pienimaki et al. observed that patients with severe carotid stenosis were four times more likely to develop collateral circulation than patients with nonstenosis and moderate stenosis [34]. In our study, we established the presence of collateral circulation in 44% of patients with unilateral severe carotid artery stenosis or occlusion by DSA (Supplementary Figure 2). Second, patients with carotid artery stenosis are at a high risk of arteriosclerosis development. Although the nonoperative side vessels were not stenosed, they might have been affected by arteriosclerosis, which could also have influenced the blood flow density. When we selected patients in the experimental and control groups, we matched their baseline data, which might have affected the blood flow density, whereas the conditions in terms of hypertension, diabetes, smoking, and drinking in the two groups were similar. By this matching, we minimized the impact of noncarotid stenosis factors on the results. Our findings provide evidence that unilateral stenosis or occlusion results in a decrease in the blood supply to the contralateral eye, while unilateral surgery improves the contralateral eye condition. Such changes cannot be observed by traditional examination approaches, whereas OCTA can be used repeatedly for monitoring the perfusion of different regions of the left and right retinal circulation longitudinally.

Besides vessel density, we were also interested to elucidate the impact of carotid blood flow on RNFL. The RNFL is composed of axons of ganglion cells. Earlier studies have established that the thickness of RNFL decreased associate with the development of cognitive impairment, stroke, and other brain diseases [22, 35]. We found that the thickness of RNFL increased (Table 3) on both sides after CEA or CAS operation. This outcome indicates that relieving carotid artery stenosis or occlusion may also influence RNFL. Previous investigations did not detect such a significant difference in RNFL [19, 36] as the resolution of EDI-OCT was not as high as that of OCTA.

Choroidal blood flow accounts for 90% of the ocular blood flow [37]. However, whether carotid artery stenosis has an impact on the choroidal blood flow remains unknown. Using the automatic stratification and quantification features of OCTA, we objectively measured the value of the choroidal vessel density (Tables 1 and 2) and found that its values in the experimental group were slightly lower than those in normal subjects. Because of the large choroidal blood low, slight changes may not have had a statistically significant difference in the limited number of observed cases in our study. The significance of the overall difference may be increased by the inclusion of more patients.

Our research has some limitations. First, it was conducted over a relatively short period of three months. Further investigations are required to establish the potential long-term existence of these early beneficial effects. Second, although we prospectively recruited well-characterized subjects, this study was exploratory, with relatively a small sample size. Further longitudinal studies with a larger sample size are needed to confirm our results. Third, despite the relatively weak correlation between OCTA and CTP results (Figures 5 and 6), we can still see the trend of improvement in the images of cerebral perfusion and eye perfusion after CEA or CAS operation. CTP is the ratio of the two sides, but the ROI area measurement is subjective. Therefore, OCTA is an objective and accurate method for retinal vessel density measurement. Nevertheless, further studies with larger sample sizes are needed to obtain additional evidence and clarify the relationship between OCTA and CTP.

5. Conclusions

In conclusion, patients with carotid artery stenosis showed a reduced vessel density in the RPC, SVC, and DVC layer when compared with healthy controls. In patients with severe carotid stenosis, unilateral CAS effectively improved the retinal microcirculation in both eyes. OCTA can detect noninvasive and rapid changes in the retinal microcirculation and, along with CTP, may help establish a new biomarker for predicting and monitoring cerebral perfusion changes in patients with carotid artery stenosis.

Data Availability

Data is available from the corresponding author on reasonable request.

Conflicts of Interest

The authors declare that there is no conflict of interest.

Authors' Contributions

Xinyue Li and Shiyi Zhu contributed equally to this work.

Supplementary Materials

Supplementary Figure 1: OCTA AngioRetina 6.0 report. Supplementary Figure 2: preoperative DSA images of patients with severe carotid stenosis. (A) Severe stenosis at the beginning of the left internal carotid artery of the patient; (B) a significant compensation was observed in the intracranial blood supply from the right internal carotid artery to the left cerebral hemisphere through anterior communication. (*Supplementary Materials*)

References

[1] R. Herzig, P. Hluštík, K. Urbánek et al., "Can we identify patients with carotid occlusion who would benefit from EC/IC bypass? Review," *Biomedical Papers of the Medical Faculty of the University Palacky, Olomouc, Czech Republic*, vol. 148, no. 2, pp. 119–122, 2004.

[2] T. Blaser, K. Hofmann, T. Buerger, O. Effenberger, C. W. Wallesch, and M. Goertler, "Risk of stroke, transient ischemic attack, and vessel occlusion before endarterectomy in patients with symptomatic severe carotid stenosis," *Stroke*, vol. 33, no. 4, pp. 1057–1062, 2002.

[3] M. de Weerd, J. P. Greving, B. Hedblad et al., "Prevalence of asymptomatic carotid artery stenosis in the general population: an individual participant data meta-analysis," *Stroke*, vol. 41, no. 6, pp. 1294–1297, 2010.

[4] J. Schröder, M. Heinze, M. Günther et al., "Dynamics of brain perfusion and cognitive performance in revascularization of carotid artery stenosis," *NeuroImage: Clinical*, vol. 22, 2019.

[5] M. Mattoli, G. Treglia, M. Calcagni, A. Mangiola, C. Anile, and G. Trevisi, "Usefulness of brain positron emission tomography with different tracers in the evaluation of patients with idiopathic normal pressure hydrocephalous," *International Journal of Molecular Sciences*, vol. 21, no. 18, p. 6523, 2020.

[6] J. Vignaud, A. N. Hasso, P. Lasjaunias, and C. Clay, "Orbital vascular anatomy and embryology," *Radiology*, vol. 111, no. 3, pp. 617–626, 1974.

[7] T. Y. Wong, R. Klein, D. J. Couper et al., "Retinal microvascular abnormalities and incident stroke: the atherosclerosis risk in communities study," *The Lancet*, vol. 358, no. 9288, pp. 1134–1140, 2001.

[8] R. Sun, X. Y. Peng, Q. S. You, L. Q. Jiao, and J. B. Jonas, "Central retinal artery pressure and carotid artery stenosis," *Experimental and Therapeutic Medicine*, vol. 11, no. 3, pp. 873–877, 2016.

[9] F. Lareyre, E. Nguyen, J. Raffort et al., "Changes in ocular subfoveal choroidal thickness after carotid endarterectomy using enhanced depth imaging optical coherence tomography: a pilot study," *Angiology*, vol. 69, no. 7, pp. 574–581, 2018.

[10] A. Machalińska, M. P. Kawa, K. Babiak et al., "Retinal vessel dynamic functionality in the eyes of asymptomatic patients with significant internal carotid artery stenosis," *International Angiology*, vol. 38, no. 3, pp. 230–238, 2019.

[11] S. Li, X. Lang, W. Wang et al., "Choroidal vascular changes in internal carotid artery stenosis: a retrospective cohort study in Chinese population," *BMC Ophthalmology*, vol. 19, no. 1, p. 215, 2019.

[12] J. Wang, W. Wang, B. Jin et al., "Improvement in cerebral and ocular hemodynamics early after carotid endarterectomy in patients of severe carotid artery stenosis with or without contralateral carotid occlusion," *BioMed Research International*, vol. 2016, Article ID 2901028, 9 pages, 2016.

[13] H. Barnett, D. Taylor, M. Eliasziw et al., "Benefit of carotid endarterectomy in patients with symptomatic moderate or severe stenosis," *The New England Journal of Medicine*, vol. 339, no. 20, pp. 1415–1425, 1998.

[14] W. N. Kernan, B. Ovbiagele, H. R. Black et al., "Guidelines for the prevention of stroke in patients with stroke and transient ischemic attack: a guideline for healthcare professionals from the American Heart Association/American Stroke Association," *Stroke*, vol. 45, no. 7, pp. 2160–2236, 2014.

[15] A. P. Sidawy and B. A. Perler, *Rutherford's Vascular Surgery and Endovascular Therapy*, Elsevier, Amsterdam, 9 ed edition, 2018.

[16] Y. Shen, S. Jin, C. Lin et al., "Safety of different carotid artery revascularization strategies in the coronary artery bypass graft population: study protocol for a systematic review and network meta-analysis," *Annals of Translational Medicine*, vol. 8, no. 23, 2020.

[17] G. Chiva-Blanch, C. Jiménez, M. Pinyol et al., "5-Cis-, trans- and total lycopene plasma concentrations inversely relate to atherosclerotic plaque burden in newly diagnosed type 2 diabetes subjects," *Nutrients*, vol. 12, no. 6, p. 1696, 2020.

[18] X. Peng, Y. Zhou, X. Wu et al., "Association of methylenetetra-hydrofolate reductase (MTHFR) variant C677T and risk of carotid atherosclerosis: a cross-sectional analysis of 730 Chinese Han adults in Chongqing," *BMC Cardiovascular Disorders*, vol. 20, no. 1, p. 222, 2020.

[19] O. Guclu, H. Guclu, S. Huseyin et al., "Retinal ganglion cell complex and peripapillary retinal nerve fiber layer thicknesses following carotid endarterectomy," *International Ophthalmology*, vol. 39, no. 7, pp. 1523–1531, 2019.

[20] S. Akca Bayar, Z. Kayaarasi Ozturker, E. Y. Pinarci, Z. E. Ercan, H. T. Akay, and G. Yilmaz, "Structural analysis of the retina and choroid before and after carotid artery surgery," *Current Eye Research*, vol. 45, no. 4, pp. 496–503, 2020.

[21] C. Y. Cheung, W. T. Tay, M. K. Ikram et al., "Retinal microvascular changes and risk of stroke: the Singapore Malay Eye Study," *Stroke*, vol. 44, no. 9, pp. 2402–2408, 2013.

[22] D. Wang, Y. Li, C. Wang et al., "Localized retinal nerve fiber layer defects and stroke," *Stroke*, vol. 45, no. 6, pp. 1651–1656, 2014.

[23] D. Gildea, "The diagnostic value of optical coherence tomography angiography in diabetic retinopathy: a systematic review," *International Ophthalmology*, vol. 39, no. 10, pp. 2413–2433, 2019.

[24] H. B. Lim, M. W. Lee, J. H. Park, K. Kim, Y. J. Jo, and J. Y. Kim, "Changes in ganglion cell-inner plexiform layer thickness and retinal microvasculature in hypertension: an optical coherence tomography angiography study," *American Journal of Ophthalmology*, vol. 199, pp. 167–176, 2019.

[25] J. Y. Lee, J. P. Kim, H. Jang et al., "Optical coherence tomography angiography as a potential screening tool for cerebral small vessel diseases," *Alzheimer's Research & Therapy*, vol. 12, no. 1, p. 73, 2020.

[26] B. E. O'Bryhim, R. S. Apte, N. Kung, D. Coble, and G. P. Van Stavern, "Association of preclinical Alzheimer disease with optical coherence tomographic angiography findings," *JAMA Ophthalmology*, vol. 136, no. 11, pp. 1242–1248, 2018.

[27] M. O. Ulusoy, B. Horasanli, and A. Kal, "Retinal vascular density evaluation of migraine patients with and without aura and association with white matter hyperintensities," *Acta Neurologica Belgica*, vol. 119, no. 3, pp. 411–417, 2019.

[28] L. Lahme, E. Marchiori, G. Panuccio et al., "Changes in retinal flow density measured by optical coherence tomography angiography in patients with carotid artery stenosis after carotid endarterectomy," *Scientific Reports*, vol. 8, no. 1, p. 17161, 2018.

[29] J. L. Whooley, B. C. David, H. H. Woo et al., "Carotid revascularization and its effect on cognitive function: a prospective nonrandomized multicenter clinical study," *Journal of Stroke and Cerebrovascular Diseases*, vol. 29, no. 5, p. 104702, 2020.

[30] X. Zhang, H. Ma, L. Li et al., "Neurocognitive changes after carotid revascularization according to perfusion parameters: a meta-analysis of current literature," *Annals of Vascular Surgery*, vol. 64, pp. 361–374, 2020.

[31] C. W. Lee, H. C. Cheng, F. C. Chang, and A. G. Wang, "Optical coherence tomography angiography evaluation of retinal microvasculature before and after carotid angioplasty and stenting," *Scientific Reports*, vol. 9, no. 1, p. 14755, 2019.

[32] J. Yan, X. Yang, J. Wu et al., "Visual outcome of carotid endarterectomy in patients with carotid artery stenosis," *Annals of Vascular Surgery*, vol. 58, pp. 347–356, 2019.

[33] C. H. Liu, C. H. Chang, T. Y. Chang et al., "Carotid artery stenting improves cerebral hemodynamics regardless of the flow direction of ophthalmic artery," *Angiology*, vol. 66, no. 2, pp. 180–186, 2015.

[34] J. P. Pienimaki, N. Sillanpaa, P. Jolma, and S. Protto, "Carotid artery stenosis is associated with better intracranial collateral circulation in stroke patients," *Cerebrovascular Diseases*, vol. 49, no. 2, pp. 200–205, 2020.

[35] M. Kim, K. H. Park, J. W. Kwon, J. W. Jeoung, T. W. Kim, and D. M. Kim, "Retinal nerve fiber layer defect and cerebral small vessel disease," *Investigative Ophthalmology & Visual Science*, vol. 52, no. 9, pp. 6882–6886, 2011.

[36] N. Sayin, N. Kara, F. Uzun, and I. F. Akturk, "A quantitative evaluation of the posterior segment of the eye using spectral-domain optical coherence tomography in carotid artery stenosis: a pilot study," *Ophthalmic Surgery, Lasers & Imaging Retina*, vol. 46, no. 2, pp. 180–185, 2015.

[37] P. K. Yu, I. L. McAllister, W. H. Morgan, S. J. Cringle, and D.-Y. Yu, "Inter-relationship of arterial supply to human retina, choroid, and optic nerve head using micro perfusion and labeling," *Investigative Ophthalmology & Visual Science*, vol. 58, no. 9, pp. 3565–3574, 2017.

Research Article

Topological Organization Alterations of Whole-Brain Functional Networks in Patients with Childhood Absence Epilepsy: Associations with Treatment Effects

Xueyu Wang [ID],[1,2] **Peng Fang,**[3] **Dongmei Jiao,**[4] **Tian Hu,**[5] **Qi Yang,**[6] **Wei Liang,**[3] **Yijun Li,**[3] **Yibing Yan,**[7] **and Libo Liu** [ID][8]

[1]*Department of Pediatrics, Shandong Provincial Hospital, Cheeloo College of Medicine, Shandong University, Jinan, Shandong 250021, China*
[2]*Department of Pediatrics, Shandong Provincial Hospital Affiliated to Shandong First Medical University, Jinan, Shandong 250021, China*
[3]*Department of Military Medical Psychology, Air Force Medical University, China*
[4]*Department of Internal Medicine, The Second Affiliated Hospital of Shandong Traditional Chinese Medicine University, Jinan, China*
[5]*Department of Radiology, Yanan University Affiliated Hospital, China*
[6]*Department of Radiology, Affiliated Hospital of Shaanxi University of Traditional Chinese Medicine, China*
[7]*Department of Pediatrics, The First Affiliated Hospital of Shandong First Medical University, Jinan, China*
[8]*Department of Cardiology, The Second Affiliated Hospital of Shandong First Medical University, Taian, China*

Correspondence should be addressed to Xueyu Wang; wangxueyu1965@sdu.edu.cn and Libo Liu; liboliu2007@126.com

Purpose. The purpose of the current study is to detect changes of topological organization of whole-brain functional networks and their relationship with the clinical treatment effects of antiepileptic drugs (AEDs) for patients with childhood absence epilepsy (CAE) using resting-state functional MRI (RS-fMRI). *Patients and Methods*. RS-fMRI data from 30 CAE patients were collected and compared with findings from 30 age- and gender-matched healthy controls (HCs). The patients were treated with first-line AEDs for 46.03 months before undergoing a second RS-fMRI scan. *Results*. CAE children at baseline showed a reduced clustering coefficient (Cp) and local efficiency (El) than the HC group, implying the reduction of functional segregation. CAE children at baseline also showed smaller characteristic path length (Lp) and higher global efficiency (Eg) compared with the HC group, implying the impairment of functional segregation. However, those metrics showed no significant differences between CAE children at follow-up and the HC group which indicated a clear renormalization of topological organization after AED treatments. CAE at follow-up also showed significantly decreased connectivity between several network regions, with which the thalamus is mainly involved. Furthermore, the reduced connectivity change between the left superior parietal gyrus and the left thalamus is positively correlated with the symptom improvements after AED treatment. *Conclusion*. We highlighted the convergence and divergence of brain functional network dysfunctions in CAE patients and provided crucial insights into pathophysiological mechanisms and the AED effects.

1. Introduction

Childhood absence epilepsy (CAE) is the most common pediatric epilepsy syndrome, and its clinical features are transient (10-20 s) nonconvulsive seizures with impairment of consciousness [1]. Electrographically, absence seizures are characterized by a typical pattern of generalized 3 Hz spike and wave bursts with normal background activity [2]. Recently, noninvasive techniques of functional magnetic resonance imaging (fMRI) have played an important role in

studying the neural mechanisms of epilepsy in the human brain [3]. Numerous efforts have been made to identify focal abnormalities of brain activity in CAE children, and higher-order association cortices (frontal cortex, parietal cortex) and subcortical (thalamus and putamen) and cerebellar regions are found to be the crucial regions in the initiation and propagation of absence seizure in patients with CAE [4]. However, CAE is thought of a dysconnectivity disorder in multiple connection circuits rather than a focal disturbance in a single brain area, and impairments of cortical-subcortical pathways have been identified [5]. As a powerful quantitative method for explaining the topological architecture of complex brain networks, graph-based connectivity analysis can reveal topological disorganization in the whole-brain network that can serve as markers for clinical diagnostic and also disease outcome estimation [6].

Medication is the primary and most commonly used treatment. The mainstay of treatment for epilepsy is antiepileptic drugs (AEDs). Ethosuximide (ETX), valproic acid (VPA), and lamotrigine (LTG) are commonly used to treat CAE [2]. However, few studies have evaluated longitudinal changes in brain activity after AED treatment. Investigations of brain changes before and after treatment can not only improve our understanding of the mechanisms and recovery of seizures but also help monitor treatment outcomes and guide the choice of the best treatment. Therefore, question raises that how the network architecture was influenced in children of CAE and whether the aberrant network organization could be adjusted along with clinical improvement after treatment.

Functional segregation and functional integration are two major fundamental organization principles of human brain functional network [7]. Functional segregation, which included clustering coefficient (Cp), normalized clustering coefficient (γ), and local efficiency (El), indicated specialized processing within interconnected brain regions, and functional integration, which included characteristic path length (Lp), normalized characteristic path length (λ), and global efficiency (Eg) indicated different brain areas in terms of functional and effective connectivity. The balance between segregation and integration is vital for effective information processing and synthesis. Another important principle of human functional network is small-worldness ($\sigma = \gamma/\lambda$), which is characterized by a high global integration and a high local specialization between brain regions. These characteristics enable the brain network to meet local and global demands and balance functional integration and segregation in order to achieve synchronization of neural activity between different brain regions. Some findings have been observed for temporal lobe epilepsy and epilepsy; however, few studies have studied the topological differences between CAE children and healthy controls and investigated the longitudinal network reorganization after AED treatment.

To address these issues, the current study employed resting-state fMRI and graph theoretical approaches to investigate topological organization of whole-brain function networks in a group of CAE children who obtained resting-state fMRI data before and after AED treatment. We hypothesized that (1) CAE children would demonstrate reduced functional segregation and impaired network integration compared to healthy children. (2) These abnormal activities might reorganize after AED treatment, and (3) these network abnormalities would be associated with the clinical efficacy of AEDs.

2. Methods

2.1. Subjects. Thirty-five children (20 males) diagnosed as childhood absence epilepsy were recruited. Clinical diagnosis was based on the International League against Epilepsy (ILAE) classification and confirmed by EEG data. Subjects were excluded if they have other psychiatric, neurological diseases or any structural abnormalities detected by routine MRI examination. At 40-50 weeks after first fMRI recording, we performed follow-up assessments of all patients and gathered information about AEDs and prognosis. In addition, thirty age- and gender-matched healthy controls (HCs) were recruited by advertisement. The Shandong Provincial Hospital affiliated to Shandong First Medical University approved the present study. All participants and their guardians signed written informed consent forms.

2.2. Functional Magnetic Resonance Imaging Data Acquisition. GE 3.0 Tesla Discovery MR scanner with an eight-channel-phased array head coil (EXCITE, General Electric, Milwaukee, Wisconsin) was used to collect the imaging data. The subjects were asked to stay still and to stay awake during the entire session [3]. Using the gradient-echo planar imaging sequence, the resting-state functional images were obtained with the following parameters: repetition time = 2000 ms, echo time = 30 ms, field of view = 240 mm × 240 mm, data matrix = 64 × 64, slices = 33, and total 210 volumes. Using a volumetric three-dimensional spoiled gradient recall sequence, the high-resolution T1-weighted image was also acquired with the following parameters: repetition time = 8.2 ms, echo time = 3.2 ms, field of view = 256 × 256 mm [2], matrix = 128 × 128, slice thickness = 1 mm, and 196 slices in the axial plane. Same parameters were used for scans of follow-up assessment of CAE children and for healthy controls.

2.3. fMRI Data Preprocessing. Preprocessing of fMRI data was conducted using the Data Processing and Analysis for Brain Imaging (DPABI) which synthesizes procedures in the Resting-State fMRI Data Analysis Toolkit (REST; http://www.restfmri.net) and Statistical Parametric Mapping (SPM12; http://www.fil.ion.ucl.ac.uk/spm) [8]. The first 10 images were removed to allow for magnetization equilibrium. The remaining 200 images were subjected to slice time correction, realigned motion (data were excluded if head motion exceeded 2 mm and 2°). Due to the heavy head motions, five CAE children were excluded for further analysis, and the final sample size includes 30 CAE children and 30 HCs. Individual T1-weighted images were coregistered to the mean of the realigned EPI images. The transformed T1 images were then segmented into gray matter, white matter, and cerebrospinal fluid. The diffeomorphic anatomical

TABLE 1: Demographics of the CAE patient.

Patients	Sex	Onset age	Seizure frequency	AEDs before MRI scan	Initial AEDs	AEDs added	Follow-up (weeks)
1	F	11	12	No	LTG	No	43
2	M	6	6	No	VPA	No	55
3	F	7	9	No	LTG	VPA	54
4	M	9	8	No	VPA	No	50
5	M	10	2	No	VPA	No	36
6	M	8	6	No	LTG	No	45
7	F	7	5	No	LTG	Lost	46
8	M	9	7	No	LTG	VPA	40
9	F	11	2	No	LTG	No	51
10	F	6	8	No	Lost	No	53
11	M	8	9	No	VPA	No	39
10	M	7	2	No	VPA	No	42
13	F	7	11	No	LTG	No	48
14	F	8	3	No	LTG	VPA	49
15	F	6	8	No	VPA	LTG	52
16	M	9	2	No	VPA	LTG	57
17	M	9	12	No	LTG	LEV	56
18	F	8	20	No	VPA	No	32
19	M	10	6	No	LTG	No	50
20	M	11	8	No	LTG	No	48
21	F	9	9	No	LTG	No	49
22	F	6	7	No	VPA	No	43
23	M	5	9	No	VPA	LTG	47
24	M	3	6	No	VPA	No	37
25	F	6	13	No	LTG	No	41
26	F	8	20	No	Lost	No	46
27	F	7	9	No	LTG	No	47
28	M	5	15	No	VPA	LTG	36
29	M	3	16	No	VPA	No	46
30	F	10	13	No	LTG	No	49

registration through exponentiated Lie algebra (DARTEL) tool was used to compute the transformation from individual space to MNI space and vice versa.

Resting-state fMRI measures were sensitive to microhead motions [9]. Therefore, the higher-level Friston-24 model (the 24 parameters include 6 head motion parameters, 6 head motion effects one time point before, and the 12 corresponding squared items) was regressed out of the realigned data. In addition, the mean frame-wise displacement (FD) was calculated as a measure of the microhead motion of each subject. Then, the nuisance signals were regressed out, including the average signals from the ventricles and white matter. We then spatially smoothed the images with a 6 mm full-width half-maximum isotropic Gaussian kernel. Finally, linear trends were removed from the time courses and temporal band-pass filtering was performed (0.01–0.08 Hz) [10].

2.4. Network Construction. GRETNA (http://www.nitrc.org/ projects/gretna/) were used to analyze the network properties

using graph theory [11]. Particularly, the automated anatomical labeling (AAL) atlas was used to parcellate the brain into 90 regions of interest (ROI). Pearson correlation coefficients between time series of all possible pairs of ROI were calculated, yielding a 90×90 correlation matrix for each participant. To ensure the number of nodes and connections were matched across participants, we used a sparsity threshold ($8\% \leq s \leq 50\%$) at the intervals of 0.01 to transform each correlation matrix into an undirected binarized matrix. Then, we computed the following measures: (1) the functional segregation metrics: clustering coefficient (Cp), normalized clustering coefficient (γ), and local efficiency (El); (2) functional integration metrics: characteristic path length (Lp), normalized characteristic path length (λ), and global efficiency (Eg); and (3) small-worldness metric: σ ($\sigma = \gamma/\lambda$). Similar with a previous study, we calculated the area under the curve (AUC) of for each network metric for further statistical comparisons [12]. Independent of single threshold selection, the AUC metric provides a summarized scalar for topological characterization of brain networks.
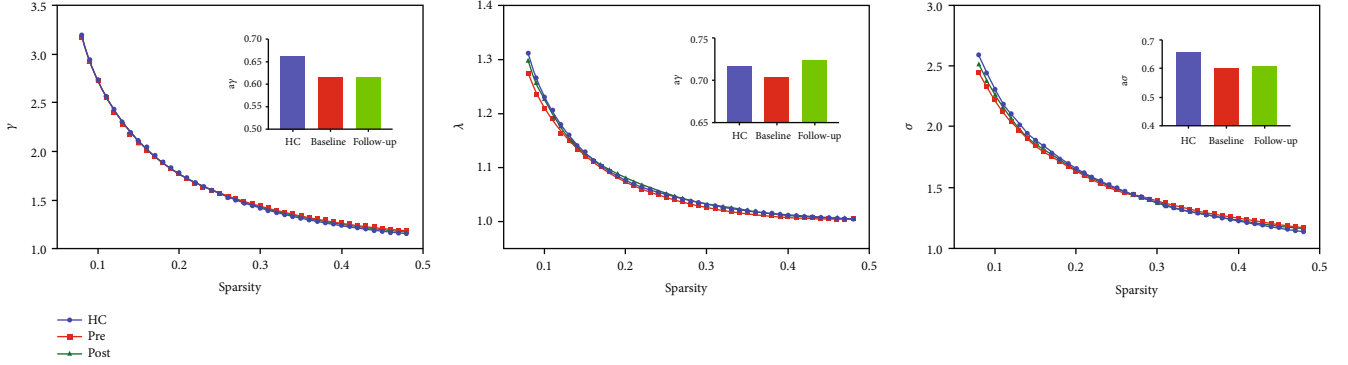
FIGURE 1: The typical small-world network architectures ($\gamma > 1$, $\lambda \approx 1$, and $\sigma > 1$) across the sparsity. Blue lines represent the healthy controls, red lines represent the CAE children at baseline, and green lines represent CAE children at follow-up. No significant differences were found across the three groups.
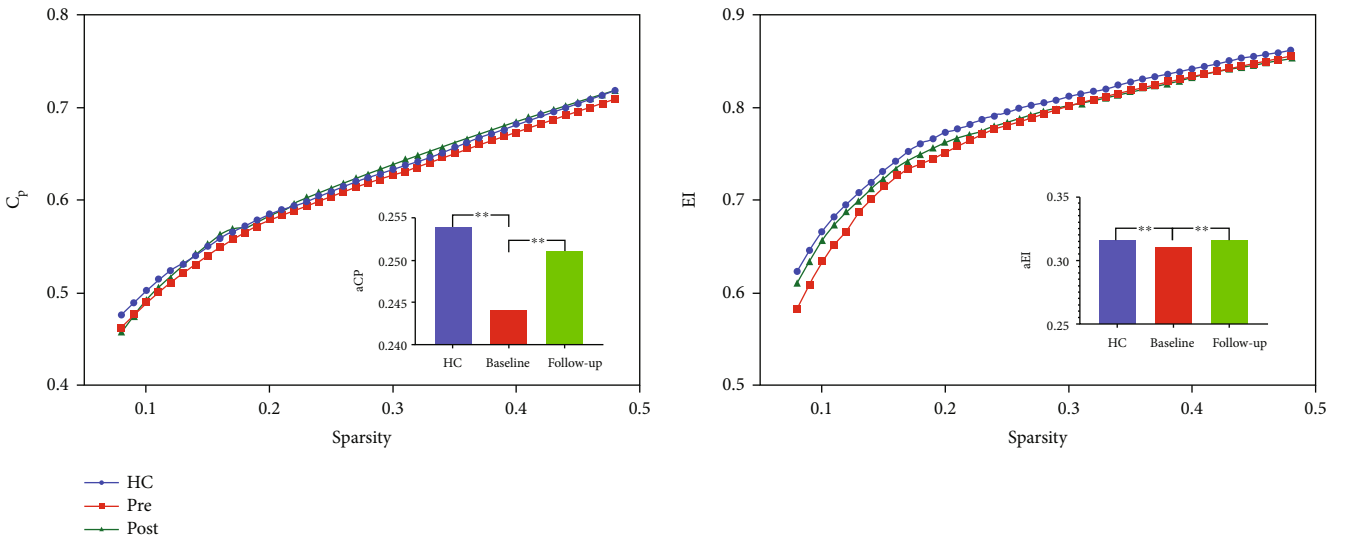
FIGURE 2: Functional segregation metrics Cp and El. The bar graph shows the value of significant AUC of the functional segregation parameters among the 3 groups. Black asterisks indicate significant differences ($p < 0.001$).

2.5. *Statistical Analysis.* The chi-square test and Student's t-test were utilized to examine group differences in demographic characteristics and clinical data at baseline between patients and healthy controls with SPSS (IBM SPSS Statistics for Windows, version 18.0, IBM Corp.). For detection of between-group differences in global network measures, a two-sample t-test (healthy controls vs. patients from baseline; healthy controls vs. patients at follow-up) or paired t-test (baseline vs. follow-up) was used to identify the changes of AUC for each network metric. The threshold for significance was $p < 0.05$, corrected with the FDR criterion. The mean frame-wise displacement (FD) calculated during the preprocessing step was accounted by including this term as a covariate for each comparison. Finally, a network-based statistic (NBS) approach was used to determine any interregional connection that was significantly changed across the three groups [13].

Values of AUC for each network metric and each pairwise connectivity showing abnormal differences were extracted, and Pearson correlation coefficients were used to examine the associations between the changes in each network metric and clinical scores using SPSS. Correction for multiple comparisons was accomplished using the false discovery rate (FDR) method, with the "mafdr" script implemented in MATLAB [14].

3. Results

3.1. Demographic Information. All participants (CAE children and healthy controls) recruited in the current study are right-handed. The mean seizure frequency was 8.69 times each day, the mean age onset was 7.77 years, and the mean follow-up time was 46.03 weeks. The treatments for each CAE child are listed in Table 1. The mean FD values calculated during fMRI preprocessing showed no significant differences across the three groups ($p = 0.70$).

3.2. Small-World Properties. Seven topologic small-world parameters were determined under a sparsity of 0.08 to 0.48 with an interval of 0.01. As shown in Figure 1, all the
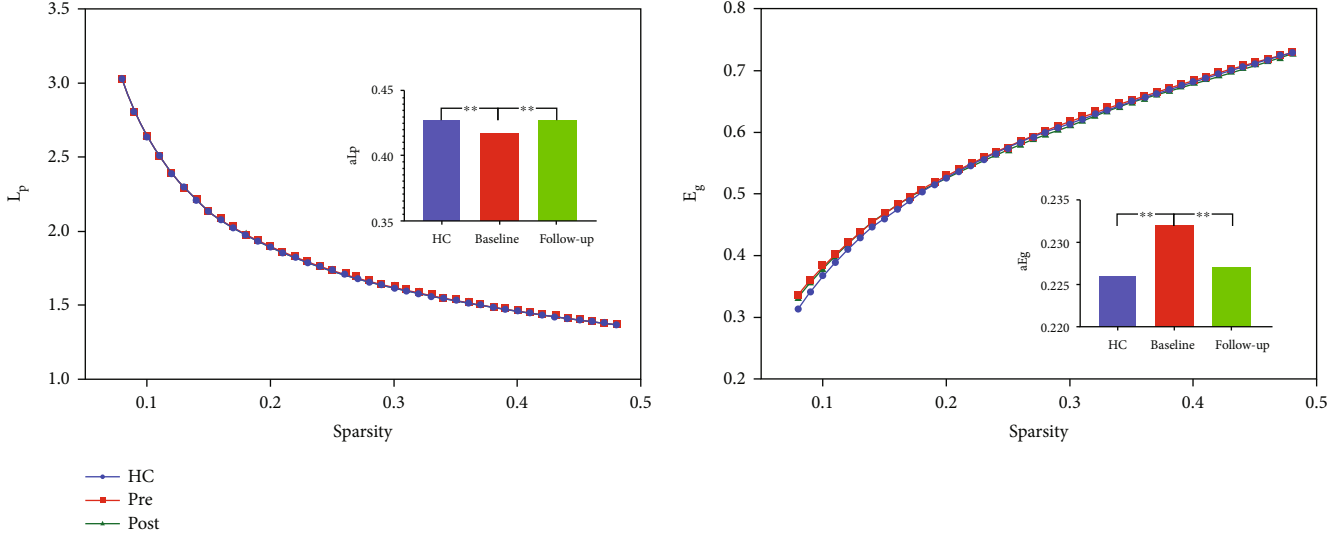
FIGURE 3: Functional integration metrics Lp and Eg. The bar graph shows the value of significant AUC of the functional segregation parameters among the 3 groups. Black asterisks indicate significant differences ($p < 0.001$).

three groups had small-world properties ($\lambda > 1$, $\gamma > 1$, and $\sigma > 1$); however, no significant differences were found across the three groups. Significant differences were found for the functional segregation metrics Cp and El, and two-sample t-test indicated that CAE children at baseline showed reduced Cp ($t = -4.29$, $p < 0.001$) and El compared with HCs ($t = -3.47$, $p < 0.001$), whereas paired t-test indicated that CAE children at follow-up showed increased Cp ($t > 5$, $p < 0.001$) and El ($t = 3.30$, $p < 0.001$) compared with baseline; no significant differences were found between CAE children at follow-up and HCs, and results are shown in Figure 2. For functional integration metrics Lp and Eg, similar comparison results were found. CAE children at baseline showed decreased Lp compared with HCs (two-sample t-test, $t = -3.19$, $p < 0.001$) and follow-up (paired t-test, $t = -3.19$, $p < 0.001$); as for Eg, CAE children at baseline are higher than HCs (two-sample t-test, $t = 4.01$, $p < 0.001$) and follow-up (paired t-test, $t > 5$, $p < 0.001$), and results are shown in Figure 3.

3.3. Connectivity and Correlation Results. Compared to the baseline, CAE patients at follow-up showed decreased brain functional connectivity (Figures 4(a)–4(c)). These mainly occurred among the left olfactory (OLF), left amygdala (AMYG), right cuneus (CUN), bilateral fusiform (FFG), superior parietal gyrus (SPG), inferior parietal gyrus (IPL), right supramarginal gyrus (SMG), left putamen (PUT), bilateral pallidum (PAL), right superior temporal pole (TPOsup), bilateral middle temporal gyrus (MTG), right middle temporal pole (TPOmid), left medial superior frontal gyrus (SFGmed), and bilateral thalamus (THA). Those differences are statistically significant under NBS correction ($p < 0.05$). Furthermore, significant positive correlation was found between the change of epilepsy frequency and change of correlation coefficient between the left superior parietal gyrus and the left thalamus (Figure 4(d)).

4. Discussion

This study explores the abnormalities of brain network architecture and AED effect on CAE children using resting-state fMRI. At baseline, significantly reduced functional segregation and integration were found whereas these abnormalities showed a clear rebound at follow-up. Decreased region-region connectivity was also found, which is mainly involved the thalamus. Furthermore, the connectivity change between the left superior parietal gyrus and the left thalamus is positively correlated with the symptom improvements after AED treatment. Our results suggest that the involvement of specific regions in cortical and subcortical networks may be associated with the mechanisms of seizure generation and the neurological deficits observed in CAE patients and might shed new light about the AED effects on CAE patients.

Numerous efforts have been made to identify focal abnormalities of the brain in CAE children. However, CAE is thought of as a dysconnectivity disorder in multiple neuronal circuits rather than a focal pathology in a single region [15]. Modeling the brain as a complex network in the context of graph theory will help to reveal topological disorganization in the whole-brain networks. Functional segregation and functional integration refer to the ability for local specialization and parallel information transfer in the brain network, respectively. One of the most significant characteristics of the healthy human brain network is a short path length and high transmission efficiency, known as small-world attributes. A balance between local segregation and global integration of signals associated with interconnected neurons allows efficient information transmission at low wiring cost and enables the brain network to meet local and global demands in order to achieve synchronization of neural activity between different brain regions. Both El and Cp are the metrics of functional segregation. The present study found that CAE children exhibited reduced local network efficiency

(a)

(b)

(c)

(d)
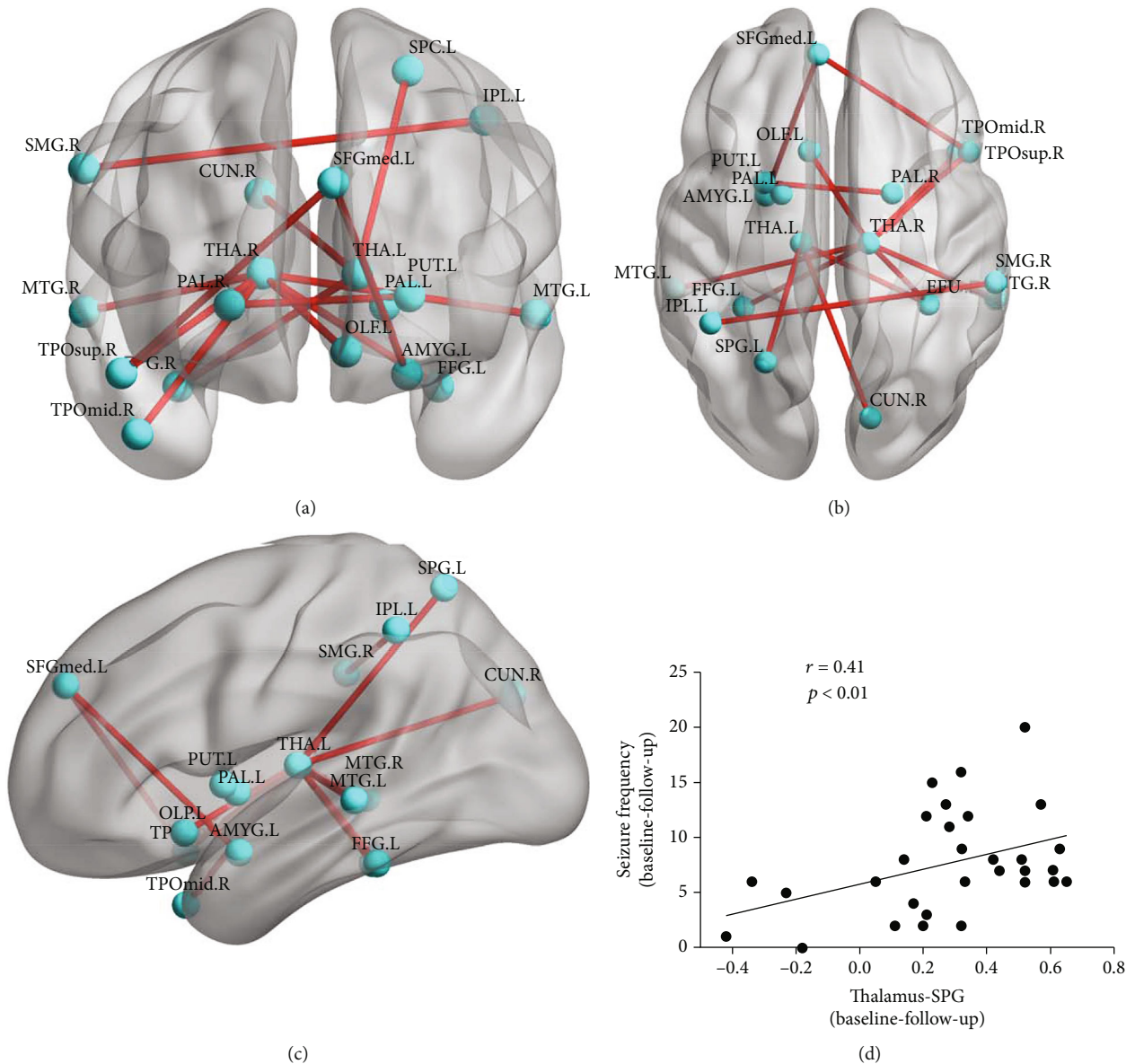
FIGURE 4: (a–c) Reduced connectivity after AED treatment. (d) Correlation results between the connectivity change from the left superior parietal gyrus to the left thalamus and the symptom improvements after AED treatment.

(lower Cp and El), which indicate that the efficiency or "speed" of information transfer among the adjacent nodes, and the density of the local interconnectivity within a network is compromised. It might be plausible that the observed reduced local communication efficiency (functional segregation) of brain functional networks may arise from neurodevelopmental dysfunction such as excessive synaptic pruning in CAE children [16]. CAE patients also demonstrated abnormal enhanced functional integration (lower Lp and higher Eg) in the brain network. As functional integration ensures interregional prompt transfer of information in brain networks, the abnormal functional integration might lead to cognitive maldevelopment of higher-order cognitive tasks and conscious processing.

The significant connectivity changes in the thalamus are consistent with the known important role of the subcortical structure in the generalization of epileptic seizures [17]. The thalamus is involved in absence seizures as ictal activity during absence seizures has been found to propagate through cortico-thalamic-cortical pathways. The generation of absence seizures has been explained by a highly synchronized functional interplay between discrete thalamocortical regions [18]. Previous studies have found abnormalities of the thalamus in CAE patients including less GM volume [19], neuronal metabolic dysfunction, and white matter microstructural properties (fractional anisotropy) in the bilateral thalamus [20]. Long-term use of antiepileptic drugs may affect functional changes in CAE patients. A previous study reported similar results that significantly altered network organizations in the thalamus were found after surgery [21]. Another study that analyzed EEG characteristics in children with benign epilepsy reported significantly

reduced discharges and significantly improved EEG findings after treatment [22]. As one core hubs in the brain network, the findings of the thalamus led us to conclude that these interventions may exert a therapeutic effect by engaging these disconnected hubs within the network architecture of the brain.

The bilateral middle temporal gyrus, the right middle temporal pole, and the left medial superior frontal gyrus are the main regions of default mode network (DMN). The absence seizures in CAE mainly arise from regions of the brain that are associated with conscious awareness, and the DMN has been shown to be more significantly influenced than other resting-state networks. Using seed-based analysis and independent component analysis, previous studies have indicated the disruption of DMN in CAE [23, 24]. Consistent with these previous studies, the finding on the DMN core regions suggests that the graph theory-based evaluation of functional brain networks can provide detailed insight into the activity of a pathological brain and can also be regarded as a support for further treatment.

5. Conclusion

We showed a normalization of the brain network architecture in patients with childhood absence epilepsy after AED treatments, based on the findings of clear rebound of functional segregation, functional integration, and reduced connectivity within cortico-thalamic-cortical pathways. In addition, our results indicated the graph-theory-based analysis can serve as a sensitive measure to provide crucial insights into pathophysiological mechanisms of CAE.

Data Availability

The datasets generated during and/or analyzed during the current study are available from the corresponding author on reasonable request.

Conflicts of Interest

There are no conflicts of interest.

Authors' Contributions

Xueyu Wang and Peng Fang contributed equally to this work.

Acknowledgments

References

[1] A. T. Knox, T. Glauser, J. Tenney, W. W. Lytton, and K. Holland, "Modeling pathogenesis and treatment response in childhood absence epilepsy," *Epilepsia*, vol. 59, no. 1, pp. 135–145, 2018.

[2] H. Hwang, H. Kim, S. H. Kim et al., "Long-term effectiveness of ethosuximide, valproic acid, and lamotrigine in childhood absence epilepsy," *Brain and Development*, vol. 34, no. 5, pp. 344–348, 2012.

[3] J. R. Tenney, D. S. Kadis, W. Agler et al., "Ictal connectivity in childhood absence epilepsy: associations with outcome," *Epilepsia*, vol. 59, no. 5, pp. 971–981, 2018.

[4] C. Wu, J. Xiang, J. Sun et al., "Quantify neuromagnetic network changes from pre-ictal to ictal activities in absence seizures," *Neuroscience*, vol. 357, pp. 134–144, 2017.

[5] W. Jiang, C. Wu, J. Xiang et al., "Dynamic neuromagnetic network changes of seizure termination in absence epilepsy: a magnetoencephalography study," *Frontiers in Neurology*, vol. 10, p. 703, 2019.

[6] M. Yu, Z. Dai, X. Tang et al., "Convergence and divergence of brain network dysfunction in deficit and non-deficit schizophrenia," *Schizophrenia Bulletin*, vol. 43, no. 6, pp. 1315–1328, 2017.

[7] J. Duan, M. Xia, F. Y. Womer et al., "Dynamic changes of functional segregation and integration in vulnerability and resilience to schizophrenia," *Human Brain Mapping*, vol. 40, no. 7, pp. 2200–2211, 2019.

[8] C. Yan, X. Wang, X. Zuo, and Y. Zang, "DPABI: data processing & analysis for (resting-state) brain imaging," *Neuroinformatics*, vol. 14, no. 3, pp. 339–351, 2016.

[9] Y. Zhu, Z. Feng, J. Xu et al., "Increased interhemispheric resting-state functional connectivity after sleep deprivation: a resting-state fMRI study," *Brain Imaging & Behavior*, vol. 10, no. 3, pp. 911–919, 2016.

[10] K. Song, J. Li, Y. Zhu et al., "Altered small-world functional network topology in patients with optic neuritis: a resting-state fMRI study," *BioRxiv*, 2020.

[11] J. Wang, X. Wang, M. Xia, X. Liao, A. Evans, and Y. He, "GRETNA: a graph theoretical network analysis toolbox for imaging connectomics," *Frontiers in Human Neuroscience*, vol. 9, p. 386, 2015.

[12] L.-X. Wang, F. Guo, Y.-Q. Zhu et al., "Effect of second-generation antipsychotics on brain network topology in first- episode schizophrenia: a longitudinal rs-fMRI study," *Schizophrenia Research*, vol. 208, pp. 160–166, 2019.

[13] A. Zalesky, A. Fornito, and E. T. Bullmore, "Network-based statistic: identifying differences in brain networks," *NeuroImage*, vol. 53, no. 4, pp. 1197–1207, 2010.

[14] Y. Zhu, Y. Xi, J. Sun et al., "Neural correlates of dynamic changes in working memory performance during one night of sleep deprivation," *Human Brain Mapping*, vol. 40, no. 11, pp. 3265–3278, 2019.

[15] X. Wang, D. Jiao, X. Zhang, and X. Lin, "Altered degree centrality in childhood absence epilepsy: a resting-state fMRI study," *Journal of the Neurological Sciences*, vol. 373, pp. 274–279, 2017.

[16] M. Andoh, Y. Ikegaya, and R. Koyama, "Synaptic pruning by microglia in epilepsy," *Journal of Clinical Medicine*, vol. 8, no. 12, p. 2170, 2019.

[17] V. Youssofzadeh, W. Agler, J. R. Tenney, and D. S. Kadis, "Whole-brain MEG connectivity-based analyses reveals critical hubs in childhood absence epilepsy," *Epilepsy Research*, vol. 145, pp. 102–109, 2018.

[18] V. Menon, "Large-scale brain networks and psychopathology: a unifying triple network model," *Trends in Cognitive Sciences*, vol. 15, no. 10, pp. 483–506, 2011.

[19] H. Pardoe, G. S. Pell, D. F. Abbott, A. T. Berg, and G. D. Jackson, "Multi-site voxel-based morphometry: methods and a feasibility demonstration with childhood absence epilepsy," *NeuroImage*, vol. 42, no. 2, pp. 611–616, 2008.

[20] T. Yang, Z. Guo, C. Luo et al., "White matter impairment in the basal ganglia-thalamocortical circuit of drug- naive childhood absence epilepsy," *Epilepsy Research*, vol. 99, no. 3, pp. 267–273, 2012.

[21] Y. Li, Z. Tan, J. Wang et al., "Alterations in spontaneous brain activity and functional network reorganization following surgery in children with medically refractory epilepsy: a resting-state functional magnetic resonance imaging study," *Frontiers in Neurology*, vol. 8, p. 374, 2017.

[22] Z. Zhang, Q. Xu, G. Lu, W. Liao, Z. Wang, and Q. Jiao, "Dynamic functional MRI study of absence seizures," *Chinese Journal of Magnetic Resonance Imaging*, vol. 4, pp. 3–7, 2013.

[23] C. Luo, Q. Li, Y. Lai et al., "Altered functional connectivity in default mode network in absence epilepsy: a resting-state fMRI study," *Human Brain Mapping*, vol. 32, no. 3, pp. 438–449, 2011.

[24] T. Yang, C. Luo, Q. Li et al., "Altered resting-state connectivity during interictal generalized spike-wave discharges in drug-naïve childhood absence epilepsy," *Human Brain Mapping*, vol. 34, no. 8, pp. 1761–1767, 2013.

Research Article

Enhanced Visualization of Retinal Microvasculature via Deep Learning on OCTA Image Quality

Yishuang Xu [ID],[1,2] **Yu Su** [ID],[1] **Dihao Hua** [ID],[1,2] **Peter Heiduschka** [ID],[2] **Wenliang Zhang** [ID],[2] **Tianyue Cao** [ID],[1] **Jingcheng Liu** [ID],[3] **Zhenyu Ji** [ID],[1] and **Nicole Eter** [ID][2]

[1]*Eye Center, Renmin Hospital of Wuhan University, Wuhan, China*
[2]*Department of Ophthalmology, University of Muenster Medical Center, Muenster, Germany*
[3]*Department of Endocrinology & Metabolism, Renmin Hospital of Wuhan University, Wuhan, China*

Correspondence should be addressed to Zhenyu Ji; happyjzy@whu.edu.cn and Nicole Eter; nicole.eter@ukmuenster.de

Purpose. To investigate the impact of denoising on the qualitative and quantitative parameters of optical coherence tomography angiography (OCTA) images of the optic nerve and macular area. *Methods.* OCTA images of the optic nerve and macular area were obtained using a Canon-HS100 OCT device for 48 participants (48 eyes). Multiple image averaging (MIA) and denoising techniques were used to improve the quality of the OCTA images. The peak signal-to-noise ratio (PSNR) as an image quality parameter and vessel density (VD) as a quantitative parameter were obtained from single-scan, MIA, and denoised OCTA images. The parameters were compared, and the correlation was analyzed between different imaging protocols. *Results.* In the optic nerve area, there were significant differences in the PSNR and VD in all measured regions between the three groups ($P < 0.0001$). The PSNR of the denoised group was significantly higher than that of the other two groups ($P < 0.0001$). The VD in the denoised group was significantly lower than that in the single-scan group in all measured regions ($P < 0.0001$). In the macular area, there were significant differences in the PSNR and VD in all measured regions among the three groups. The PSNR of the denoised group was significantly higher than that of the other two groups ($P < 0.0001$). The VD in the denoised group was significantly lower than that in the single-scan group in all measured regions. The VD around the optic nerve in the denoised group was correlated with that in the single-scan group ($R = 0.9403$, $P < 0.0001$), but the VD in the MIA group was not correlated with that in the single-scan group ($R = 0.2505$, $P = 0.2076$). The VD around the fovea in the denoised and MIA images was correlated with that in the single-scan group ($R = 0.7377$, $P < 0.0001$; $R = 0.7005$, $P = 0.0004$, respectively). *Conclusion.* Denoising could provide an easy and quick way to improve image quality parameters, such as PSNR. It shows great potential in improving the sensitivity of OCTA images as retinal disease markers.

1. Introduction

Optical coherence tomography angiography (OCTA) is a noninvasive imaging method that offers depth-selective and three-dimensional mapping of the retinal microvasculature without dye injection [1]. OCTA provides microvasculature images with higher contrast and better resolution than with fluorescein angiography; furthermore, it contributes to the quantitative evaluation of retinal microvasculature [2]. Currently, OCTA images and quantitative parameters, such as vessel density (VD), have become important markers for retinal disease, and the detailed information of blood flow it

provides has contributed greatly to the early detection of multiple eye diseases [3–5].

The quality of OCTA images is crucial for the accurate interpretation of morphological changes in the retinal vasculature and also affects the quantitative analysis results; therefore, improvement of image quality has become a hot research topic [6, 7]. Several protocols have been used to evaluate the image quality of OCTA, including objective evaluations, such as single strength, contrast-to-noise ratio (CNR), and peak signal-to-noise ratio (PSNR), and subjective retinal expert evaluation [8–11]. Of these, the PSNR is one of the most outstanding and widely used objective

parameter of image quality evaluation between different images [11, 12]. Recently, it has been reported that multiple en face image averaging (MIA) techniques were able to increase the PNSR of OCTA images, which indicates an improvement in image quality. This technique allows the extraction of a false positive flow signal from multiple images, which lowers the background noise and enhances the positive signal to anneal discontinuous vessel segments [12, 13]. However, acquiring multiple images requires a longer time, which makes it less practical in clinical applications owing to the higher demand of patients' tolerance [13].

Deep learning has become the most common artificial intelligence (AI) techniques, and it shows great potential for automated data analysis and improved image quality [11]. Numerous paired single-scan OCTA and MIA images were applied to deep learning training to develop an algorithm for denoising images. Therefore, an MIA image could be generated from a single-scan image without acquiring multiple OCTA images by using this algorithm [14]. The OCT-HS100 (Canon, Tokyo, Japan), commercialized in recent years, has built-in software to average multiple OCTA images and acquire denoised images using deep learning. It provides a convenient method for the application of the denoising technique in clinical settings. Although previous studies have reported that denoised images show lower background noise and higher image quality than that of single-scan images of the macular area [11, 14], the influence of denoising using commercially available devices on the qualitative and quantitative parameters of the images of both macular and optic areas has not been investigated. The VD is considered an important marker for the early detection of multiple eye diseases; for example, the VD in the macular area can help detect retinal damage in patients with diabetes and hypertension at an early stage, and the VD in the optic area can help in the early diagnosis of glaucoma [3–5]. Thus, the VD in both macular and optic areas acquired from denoised images needs to be verified as credible data before its application in the clinical setting.

Therefore, in this study, we aimed to evaluate the effect of denoising on the qualitative and quantitative parameters of OCTA images in both macular and optic areas by using OCT-HS100, to elucidate if denoising could provide a promising improvement in image quality and reliable quantitative data, and further facilitate the clinical practice with OCTA images as a retinal disease marker.

2. Methods

2.1. Subjects. Forty-eight eyes of 48 healthy subjects were prospectively included in this study. Eyes with dense lens opacities, corneal opacities, refractive surgery, or a history of intraocular inflammation were excluded. The optic nerve area was scanned in 27 eyes of 27 patients, and the macular area was scanned in 21 eyes of 21 patients. Informed consent was obtained from each enrolled study patient, and the procedures adhered to the tenets of the Declaration of Helsinki.

2.2. Optical Coherence Tomography Angiography Imaging. The OCT-HS100 (Ophthalmic Software Platform RX V4.5)

TABLE 1: Demographic information.

	Optic	Macular
Subjects (*N*)	27	21
Eyes (*N*)	27	21
Age (years)	50.49 ± 13.00	56.29 ± 14.12
Gender (F/M)	13/14	10/11

Notes: age is presented as mean ± SD. Abbreviation: F: female; M: male; SD: standard deviation.

built-in software offers a specialized acquisition mode to repeatedly capture consecutive OCTA cube scans at the same position in a short time and can compound multiple OCTA images into a single high-quality image. In addition, this built-in software offers a "denoised OCTA image" assisted by deep learning. In this study, a $3 \times 3 \, mm^2$ scan was chosen for the macular area exam, and a $4.5 \times 4.5 \, mm^2$ scan was chosen for an optic nerve area exam. OCTA imaging was performed by an experienced examiner, and each patient underwent several scans until five OCTA scans that met the criteria were obtained. Images of poor quality (signal strength < 6, motion artifact score (MAS) of 3 or 4, or segmentation errors) were excluded from the quantitative analysis. An MIA image was obtained by choosing five images and applying the MIA function. A denoised image was obtained by choosing one image and applying the denoised function. The PSNR was also recorded and is expressed as the maximum signal divided by the standard deviation [15]. Images were exported and opened in ImageJ (histogram function). The maximum pixel value and standard deviation of the image luminance were calculated [12]. With the exception of PSNR, all measured values were automatically determined using the manufacturer's software.

2.3. Statistical Methods. Data management was performed using Microsoft Excel 2010 software. IBM SPSS Statistics 22 for Windows (IBM Corporation, Somers, NY, USA) was used for all statistical analyses. Continuous parametric variables are presented as means ± standard deviations (SD). Repeated-measure one-way analysis of variance (ANOVA) was used to compare the differences between the PSNR and the VD. Tukey's correction was used for multiple comparisons. Pearson's correlation coefficient was used to analyze the correlation between groups. Statistical significance was set at $P < 0.05$.

3. Results

3.1. Demographic Information. Forty-eight eyes of 48 subjects were prospectively included in this study. The optic nerve area was scanned in 27 patients, of which 13 were women (48.1%). The mean age of the subjects was 50.49 ± 13.00 years. The macular area was scanned in 21 patients; of these, 10 were women (47.6%), and the mean age was 56.29 ± 14.12 years (Table 1).

3.2. OCTA Parameters of the Optic Nerve Area. In the optic nerve area, there were significant differences in the PSNR

TABLE 2: OCTA parameters of the optic nerve area.

Optic nerve	Single	MIA	Denoise	F	P value*
PSNR	12.09 ± 0.23	12.82 ± 0.18	13.64 ± 0.26	550.00	<0.0001
Optic	48.34 ± 6.20	48.79 ± 4.63	43.39 ± 7.85	33.36	<0.0001
Superior	56.99 ± 1.97	51.14 ± 2.84	51.34 ± 2.20	87.05	<0.0001
Nasal	56.47 ± 2.78	51.65 ± 2.95	51.07 ± 2.41	69.35	<0.0001
Inferior	57.75 ± 1.69	52.07 ± 3.51	51.68 ± 1.69	71.51	<0.0001
Temporal	54.57 ± 2.97	47.62 ± 2.46	47.81 ± 2.65	197.90	<0.0001

Notes: *repeated-measure ANOVA was used to compare the differences in the PSNR and VD. Abbreviations: OCTA: optical coherence tomography angiography; PSNR: peak signal-to-noise ratio; MIA: multiple image averaging; VD: vessel density; ANOVA: analysis of variance.

and VD in all measured regions between the three groups ($P < 0.0001$); details are shown in Table 2.

Upon further comparison between the two groups, the PSNR of the denoised group was significantly higher than that of the other two groups ($P < 0.0001$). As for the VD, the denoised group had a significantly lower value than the single-scan group in all measured regions ($P < 0.0001$), and only a statistically significant decrease in the optic region was observed when comparing the denoised and MIA groups ($P < 0.0001$) (Table 3 and Figure 1).

A comparison of the optic area image between the three groups showed that the denoised image exhibited lower background noise and smoother vessels compared to the MIA and single-scan images, especially on the nasal side. A radial peripheral capillary was observed in the enlargement of the inferior temporal side of the optic nerve in a single-scan image, and it became vague in the MIA image and disappeared in the denoised image (Figure 2).

3.3. OCTA Parameters of the Macular Area. In the macular area, there were significant differences in the PSNR and VD in all measured regions between the three groups; the details are shown in Table 4.

Upon further comparison between the two groups, the PSNR of the denoised group was significantly higher than that of the other two groups ($P < 0.0001$). The VD of the denoised group was significantly decreased compared to that of the single-scan group in all measured regions. Interestingly, the VD in the denoised group was significantly lower in the foveal region compared to that of the MIA group ($P = 0.0001$), but was higher in the superior and inferior regions ($P < 0.0001$, $P = 0.0089$) (Table 5 and Figure 3).

Comparing the macular area image between the three groups showed that the denoised images exhibited lower background noise and smoother vessels compared to the MIA and single-scan images. In the enlargement of the avascular zone, a vessel dropped out in an MIA image and was enhanced in the denoised image, and enlargement of the temporal side showed a black shadow covering the blood flow signal in a single-scan image, which recovered in the MIA image, and persisted in the denoised image (Figure 4).

3.4. Correlation Analysis. The VD around the optic nerve in the denoised group was correlated with that in the single-scan group ($R = 0.9403$, $P < 0.0001$), but the VD of the

TABLE 3: Multiple comparison between groups in the optic nerve area.

Optic nerve		MIA*	Denoise*
PSNR	Single	<0.0001	<0.0001
	MIA		<0.0001
Optic	Single	0.7441	<0.0001
	MIA		<0.0001
Superior	Single	<0.0001	<0.0001
	MIA		0.9338
Nasal	Single	<0.0001	<0.0001
	MIA		0.6178
Inferior	Single	<0.0001	<0.0001
	MIA		0.8377
Temporal	Single	<0.0001	<0.0001
	MIA		0.9011

Notes: *Tukey correction was applied for multiple comparisons between two groups. Abbreviations: PSNR: peak signal-to-noise ratio; MIA: multiple image averaging.

MIA group was not correlated with that of the single-scan group ($R = 0.2505$, $P = 0.2076$). The VD around the foveal region in the denoised and MIA images were both correlated with that in the single-scan group ($R = 0.7377$, $P < 0.0001$; $R = 0.7005$, $P = 0.0004$, respectively) (Figure 5).

4. Discussion

OCTA is a noninvasive and fast tool to exhibit retinal microvasculature and has been widely applied in patients with optic and retinal diseases [1]. Morphological changes in retinal vascular and quantitative parameters, including vessel density in the OCTA images, have become an outstanding disease marker in the diagnosis and treatment of optic and retinal diseases. Recent studies have focused on the improvement of OCTA image quality and accordingly increase its sensitivity as a disease marker using different techniques. Among them, AI techniques have shown great prospects [6, 7, 11]. However, research on the application of AI to improve the OCTA image quality was limited in each research group, and the manufacturer's built-in AI denoising function has not been evaluated in the macular and optic nerve areas for practical clinical use.
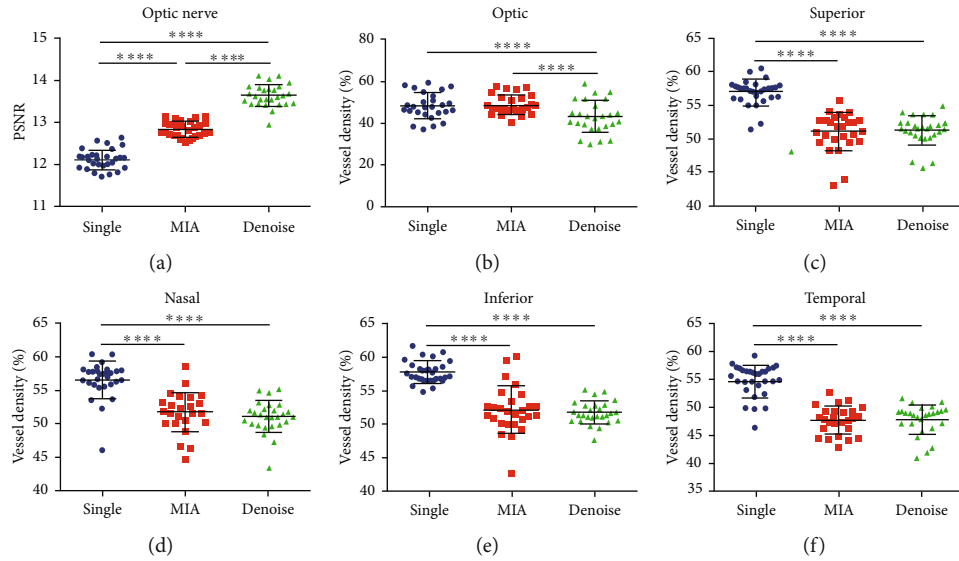
FIGURE 1: Comparison of three groups in the optic nerve area. Notes: (a) PSNR; (b–f) VD in the optic and superior, nasal, inferior, and temporal sides of the optic nerve. Data are presented as mean ± SD, ****$P < 0.0001$. Abbreviations: PSNR: peak signal-to-noise ratio; MIA: multiple image averaging; VD: vessel density; SD: standard deviation.
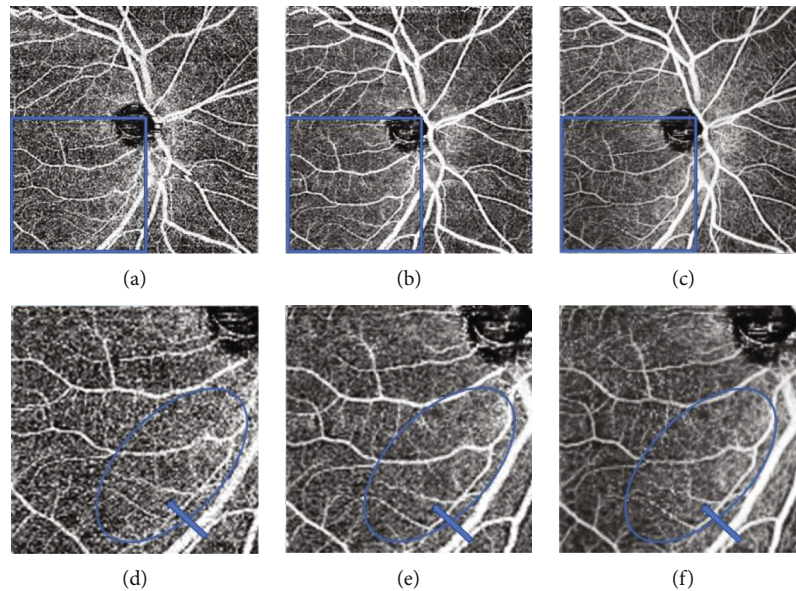
FIGURE 2: OCTA 4.5×4.5 mm^2 representative images in the optic nerve area of the same subject. Notes: (a, d) single-scan group, (b, e) MIA group, and (c, f) denoised group. (c) shows obviously less background noise and smoother vessels compared to those of (a) and (b), especially on the nasal side. The enlargement of the inferior temporal side of the optic nerve shows a radial peripheral capillary (d) (blue circle), which appeared vague in the MIA group (e) and disappeared in the denoised group (f). Abbreviations: OCTA: optical coherence tomography angiography; MIA: multiple image averaging.

Image quality has been evaluated objectively and subjectively in past researches. Subjective assessment is easily affected by varies reasons, such as the level of retinal expertise [9]. Objective assessment includes several protocols, such as single strength, CNR, and PSNR, of which the PSNR is one of the most outstanding and widely used objective parameter of image quality evaluation in different images [8, 10–12]. The PSNR is defined as the maximum signal divided by the standard deviation. The PSNR is generally used for a project between the maximum signal and the background noise. Higher PNSR value represents smaller distortion, indicating a higher image quality. Usually after image compression, the output image will be different from the original image to some extent. While evaluating the image quality after processing, the PSNR is usually used to ascertain whether a certain processing procedure is satisfactory. Therefore, in our

TABLE 4: OCTA parameters of macular area.

Macular	Single	MIA	Denoise	F	P value*
PSNR	12.37 ± 0.19	12.98 ± 0.37	13.87 ± 0.33	344.50	<0.0001
Foveal	28.32 ± 3.15	27.80 ± 2.38	25.85 ± 2.67	9.22	0.0035
Superior	46.71 ± 1.05	43.93 ± 1.66	45.3 ± 1.18	63.89	<0.0001
Nasal	44.52 ± 1.92	42.35 ± 1.88	42.74 ± 1.60	25.52	<0.0001
Inferior	46.10 ± 2.52	43.79 ± 1.94	44.88 ± 1.85	21.80	<0.0001
Temporal	43.74 ± 2.20	41.78 ± 1.49	42.24 ± 1.39	18.40	<0.0001

Notes: *repeated-measure ANOVA was used to compare the differences in the PSNR and VD. Abbreviations: OCTA: optical coherence tomography angiography; ANOVA: analysis of variance; PSNR: peak signal-to-noise ratio; MIA: multiple image averaging; VD: vessel density.

TABLE 5: Multiple comparison between groups in the macular area.

Macular		MIA*	Denoise*
PSNR	Single	<0.0001	<0.0001
	MIA		<0.0001
Foveal	Single	0.6470	0.0151
	MIA		0.0001
Superior	Single	<0.0001	<0.0001
	MIA		<0.0001
Nasal	Single	<0.0001	0.0002
	MIA		0.4388
Inferior	Single	<0.0001	0.0026
	MIA		0.0089
Temporal	Single	0.0001	0.0005
	MIA		0.3090

Notes: *Tukey correction was applied for multiple comparisons between two groups. Abbreviations: PSNR: peak signal-to-noise ratio; MIA: multiple image averaging.
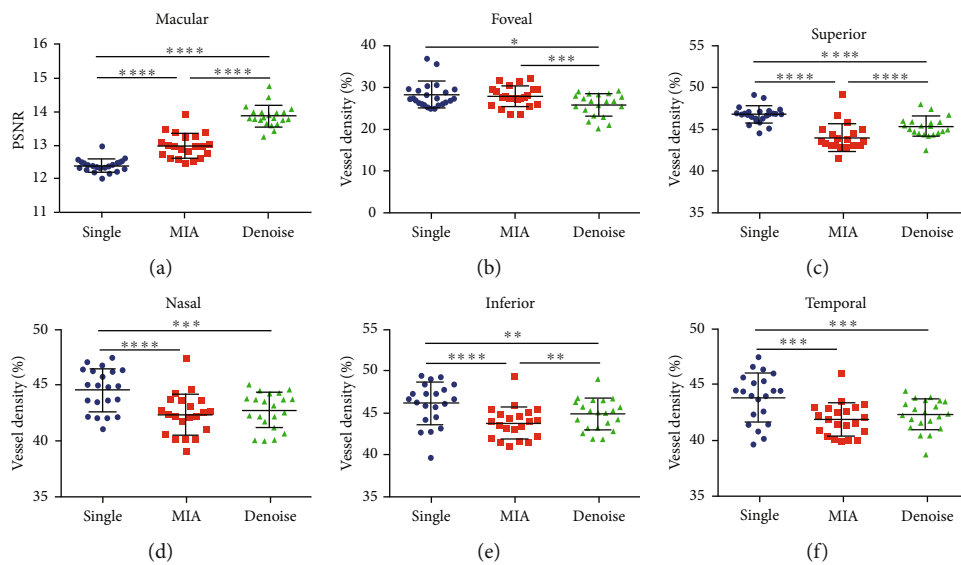
FIGURE 3: Comparisons of the three groups in the macular area. Notes: (a) PSNR; (b–f) VD in the foveal region and superior, nasal, inferior, and temporal side of the macula. Data are presented as mean ± SD, *P < 0.05, **P < 0.01, ***P < 0.001, and ****P < 0.0001. Abbreviations: PSNR: peak signal-to-noise ratio; MIA: multiple image averaging; VD: vessel density; SD: standard deviation.
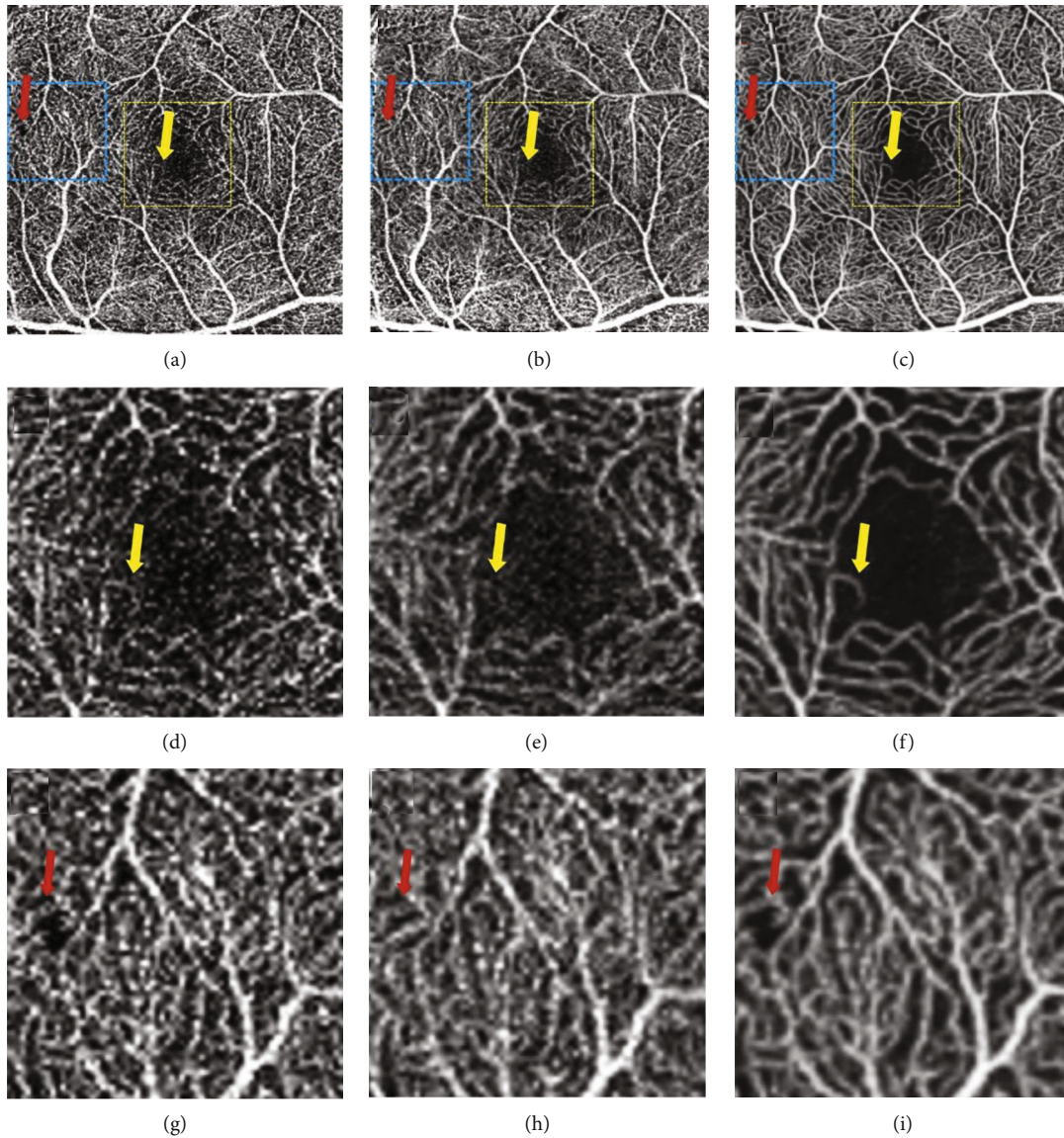
FIGURE 4: OCTA 3×3 mm^2 representative images on the macular area of the same subject. Notes: (a, d, g) single-scan group, (b, e, h) MIA group, and (c, f, i) denoised group. In the enlargement of the avascular zone (d–f), (f) shows obviously less background noise and smoother vessels compared with those of (d) and (e), and a vessel dropped out in the MIA group and enhanced in the denoised group (yellow arrow); enlargement of the temporal side shows a black shadow covering the blood flow signal in the single-scan group (g) (red arrow), which recovered in the MIA group (h), and persisted in the denoised group (i). Abbreviations: OCTA: optical coherence tomography angiography; MIA: multiple image averaging.

study, the PNSR was an ideal parameter to compare image quality between the original image and differently processed image [15]. In this study, we compared the impact of two different methods: denoising and MIA on OCTA image quality and VD in both macular and optic nerve areas. Our results showed that the PSNR was significantly higher in the denoised group than in the MIA and single-scan groups, indicating that denoising can improve OCTA image quality even better than MIA by reducing the background noise within a shorter time in both the optic nerve and the macular area. Previous studies also demonstrated better image quality in denoised images than in MIA images [11], which may be because the images used for image averaging have relatively low image quality. Thus, a well-trained denoised algorithm,

which outputs high-contrast images, improves the image quality to a greater extent than image averaging. We observed the enhancement of low signal flow in the denoised group, which was eliminated by image averaging (Figures 4(d)–4(f)). This also indicates a more accurate vessel exhibition in the denoised group than in the MIA group, which could improve the diagnosis of early retinal vasculature diseases, such as diabetic retinopathy.

In our study, a significantly lower VD was observed after denoising compared to single-scan OCTA images in both the macular and optic nerve areas. A previous study reported that the VD decreased significantly after MIA, which is in accordance with our results [11]. The denoising algorithm was developed by applying paired single-scan and MIA
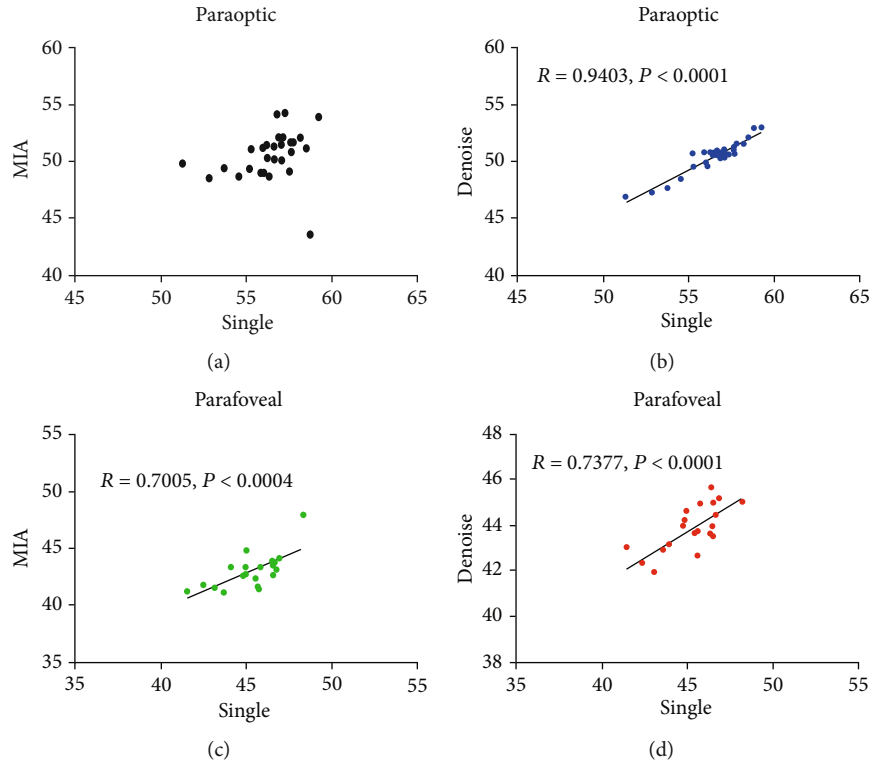
FIGURE 5: Correlation of the vessel density between two groups. Notes: (a, b) correlation of vessel density in the paraoptic area; (c, d) correlation of vessel density in the parafoveal area.

OCTA images in deep learning training [14]. Eventually, a denoising algorithm was built to generate a similar averaged OCTA image from a single image. This may explain the decrease in VD in both MIA and denoised OCTA images. Using the denoising technique and MIA to process OCTA images, different mechanisms can affect VD. On the one hand, a reduction of noise (and an increase of PSNR) can decrease VD. On the other hand, an increase in continuous vessels can increase VD, as well as an enlargement of vessel caliber [16]. The previous study also reported the lower background noise and better continuity of vessels in the denoised image compare to the MIA image [11]. Therefore, the proportion of vessel and none vessel would determine which factor became the stronger one. In our study, VD in the foveal of the MIA image was significantly higher than that of the denoised image. This may due to the low proportion of vessels in the foveal and result in the reduction of noise which shows a stronger effect on VD in the denoised image. Vice versa, VD in the superior and inferior foveal were a relatively high value compared with those in the nasal and temporal sides in our study, and this could result in the enhancement of vessel continuity which became the stronger factor to impact VD in these two areas which explains why the VD in MIA images was lower than that in the denoised images in areas. In addition, the VD in the denoised images was more correlated with that in the single-scan images than that in the MIA images. The MIA records the exact flow signal from several images, whereas the flow signal of the denoised images was only extracted from the original single OCTA scan. This could be the reason that the VD in the denoised

images had a higher correlation to a single OCTA scan than that in the MIA images. In general, VD in the denoised image was significantly changed but still related to VD in the single-scan image. With the reduction of noise and increase in the continuous vessel process, VD in the denoised image should represent the real status of the microvasculature in the retina than that in the single-scan image.

Although the denoising function provides a quicker way to greater image quality acquisition, MIA has some advantages that we observed in this study. Artifacts caused by vitreous turbidity and eye rolling were more likely to be eliminated by image averaging than denoising. Heisler et al. also reported the advantages of MIA in reducing motion artifacts [17]. Such artifacts that change with the movement of the eye were unlikely to be exhibited in the exact position in different scans. However, in the denoised images, these artifacts presented as flakes of low signal, which were difficult to distinguish from the nonperfusion area by morphologic features (Figures 4(g)– 4(i), red arrows). This difference between the denoised and MIA images may be because the denoising algorithm only extracts information from a single scan, which cannot recover the flow information covered by vitreous turbidity. In addition, the application of denoising and image averaging seems less effective in the optic nerve area than in the macular area (Figure 2). The radial peripheral capillary area was difficult to exhibit clearly in the three modes mentioned above, which could be because of the small caliber vessels with a discontinuous image exhibiting a spot-like high signal similar to background noise. This could be eliminated by image averaging and denoising, leading to a

loss of flow information. This discovery indicates that there are still some limitations in applying the denoising function of the Canon-HS100 OCTA device in optic nerve diseases, since the potential risk of flow signal is missing. Further deep learning training may help address these problems.

The denoising technique provides a convenient way to enhance the OCTA image quality by processing with AI, which could be a useful tool for patients in whom it is difficult to acquire enough qualified OCTA images because of poor visual acuity. For example, patients with age-related macular degeneration and myopia with poor visual acuity and fixation are likely to benefit from this technique. Theoretically, a more precise VD value, which might improve the detection of sensitivity for the changes retinal vasculature disease such as diabetic retinopathy, can be obtained by this denoising process.

Our study has some limitations. First, we only conducted research in a small sample size, which may influence the accuracy of the statistical results. Second, we only used one OCTA device; it would be better to compare multiple devices to acquire more subject data to verify the reliability of our OCTA parameter results.

5. Conclusion

In general, denoising provides an easy and quick way to improve image quality, including PSNR, and shows great potential in improving the sensitivity of OCTA images as retinal disease markers. Although this new technique has some limitations at the current stage, additional training should be conducted for further clinical use.

Data Availability

Data are available from corresponding authors upon request.

Conflicts of Interest

The authors declare that there is no conflict of interest.

Authors' Contributions

Yishuang Xu and Yu Su contributed equally to this work.

Acknowledgments

References

[1] R. F. Spaide, J. G. Fujimoto, N. K. Waheed, S. R. Sadda, and G. Staurenghi, "Optical coherence tomography angiography," *Progress in Retinal and Eye Research*, vol. 64, pp. 1–55, 2018.

[2] A. Y. Kim, Z. Chu, A. Shahidzadeh, R. K. Wang, C. A. Puliafito, and A. H. Kashani, "Quantifying microvascular density and morphology in diabetic retinopathy using spectral-domain optical coherence tomography angiography," *Investigative Ophthalmology & Visual Science*, vol. 57, no. 9, pp. OCT362–OCT370, 2016.

[3] L. Frizziero, G. Midena, E. Longhin et al., "Early retinal changes by OCT angiography and multifocal electroretinography in diabetes," *Journal of Clinical Medicine*, vol. 9, no. 11, article 3514, 2020.

[4] D. Hua, Y. Xu, X. Zhang et al., "Retinal microvascular changes in hypertensive patients with different levels of blood pressure control and without hypertensive retinopathy," *Current Eye Research*, vol. 46, no. 1, pp. 107–114, 2021.

[5] H. Hou, S. Moghimi, L. M. Zangwill et al., "Macula vessel density and thickness in early primary open-angle glaucoma," *American Journal of Ophthalmology*, vol. 199, pp. 120–132, 2019.

[6] J. L. Lauermann, M. Treder, P. Heiduschka, C. R. Clemens, N. Eter, and F. Alten, "Impact of eye-tracking technology on OCT-angiography imaging quality in age-related macular degeneration," *Graefe's Archive for Clinical and Experimental Ophthalmology*, vol. 255, no. 8, pp. 1535–1542, 2017.

[7] M. Zhang, T. S. Hwang, J. P. Campbell et al., "Projection-resolved optical coherence tomographic angiography," *Biomedical Optics Express*, vol. 7, no. 3, pp. 816–828, 2016.

[8] C. Czakó, L. István, M. Ecsedy et al., "The effect of image quality on the reliability of OCT angiography measurements in patients with diabetes," *International Journal of Retina and Vitreous*, vol. 5, no. 1, p. 46, 2019.

[9] A. K. Woetzel, J. L. Lauermann, K. Kreitz et al., "Optical coherence tomography angiography image quality assessment at varying retinal expertise levels," *Journal of Current Ophthalmology*, vol. 31, no. 2, pp. 161–167, 2019.

[10] A. Uji, S. Balasubramanian, J. Lei et al., "Multiple enface image averaging for enhanced optical coherence tomography angiography imaging," *Acta Ophthalmologica*, vol. 96, no. 7, pp. e820–e827, 2018.

[11] S. Kadomoto, A. Uji, Y. Muraoka, T. Akagi, and A. Tsujikawa, "Enhanced visualization of retinal microvasculature in optical coherence tomography angiography imaging via deep learning," *Journal of Clinical Medicine*, vol. 9, no. 5, p. 1322, 2020.

[12] S. Murakawa, I. Maruko, T. Kawano, T. Hasegawa, and T. Iida, "Choroidal neovascularization imaging using multiple en face optical coherence tomography angiography image averaging," *Graefe's Archive for Clinical and Experimental Ophthalmology*, vol. 257, no. 6, pp. 1119–1125, 2019.

[13] J. L. Lauermann, Y. Xu, P. Heiduschka et al., "Impact of integrated multiple image averaging on OCT angiography image quality and quantitative parameters," *Graefe's Archive for Clinical and Experimental Ophthalmology*, vol. 257, no. 12, pp. 2623–2629, 2019.

[14] K. Kawai, A. Uji, T. Murakami et al., "Image evaluation of artificial intelligence supported optical coherence tomography angiography imaging using Oct-Hs100 device in diabetic retinopathy," *Retina*, 2020.

[15] S. T. Welstead, *Fractal and wavelet image compression techniques*, Spie Press, 1999.

[16] A. Uji, S. Balasubramanian, J. Lei, E. Baghdasaryan, M. Al-Sheikh, and S. R. Sadda, "Impact of multiple en face image averaging on quantitative assessment from optical coherence tomography angiography images," *Ophthalmology*, vol. 124, no. 7, pp. 944–952, 2017.

[17] M. Heisler, S. Lee, Z. Mammo et al., "Strip-based registration of serially acquired optical coherence tomography angiography," *Journal of Biomedical Optics*, vol. 22, no. 3, p. 036007, 2017.

Research Article

Altered Small-World Functional Network Topology in Patients with Optic Neuritis: A Resting-State fMRI Study

Ke Song,[1,2] **Juan Li,**[3] **Yuanqiang Zhu,**[4] **Fang Ren,**[4] **Lingcan Cao,**[1] **and Zi-Gang Huang** [1]

[1]*The Key Laboratory of Biomedical Information Engineering of Ministry of Education, Institute of Health and Rehabilitation Science, School of Life Science and Technology, Xi'an Jiaotong University, The Key Laboratory of Neuro-informatics & Rehabilitation Engineering of Ministry of Civil Affairs, Xi'an, Shaanxi 710049, China*
[2]*Department of Equipment, Xi'an People's Hospital (Xi'an Fourth Hospital), China*
[3]*Shaanxi Eye Hospital, Xi'an People's Hospital (Xi'an Fourth Hospital), Affiliated Guangren Hospital, School of Medicine, Xi'an Jiaotong University, Xi'an, 710004, China*
[4]*Department of Radiology, Xijing Hospital, Fourth Military Medical University, Xi'an, 710032 Shaanxi, China*

Correspondence should be addressed to Zi-Gang Huang; huangzg@xjtu.edu.cn

Aim. This study investigated changes in small-world topology and brain functional connectivity in patients with optic neuritis (ON) by resting-state functional magnetic resonance imaging (rs-fMRI) and based on graph theory. *Methods.* A total of 21 patients with ON (8 males and 13 females) and 21 matched healthy control subjects (8 males and 13 females) were enrolled and underwent rs-fMRI. Data were preprocessed and the brain was divided into 116 regions of interest. Small-world network parameters and area under the integral curve (AUC) were calculated from pairwise brain interval correlation coefficients. Differences in brain network parameter AUCs between the 2 groups were evaluated with the independent sample t-test, and changes in brain connection strength between ON patients and control subjects were assessed by network-based statistical analysis. *Results.* In the sparsity range from 0.08 to 0.48, both groups exhibited small-world attributes. Compared to the control group, global network efficiency, normalized clustering coefficient, and small-world value were higher whereas the clustering coefficient value was lower in ON patients. There were no differences in characteristic path length, local network efficiency, and normalized characteristic path length between groups. In addition, ON patients had lower brain functional connectivity strength among the rolandic operculum, medial superior frontal gyrus, insula, median cingulate and paracingulate gyri, amygdala, superior parietal gyrus, inferior parietal gyrus, supramarginal gyrus, angular gyrus, lenticular nucleus, pallidum, superior temporal gyrus, and cerebellum compared to the control group ($P < 0.05$). *Conclusion.* Patients with ON show typical "small world" topology that differed from that detected in HC brain networks. The brain network in ON has a small-world attribute but shows reduced and abnormal connectivity compared to normal subjects and likely causes symptoms of cognitive impairment.

1. Introduction

Optic neuritis (ON) is a condition affecting 115 out of every 100,000 persons [1]; it is characterized by inflammation and demyelination of the optic nerve as a result of infection or systemic autoimmune disease. The main clinical symptoms are sudden loss of visual acuity in one or both eyes within a short period of time, relative afferent pupil disorder (RAPD), papillary edema, pain during eye rotation, and visual field defect. ON is closely related to demyelinating diseases of the central nervous system such as optic neuromyelitis and multiple sclerosis, among others [2]. Thinning of the retinal nerve fiber layer around the optic papilla in ON is observable by optical coherence tomography. ON can cause severe visual impairment but the pathogenesis is not fully understood, although it is thought to involve inflammation or immune factors that lead to optic nerve damage and ganglion cell apoptosis. In addition to demyelination, ON patients have abnormal activity in many brain regions [3]. For example, brain atrophy was observed in patients with chronic

recurrent solitary ON [4], along with Wallerian degeneration in the optic tract, cerebellum, thalamus, posterior cingulate, and other brain areas [5], indicating that specific brain areas are affected in ON. Given that the visual loss caused by ON can negatively affect the quality of life of patients, it is important to clarify the pathogenesis and associated changes in the brain. Resting-state functional magnetic resonance imaging (rs-fMRI) is a safe and widely used method for evaluating brain activity based on the detection of the balance between local segregation and global integration of signals associated with interconnected neurons. The normal human brain network has a short path length and high transmission efficiency, known as small-world attributes [6]; these enable the brain network to meet local and global demands and balance functional integration and segregation in order to achieve synchronization of neural activity between different brain regions. Thus, small-world attributes allow efficient information transmission at low wiring cost [7].

Graph theory, which is the study of the topologic structure of networks, provides a means of quantifying network changes in the brain [8] by considering these as a set of general elements sharing a specific relationship beyond anatomic connections [9]. Graph theory can be applied to rs-fMRI to characterize the functional connectivity and obtain a structural map of the brain from functional data, which can provide insight into the anatomic basis of brain dysfunction [10] and thus serves as an important reference for the diagnosis and treatment of diseases. Graph theory analysis has been widely used in studies on the mechanisms of posttraumatic stress disorder [11], Alzheimer's disease [12], schizophrenia [13], stroke [14], epilepsy [15], and concussion [16].

Most previous studies on brain abnormalities in ON have focused on abnormal activity in specific brain regions. However, changes in small-world attributes and brain functional connectivity caused by ON have not been assessed. This was investigated in the present study by comparing small-world attributes and brain network connectivity in patients with ON and normal subjects by rs-MRI and the application of graph theory.

2. Materials and Methods

2.1. Subjects. A total of 21 ON patients (8 males and 13 females) were recruited at the Department of Ophthalmology, the First Affiliated Hospital of Nanchang University Hospital. Inclusion criteria were as follows: (1) sudden loss of visual acuity in one or both eyes within a short period of time; (2) positive RAPD or abnormal visual evoked potentials; (3) no visual field abnormalities related to nerve fiber injury; (4) none of the subjects had a history of psychiatric or neurological disorders; (5) no acute visual loss caused by other ophthalmologic or nervous system diseases; (6) no history of mental disorders, diabetes, hypertension, and taking psychotropic drugs; (7) no history of drug, smoking, or alcohol addiction; and (8) average somatotype and weight (Figure 1). We also recruited 21 age-, sex-, and weight-matched healthy control (HC) subjects (8 males and 13 females) who met the following criteria: (1) no pathway or brain parenchyma abnormalities observed by head MRI, (2) no ophthalmic disease and

maximum corrected visual acuity >1.0, (3) no neuropsychiatric abnormalities or headache, and (4) no contraindications for MRI. After being informed of the nature of the study, all patients (or their guardians for participants under 18 years old) provided written and informed consent before participating. The study was approved by the research ethics committee of the First Affiliated Hospital of Nanchang University, and the protocol was in accordance with the Helsinki Declaration (CDYFY-LL-2015-29).

2.2. MRI Data Acquisition. A 3.0 T TrioTim (Siemens, Munich, Germany) MR scanner and 8-channel head coil were used to collect rs-fMRI data and 3-dimensional high-resolution T1-weighted anatomic images. Participants were instructed to avoid drinking alcohol or coffee before the scan and those with intracranial lesions were excluded. During the scan, the subjects lay quietly with their eyes closed, breathe evenly and remain still, and avoid any mental activities insofar as possible. The subject was used a sponge pad to fix the head to reduce head movement, and the subject wore earplugs to block noise. For rs-fMRI, the parameters were as follows: repetition time (TR) = 2000 ms, echo time (TE) = 40 ms, flip angle = 90°, field of view (FOV) = 230 mm × 230 mm, matrix = 64 × 64, slice thickness = 4 mm, and slice number = 240 mm. The scanning parameters for T1-weighted structural images were as follows: TR = 1900 ms, TE = 2.26 ms, flip angle = 9°, FOV = 250 × 250 mm, matrix = 256 × 256, layer thickness = 1 mm, and layer number = 176.

2.3. MRI Data Preprocessing. In order to eliminate the impact of magnetic field uniformity on network computing and intrasubject variability, poor-quality data were removed along with the first 10 time points. This study is based on the MATLAB 2014a (Mathworks, Natick, MA, USA) platform and uses the DPARSF V2.3 software package to preprocess the data. The preprocessing steps involved realigning, slice timing, time layer correction, spatial standardization, and smoothing with a $6 \times 6 \times 6$ mm full-width (half-height) Gaussian kernel [17]. Subjects with maximum x, y, or z displacement >1.5 mm or angular motion >1.5° were excluded from the analysis. In addition, the mean frame-wise displacement (FD) was calculated as a measure of the microhead motion of each subject. Linear regression was used to remove nuisance variables containing signals from the region of interest (ROI) in the ventricles and areas centered on white matter. After correcting for head motion, the standard echo plane imaging template was used to normalize the fMRI image space to the Montreal Neurological Institute (MNI) space with resampling at a resolution of $3 \times 3 \times 3$ mm. Finally, the data were then detrended to remove linear drift and temporally filtered by band-pass (0.01–0.08 Hz) to reduce the effects of low-frequency drift and high-frequency noise.

2.4. Construction of Brain Network Structure and Analysis of Topologic Attributes. We divided the whole brain into 116 network nodes. To define the ROI for the node region, the average processing time was calculated as the average of the fMRI time series of all voxels in the region, and the average time series of each region was obtained. We used a weighted

(a)   (b)
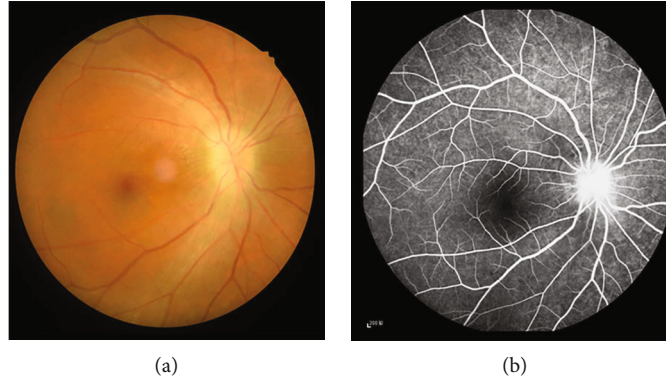
FIGURE 1: Eye examination data of ON patients. Notes: (a) The results of fundus photography in ON patients. (b) The results of fundus fluorescein angiograp (FFA) in ON patients. Abbreviations: ON: optic neuritis; FFA: fundus fluorescein angiograp.

matrix and included both positive and negative connections to construct a full-connection weighted network of the brain with sparsity as the threshold. The network analysis was carried out under a sparsity of 0.08–0.48 with an interval of 0.01. For the graph of each subject, we evaluated the whole-brain static network using this predefined range as the threshold with the following parameters: clustering coefficient (C_p), characteristic path length (Lp), normalized clustering coefficient (γ), normalized characteristic path length (λ), small-world coefficient (σ), and brain network efficiency (the global efficiency (Eg), and the local efficiency (El)) [18]. Functional segregation, which included C_p, γ, and El, indicated specialized processing within interconnected brain regions, functional integration, which included Lp, λ, and Eg, indicated different brain areas in terms of functional and effective connectivity. The balance between segregation and integration is vital for effective information processing and synthesis. The σ is characterized by a high global integration and a high local specialization between brain regions. Network-based statistics (NBS) and GRETNA v2.0 (a toolbox for topological analysis of imaging connectomics) software were used to analyze network construction and assess differences in connectivity between the groups.

2.5. Network-Based Statistical Analysis. The brain is a complex network of functionally interconnected nodes that are distributed in a specific ROI [19]. Graph theory analysis was used to describe the topologic properties of networks, but as it involved a large number of multiple comparisons, NBS provided by the false discovery rate (FDR) was used for whole-brain functional connectivity analysis at the ROI level and applied to connected components (subnets) that showed obvious differences between groups [20]. It was independently corrected for each connection in the network, and the corresponding P value for each link was independently calculated according to the strength of the paired association.

2.6. Parameter Integration. To evaluate overall differences between groups, the small-world parameters under each sparsity degree were integrated and the area under the curve

(AUC) representing the overall level was recorded as aCp, aLp, aEg, aEl, aσ, aγ, and aλ.

2.7. Statistical Analysis. The independent sample t-test ($P < 0.05$ represented statistically significant differences) was used to evaluate differences in demographic and clinical variables between the ON and HC groups using the SPSS v22.0 software (SPSS Inc, Chicago, IL, USA). Under a sparsity of 0.08–0.48, the independent sample t-test was used to assess small-world topologic differences in network metrics (aCp, aLp, aEg, aEl, aσ, aγ, and aλ), $P < 0.05$ represented statistically significant differences. All normally distributed data are expressed as mean ± standard deviation. We used NBS and link-based family-wise error rate (FWE) control provided by FDR to analyze potential brain functional connection differences and detect a contrast that was simulated between two groups, using an independent two-sample t-test with $P < 0.05$ and permutations of 5,000.

3. Results

3.1. Demographic and Clinical Characteristics. There were no statistically significant differences between the ON and HC groups in terms of weight ($P = 0.652$), age ($P = 0.821$), height ($P = 0.634$), and BMI ($P = 0.963$), while significant differences were found in VA-Right ($P < 0.001$) and best-corrected VA-Left ($P < 0.001$) between the two groups.

3.2. Analysis of Small-World Properties. Seven topologic small-world parameters were determined under a sparsity of 0.08 to 0.48 with an interval of 0.01. Cp, El, and Eg were positively correlated whereas Lp, γ, λ, and σ were negatively correlated with sparsity. Both groups had small-world attributes ($\lambda > 1$, $\gamma > 1$, $\sigma > 1$). For the small-world indices, aγ (Figure 2(b)) and aσ (Figure 2(c)) were significantly higher for ON patients than for HC subjects ($P < 0.05$). There were no statistically significant differences in aλ (Figure 2(a)) between groups (Table 1). For the other indicators of brain network topology, aCp (Figure 3(a)) was lower, whereas aEg (Figure 3(b)) was higher in ON patients compared to HC subjects (both $P < 0.05$). There were no significant

(a)   (b)   (c)
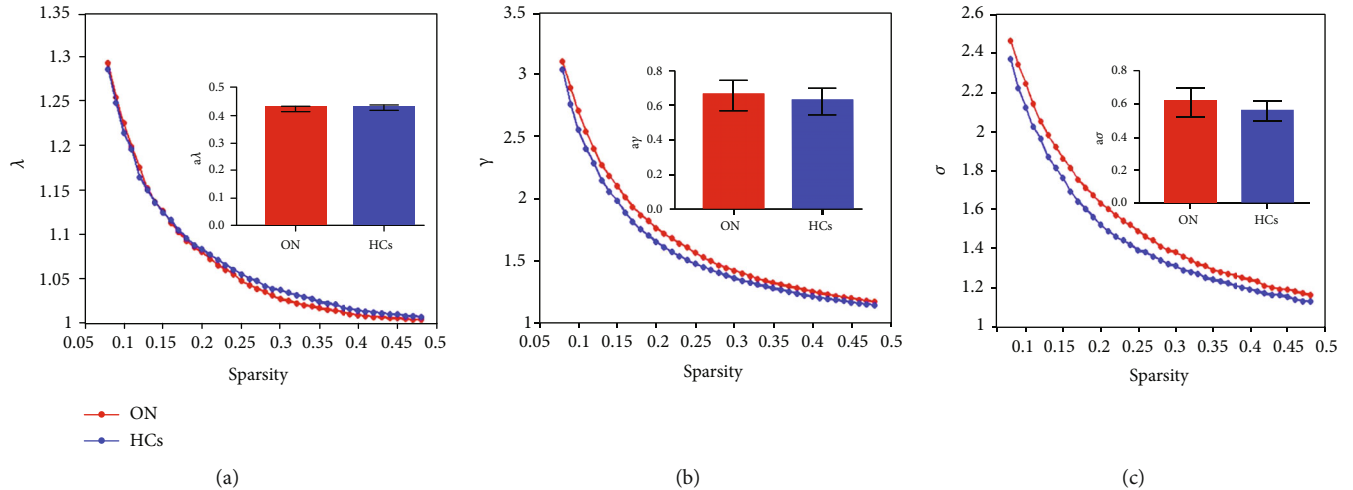
Figure 2: Comparison of analysis of small-world attribute of functional brain network between ON patients and HCs. Notes: resting-state small-world parameter analyses showing that both ONs and HCs were consistent with small-world characteristics ($\lambda > 1$, $\gamma > 1$, $\sigma > 1$). However, compared with the control group, the values of γ (b) and σ (c) in ON group increased significantly, and the difference was statistically significant ($P < 0.05$). There was no significant difference in λ value (a) between the two groups ($P > 0.05$). Abbreviation: ON: optic neuritis; HCs: healthy controls; AUC: area under curve; aγ: the AUC of normalized characteristic path length; aλ: the AUC of normalized characteristic path length; aσ: the AUC of small-worldness.

Table 1: The AUC of the small-world parameters in patients with ONs and HCs.

	ON	HCs	t	P values
Network properties	—	—	—	—
aCP	$0.245 \pm 0.100^*$	0.253 ± 0.009	-2.714	0.01
aLP	0.712 ± 0.027	0.728 ± 0.269	-1.865	0.069
aEI	0.310 ± 0.006	0.313 ± 0.008	-1.239	0.223
aEg	$0.234 \pm 0.005^*$	0.229 ± 0.006	2.812	0.008
Small-world attribute	—	—	—	—
aλ	0.425 ± 0.008	0.429 ± 0.007	-1.551	1.129
aγ	$0.655 \pm 0.087^*$	0.587 ± 0.071	2.768	0.008
aσ	$0.610 \pm 0.084^*$	0.550 ± 0.057	2.664	0.01

Notes: significant at $^*P < 0.05$, independent t-test. P, P value between ON and HCs. Abbreviation: ON: optic neuritis; HCs: healthy controls; AUC: area under curve; aCp: the AUC of clustering coefficient; aLp: the AUC of characteristic path length; aγ: the AUC of normalized clustering coefficient; aλ: the AUC of normalized characteristic path length; aσ: the AUC of small-worldness; aEg: the AUC of global network efficiency; aEl: the AUC of local network efficiency.

differences in aEI (Figure 3(c)) and aLp (Figure 3(d)) between groups (Table 1).

3.3. Graph Theory Analysis of Alterations in Brain Functional Connectivity.
Compared to the HC group, ON patients showed decreased brain functional connectivity. These mainly occurred among rolandic operculum (ROL), medial superior frontal gyrus (SFG), insula (INS), median cingulate and paracingulate gyri (DCG), amygdala (AMYG), superior parietal gyrus (SPG), inferior parietal gyrus (IPL), supramarginal gyrus (SMG), angular gyrus (ANG), lenticular nucleus, pallidum (PAL), superior temporal gyrus (STG), and cerebellum (Figure 4). The difference is statistically significant ($P < 0.05$) (Table 2). There were no instances where functional connectivity was higher in the ON group than in the HC group. These results demonstrate that optic nerve inflammation has a far-reaching effect on the functional brain network.

4. Discussion

This is the first study to use graph theory and NBS to analyze the small world and brain functional connectivity strength in ON. Inflammation and immune activation can cause demyelination of the optic nerve, leading to reduced signal transmission and visual impairment [21]. The demyelination and axon damage associated with ON was shown to result in the destruction of functional brain networks in a small-world study of craniocerebral trauma.

In the present work, we found that ON patients retained small-world characteristics ($\lambda > 1$, $\gamma > 1$, and $\sigma > 1$) although some network parameters were altered. Compared to HCs, Eg, γ, and σ were increased whereas Cp was decreased in ON patients; moreover, Cp, El, and Eg were positively correlated and Lp, γ, λ, and σ were negatively correlated with sparsity. The lower Cp in ON patients may reflect a reduced

(a)

(b)

(c)

(d)
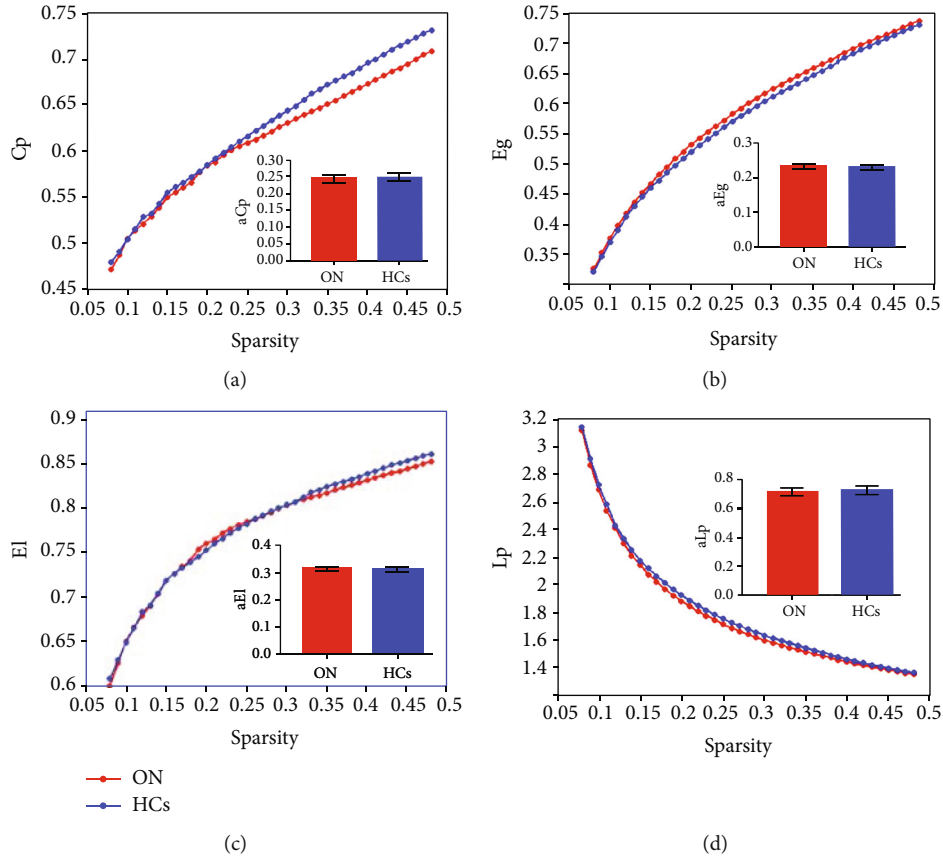
FIGURE 3: Comparison of structural properties of brain network between ON patients and HCs. Notes: compared with HCs, the value of Cp in patients with ON was significantly lower (a) and the value of Eg was significantly higher (b), and the difference was statistically significant ($P < 0.05$). There was no significant difference in the values of Lp (c) and EI (d) between the two groups ($P > 0.05$). Abbreviation: ON: optic neuritis; HCs: healthy controls; AUC: area under curve; aCp: the AUC of node clustering coefficient; aLp: the AUC of characteristic path length; aEg: the AUC of global network efficiency; aEl: the AUC of local network efficiency.

functional connectivity in some brain regions caused by extreme demyelination, which has also been observed in cases of axonal injury. Patients with long-term disturbance of consciousness also show alterations in small-world parameters. Lp measures the capacity for global information transmission and is related to cognitive function [22], while Eg represents global network efficiency. In our study, Eg was higher in ON patients than in HC subjects, suggesting greater efficiency in network information transmission. Patients with ON often have monocular disease. Insufficient stimulation of the visual cortex from the decreased visual acuity in one eye can lead to compensatory activation of the contralateral brain region [23]. We observed an increase in the amplitude of low-frequency fluctuation (ALFF) value of the left superior temporal gyrus in ON patients, consistent with findings from other MRI studies of ON. This implies that the increase in Eg in ON patients is a mechanism to offset brain network dysfunction. The decreased λ value was accompanied by a compensatory reduction in Lp. The injury caused by ON alters small-world attributes of brain connectivity networks. The parameter σ is a clustering coefficient that represents approximate shortest path length (Y. [24]). A lower σ represents a greater tendency toward a random brain network; in

concussion, these were shown to be more susceptible to pathologic insults than small-world networks.

In this study, σ was >1 in ON patients, indicating that they have small-world characteristics; however, the value was higher than that in HC subjects. The optic nerve is rich in macrophages and T cells [25]; thus, the increase in σ may be attributable to inflammation or damage. γ is the standardized clustering coefficient and is used to measure dispersion within the network, with a higher value indicating a higher degree of grouping. In patients with ON, damage to the optic nerve may lead to damage to the related cerebral hemispheres, which may lead to changes in the value of brain function areas and cognitive dysfunction. The significant difference in the static state connection network between ON patients and HC subjects emphasizes the role of NBS in multivariate comparisons.

We observed a decrease in the connection strength of multiple brain regions in ON patients. The INS is located in the deep part of the lateral sulcus at the boundary between the annular sulcus and frontal, temporal, and parietal lobes. Abnormal activation of the insular-interstitial area has been reported in ON patients [26]; additionally, the latency of visual evoked potentials decreased with REHO signal in the
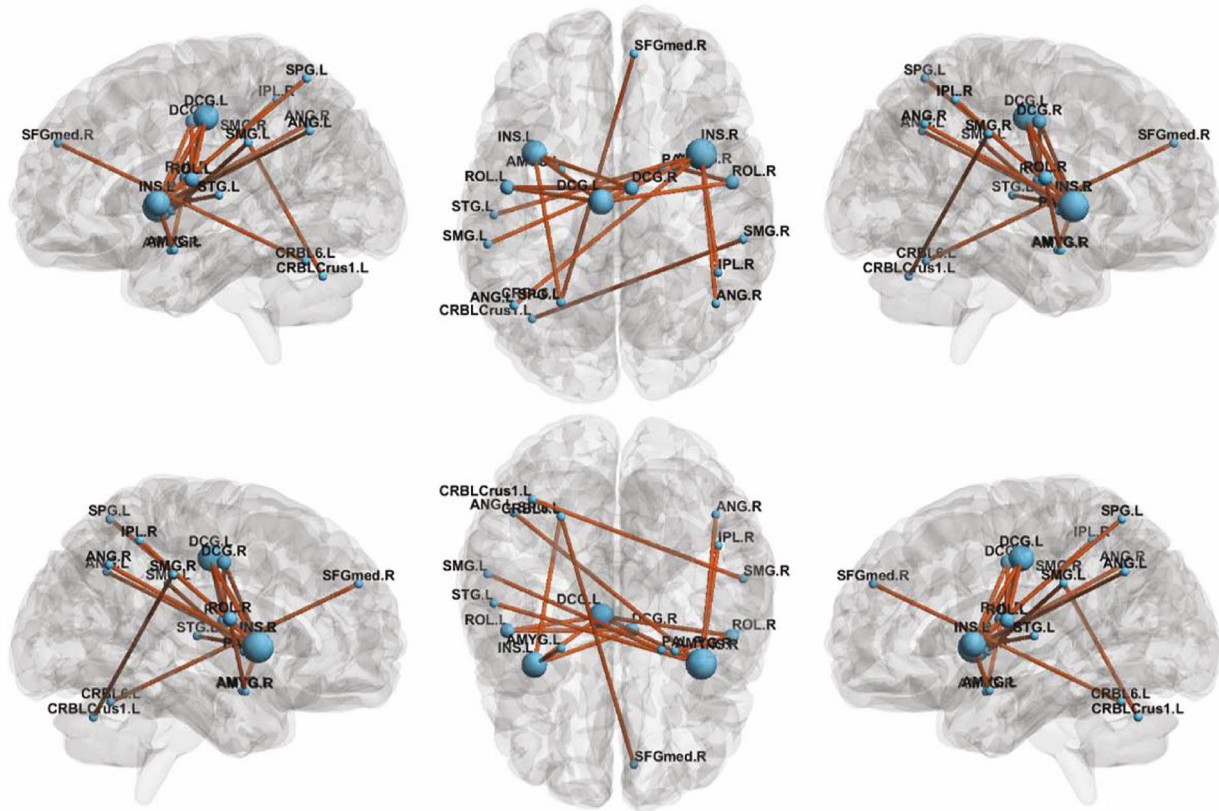
FIGURE 4: Graph theory analysis of alterations in brain functional connectivity. Notes: The figure shows the subnetwork with decreased connectivity in ON patients compared to controls, identified by the NBS. Decreased brain functional connectivity in individuals with optic neuritis (ONs) compared to healthy controls. (NBS: $T > 3.92$, $P < 0.05$ and 5,000 permutations). Abbreviation: ON: optic neuritis; HCs: healthy controls; ROL: rolandic operculum; SFGmed: superior frontal gyrus, medial; INS: insula; DCG: median cingulate and paracingulate gyri; AMYG: amygdala; SPG: superior parietal gyrus; IPL: inferior parietal gyrus; SMG: supramarginal gyrus; ANG: angular gyrus; PAL: lenticular nucleus, pallidum; STG: superior temporal gyrus; CRBLCrus1: cerebellum_Crus1; CRBL 6: cerebellum_Crus6; L: left hemisphere; R: right hemisphere.

INS, which could decrease the connection strength between this and other brain regions [3]. The cerebellum is located in the inferior part of the brain posterior to the medulla oblongata and pons. Cerebellar demyelination has been reported in ON [27], which could explain the reduced connectivity between the cerebellum and other brain regions in patients.

The STG is located in the temporal lobe between the lateral and superior temporal sulci and plays a key role in sound processing. An fMRI study revealed that the ALFF signal was decreased in the superior temporal gyrus of ON patients, which may be related to the severity of ON. The STG is also involved in visual searching and decreased magnetic resonance-related signals in this region have been observed in patients with retinal detachment [28]. An impaired STG in patients with ON could result in decreased connectivity with surrounding brain regions. The AMYG is located in the dorsomedial part of the anterior temporal lobe, slightly anterior to the top of the hippocampus and inferior horn of the lateral ventricle. As part of the limbic system, the AMYG plays an important role in generating, identifying, and regulating emotion, and it is among the key brain areas responsible for normal and pathologic stress responses. A decreased connection strength between the AMYG and other

brain areas in ON patients may indicate a reduced ability to respond to pathologic events, leading to the destruction of the brain network structure. The SMG contributes to the maintenance of short-term auditory-language, motor, and visual-spatial memory sequence [29]; the reduced connectivity between the SMG and surrounding areas in ON patients suggests that the normal perception of visual space is disrupted.

The ANG, which is the visual language (reading) center, is arched around the end of the supratemporal sulcus in the temporal lobe. The ANG integrates incoming sensory and cognitive information, responds to stimuli in memory and learning, and functions in memory retrieval [30]. The activity of ANG-related neural circuits is increased during eye-to-eye communication, and both the ANG and STG have been implicated in Wernicke's (sensory) aphasia. Therefore, the decreased connectivity between the ANG and STG in ON may be associated with reading dysfunction. The SFG, located in the upper part of the prefrontal lobe, is involved in motor coordination, working memory, and resting-state and cognitive control. The fractional ALFF signal of the SFG was shown to be positively correlated with perceived stress, and the gray matter structure of the SFG has been

TABLE 2: Brain functional connectivity between ON patients and HCs identified by NBS analysis.

Connectivity	t value	P_{NBS}
ROL.L to DCG.L	6.026	<0.05
ROL.L to DCG.R	5.747	<0.05
ROL.R to DCG.L	5.239	<0.05
ROL.R to AMYG.R	5.212	<0.05
SFG med.R to CRBL_Crus6_L	5.205	<0.05
INS.L to DCG.L	6.066	<0.05
INS.L to DCG.R	5.169	<0.05
INS.L to AMYG.L	5.284	<0.05
INS.L to SPG.L	5.129	<0.05
INS.R to DCG.L	5.454	<0.05
INS.R to IPL.R	5.365	<0.05
INS.R to ANG.L	5.071	<0.05
INS.R to ANG.R	5.220	<0.05
INS.R to STG.L	5.085	<0.05
SMG.L to PAL.R	5.444	<0.05
SMG.R to CRBL_6_L	5.257	<0.05

Notes: NBS: $T > 3.92$, $P < 0.05$ and 5,000 permutations, $P < 0.05$ indicates a significant difference between the groups. Abbreviation: ON: optic neuritis; HCs: healthy controls; ROL: rolandic operculum; SFGmed: superior frontal gyrus, medial; INS: insula; DCG: median cingulate and paracingulate gyri; AMYG: amygdala; SPG: superior parietal gyrus; IPL: inferior parietal gyrus, but supramarginal and angular gyri; SMG: supramarginal gyrus; ANG: angular gyrus; PAL: lenticular nucleus, pallidum; STG: superior temporal gyrus; CRBLCrus1: cerebellum_Crus1; CRBL 6: cerebellum_Crus6; L: left hemisphere; R: right hemisphere.

implicated in the processing of early and recent life stress events. The reduced SFG connection strength in ON patients may be due to stress caused by optic nerve inflammation. The SPG is located in the dorsomedial parietal lobe anterior to the parietal-occipital sulcus and above the parietal sulcus. In the posterior part of the retrocentral sulcus, the SPG participates in stereoscopic visual processing and plays a key role in defining visual space in language and motor areas. Additionally, the SPG controls eye movement. Eye rotation pain is common in ON and may also be associated with changes in brain connectivity; however, in our study, the strength of the connection between the SPG and surrounding brain regions was decreased, suggesting that there was damage to the area corresponding to eye movement pain. The PAL is located in the lentiform nucleus of the striatum. Lesions involving the extrapyramidal system and pyramidal tract may cause movement disorder and nystagmus in the eyes. The DCG, which is crescent-shaped and surrounds the corpus callosum, is a major component of the limbic system and is related to memory and spatial orientation. The reduced connection strength between the DCG and other brain areas in patients with ON could affect their capacity for spatial localization. ROL is the cortex adjacent to the insular, which is one of the major regions involved in the language processing system, and it also involves in motor, sensory, autonomic, and cognitive processing. Relevant research data also confirms the role of rolandic operculum and neighboring areas (such as insular) in processing sensory signals related to other con-

scious operations (such as visual awareness). The decrease of the connection strength between ROL and the surrounding brain area may reflect the impairment of visual function. IPL is a part of the parietal lobe and is related to visual recognition and selective scanning targets. Finally, the observed changes in the IPL imply the impairment of stereoscopic visual function. Taken together, these results demonstrate that optic nerve inflammation has far-reaching effects on the functional brain network.

4.1. Limitations and Strengths. There were some limitations to this study. Because of the small sample size, we did not examine the correlation between brain topologic characteristics and clinical manifestations of ON or between changes in brain structure and function. In the future, brain network changes in ON will be analyzed in a larger cohort by multimodal analysis.

5. Conclusion

The results of this study show that the functional brain network of ON patients has small-world properties, but that these are significantly impaired relative to HC subjects. The changes in small-world properties observed in ON may be caused by demyelination resulting from inflammation and could reflect functional impairment in the brain. Our findings have found that optic neuritis may have a certain impact on the functional areas of the brain. Based on this, we can diagnose optic neuritis through brain image analysis and prevent possible complications related to brain dysfunction.

Data Availability

The datasets generated during and/or analyzed during the current study are available from the corresponding author on reasonable request.

Consent

All authors agree to publish.

Conflicts of Interest

This was not an industry-supported study. The authors report no conflicts of interest in this work.

Authors' Contributions

KS, JL, and YQZ designed the current study. FR collected the data. ZGH analyzed the data. KS wrote the manuscript. All the authors read and approved the final manuscript.

Acknowledgments

References

[1] H. Wilhelm and M. Schabet, "The diagnosis and treatment of optic neuritis," *Deutsches rzteblatt International*, vol. 112, no. 37, p. 616, 2015.

[2] C. A. Wicki, P. Manogaran, T. Simic, J. V. M. Hanson, and S. Schippling, "Bilateral retinal pathology following a first-ever clinical episode of autoimmune optic neuritis," *Neurology Neuroimmunology & Neuroinflammation*, vol. 7, no. 2, article e671, 2020.

[3] Y. Shao, F. Cai, Y. Zhong et al., "Altered intrinsic regional spontaneous brain activity in patients with optic neuritis: a resting-state functional magnetic resonance imaging study," *Neuropsychiatric Disease & Treatment*, vol. 11, pp. 3065–3073, 2015.

[4] L. N. Cantó, S. C. Boscá, C. A. Vicente et al., "Brain atrophy in relapsing optic neuritis is associated with crion phenotype," *Frontiers in Neurology*, vol. 10, p. 1157, 2019.

[5] A. I. Colpak, A. T. Kurne, K. K. Oguz, A. C. Has, A. Dolgun, and T. Kansu, "White matter involvement beyond the optic nerves in CRION as assessed by diffusion tensor imaging," *International Journal of Neuroscience*, vol. 125, no. 1, pp. 10–17, 2015.

[6] L. T. Chen, X. L. Fan, H. J. Li et al., "Disrupted small-world brain functional network topology in male patients with severe obstructive sleep apnea revealed by resting-state fMRI," *Neuropsychiatric Disease & Treatment*, vol. Volume 13, pp. 1471–1482, 2017.

[7] L. X. Wang, F. Guo, Y. Q. Zhu et al., "Effect of second-generation antipsychotics on brain network topology in first-episode schizophrenia: a longitudinal rs-fMRI study," *Schizophrenia Research.*, vol. 208, pp. 160–166, 2019.

[8] Z. A. Gaál, R. Boha, C. J. Stam, and M. Molnár, "Age-dependent features of EEG-reactivity–Spectral, complexity, and network characteristics," *Neuroscience Letters*, vol. 479, no. 1, pp. 79–84, 2010.

[9] D. Papo, J. M. Buldú, S. Boccaletti, and E. T. Bullmore, "Complex network theory and the brain," *Philosophical Transactions of the Royal Society B: Biological Sciences*, vol. 369, no. 1653, article 20130520, 2014.

[10] F. Miraglia, F. Vecchio, and P. M. Rossini, "7\. EEG characteristics in "eyes open" vs "eyes closed" conditions: Small world network architecture in healthy aging and age-related brain degeneration," *Clinical Neurophysiology Official Journal of the International Federation of Clinical Neurophysiology*, vol. 127, no. 4, pp. e134–1268, 2016.

[11] J. A. Rowland, J. R. Stapleton-Kotloski, D. L. Dobbins, E. Rogers, D. W. Godwin, and K. H. Taber, "Increased Small-World Network Topology Following Deployment-Acquired Traumatic Brain Injury Associated with the Development of Post-Traumatic Stress Disorder," *Brain Connectivity*, vol. 8, no. 4, pp. 205–211, 2018.

[12] C. A. Frantzidis, A. B. Vivas, A. Tsolaki, M. A. Klados, M. Tsolaki, and P. D. Bamidis, "Functional disorganization of small-world brain networks in mild Alzheimer's disease and amnestic mild cognitive impairment: an EEG study using relative wavelet entropy (RWE)," *Frontiers in Aging Neuroscience*, vol. 6, 2014.

[13] A. Anderson and M. S. Cohen, "Decreased small-world functional network connectivity and clustering across resting state networks in schizophrenia: an fMRI classification tutorial," *Frontiers in Human Neuroscience*, vol. 7, p. 520, 2013.

[14] F. Vecchio, F. Miraglia, A. Romano, P. Bramanti, and P. M. Rossini, "Small world brain network characteristics during EEG Holter recording of a stroke event," *Clinical Neurophysiology*, vol. 128, no. 1, pp. 1–3, 2017.

[15] R. D. Bharath, G. Chaitanya, R. Panda et al., "Reduced small world brain connectivity in probands with a family history of epilepsy," *European Journal of Neurology*, vol. 23, no. 12, pp. 1729–1737, 2016.

[16] Y. A. Yan, J. Song, G. Xu et al., "Correlation between standardized assessment of concussion scores and small- world brain network in mild traumatic brain injury," *Journal of Clinical Neuroscience*, vol. 44, pp. 114–121, 2017.

[17] X. Liu, Z. Yan, T. Wang et al., "Connectivity pattern differences bilaterally in the cerebellum posterior lobe in healthy subjects after normal sleep and sleep deprivation: a resting-state functional MRI study," *Neuropsychiatric Disease & Treatment*, vol. 11, p. 1279, 2015.

[18] Y. Huang, Y. Liu, D. Zhao et al., "Small-world properties of the whole-brain functional networks in patients with obstructive sleep apnea-hypopnea syndrome," *Sleep Medicine*, vol. 62, pp. 53–58, 2019.

[19] F. de Vico Fallani, J. Richiardi, M. Chavez, and S. Achard, "Graph analysis of functional brain networks: practical issues in translational neuroscience," *Philosophical Transactions of the Royal Society B: Biological Sciences*, vol. 369, no. 1653, article 20130521, 2014.

[20] A. Zalesky, A. Fornito, and E. T. Bullmore, "Network-based statistic: identifying differences in brain networks," *Neuro-Image*, vol. 53, no. 4, pp. 1197–1207, 2010.

[21] T. H. Lee, Y. S. Ji, S. W. Park, and H. Heo, "Retinal ganglion cell and axonal loss in optic neuritis: risk factors and visual functions," *Eye*, vol. 31, no. 3, pp. 467–474, 2017.

[22] C. Y. Wee, Z. Zhao, P. T. Yap et al., "Disrupted brain functional network in internet addiction disorder: a resting-state functional magnetic resonance imaging study," *Plos One*, vol. 9, no. 9, article e107306, 2014.

[23] Y. Shao, X. Huang, F. Cai et al., "Disturbed spontaneous brain-activity pattern in patients with optic neuritis using amplitude of low-frequency fluctuation: a functional magnetic resonance imaging study," *Neuropsychiatric Disease & Treatment*, vol. 11, pp. 3075–3083, 2015.

[24] Y. Zhang, J. Liu, L. Li et al., "A study on small-world brain functional networks altered by postherpetic neuralgia," *Magnetic Resonance Imaging*, vol. 32, no. 4, pp. 359–365, 2014.

[25] J. D. Glenn, P. Xue, and K. A. Whartenby, "Gemcitabine directly inhibits effector CD4 T cell activation and prevents experimental autoimmune encephalomyelitis," *Journal of Neuroimmunology*, vol. 316, pp. 7–16, 2018.

[26] A. T. Toosy, D. J. Werring, E. T. Bullmore et al., "Functional magnetic resonance imaging of the cortical response to photic

stimulation in humans following optic neuritis recovery," *Neuroscience Letters*, vol. 330, no. 3, pp. 255–259, 2002.

[27] A. Kutzelnigg, J. C. Faber-Rod, J. Bauer et al., "Widespread Demyelination in the Cerebellar Cortex in Multiple Sclerosis," *Brain Pathology*, vol. 17, no. 1, pp. 38–44, 2007.

[28] Q. Yuan, H. H. Kang, W. Q. Shi et al., "Disturbed interhemispheric functional connectivity in visual pathway in individuals with unilateral retinal detachment: a resting state fMRI study," *Visual Neuroscience*, vol. 35, p. 35, 2018.

[29] J. T. Zhang, Y. Liu, L. X. Li, K. Li, J. G. Chen, and F. Wang, "Activation of EphB2 in the basolateral amygdala promotes stress vulnerability of mice by increasing NMDA-dependent synaptic function," *Neuropharmacology*, vol. 167, article 107934, 2020.

[30] A. W. Gilmore, S. M. Nelson, and K. B. Mcdermott, "A parietal memory network revealed by multiple MRI methods," *Trends in Cognitive Sciences*, vol. 19, no. 9, pp. 534–543, 2015.

Research Article

Machine Learning of Schizophrenia Detection with Structural and Functional Neuroimaging

Dafa Shi ⓘ**, Yanfei Li** ⓘ**, Haoran Zhang** ⓘ**, Xiang Yao** ⓘ**, Siyuan Wang** ⓘ**, Guangsong Wang, and Ke Ren** ⓘ

Department of Radiology, Xiang'an Hospital of Xiamen University, Xiamen 361002, China

Correspondence should be addressed to Ke Ren; renke815@sina.com

Schizophrenia (SZ) is a severe psychiatric illness, and it affects around 1% of the general population; however, its reliable diagnosis is challenging. Functional MRI (fMRI) and structural MRI (sMRI) are useful techniques for investigating the functional and structural abnormalities of the human brain, and a growing number of studies have reported that multimodal brain data can improve diagnostic accuracy. Machine learning (ML) is widely used in the diagnosis of neuroscience and neuropsychiatry diseases, and it can obtain high accuracy. However, the conventional ML which concatenated the features into a longer feature vector could not be sufficiently effective to combine different features from different modalities. There are considerable controversies over the use of global signal regression (GSR), and few studies have explored the role of GSR in ML in diagnosing neurological diseases. The current study utilized fMRI and sMRI data to implement a new method named multimodal imaging and multilevel characterization with multiclassifier (M3) to classify SZs and healthy controls (HCs) and investigate the influence of GSR in SZ classification. We found that when we used Brainnetome 246 atlas and without performed GSR, our method obtained a classification accuracy of 83.49%, with a sensitivity of 68.69%, a specificity of 93.75%, and an AUC of 0.8491, respectively. We also got great classification performances with different processing methods (with/without GSR and different brain parcellation schemes). We found that the accuracy and specificity of the models without GSR were higher than that of the models with GSR. Our findings indicate that the M3 method is an effective tool to distinguish SZs from HCs, and it can identify discriminative regions to detect SZ to explore the neural mechanisms underlying SZ. The global signal may contain important neuronal information; it can improve the accuracy and specificity of SZ detection.

1. Introduction

Schizophrenia (SZ) is a severe psychiatric illness characterized by aberrant sensory perceptions, cognition, concrete thinking, and a restricted range of emotion, and it affects about 1% of the general population [1–5]. SZ is a heterogeneous disorder, and current diagnoses are based on subjective indicators such as self-report, observation, and clinical history, and its reliable diagnosis is challenging [1, 4, 6, 7], and the pathological mechanism is still unclear [4].

Functional MRI (fMRI) and structural MRI (sMRI) are gaining importance and becoming more widely acceptable techniques with the potential to help diagnose neurological illnesses [8–11], including schizophrenia [5, 12, 13]. An increasing number of studies have reported that multimodal brain data can improve diagnostic accuracy by combining the information obtained from different MRI imaging modalities [8, 14–16]. The machine learning (ML) technique is a new approach that can extract relevant information from images and construct models to determine the probability of disease onset, and it can make a higher accurate prediction compared with conventional methods [5, 6, 13, 17, 18]. Salvador et al. [15] achieved 75.76% accuracy in schizophrenia diagnosis, and de Filippis et al. [5] reported that support vector machine associated with other ML techniques could achieve accuracy close to 100%.

In conventional ML methods, most studies usually concatenated the features into a longer feature vector [19–21]. However, these methods may be insufficiently effective to combine different features from different modalities.

Some studies [16, 22, 23] have introduced novel methods to convey comprehensive and complementary information more effectively. Dai et al. [16] proposed a new method named multimodal imaging and multilevel characterization with multiclassifier (M3), which can effectively integrate different information from different modalities and can achieve higher classification accuracy than traditional feature combination methods and any single modality feature.

Global signal regression (GSR) is widely used to remove the effects of global BOLD signal variations in the analysis of fMRI studies; however, there are considerable controversies over its implementation [24–26], and few studies have explored the effect of GSR in ML of diagnosing neurological diseases [19, 27]. Different studies have reported inconsistent results on the effect of GSR on SZ [28–30]. As far as we know, very few studies reported the effect of GSR on ML of SZ classification [31]. However, the sample size of that study was limited, and it did not specifically discuss the effect of GSR on SZ classification. The brain parcellation is likely to affect classification accuracy [19, 27]. However, the influence of those factors in SZ classification is not very clear.

In this study, our goals are to classify SZ patients and healthy controls (HCs) using the M3 method and find the most relevant brain regions to explore its potential pathological mechanism. Furthermore, we investigate the influence of GSR and brain parcellation strategy in SZ classification.

2. Materials and Methods

2.1. Participants. The data in this study were selected from the Center for Biomedical Research Excellence (COBRE) (http://fcon_1000.projects.nitrc.org/indi/retro/cobre.html), an open neuroimaging dataset which includes fMRI and sMRI data from 71 SZs and 74 HCs with complete clinical and imaging information. Diagnostic information was collected by the Structured Clinical Interview used for DSM Disorders (SCID). Subjects were excluded if they had a history of neurological disorder, intellectual disability, severe head trauma with more than 5-minute loss of consciousness, substance abuse, or dependence within the last 12 months. Details of the diagnostic procedure and clinical information are available online (http://fcon_1000.projects.nitrc.org/indi/retro/cobre.html). To rule out the influence of handedness, we only included right-handed participants, so 15 subjects were excluded. And 21 subjects with maximum head motion larger than 2 mm or 2° were removed from the analysis. In the end, 109 subjects (64 HCs and 45 SZs) were included in this study. Demographic information of subjects is summarized in Table 1. Ethical approval was obtained by COBRE investigators; all participants provided written informed consent.

2.2. Data Acquisition. All subjects' resting-state fMRI (rs-fMRI) and sMRI data were collected from a 3.0 T Siemens TrioTim scanner. The sMRI data were acquired with T1-weighted magnetization prepared rapid acquisition gradient echo (MPRAGE) sequences: 176 slices, TR = 2530 ms, TE = 1.64, 3.5, 5.36, 7.22, and 9.08 ms, TI = 900 ms, flip angle = 7°, FOV = 256 mm × 256 mm, matrix = 256 × 256, and voxel

TABLE 1: Demographic and clinical data.

Items	SZs	HCs	Statistic	P value
Sample size	45	64	—	—
Gender (M/F)	36/9	44/20	1.71[a]	0.19
Age (years)	37.42 ± 13.55	35.22 ± 11.40	0.92[b]	0.26

[a]The chi-squared value was obtained by the chi-square test. [b]The t value was obtained by the two-sample two-tailed t-test. SZ: schizophrenia; HC: healthy control.

size = $1 \times 1 \times 1 \, mm^3$. Rs-fMRI scans were acquired single-shot echo-planar imaging sequence with the following parameters: 150 volumes, 33 slices, TR = 2000 ms, TE = 29 ms, matrix = 64×64, and voxel size = $3.75 \times 3.75 \times 4.55 \, mm^3$.

2.3. Data Preprocessing, fMRI, and sMRI Index Calculation. All data standard preprocessing was performed by Data Processing & Analysis of Brain Imaging (DPABI, http://rfmri.org/DPABI) [32], which is based on the Statistical Parametric Mapping (SPM12) package (http://www.fil.ion.ucl.ac.uk/spm) and the toolbox for Data Processing Assistant for Resting-State fMRI (DPARSF) toolbox [33] (http://rfmri.org/DPARSF).

The fMRI data preprocessing steps were as follows: (1) The first ten volumes of each subject were removed to ensure a steady-state condition. (2) Slice timing and realignment were carried out, and we excluded the subjects with maximum translation more than 2.0 mm or maximum rotation more than 2.0° in our study. (3) The T1 structural images were segmented into grey matter (GM), white matter (WM), and cerebrospinal fluid (CSF) and were coregistered to the mean functional image by using the Diffeomorphic Anatomical Registration Through Exponentiated Lie Algebra (DARTEL). (4) Functional data were spatially normalized to the Montreal Neurological Institute (MNI) space and resampled to $3 \times 3 \times 3 \, mm^3$ voxels. (5) The WM, CSF, 24 head motion parameters, and linear drift were removed as nuisance covariates by a multiple linear regression analysis. (6) Bandpass filter (0.01–0.10 Hz) was used to reduce the effects of low-frequency drift and high-frequency physiological noise.

We calculated the following fMRI measurements: amplitude of low-frequency fluctuations (ALFF) [34, 35], regional homogeneity (ReHo) [35, 36], degree centrality (DC) [37, 38], and voxel-mirrored homotopic connectivity (VMHC) [19, 39]. We used the DPARSF software default settings to calculate these indices. It is worth noting that we did not perform bandpass filter before calculating ALFF, and we set the connection's correlation coefficient threshold of $r > 0.25$ for DC calculation, and the individual functional data was registered to a symmetric template and smoothed with a Gaussian kernel of 4 mm before calculating VMHC. Those functional maps were then performed Fisher-Z transformation. Eventually, we smoothed these Z maps with a Gaussian kernel of 4 mm except for WMHC.

The GM images obtained from the previous segmentation step were then spatially normalized into standard space, smoothed with a Gaussian kernel of 8 mm, and
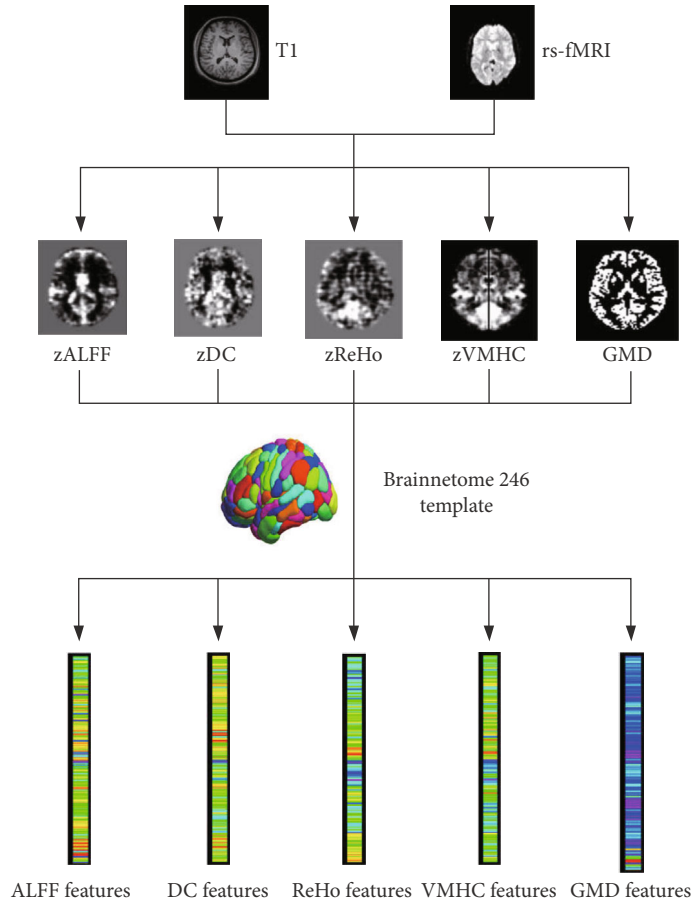
FIGURE 1: The flowchart of feature extraction. The data preprocessing and index calculation of fMRI and sMRI were performed by the DPABI toolbox, and then, functional maps were then performed Fisher-Z transformation. Finally, we obtained fMRI and sMRI measurement maps, including zALFF, zDC, zReHo, zVMHC, and GMD. The fMRI and sMRI maps were segmented into 246 regions of interest using the Brainnetome 246 atlas, and then, we got 246 features for each fMRI and sMRI map. ALFF: amplitude of low-frequency fluctuations; ReHo: regional homogeneity; DC: degree centrality; VMHC: voxel-mirrored homotopic connectivity.

resampled to $3 \times 3 \times 3 \, \text{mm}^3$ voxels, and we got grey matter density (GMD) images.

2.4. Feature Extraction.

The fMRI and sMRI maps were segmented into 246 regions of interest (ROIs) using the Brainnetome (BN) 246 atlas (see Table S1) [40], which consists of 210 cortical and 36 subcortical subregions in the cerebrum. Each ROI from the brain parcellation atlas was used to mask each individual's fMRI and sMRI map, and the signal value of each ROI was obtained by averaging the fMRI and sMRI signals of all the voxels included in the ROI. This process was repeated for all individuals and regions. Finally, we got 246 features for each fMRI and sMRI map and a total of 1230 features for each individual, as shown in Figure 1. This ROI-based feature extraction method is widely used in neuroimaging ML studies [41–44]. It is an effective method to reduce feature dimensionality and improve computational efficiency [45]. Previous studies have shown that ROI-based feature extraction could denote pathological changes in brain regions, identify abnormal brain regions, and assist in the diagnosis of the disease

[20, 41, 46–48]. Then, these features were used in the subsequent analysis.

2.4.1. Discriminative Analysis and Identification of the Most Discriminative Features.

We constructed the model according to the method introduced by Dai et al. [16], which mainly includes feature selection, maximum uncertainty linear discriminate analysis- (MLDA-) based classification, and multiclassifier. Leave-one-out crossvalidation (LOOCV) was conducted to estimate the performance of our classifier (Figure 2).

The feature selection process was carried out on the training set only. First, all features were standardized by z-score, the normalization of the training and test datasets was performed, respectively, and then, two-sample two-tailed t-tests were performed to determine the features that showed differences between the SZ patients and HC groups. LOOCV was conducted to estimate the performance of our classifier and to determine the optimal P value threshold, as shown in Figures 2 and 3. In brief, we used each subject as the test set to test the performance of the model and the remaining
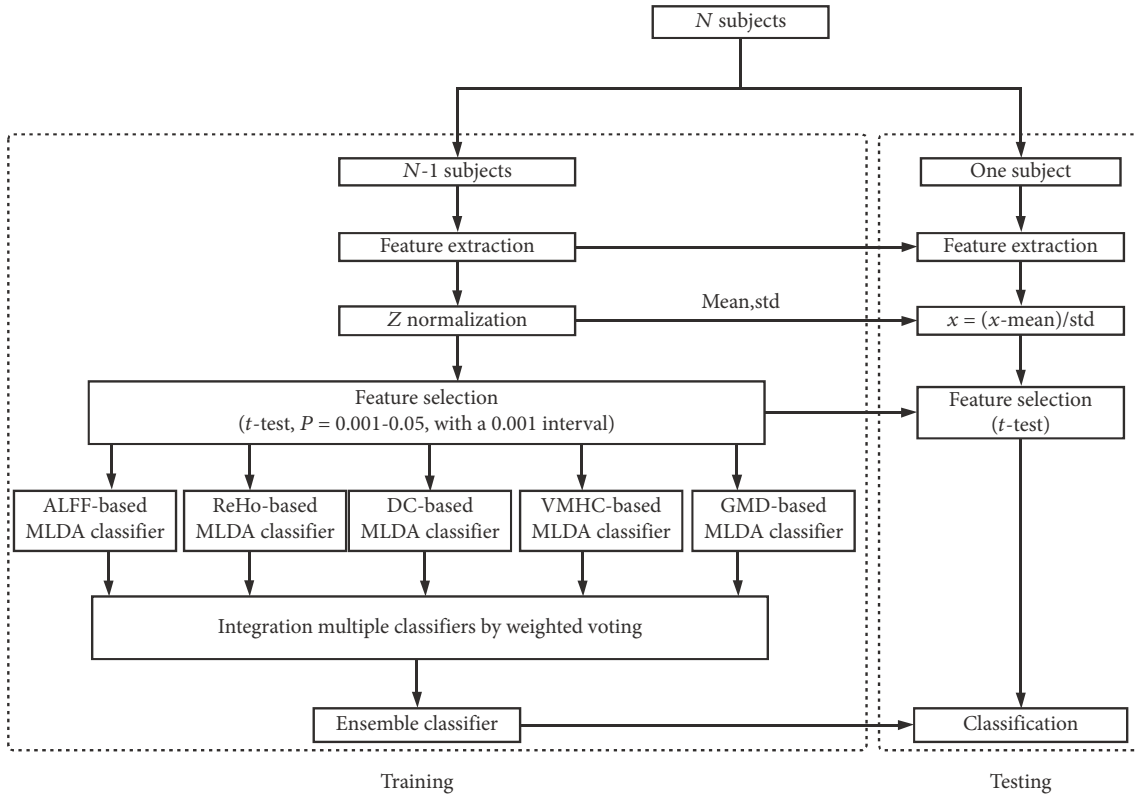
FIGURE 2: The flowchart of the optimal P value threshold selection and M3 method used in our study. We used leave-one-out crossvalidation (LOOCV) to estimate the performance of our classifier. All features in the training and test sets were standardized by z-score, and then, two-sample two-tailed t-tests with P threshold from 0.001 to 0.05 with a 0.001 interval (50 iterations) were performed to select discriminative features. We used MLDA with five category features (ALFF, ReHo, DC, VMHC, and GMD) to obtain five base classifiers, and then, we combined five classifiers into one classifier by weighted voting. Subsequently, we evaluate the performance of the classifier and obtained 50 classification accuracies, and the P threshold with the highest classification accuracy was defined as the optimal threshold.

subjects as the training set to train the model, repeated N times in turn, where N represented the number of subjects. We calculate the performance of the model based on the predicted labels (SZ or HC) and the actual labels of N iterations, including accuracy, sensitivity, and specificity. We applied the P threshold from 0.001 to 0.05 with a 0.001 interval (50 iterations) and obtained 50 classification accuracies, and the P threshold with the highest classification accuracy was defined as the optimal P threshold based on the classification accuracy values of the 50 iterations (Figures 2 and 3) [20, 44].

We performed the MLDA-based classifier, multiclassifier, crossvalidation, and identification of the most discriminative feature procedures as previously described [16]. Briefly, we used MLDA with five-category features (ALFF, ReHo, DC, VMHC, and GMD) to obtain five base classifiers. Then, we combined five classifiers into one classifier by weighted voting. Subsequently, LOOCV was used to evaluate the performance of the classifier. For each of the 5 base classifiers, we could obtain the coefficients of the features, and we normalized the coefficients by dividing by the maximum coefficient value. We multiplied the absolute value of normalized coefficients by the base classifier's weight of voting as feature weights. The feature weight of each base classifier is the average of each fold of LOOCV, and finally, we summed the feature weights of each base classifier to obtain the final

feature weights of multiclassifier. The most discriminative features were restricted to features that appeared in each fold of LOOCV.

A permutation test was applied 1000 times to test the significance of the prediction performance [20, 44, 47]. First, the class label of each subject was randomly permutated 1000 times without replacement and assigned to all the subjects, and then, the entire M3 procedure was reapplied each time to obtain the permutated classification accuracy, and at last, the P value for the accuracy was calculated by dividing the number of permutations that showed a higher accuracy than the actual accuracy for the real sample by the total number of permutations. We applied the same method to calculate the P value of AUC by permutating the value of the sum predicted label randomly.

2.5. Validating the Influences of GSR and Brain Parcellation. To evaluate the influence of GSR and brain parcellation on our classifier, we did additional analysis: (1) we did regress out global signal in the regressing out nuisance covariate step and (2) we use another additional brain parcellation atlas (Power-264 atlas [49]) to segment brain ROIs. For Power-264 atlas, to be consistent with BN-246 atlas (without cerebellum), we did not include the ROIs of the cerebellum. We performed the same M3 method and evaluated the

(a)

(b)

(c)

(d)
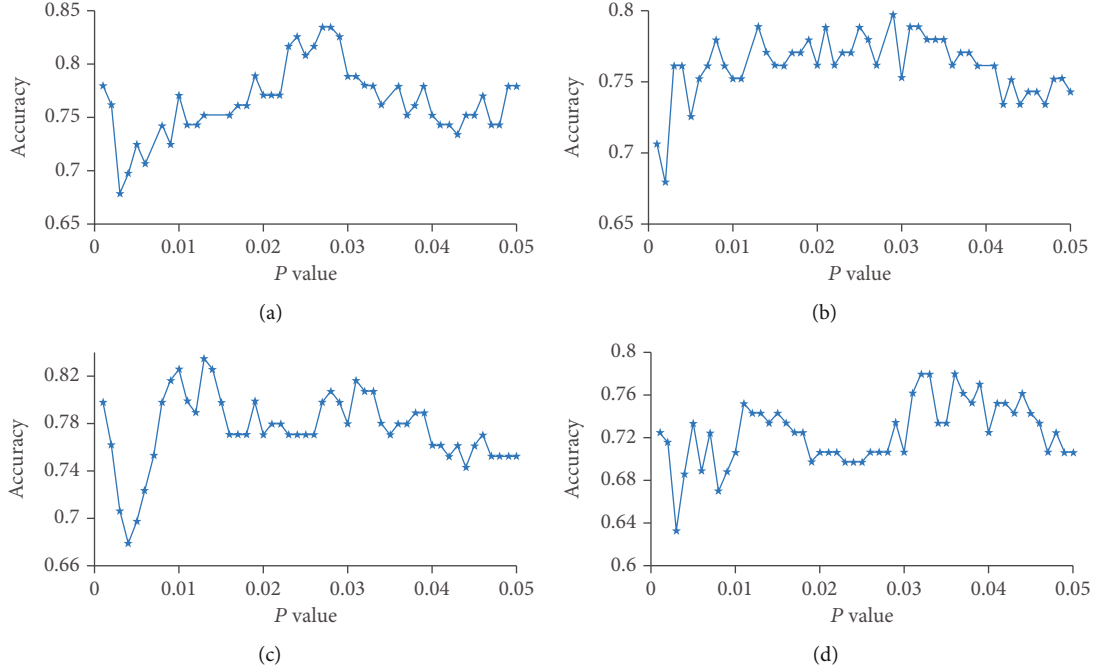
FIGURE 3: Selection of the optimal P threshold via the grid search and LOOCV method. (a–d) Represent the classification accuracy versus the P value with BN-246 atlas+noGSR (a), Power-264 atlas+noGSR (b), BN-246 atlas+GSR (c), and Power-264 atlas+GSR (d). BN: Brainnetome atlas; GSR: global signal regression; noGSR: no global signal regression.

TABLE 2: Classification performance of the M3 classifiers.

Items	Optimal P threshold	AUC	Accuracy (%)	Sensitivity (%)	Specificity (%)
BN-246_noGSR	0.027	0.8491	83.49	68.89	93.75
Power-264_noGSR	0.029	0.7785	79.82	73.33	84.38
BN-246_GSR	0.013	0.8215	83.49	86.67	81.25
Power-264_GSR	0.032	0.8165	77.98	71.11	82.81

M3: multimodal imaging and multilevel characterization with multiclassifier; BN: Brainnetome atlas; GSR: global signal regression; noGSR: no global signal regression.

classification performance. We compare the classification performance of the models with the AUC to determine the effect of GSR and brain parcellation on classifiers with the Delong test.

3. Results

3.1. Classification Performance. To optimize the P threshold value to select the features of the classifier, we performed the grid search method using the training set. We applied the P threshold from 0.001 to 0.05 with a 0.001 interval, we found that the optimal P threshold was 0.027, and the corresponding classifier obtained a classification accuracy of 83.49%, with a sensitivity of 68.69%, a specificity of 93.75%, and an AUC of 0.8491, respectively (Table 2, Figures 3(a) and 4(a)). The P values of the model accuracy and AUC both were $P < 0.001$ (Figure 4(b), Figure S1a), which suggests that the classifier prediction performance was significantly higher than chance.

3.2. Discriminative Brain Regions. To determine which brain regions contributed to single-subject classification, we computed the model feature weights and obtained the order of feature contribution of the classification [16]. The most discriminative features were restricted to features that appeared in each fold of LOOCV. The top 15 brain regions with the highest feature weights are reported in Table 3 and Figure 5. The most discriminative regions included the left superior parietal lobule, inferior parietal lobule, inferior temporal gyrus, middle frontal gyrus, lateral occipital cortex, fusiform gyrus, right basal ganglia, cingulate gyrus, superior frontal gyrus, posterior superior temporal sulcus, bilateral medioventral occipital cortex, and parahippocampal gyrus (Table 3; Figure 5).

3.3. Influence of Brain Regional Parcellation Schemes. To evaluate the influence of the parcellation schemes on our M3 classifier, we performed our analysis approach with Power-264 atlas to test the classification performance of the model. We obtained a high classification performance with
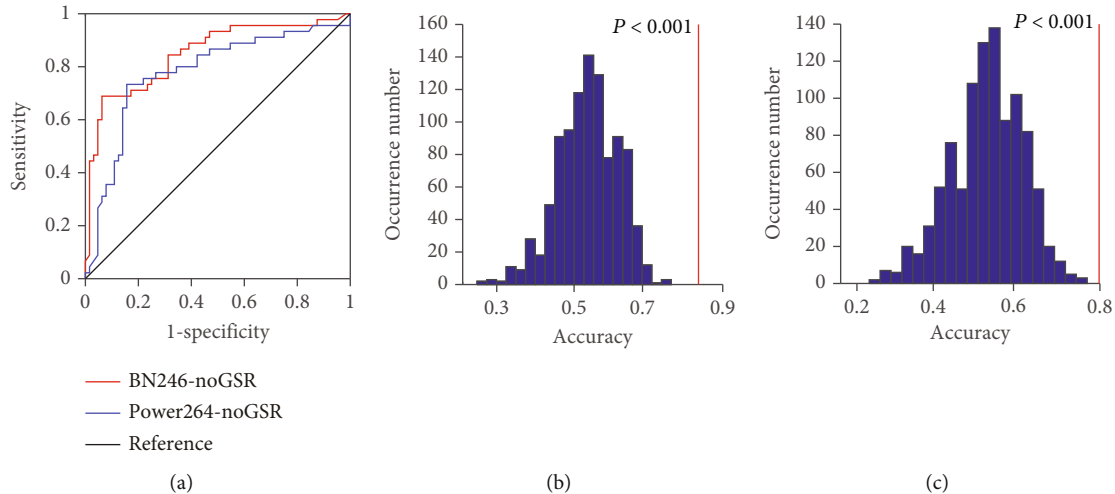
FIGURE 4: Classification performance of the classifiers without GSR. (a) The ROC curve of the classifiers based on BN-246 atlas and Power-264 atlas without GSR. The distributions of the permutated accuracy values of BN-246 atlas (b) and Power-264 atlas (c) without GSR. The red line indicates the values obtained using the real labels. BN: Brainnetome atlas; noGSR: no global signal regression.

AUC of 0.7785, and the accuracy, sensitivity, and specificity were 79.82%, 73.33%, and 84.38%, respectively (Table 2, Figures 3(b), 4(a), and 4(c), Figure S1b). We compared the AUC of two classifier performances using the Delong test, and we did not find a significant difference between them ($z = 0.095$, $P = 0.92$).

3.4. Influence of Global Signal Regression. In order to evaluate the influence of global signal regression, we performed the above M3 methods with GSR. We found that the accuracy and specificity of the classifiers without GSR were equal or higher than that of the classifiers with GSR both with BN-246 atlas and Power-264 atlas (Table 2; Figures 3(c), 3(d), and 6 and Figure S2), but we did not find significant differences between them (BN-246_GSR vs. BN-246_noGSR: $z = -0.74$, $P = 0.46$; Power-264_GSR vs. Power-264_noGSR: $z = 0.93$, $P = 0.35$).

4. Discussion

In the current study, we combined functional and structural MRI measures to distinguish SZs from HCs by the M3 method. We found that we got great classification performances using different processing methods (with/without GSR and different brain regional parcellation schemes) and a set of discriminative regions to distinguish SZs from HCs. Our study demonstrates that the M3 method is a great tool to effectively distinguish SZs from HCs and explore the neural mechanisms underlying SZ.

Previous neuroimaging ML studies focused on a single modal image [50, 51] or concatenated multimodal features into a longer feature vector [19, 21, 44, 47]. Recent studies have shown that multimodal imaging using integrated information can significantly improve the classification accuracy [16, 20, 21, 23, 47]. And conventional multimodal direct feature concatenation method may not be sufficiently effective in combining features from different modalities [16, 52]. Previous studies have shown that the

M3 method can improve classification performance than any single-modal feature and conventional multimodal feature combination methods [16]. Our study also found that the M3 method can effectively distinguish SZs from HCs. Dai et al. [16] found that the M3 method can identify the most discriminative features to classify Alzheimer's disease patients and HCs which are consistent with previous studies that have used conventional univariate statistical analysis of structural and functional MRI. It may be able to explore the underlying mechanisms of neuropsychiatric diseases. Our results are consistent with the previous study.

In previous studies, most researchers empirically chose $P < 0.01$ or $P < 0.05$ as the threshold for feature selection in the data dimensionality reduction step [16, 18, 19]. In our study, we performed grid search [20, 44, 53] to select the optimal P threshold to obtain the relatively highest prediction accuracy of the classifier. Most current ML studies [8, 19, 21, 47] usually concatenated the features into a longer feature vector. However, these methods are insufficiently effective to combine different features from different modalities. It has been confirmed that the M3 method can effectively integrate different information from different modalities and can achieve higher classification accuracy than traditional feature combination methods and any single modality features [16]. In our study, we used the BN-246 atlas and M3 method with five types of modality features (ALFF, ReHo, DC, VMHC, and GMD), and we obtained a classification accuracy of 83.49%, a sensitivity of 68.69%, and a specificity of 93.75%, respectively. In addition, we obtained close classification performance using different preprocessing methods (with/without GSR) and different brain regional parcellation schemes. Our classification accuracy is close to or even higher than the results of SZ ML studies [1, 2, 5, 6, 14, 18] and other disease studies [9, 19, 44, 51]. These results are consistent with a previous study which reported that the M3 method can obtain great classification accuracy [16].

TABLE 3: Top 15 most discriminative features for classification.

Regions	ALFF	DC	ReHo	VMHC	GMD	Weight
SPL_L_5_2	$t = -3.22$ ($P = 0.0017$)	$t = -2.69$ ($P = 0.0082$)	NS	$t = -2.62$ ($P = 0.0102$)	NS	1.3275
IPL_L_6_2	NS	$t = 2.70$ ($P = 0.0080$)	$t = 2.97$ ($P = 0.0037$)	NS	NS	1.2037
MVOcC_L_5_1	$t = -2.77$ ($P = 0.0066$)	$t = -4.49$ ($P < 0.0001$)	$t = -3.75$ ($P = 0.0002$)	$t = -3.82$ ($P = 0.0002$)	NS	1.1467
ITG_L_7_3	$t = 4.78$ ($P < 0.0001$)	$t = 4.18$ ($P < 0.0001$)	$t = 3.66$ ($P = 0.0004$)	NS	NS	1.0778
MFG_L_7_5	$t = 2.66$ ($P = 0.0091$)	$t = 3.54$ ($P = 0.0006$)	$t = 2.83$ ($P = 0.0056$)	$t = 2.88$ ($P = 0.0048$)	$t = -2.42$ ($P = 0.0172$)	0.9969
MVOcC_R_5_1	NS	$t = -2.85$ ($P = 0.0053$)	$t = -3.94$ ($P = 0.0001$)	$t = -3.44$ ($P = 0.0008$)	NS	0.9484
PhG_L_6_5	NS	$t = 3.10$ ($P = 0.0025$)	NS	$t = 2.86$ ($P = 0.0051$)	$t = -2.96$ ($P = 0.0037$)	0.9476
LOcC_L_2_2	$t = -3.18$ ($P = 0.0019$)	$t = -3.57$ ($P = 0.0005$)	$t = -2.69$ ($P = 0.0084$)	$t = -4.00$ ($P = 0.0001$)	NS	0.9099
FuG_L_3_2	$t = -2.81$ ($P = 0.0058$)	$t = -4.55$ ($P < 0.0001$)	$t = -3.49$ ($P = 0.0007$)	$t = -3.56$ ($P = 0.0006$)	NS	0.8904
BG_R_6_5	NS	$t = 2.70$ ($P = 0.0081$)	$t = 3.40$ ($P = 0.0010$)	$t = 2.39$ ($P = 0.0188$)	$t = -3.84$ ($P = 0.0002$)	0.8877
MVOcC_R_5_3	$t = -2.46$ ($P = 0.016$)	$t = -2.89$ ($P = 0.0046$)	$t = -3.12$ ($P = 0.0023$)	$t = -3.75$ ($P = 0.0003$)	NS	0.8413
CG_R_7_7	NS	NS	$t = -3.07$ ($P = 0.0027$)	$t = -2.35$ ($P = 0.0204$)	NS	0.7860
SFG_R_7_2	$t = 3.89$ ($P = 0.0002$)	$t = 3.45$ ($P = 0.0008$)	$t = 3.95$ ($P = 0.0001$)	$t = 2.60$ ($P = 0.0107$)	NS	0.7672
PhG_R_6_5	NS	$t = 3.59$ ($P = 0.0005$)	NS	$t = 2.61$ ($P = 0.0104$)	NS	0.7664
pSTS_R_2_2	NS	$t = -4.05$ ($P < 0.0001$)	$t = -2.28$ ($P = 0.0246$)	$t = -2.76$ ($P = 0.0068$)	$t = -2.78$ ($P = 0.0064$)	0.7283

NS: not significant, $P > 0.027$ (optimal P threshold); positive t value means increased values in the SZ group. ALFF: amplitude of low-frequency fluctuations (ALFF); ReHo: regional homogeneity; DC: degree centrality; VMHC: voxel-mirrored homotopic connectivity; SPL: superior parietal lobule; IPL: inferior parietal lobule; MVOcC: medioventral occipital cortex; ITG: inferior temporal gyrus; MFG: middle frontal gyrus; PhG: parahippocampal gyrus; LOcC: lateral occipital cortex; FuG: fusiform gyrus; BG: basal ganglia; CG: cingulate gyrus; SFG: superior frontal gyrus; pSTS: posterior superior temporal sulcus; L: left; R: right.
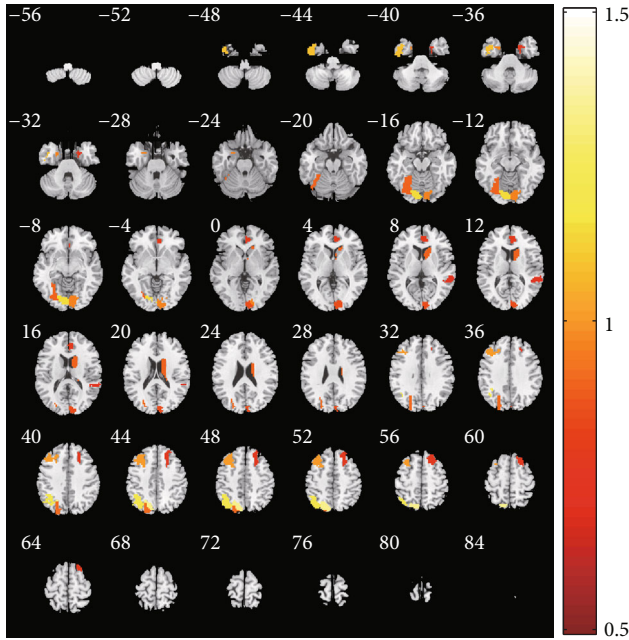
FIGURE 5: The most discriminative brain regions. The most discriminative regions included the left superior parietal lobule, inferior parietal lobule, inferior temporal gyrus, middle frontal gyrus, lateral occipital cortex, fusiform gyrus, right basal ganglia, cingulate gyrus, superior frontal gyrus, posterior superior temporal sulcus, bilateral medioventral occipital cortex, and parahippocampal gyrus. The color bar value represents the weight value of the brain regions.

The debate about the complex composition of global signals and the necessity of GSR in data preprocessing and data analysis always exists in most cases [24, 54, 55]. Some studies reported that the global signal was likely to reflect important neuronal components in rs-fMRI data [17, 18, 39]. Qing et al. [26] reported that GSR effects are region-specific and suggested that it is great to report results both with and without GSR in ReHo study. Li et al. [56] reported that GSR strengthens association between resting-state functional connectivity and behavior in young healthy adults. And in some studies [57, 58], the authors regressed out global signal as a nuisance variable to reduce the effects of nonneuronal BOLD fluctuations.

Controversies also root in the influence of the global signal in distinguishing SZs from HCs. Yang et al. [28] reported that the variance of the global BOLD signal was significantly higher in patients with SZ as compared to HCs, but not in bipolar disorder, they pointed that the global signal had important biological significance for SZ, and its effects were disease-specific. Similarly, Hahamy et al. [29] reported that GSR reduced variance in subjects with SZ. On the contrary, a recent study showed that there was no overall increase or reduction in resting-state global signal in SZ patients [30]. In our study, we did not find a significant difference in classification performance between the classifiers with and without GSR, which is consistent with a previous study [19]. These results indicated that our model was robust, but we found that the accuracy and specificity of the models without

GSR were higher than that of the models with GSR both with BN-246 atlas and Power-264 atlas (Table 2, Figures 4 and 6), which are consistent with previous studies [27, 28]. This could facilitate accurate SZ patient identification and early intervention. Chen et al. reported [27] that the model without GSR enhanced the sensitivity of the detection of differences between Alzheimer's disease and HCs. A recent study also found that global network metrics without GSR have more significant differences than that with GSR between major depression patients and HCs. For SZ, previous studies reported that the global signal was of functional relevance, as it differentiated between SZs and HCs [28, 29], which are consistent with our result, but Umeh et al. [30] reported a contradictory finding. However, in that study, the sample size was limited (38 SZs and 35 HCs). All these findings suggest that the global signal may contain important neuronal information, at least in the case of SZ.

We repeated our M3 pipeline using Power-264 atlas to evaluate whether our results were affected by brain parcellation. Previous studies reported that functionally defined parcellation or high spatial resolution parcellation is probably to detect more significant differences, and anatomical boundaries do not necessarily match functional ones [27, 59]. Therefore, we utilized functional atlas in our study (BN-246 and Power-264 atlas). In our study, we got high classification performances and did not find any significant difference in different brain regional parcellation schemes, which suggested that brain parcellation did not influence our prediction performance, and it is consistent with previous studies [19, 60]. The result indicated that our model had good robustness and generalizability.

Many studies reported abnormal structures and functional brain regions of SZ. In the current study, we found that the most discriminate regions between SZs and HCs mainly locate in the left superior parietal lobule, inferior parietal lobule, inferior temporal gyrus, middle frontal gyrus, lateral occipital cortex, fusiform gyrus, right basal ganglia, cingulate gyrus, superior frontal gyrus, posterior superior temporal sulcus, bilateral medioventral occipital cortex, and parahippocampal gyrus (Figure 5). A meta-analysis that included 79 studies reported that SZ was associated with structural and functional abnormalities in the bilateral anterior cingulate gyrus and middle frontal gyrus [61]. Ren et al. [62] also reported the abnormalities in bilateral anterior cingulate gyrus cortex, occipital gyrus, and left inferior parietal lobule in drug-naive first-episode SZ patients. Zhao et al. [63] reported that SZ patients had extensive structural and functional abnormalities, including bilateral occipital lobe, left orbital frontal cortex, bilateral superior parietal lobule, right middle temporal gyrus, gyrus rectus and superior frontal gyrus, bilateral inferior parietal lobule, and precuneus. Machine learning studies also reported that the bilateral fusiform gyrus, superior parietal lobule, superior temporal gyrus, cingulate gyrus, middle frontal gyrus, inferior parietal lobule, parahippocampal gyrus, and right medial superior frontal gyrus contributed to discrimination between SZ patients and HCs [3, 5, 7, 18, 64–66]. Our results are consistent with these previous studies.
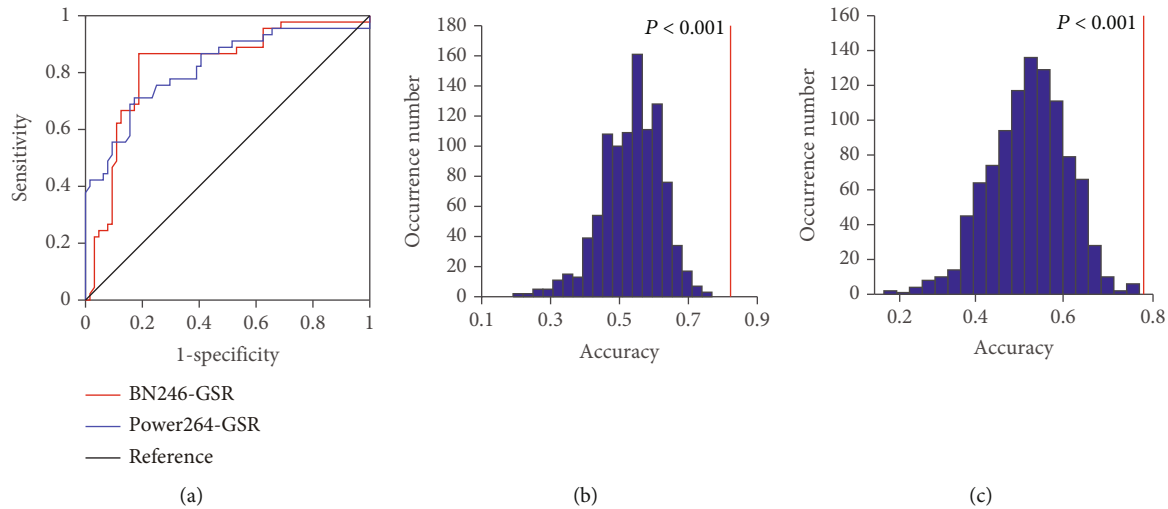
FIGURE 6: Classification performance of the classifiers with GSR. (a) The ROC curve of the classifiers based on BN-246 atlas and Power-264 atlas with GSR. The distributions of the permutated accuracy values of BN-246 atlas (b) and Power-264 atlas (c) with GSR. The red line indicates the values obtained using the real labels. BN: Brainnetome atlas; AAL: automated anatomical labeling; GSR: global signal regression.

Our study has some limitations. First, although the sample size is limited, it is relatively larger when compared to previous studies [1, 21, 31, 50, 65]. A larger sample size should be recruited in the future to replicate and enrich our findings. Second, some studies [5, 67] have reported differences in the cerebellum between SZ patients and HCs, but in some cases, in our study, the cerebellum was not fully covered during rs-fMRI scanning, so the cerebellum was not considered in our study, and we selected the atlas that does not contain the cerebellum or excluded the cerebellar ROI in the brain atlas. Third, the head motion in subjects with SZ was greater than that in subjects with HC (mean framewise displacement Jenkinson: SZ, 0.19 ± 0.10 mm; HC, 0.14 ± 0.08 mm). Although we adopted strict control inclusion criteria (less than 2 mm and 2.0°), regressed out head motion (with 24 head motion parameters), we cannot guarantee the complete removal of the head motion effect.

5. Conclusion

In conclusion, our findings indicated that the M3 method is a great tool to distinguish SZs from HCs effectively with high classification accuracy; it can be generalized in different brain parcellation schemes. The global signal may contain important neuronal information; it can improve the accuracy and specificity to detect SZ patients. The M3 method without GSR is helpful to identify patient accuracy and early intervention, and it can identify discriminative regions to detect SZ to explore the neural mechanisms underlying SZ.

Data Availability

Publicly available datasets were analyzed in this study. This data can be found here: http://fcon_1000.projects.nitrc.org/indi/retro/cobre.html. The code is available on request to the corresponding author.

Conflicts of Interest

The authors declare that the research was conducted in the absence of any commercial or financial relationships that could be construed as a potential conflict of interest.

Authors' Contributions

DS conducted the experiment, performed the data processing and analysis, and wrote the manuscript. YL and HZ collected the data and performed the data processing and analysis and edited the manuscript. XY, GW, and SW collected the data and performed the data processing and analysis. KR supervised the whole including experiments and manuscript writing. All authors contributed to the article and approved the submitted version.

Supplementary Materials

Table S1: cortical and subcortical regions of interest defined in Brainnetome atlas. Figure S1: the distributions of the permutated AUC values without GSR. The distributions of the permutated AUC values of BN-246 atlas (a) and Power-264 atlas (b) without GSR. The red line indicates the values obtained using the real sum predicted label. Figure S2: the distributions of the permutated AUC values with GSR. The distributions of the permutated AUC values of BN-246 atlas (a) and Power-264 atlas (c) with GSR. The red line indicates the values obtained using the real sum predicted label. *(Supplementary Materials)*

References

[1] Y. Bae, K. Kumarasamy, I. M. Ali, P. Korfiatis, Z. Akkus, and B. J. Erickson, "Differences between schizophrenic and normal subjects using network properties from fMRI," *Journal of Digital Imaging*, vol. 31, no. 2, pp. 252–261, 2018.

[2] K. C. Skåtun, T. Kaufmann, N. T. Doan et al., "Consistent functional connectivity alterations in schizophrenia spectrum disorder: a multisite study," *Schizophrenia Bulletin*, vol. 43, no. 4, pp. 914–924, 2017.

[3] V. D. Calhoun, J. Sui, K. Kiehl, J. Turner, E. Allen, and G. Pearlson, "Exploring the psychosis functional connectome: aberrant intrinsic networks in schizophrenia and bipolar disorder," *Frontiers in Psychiatry*, vol. 2, p. 75, 2012.

[4] M. Wang, X. Hao, J. Huang et al., "Hierarchical structured sparse learning for schizophrenia identification," *Neuroinformatics*, vol. 18, no. 1, pp. 43–57, 2020.

[5] R. de Filippis, E. A. Carbone, R. Gaetano et al., "Machine learning techniques in a structural and functional MRI diagnostic approach in schizophrenia: a systematic review," *Neuropsychiatric Disease and Treatment*, vol. 15, pp. 1605–1627, 2019.

[6] K. Oh, W. Kim, G. Shen et al., "Classification of schizophrenia and normal controls using 3D convolutional neural network and outcome visualization," *Schizophrenia Research*, vol. 212, pp. 186–195, 2019.

[7] D. Chyzhyk, A. Savio, and M. Grana, "Computer aided diagnosis of schizophrenia on resting state fMRI data by ensembles of ELM," *Neural Networks*, vol. 68, pp. 23–33, 2015.

[8] S. H. Hojjati, A. Ebrahimzadeh, A. Khazaee, A. Babajani-Feremi, and Alzheimer's Disease Neuroimaging Initiative, "Predicting conversion from MCI to AD by integrating rs-fMRI and structural MRI," *Computers in Biology and Medicine*, vol. 102, pp. 30–39, 2018.

[9] S. N. Gosnell, J. C. Fowler, and R. Salas, "Classifying suicidal behavior with resting-state functional connectivity and structural neuroimaging," *Acta Psychiatrica Scandinavica*, vol. 140, no. 1, pp. 20–29, 2019.

[10] S. Kiryu, K. Yasaka, H. Akai et al., "Deep learning to differentiate parkinsonian disorders separately using single midsagittal MR imaging: a proof of concept study," *European Radiology*, vol. 29, no. 12, pp. 6891–6899, 2019.

[11] X. Yang, X. Hu, W. Tang et al., "Multivariate classification of drug-naive obsessive-compulsive disorder patients and healthy controls by applying an SVM to resting-state functional MRI data," *BMC Psychiatry*, vol. 19, no. 1, p. 210, 2019.

[12] S. M. Plis, M. F. Amin, A. Chekroud et al., "Reading the (functional) writing on the (structural) wall: multimodal fusion of brain structure and function via a deep neural network based translation approach reveals novel impairments in schizophrenia," *NeuroImage*, vol. 181, pp. 734–747, 2018.

[13] K. Dillon, V. Calhoun, and Y. P. Wang, "A robust sparse-modeling framework for estimating schizophrenia biomarkers from fMRI," *Journal of Neuroscience Methods*, vol. 276, pp. 46–55, 2017.

[14] J. Sui, H. He, Q. Yu et al., "Combination of resting state fMRI, DTI, and sMRI data to discriminate schizophrenia by N-way MCCA + jICA," *Frontiers in Human Neuroscience*, vol. 7, p. 235, 2013.

[15] R. Salvador, E. Canales-Rodríguez, A. Guerrero-Pedraza et al., "Multimodal integration of brain images for MRI-based diagnosis in schizophrenia," *Frontiers in Neuroscience*, vol. 13, p. 1203, 2019.

[16] Z. Dai, C. Yan, Z. Wang et al., "Discriminative analysis of early Alzheimer's disease using multi-modal imaging and multi-level characterization with multi-classifier (M3)," *NeuroImage*, vol. 59, no. 3, pp. 2187–2195, 2012.

[17] P. Orban, C. Dansereau, L. Desbois et al., "Multisite generalizability of schizophrenia diagnosis classification based on functional brain connectivity," *Schizophrenia Research*, vol. 192, pp. 167–171, 2018.

[18] J. Li, Y. Sun, Y. Huang, A. Bezerianos, and R. Yu, "Machine learning technique reveals intrinsic characteristics of schizophrenia: an alternative method," *Brain Imaging and Behavior*, vol. 13, no. 5, pp. 1386–1396, 2019.

[19] Y. Wang, K. Sun, Z. Liu et al., "Classification of unmedicated bipolar disorder using whole-brain functional activity and connectivity: a radiomics analysis," *Cerebral Cortex*, vol. 30, no. 3, pp. 1117–1128, 2020.

[20] B. Zhou, D. An, F. Xiao et al., "Machine learning for detecting mesial temporal lobe epilepsy by structural and functional neuroimaging," *Frontiers in Medicine*, vol. 14, no. 5, pp. 630–641, 2020.

[21] H. Sun, Y. Chen, Q. Huang et al., "Psychoradiologic utility of MR imaging for diagnosis of attention deficit hyperactivity disorder: a radiomics analysis," *Radiology*, vol. 287, no. 2, pp. 620–630, 2018.

[22] D. Zhang, D. Shen, and Alzheimer's Disease Neuroimaging Initiative, "Multi-modal multi-task learning for joint prediction of multiple regression and classification variables in Alzheimer's disease," *NeuroImage*, vol. 59, no. 2, pp. 895–907, 2012.

[23] J. Sui, S. Qi, T. G. M. van Erp et al., "Multimodal neuromarkers in schizophrenia via cognition-guided MRI fusion," *Nature Communications*, vol. 9, no. 1, p. 3028, 2018.

[24] T. T. Liu, A. Nalci, and M. Falahpour, "The global signal in fMRI: nuisance or information?," *NeuroImage*, vol. 150, pp. 213–229, 2017.

[25] S. Shahsavarani, I. T. Abraham, B. J. Zimmerman, Y. M. Baryshnikov, and F. T. Husain, "Comparing cyclicity analysis with pre-established functional connectivity methods to identify individuals and subject groups using resting state fMRI," *Frontiers in Computational Neuroscience*, vol. 13, p. 94, 2020.

[26] Z. Qing, Z. Dong, S. Li, Y. Zang, and D. Liu, "Global signal regression has complex effects on regional homogeneity of resting state fMRI signal," *Magnetic Resonance Imaging*, vol. 33, no. 10, pp. 1306–1313, 2015.

[27] X. Chen, X. Liao, Z. Dai et al., "Topological analyses of functional connectomics: a crucial role of global signal removal, brain parcellation, and null models," *Human Brain Mapping*, vol. 39, no. 11, pp. 4545–4564, 2018.

[28] G. J. Yang, J. D. Murray, G. Repovs et al., "Altered global brain signal in schizophrenia," *Proceedings of the National Academy of Sciences of the United States of America*, vol. 111, no. 20, pp. 7438–7443, 2014.

[29] A. Hahamy, V. Calhoun, G. Pearlson et al., "Save the global: global signal connectivity as a tool for studying clinical populations with functional magnetic resonance imaging," *Brain Connectivity*, vol. 4, no. 6, pp. 395–403, 2014.

[30] A. Umeh, J. Kumar, S. T. Francis, P. F. Liddle, and L. Palaniyappan, "Global fMRI signal at rest relates to symptom severity in schizophrenia," *Schizophrenia Research*, vol. 220, pp. 281-282, 2020.

[31] B. Bohaterewicz, A. M. Sobczak, I. Podolak et al., "Machine learning-based identification of suicidal risk in patients with schizophrenia using multi-level resting-state fMRI features," *Frontiers in Neuroscience*, vol. 14, p. 605697, 2021.

[32] C. G. Yan, X. D. Wang, X. N. Zuo, and Y. F. Zang, "DPABI: data processing & analysis for (resting-state) brain imaging," *Neuroinformatics*, vol. 14, no. 3, pp. 339–351, 2016.

[33] C. G. Yan and Y. F. Zang, "DPARSF: a MATLAB toolbox for "pipeline" data analysis of resting-state fMRI," *Frontiers in Systems Neuroscience*, vol. 4, p. 13, 2010.

[34] L. Lin, L. J. Zheng, U. Joseph Schoepf et al., "Uric acid has different effects on spontaneous brain activities of males and females: a cross-sectional resting-state functional MR imaging study," *Frontiers in Neuroscience*, vol. 13, p. 763, 2019.

[35] Z. Chen, Q. Wang, M. Liang et al., "Visual cortex neural activity alteration in cervical spondylotic myelopathy patients: a resting-state fMRI study," *Neuroradiology*, vol. 60, no. 9, pp. 921–932, 2018.

[36] J. Zhang, J. Su, M. Wang et al., "The sensorimotor network dysfunction in migraineurs without aura: a resting-state fMRI study," *Journal of Neurology*, vol. 264, no. 4, pp. 654–663, 2017.

[37] Q. Zhang, Y. Shu, X. Li et al., "Resting-state functional magnetic resonance study of primary open-angle glaucoma based on voxelwise brain network degree centrality," *Neuroscience Letters*, vol. 712, p. 134500, 2019.

[38] M. Li, Y. Liu, H. Chen et al., "Altered global synchronizations in patients with Parkinson's disease: a resting-state fMRI study," *Frontiers in Aging Neuroscience*, vol. 11, p. 139, 2019.

[39] W. Jiang, Y. Lei, J. Wei et al., "Alterations of interhemispheric functional connectivity and degree centrality in cervical dystonia: a resting-state fMRI study," *Neural Plasticity*, vol. 2019, Article ID 7349894, 11 pages, 2019.

[40] L. Fan, H. Li, J. Zhuo et al., "The human Brainnetome atlas: a new brain atlas based on connectional architecture," *Cerebral Cortex*, vol. 26, no. 8, pp. 3508–3526, 2016.

[41] D. Jin, P. Wang, A. Zalesky et al., "Grab-AD: generalizability and reproducibility of altered brain activity and diagnostic classification in Alzheimer's disease," *Human Brain Mapping*, vol. 41, no. 12, pp. 3379–3391, 2020.

[42] K. Zhao, Y. Ding, Y. Han et al., "Independent and reproducible hippocampal radiomic biomarkers for multisite Alzheimer's disease: diagnosis, longitudinal progress and biological basis," *Science Bulletin*, vol. 65, no. 13, pp. 1103–1113, 2020.

[43] V. Wottschel, D. T. Chard, C. Enzinger et al., "SVM recursive feature elimination analyses of structural brain MRI predicts near-term relapses in patients with clinically isolated syndromes suggestive of multiple sclerosis," *Neuroimage Clin*, vol. 24, p. 102011, 2019.

[44] Z. Cui, Z. Xia, M. Su, H. Shu, and G. Gong, "Disrupted white matter connectivity underlying developmental dyslexia: a machine learning approach," *Human Brain Mapping*, vol. 37, no. 4, pp. 1443–1458, 2016.

[45] L. Wang, Y. Liu, X. Zeng, H. Cheng, Z. Wang, and Q. Wang, "Region-of-interest based sparse feature learning method for Alzheimer's disease identification," *Computer Methods and Programs in Biomedicine*, vol. 187, p. 105290, 2020.

[46] B. Peng, S. Wang, Z. Zhou et al., "A multilevel-ROI-features-based machine learning method for detection of morphometric biomarkers in Parkinson's disease," *Neuroscience Letters*, vol. 651, pp. 88–94, 2017.

[47] Z. Tang, Z. Liu, R. Li et al., "Identifying the white matter impairments among ART-naïve HIV patients: a multivariate pattern analysis of DTI data," *European Radiology*, vol. 27, no. 10, pp. 4153–4162, 2017.

[48] J. Mo, Z. Liu, K. Sun et al., "Automated detection of hippocampal sclerosis using clinically empirical and radiomics features," *Epilepsia*, vol. 60, no. 12, pp. 2519–2529, 2019.

[49] J. D. Power, A. L. Cohen, S. M. Nelson et al., "Functional network organization of the human brain," *Neuron*, vol. 72, no. 4, pp. 665–678, 2011.

[50] Y. Hou, C. Luo, J. Yang et al., "Prediction of individual clinical scores in patients with Parkinson's disease using resting-state functional magnetic resonance imaging," *Journal of the Neurological Sciences*, vol. 366, pp. 27–32, 2016.

[51] T. Zhang, Z. Zhao, C. Zhang, J. Zhang, Z. Jin, and L. Li, "Classification of early and late mild cognitive impairment using functional brain network of resting-state fMRI," *Frontiers in Psychiatry*, vol. 10, p. 572, 2019.

[52] D. Zhang, Y. Wang, L. Zhou, H. Yuan, D. Shen, and Alzheimer's Disease Neuroimaging Initiative, "Multimodal classification of Alzheimer's disease and mild cognitive impairment," *NeuroImage*, vol. 55, no. 3, pp. 856–867, 2011.

[53] H. Sun, R. Jiang, S. Qi et al., "Preliminary prediction of individual response to electroconvulsive therapy using whole-brain functional magnetic resonance imaging data," *NeuroImage: Clinical*, vol. 26, p. 102080, 2020.

[54] H. Xu, J. Su, J. Qin et al., "Impact of global signal regression on characterizing dynamic functional connectivity and brain states," *NeuroImage*, vol. 173, pp. 127–145, 2018.

[55] K. Murphy and M. D. Fox, "Towards a consensus regarding global signal regression for resting state functional connectivity MRI," *NeuroImage*, vol. 154, pp. 169–173, 2017.

[56] J. Li, R. Kong, R. Liégeois et al., "Global signal regression strengthens association between resting-state functional connectivity and behavior," *NeuroImage*, vol. 196, pp. 126–141, 2019.

[57] H. Yu, L. Chen, H. Li et al., "Abnormal resting-state functional connectivity of amygdala subregions in patients with obstructive sleep apnea," *Neuropsychiatric Disease and Treatment*, vol. 15, pp. 977–987, 2019.

[58] X. Mu, Z. Wang, B. Nie et al., "Altered regional and circuit resting-state activity in patients with occult spastic diplegic cerebral palsy," *Pediatrics and Neonatology*, vol. 59, no. 4, pp. 345–351, 2018.

[59] M. D. Rosenberg, E. S. Finn, D. Scheinost et al., "A neuromarker of sustained attention from whole-brain functional connectivity," *Nature Neuroscience*, vol. 19, no. 1, pp. 165–171, 2016.

[60] R. Jiang, V. D. Calhoun, Y. Cui et al., "Multimodal data revealed different neurobiological correlates of intelligence between males and females," *Brain Imaging and Behavior*, vol. 14, no. 5, pp. 1979–1993, 2020.

[61] E. Bora, A. Fornito, J. Radua et al., "Neuroanatomical abnormalities in schizophrenia: a multimodal voxelwise meta-analysis and meta-regression analysis," *Schizophrenia Research*, vol. 127, no. 1-3, pp. 46–57, 2011.

[62] W. Ren, S. Lui, W. Deng et al., "Anatomical and functional brain abnormalities in drug-naive first-episode schizophrenia," *The American Journal of Psychiatry*, vol. 170, no. 11, pp. 1308–1316, 2013.

[63] C. Zhao, J. Zhu, X. Liu et al., "Structural and functional brain abnormalities in schizophrenia: a cross-sectional study

at different stages of the disease," *Progress in Neuro-Psychopharmacology & Biological Psychiatry*, vol. 83, pp. 27–32, 2018.

[64] F. M. Hanlon, J. M. Houck, C. J. Pyeatt et al., "Bilateral hippocampal dysfunction in schizophrenia," *NeuroImage*, vol. 58, no. 4, pp. 1158–1168, 2011.

[65] D. Chyzhyk, M. Graña, D. Öngür, and A. K. Shinn, "Discrimination of schizophrenia auditory hallucinators by machine learning of resting-state functional MRI," *International Journal of Neural Systems*, vol. 25, no. 3, p. 1550007, 2015.

[66] Y. Xiao, Z. Yan, Y. Zhao et al., "Support vector machine-based classification of first episode drug-naïve schizophrenia patients and healthy controls using structural MRI," *Schizophrenia Research*, vol. 214, pp. 11–17, 2019.

[67] W. H. Pinaya, A. Gadelha, O. M. Doyle et al., "Using deep belief network modelling to characterize differences in brain morphometry in schizophrenia," *Scientific Reports*, vol. 6, no. 1, p. 38897, 2016.

Research Article

Association between Inflammatory Factors in the Aqueous Humor and Hyperreflective Foci in Patients with Intractable Macular Edema Treated with Antivascular Endothelial Growth Factor

Min Li,[1] **Jing Li,**[2] **Kaichuan Chen,**[2] **Jia Wang,**[2] **Minjie Sheng,**[2] **and Bing Li** [ID][2]

[1]*Department of Ophthalmology, Zhongshan Hospital Affiliated with Fudan University, Shanghai, China*
[2]*Department of Ophthalmology, Yangpu Hospital, Tongji University School of Medicine, Shanghai, China*

Correspondence should be addressed to Bing Li; bing-li-2007@163.com

Background. To evaluate the correlations between the inflammatory factors in the aqueous humor and hyperreflective foci (HRF) in patients with intractable macular edema treated with antivascular endothelial growth factor (anti-VEGF). *Methods.* This study included 17 patients with intractable macular edema (ME) treated with anti-VEGF agents. Inflammatory factors in the aqueous humor were measured by the Cytometric Beads Array before injection, and the numbers of HRF pre- and post-anti-VEGF treatment were counted from four different directions (90 degrees, 45 degrees, 180 degrees, and 135 degrees) in the SD-OCT images, respectively, before treatment and one month after treatment. The correlations between inflammatory factors and the numbers of HRF were assessed. *Results.* The numbers of HRF were reduced significantly after anti-VEGF treatment. The change in the HRFs at the 90-degree location was significantly positively correlated with IL-8 and VCAM-1. The change of all HRFs was significantly positively correlated with IL-8. The HRFs before the treatment also had a positive correlation with IL-8 and VCAM-1. *Conclusion.* After anti-VEGF treatment, the numbers of HRF in intractable ME declined greatly. The higher the levels of IL-8 and VCAM-1 before treatment, the more significant the reduction of HRF after anti-VEGF treatment, which indicated that HRF could be an effective noninvasive imaging indicator for evaluating the effect of anti-VEGF on intractable macular edema. The OCT images at the 90-degree location could better show the inflammatory reaction of patients and also had better clinical significance for the prognosis evaluation of ME associated with inflammation.

1. Introduction

The macular is the most sensitive location of vision, and macular edema (ME) is one of the main reasons for visual impairment in the presence of macular lesions. In clinical circumstances, ME is mainly caused by diabetic retinopathy [1] and retinal vein occlusion [2]. Research has revealed that the major cause of ME is the production of vascular endothelial growth factor (VEGF) [3]. Anti-VEGF agents are currently the most cutting-edge treatment options for ME. However, some of the patients treated with the same anti-VEGF drug for ME have poor visual outcomes [3]. Moreover, after several treatments with anti-VEGF, ME is still existing or recurring, known as intractable ME [4]. For this reason, clinicians have to find other methods of predicting the final visual outcomes of intractable ME.

Hyperreflective foci (HRF) is defined as "discrete, well-circumscribed dots with equal or greater reflectivity than the RPE band" in the images of spectral domain optical coherence tomography (SD-OCT) [5, 6]. HRF can be found throughout all retinal layers, but with special accumulations in the intraretinal cystoid spaces. Moreover, HRF has been reported in various retinal diseases, such as retinal vein occlusion [7], diabetic macular edema (DME) [8], and neovascular age-related macular degeneration (AMD) [9]. Some researchers reported that HRF in the AMD and diabetic maculopathy patients showed dynamic changes after anti-VEGF therapy [10–12]. Recent studies demonstrated that

HRF could predict the final visual outcome in ME patients with anti-VEGF agents [13, 14]. Therefore, HRFs can be a new biomarker in patients with ME treated with anti-VEGF agents. However, it was reported that in a group of intractable ME patients treated with anti-VEGF agents, the mechanism underlying the change in HRF remained unclear.

In this study, we compared the changes in numbers of HRF and measured its correlation with inflammatory factors in intractable ME patients treated with anti-VEGF drugs, in order to find the possible roles and mechanism of HRF in the clinical follow-up of intractable ME.

2. Methods

2.1. Subjects. This study included 17 patients with intractable ME, who had been treated with anti-VEGF agents at least twice based on a previous study [4]. The last intravitreal injection was at least two months before extraction of aqueous humor. Only ME related with diabetic retinopathy or retinal vein occlusion was taken into account and recorded in this study. All the eyes of the studied subjects with the following symptoms were excluded: ME with hard exudate at the macula, epiretinal membrane or foveal traction, vitreous hemorrhage or pre- and subretinal hemorrhage, uveitis, glaucoma, or other retinal diseases. These data were collected at the Department of Ophthalmology, Yangpu Hospital, Tongji University School of Medicine, Shanghai, between March 2019 and October 2019, with the approval of the Ethics Committee of the Hospital (ethical approval no. LL-2018-ZRKX-031). All the processes were performed in accordance with the tenets of the Declaration of Helsinki. All the subjects were informed about the purpose and study method and signed their informed consent before examination. Using a 23 gauge needle, we extracted $100 \mu l$ aqueous humor from every intractable ME patient before an intravitreal injection of anti-VEGF.

The levels of inflammatory factors (VEGF, BFGF, IL-6, IL-10, IL-8, and vascular cell adhesion molecule-1 (VCAM-1)) in the aqueous humor were analyzed and quantified using Cytometric Beads Array (BD Biosciences, USA) and flow cytometry.

2.2. Characteristic Analysis of HRF in the SD-OCT Images. A volume scan covering a 6×6 mm area of the macular area centered on the fovea was acquired using SD-OCT (RTvue XR, OPTOVUE, USA). HRF in the SD-OCT images is a small, well-circumscribed, dot-shaped lesion with similar or higher reflectivity than RPE in all retinal layers. The range of diameters of HRF was limited to 20 to 50 μm [5, 6]. Therefore, we excluded small noise signals and large hyperreflective lesions considered to be hard exudates. We collected OCT images of each patient at four locations (90-degree, 45-degree, 180-degree, and 135-degree), respectively, before and one month after anti-VEGF treatment (Figure 1). The numbers of HRF were counted separately by two independent observers, and then, an average value was taken.

2.3. Statistical Analysis. The statistical analysis was performed with SPSS software version 19.0 (SPSS, Inc., Chicago, IL, USA). All values are reported as mean ± standard deviation (mean ± SD). A paired Student's *t*-test was used to compare the differences in HRF pre- and posttreatments with anti-VEGF. The correlations between the levels of inflammatory factors and the change in the numbers of HRF were assessed with Pearson's or Spearman's correlation analysis. A value of was considered statistically significant.

3. Results

17 eyes of 17 subjects were recorded and enrolled in this study (8 males and 9 females, mean ± SD, 58 years ± 12 years). All the subjects had been treated with anti-VEGF agents at least twice prior to their aqueous humor measurement. The anti-VEGF agent names, the previous injections of anti-VEGF, and the inflammatory factors in aqueous humor for this treatment are listed in Table 1. Foveal thickness and HRFs in OCT images before and after anti-VEGF treatment are shown in Table 2.

3.1. The Changes of Fovea Thickness and the Numbers of HRF after Anti-VEGF Treatment. After treatment, the fovea was significantly thinner than before ($P < 0.01$), which indicated that after more than two times anti-VEGF treatments, macular edema had been effectively controlled. In the meantime, the numbers of HRF significantly decreased at four locations (90-degree, 45-degree, 180-degree, and 135-degree) after the treatments compared with before the treatment. (Figure 2).

3.2. Correlation between the Changes of HRF and the Inflammatory Factors in the Aqueous Humor. In this study, the numbers of total HRF before the treatments had a positive correlation with IL-8 ($r = 0.638$, $P = 0.006$) (Figure 3(a)) and VCAM-1 ($r = 0.539$, $P = 0.025$) (Figure 3(b)), which indicated that the higher the levels of IL-8 and VCAM-1, the more HRF were found in their OCT images. Also, the changes of HRFs after treatments at the 90-degree location of the SD-OCT images were significantly positively correlated with the levels of IL-8 ($r = 0.524$, $P = 0.031$) (Figure 4(a)) and VCAM-1 ($r = 0.616$, $P = 0.008$) (Figure 4(b)). In contrast to the 90-degree location, the changes in numbers of HRF after treatments at the 45-degree, 135-degree, and 180-degree locations in the OCT images showed no correlation with IL8 or VCAM-1 ($P > 0.05$).

More interestingly, we found that the changes of total HRFs after treatments were also significantly positively correlated with its levels of IL-8 ($r = 0.510$, $P = 0.044$) (Figure 5(a)) and the changes of fovea thickness ($r = 0.518$, $P = 0.033$) (Figure 5(b)), which indicated that, if the levels of IL-8 and VCAM-1 in aqueous humor were higher before treatments, the numbers of HRF should decrease more after anti-VEGF treatments. In addition, there were no significant correlation between the changes of HRFs and other inflammatory factors (VEGF, BFGF, IL-6, and IL-10) ($P > 0.05$).

4. Discussion

ME is clinically defined as an accumulation of serous fluid within the neurosensory retina, with increased thickness of the central retina. Some researches have shown that the leakage from the choroidal new vessels, predominantly VEGF-induced, may produce a large accumulation of fluid under
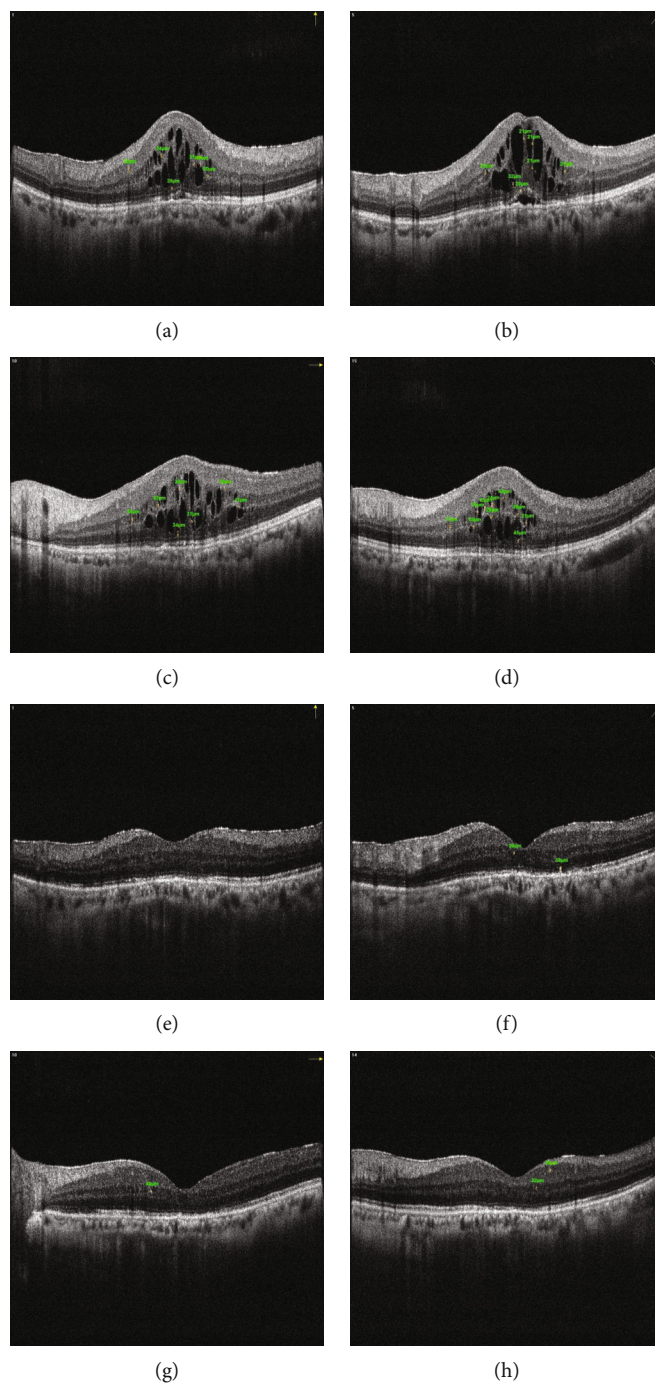
Figure 1: The change of HRFs in a female patient at OCT images at four locations before and after anti-VEGF treatment (90-degree, 45-degree, 180-degree, and 135-degree). Before this time of collecting aqueous humor and anti-VEGT treatment, this patient had already accepted three times of anti-VEGT treatment whose ME was still persistent. (a) Image at 90 degrees before treatment. (b) Image at 45 degrees before treatment. (c) Image at 180 degrees before treatment. (d) Image at 135 degrees before treatment. (e) Image at 90 degrees after treatment. (f) Image at 45 degrees after treatment. (g) Image at 180 degrees after treatment. (h) Image at 135 degrees after treatment.

the neurosensory retina [15]. Anti-VEGF has now become the cutting-edge treatment choice for ME, due to its excellent visual and anatomic improvement [16]. However, along with the widespread application of this treatment scheme, clinicians have found that some patients with the same intractable ME did not achieve satisfactory visual recovery postoperatively. Some indicators are therefore needed to evaluate the

outcome of postoperative treatments in advance in intractable ME patients. Prior researches found that HRF showed dynamic changes after anti-VEGF therapy in patients with neovascular DME [16], AMD [17], and retinal vein occlusion [18]. In our study, HRFs in the SD-OCT were found scattered throughout all retinal layers, primarily around fluid accumulation in the intraretinal cystoid spaces. This study found that

TABLE 1: Basic information and inflammatory factors in aqueous humor measurement.

No.	Anti-VEGF agent(s)	Previous injections	VEGF	BFGF	IL-6	IL-10	IL-8	VCAM-1
1	Ranibizumab	2	670.6	0	0	0	0	0
2	Conbercept	4	7.4	0	4503.1	1.5	86.5	0
3	Conbercept	3	17.8	8.8	4.6	0.4	3.3	38.7
4	Conbercept	3	4.9	12.4	5.5	0.6	4.2	113.3
5	Ranibizumab	2	34.3	8.8	9.6	0	12.3	523.7
6	Conbercept	3	6.3	11.6	18.2	0	10.8	544.5
7	Conbercept	2	188.2	11.3	53.5	0	26.6	391.8
8	Ranibizumab	4	38.7	7.4	0	0	4.2	136.9
9	Ranibizumab	2	115.4	10.2	15.7	0	18.9	459
10	Conbercept	3	49	6.8	23.7	0	14.1	149.4
11	Conbercept	3	19.1	0	11.3	0	26.2	352.9
12	Conbercept	3	5.9	0	2.4	0	0.2	78.3
13	Ranibizumab	3	64.6	9.7	17.1	0	26.9	285.3
14	Ranibizumab	2	90.1	6.7	101.8	0	62.3	2867.1
15	Ranibizumab	3	101.2	6.5	4.5	0	18.3	197.2
16	Ranibizumab	3	140.4	0	91.7	0.6	35.1	843.1
17	Ranibizumab	3	308.3	13.7	22.4	1.1	25.5	704.5

The unit of inflammatory factors is pg/ml.

TABLE 2: Foveal thickness and HRFs in OCT images before and after anti-VEGF treatment.

No.	Before treatment					After treatment				
	HRF-90°	HRF-180°	HRF-45°	HRF-135°	Foveal thickness	HRF-90°	HRF-180°	HRF-45°	HRF-135°	Foveal thickness
1	3	2	4	2	177	2	1	1	4	165
2	6	7	7	9	619	0	1	2	2	162
3	4	0	0	4	187	0	1	1	1	167
4	0	0	0	1	351	0	0	2	0	162
5	5	7	7	6	540	2	0	1	1	179
6	1	1	3	1	643	1	0	0	1	566
7	3	3	8	2	221	1	0	2	0	197
8	8	3	6	3	521	0	1	2	0	235
9	2	1	2	3	307	0	2	3	2	214
10	3	1	3	2	684	0	0	0	0	381
11	8	9	5	4	716	4	5	7	2	651
12	1	0	2	0	566	1	0	0	0	469
13	0	15	4	8	322	1	7	1	3	259
14	20	7	14	2	209	8	5	6	1	184
15	1	3	0	2	272	0	0	2	1	199
16	3	0	0	4	195	0	0	0	0	162
17	1	0	2	0	201	0	0	0	0	185

The unit of foveal thickness is μm.

patients with intractable ME were taking a turn for the better and HRFs in four directions were significantly reduced after receiving more than two times anti-VEGF drug treatments. As a result, we considered HRF could be a reliable biomarker of patients with intractable ME after treatments with anti-VEGF agents.

HRF may appear in vivo inflammatory components of ME, and HRF can be presumed to activate microglia [17, 18]. Inflammatory mediators and the accumulation of inflammatory cells induced subretinal and intraretinal fluid accumulation in macular edema [18]. Moreover, HRF, as an indirect clinical sign of inflammation, was involved in
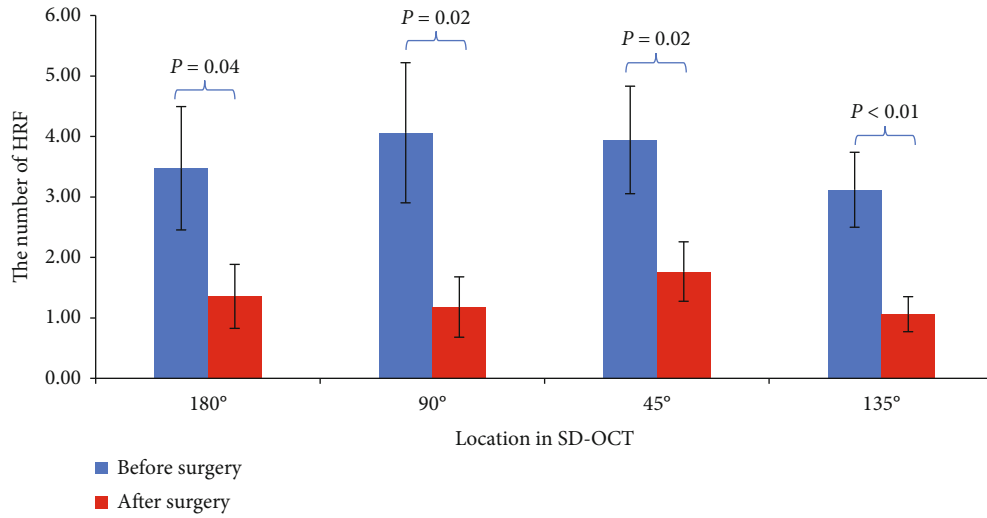
FIGURE 2: Comparison of the numbers of HRF at four locations in SD-OCT images before and after anti-VEGF treatment.

(a)

(b)
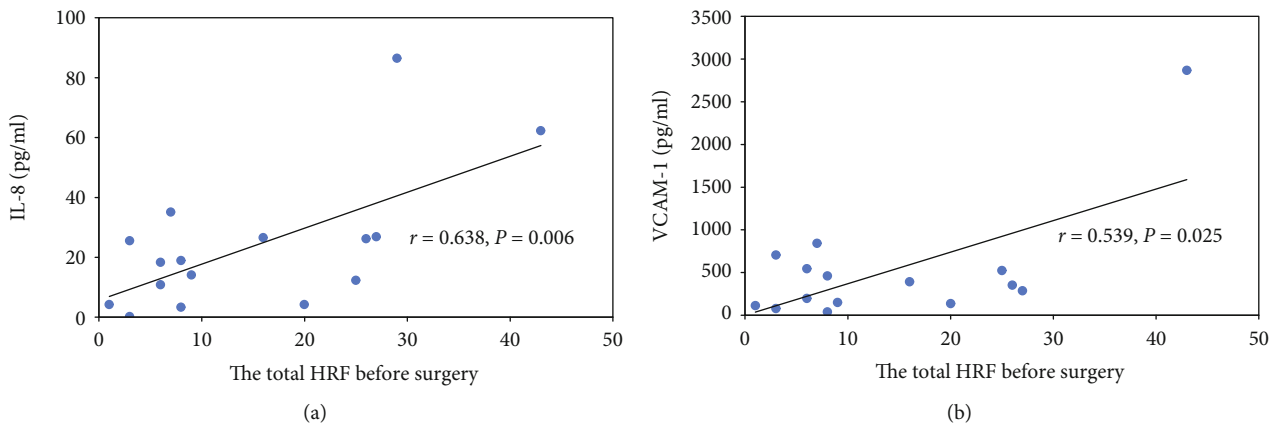
FIGURE 3: Correlation between the total HRF before anti-VEGF treatment and expression of inflammatory factors (IL-8 and VCAM-1) in the aqueous humor.

(a)

(b)
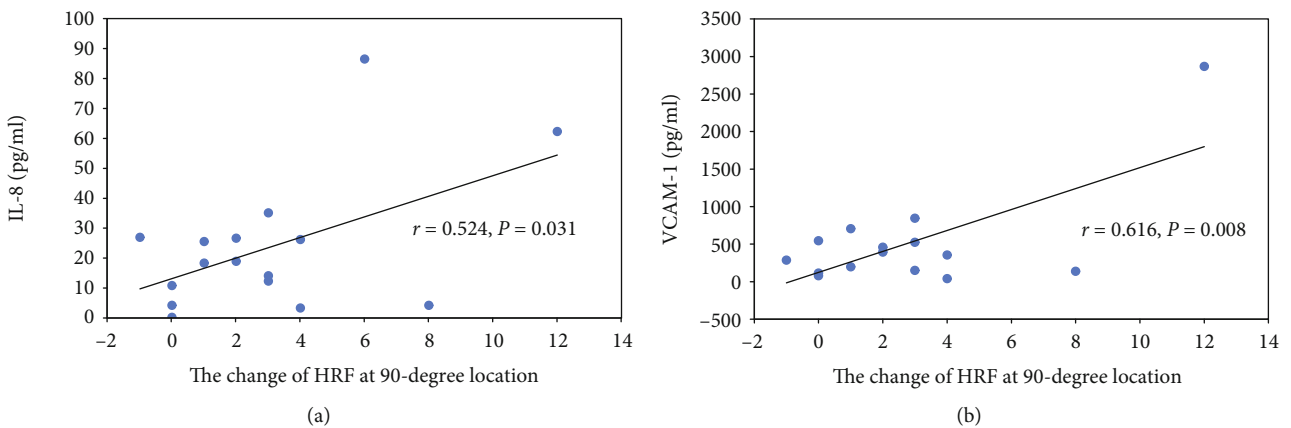
FIGURE 4: Correlation between the change of HRFs at 90-degree location after anti-VEGF treatment and expression of inflammatory factors (IL-8 and VCAM-1) in the aqueous humor.
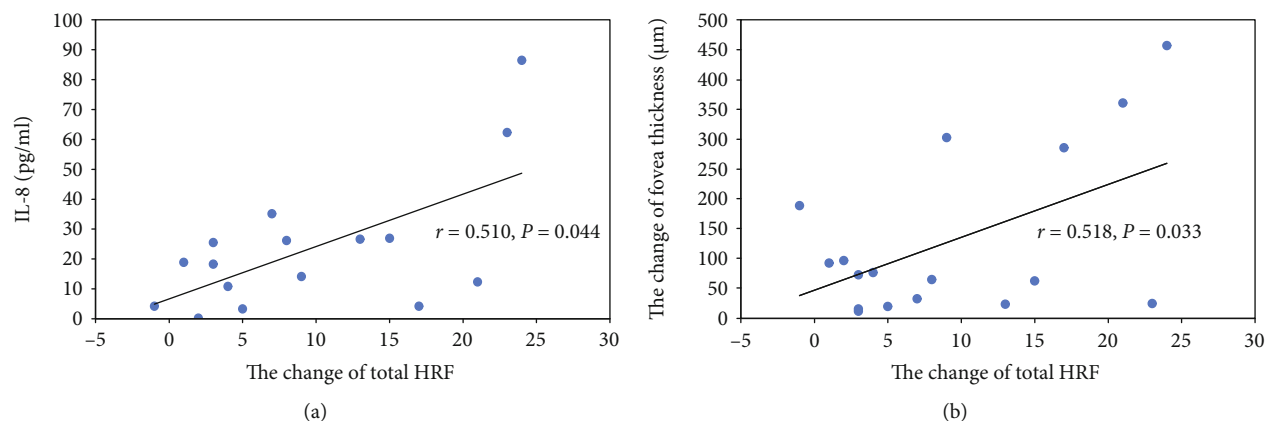
FIGURE 5: Correlation between the change of total HRFs after anti-VEGF treatment, levels of IL-8 in the aqueous humor and the change of fovea thickness.

retinal inflammatory response [8, 18]. In addition, HRF, also as an earlier manifestation of microvascular damage, may be important in the risk assessment of the progression of DME and vision loss [8]. HRFs have also been found to be a sign of vascular hyperpermeability [19]. In animal studies, a VEGF blockade has been shown to inhibit or reduce microglia activation [17]. Recent studies showed that, after anti-VEGF treatment, retinal vessel hyperpermeability improved and the number of HRF decreased in DME patients [16]. In this study, the number of HRF significantly decreased, which can be explained, to some extent, by the blockade of vascular hyperpermeability. Additionally, there may be other inflammatory mechanisms involved in this process.

Research shows that the origin of HRF might be from activated microglia related with the inflammatory environment in age-related macular degeneration. Anti-VEGF treatment is associated with a reduction of HRF in DME, and HRF has been considered a marker of active inflammatory status [20]. The detection of inflammatory factors in aqueous humor is a new approach to assess the status of ocular inflammation [21]. In this study, we detected inflammatory factors in the aqueous solution of patients with intractable ME and further studied their relationship with HRF, thereby providing more evidence on HRF's involvement in the inflammatory pathological process of ME. The study showed the total HRF before treatments and the change in numbers of HRF after treatments were both significantly positively correlated with IL-8 and VCAM-1.

IL-8 is a well-known proinflammatory cytokine that acts as a neutrophil chemoattractant and a T-cell activator. Researchers have reported that IL-8 directly stimulates VEGF expression and the autocrine activation of VEGF receptor-2 in vascular endothelial cells. Some research also found the aqueous humor levels of IL-8 increased significantly in patients with DME [22]. Many studies have shown that IL-8 levels in the aqueous humor of DME patients may be associated with inflammation-induced damage to the blood-retina barrier. VCAM-1, an endothelial cell adhesion molecule, is upregulated to the endothelium in response to inflammation and transmigration into tissues [23]. The levels of

VCAM-1 in the aqueous humor increased with the severity of diabetic retinopathy, which suggests that VCAM-1 may play a role in the progression of diabetic retinopathy [24]. Therefore, these cytokines have the potential to be used as biomarkers to predict the progress of inflammation in ME. In this study, for patients with ME prior to treatments, the higher levels of IL-8 and VCAM-1, the more HRF were found in their OCT images and the more significant the reduction in HRF after the treatments. Besides that, the change in numbers of HRF at the 90-degree location in the OCT images was significantly positively correlated with IL-8 and VCAM-1. We think that the OCT image at the 90-degree location may better reflect the inflammatory reaction of patients and also have better clinical significance for the prognosis evaluation of macular edema associated with inflammation.

The previous further studies showed that IL-8 was secreted by microglia [25], and VCAM-1 could increase microglial reactivity [23]. The correlation between the numbers of HRF and the levels of IL-8 and VCAM-1 in ME in this study also supported our hypothesis that HRF represented activated microglia. We observed that, in the pathological process of ME, as the permeability of retinal vascular and subretinal fluid increased, the levels of IL-8 and VCAM-1 increased, thus promoting the activation of microglia. After anti-VEGF treatments, retinal vascular permeability was improved, inflammatory factor expression was decreased, and microglia activation was decreased. According to our results, the whole pathological process can be monitored by comparing the changes in HRF seen on OCT before and after anti-VEGF treatments. To sum up, HRF could be a new, noninvasive biomarker of functional and structural responses to anti-VEGF treatments or other drugs targeting the inflammatory microenvironment in intractable ME.

This study has still several limitations. Since aqueous humor accumulation is an invasive operation, we could not obtain the samples of aqueous humor from patients, which results in that we could not compare the change in inflammatory factors in the aqueous humor before and after treatments. However, according to our results, HRF, as an indirect indicator, can be used to evaluate changes in

inflammatory factors postoperation. Although we obtained some significant results from this not too large sample, a further study can be conducted to test and verify our results based on large enough samples in the future.

5. Conclusion

In conclusion, we have observed that the numbers of HRF in intractable ME significantly decreased after anti-VEGF treatments, and there was a positive correlation between the levels of IL-8 and VCAM1, and the numbers of HRF shown by SD-OCT. The marked change in HRF and the relationship with the inflammatory factors suggest that HRF can act as a clinical marker for inflammatory reaction in patients with intractable ME. Moreover, they can provide as an effective noninvasive imaging indicator for evaluating the effect of anti-VEGF on inflammation-related diseases.

Data Availability

The data used to support the findings of this study are available from the corresponding author upon request.

Conflicts of Interest

There were not any competing financial interests in relation to the work described. The authors disclosed there were no sources of any support for the work, received in the form of grants and equipment and drugs.

Acknowledgments

References

[1] J. W. Yau, S. L. Rogers, R. Kawasaki et al., "Global prevalence and major risk factors of diabetic retinopathy," *Diabetes Care*, vol. 35, no. 3, pp. 556–564, 2012.

[2] J. W. Kang, H. Lee, H. Chung, and H. C. Kim, "Correlation between optical coherence tomographic hyperreflective foci and visual outcomes after intravitreal bevacizumab for macular edema in branch retinal vein occlusion," *Graefe's Archive for Clinical and Experimental Ophthalmology*, vol. 252, no. 9, pp. 1413–1421, 2014.

[3] A. E. Hoeh, T. Ach, K. B. Schaal, A. F. Scheuerle, and S. Dithmar, "Long-term follow-up of OCT-guided bevacizumab treatment of macular edema due to retinal vein occlusion," *Graefe's Archive for Clinical and Experimental Ophthalmology*, vol. 247, no. 12, pp. 1635–1641, 2009.

[4] A. M. Saeed, "Combined vitrectomy and intravitreal injection versus combined laser and injection for treatment of intractable diffuse diabetic macular edema," *Clinical Ophthalmology*, vol. 7, pp. 283–297, 2013.

[5] J. Ho, A. J. Witkin, J. Liu et al., "Documentation of intraretinal retinal pigment epithelium migration via high-speed ultrahigh-resolution optical coherence tomography," *Ophthalmology*, vol. 118, no. 4, pp. 687–693, 2011.

[6] M. Nassisi, W. Fan, Y. Shi et al., "Quantity of intraretinal hyperreflective foci in patients with intermediate age-related macular degeneration correlates with 1-year progression," *Investigative Ophthalmology & Visual Science*, vol. 59, no. 8, pp. 3431–3439, 2018.

[7] K. Ogino, T. Murakami, A. Tsujikawa et al., "Characteristics of optical coherence tomographic hyperreflective foci in retinal vein occlusion," *Retina*, vol. 32, no. 1, pp. 77–85, 2012.

[8] V. Schreur, L. Altay, F. van Asten et al., "Hyperreflective foci on optical coherence tomography associate with treatment outcome for anti-VEGF in patients with diabetic macular edema," *PLoS One*, vol. 13, no. 10, article e0206482, 2018.

[9] Y. Hsia, C. H. Yang, Y. T. Hsieh, C. M. Yang, T. C. Ho, and T. T. Lai, "Hyperreflective foci in predicting the treatment outcome of antivascular endothelial growth factor in neovascular age-related macular degeneration," *Graefe's Archive for Clinical and Experimental Ophthalmology*, vol. 258, no. 2, pp. 273–280, 2020.

[10] K. Abri Aghdam, A. Pielen, C. Framme, and B. Junker, "Correlation between hyperreflective foci and clinical outcomes in neovascular age-related macular degeneration after switching to aflibercept," *Investigative Ophthalmology & Visual Science*, vol. 56, no. 11, pp. 6448–6455, 2015.

[11] R. Ores, N. Puche, G. Querques et al., "Gray hyper-reflective subretinal exudative lesions in exudative age-related macular degeneration," *American Journal of Ophthalmology*, vol. 158, no. 2, pp. 354–361, 2014.

[12] C. Framme, P. Schweizer, M. Imesch, S. Wolf, and U. Wolf-Schnurrbusch, "Behavior of SD-OCT-detected hyperreflective foci in the retina of anti-VEGF-treated patients with diabetic macular edema," *Investigative Ophthalmology & Visual Science*, vol. 53, no. 9, pp. 5814–5818, 2012.

[13] K. Nishijima, T. Murakami, T. Hirashima et al., "Hyperreflective foci in outer retina predictive of photoreceptor damage and poor vision after vitrectomy for diabetic macular edema," *Retina*, vol. 34, no. 4, pp. 732–740, 2014.

[14] I. P. Chatziralli, T. N. Sergentanis, and S. Sivaprasad, "Hyperreflective foci as an independent visual outcome predictor in macular edema due to retinal vascular diseases treated with intravitreal dexamethasone or ranibizumab," *Retina*, vol. 36, no. 12, pp. 2319–2328, 2016.

[15] G. Soubrane, "Macular edema of choroidal origin," *Developments in Ophthalmology*, vol. 58, pp. 202–219, 2017.

[16] S. Liu, D. Wang, F. Chen, and X. Zhang, "Hyperreflective foci in OCT image as a biomarker of poor prognosis in diabetic macular edema patients treating with conbercept in China," *BMC Ophthalmology*, vol. 19, no. 1, p. 157, 2019.

[17] L. Altay, P. Scholz, T. Schick et al., "Association of hyperreflective foci present in early forms of age-related macular degeneration with known age-related macular degeneration risk polymorphisms," *Investigative Ophthalmology & Visual Science*, vol. 57, no. 10, pp. 4315–4320, 2016.

[18] G. Coscas, U. de Benedetto, F. Coscas et al., "Hyperreflective dots: a new spectral-domain optical coherence tomography entity for follow-up and prognosis in exudative age-related macular degeneration," *Ophthalmologica*, vol. 229, no. 1, pp. 32–37, 2013.

[19] T. Yoshitake, T. Murakami, K. Suzuma, Y. Dodo, M. Fujimoto, and A. Tsujikawa, "Hyperreflective foci in the outer retinal layers as a predictor of the functional efficacy of ranibizumab for diabetic macular edema," *Scientific Reports*, vol. 10, no. 1, p. 873, 2020.

[20] H. Lee, H. Jang, Y. A. Choi, H. C. Kim, and H. Chung, "Association between soluble CD14 in the aqueous humor and hyperreflective foci on optical coherence tomography in patients with diabetic macular edema," *Investigative Ophthalmology & Visual Science*, vol. 59, no. 2, pp. 715–721, 2018.

[21] J. W. Kwon and D. Jee, "Aqueous humor cytokine levels in patients with diabetic macular edema refractory to anti-VEGF treatment," *PLoS One*, vol. 13, no. 9, article e0203408, 2018.

[22] J. Wu, Y. Zhong, S. Yue et al., "Aqueous humor mediator and cytokine aberrations in diabetic retinopathy and diabetic macular edema: a systematic review and meta-analysis," *Disease Markers*, vol. 2019, Article ID 6928524, 12 pages, 2019.

[23] H. Yousef, C. J. Czupalla, D. Lee et al., "Aged blood impairs hippocampal neural precursor activity and activates microglia via brain endothelial cell VCAM1," *Nature Medicine*, vol. 25, no. 6, pp. 988–1000, 2019.

[24] S. Song, X. Yu, P. Zhang, and H. Dai, "Increased levels of cytokines in the aqueous humor correlate with the severity of diabetic retinopathy," *Journal of Diabetes and its Complications*, vol. 34, no. 9, article 107641, 2020.

[25] I. Valekova, K. Jarkovska, E. Kotrcova et al., "Revelation of the IFNα, IL-10, IL-8 and IL-1β as promising biomarkers reflecting immuno-pathological mechanisms in porcine Huntington's disease model," *Journal of Neuroimmunology*, vol. 293, pp. 71–81, 2016.

Research Article

Combination Model of Thyrotrophin Receptor Antibody and Volumetric Orbital Apex Crowding Index as an Indicator of Dysthyroid Optic Neuropathy

Zhihong Deng,[1] Lu Chen [iD],[2,3] Jia Tan [iD],[2,3] Sha Wang,[2,3] Dan Liu,[2,3] Jinwei Wang,[2,3] Chengzhi Jiang,[4] Jie Yang,[2,3] and Bei Xu[2,3]

[1]*Department of Ophthalmology, The Third Xiangya Hospital, Central South University, Changsha, Hunan, China*
[2]*Eye Center of Xiangya Hospital, Central South University, Changsha, Hunan, China*
[3]*Hunan Key Laboratory of Ophthalmology, Changsha, Hunan, China*
[4]*PET-CT Center, Hunan Cancer Hospital, Changsha, Hunan, China*

Correspondence should be addressed to Lu Chen; weather59@163.com and Jia Tan; jasmintj@126.com

Background. Dysthyroid optic neuropathy (DON) is one of the most serious vision-threatening complications of thyroid eye disease (TED); however, accurate and established diagnostic tools for DON are yet lacking. The present study was aimed at identifying new diagnostic factors for the accurate diagnosis of DON. *Methods.* This retrospective cross-sectional study included 25 TED patients (50 eyes) with enlarged extraocular muscles, no previous anti-inflammatory therapy, and the absence of other vision-affecting diseases between May 2017 and August 2019. Baseline data, such as gender, age, ophthalmological history, thyroid disease and management, TED history including clinical features, management, and long-term results, ophthalmological examinations, serology examinations, and single-photon emission computed tomography/computed tomography (SPECT/CT) results, were extracted. The diagnostic criteria were as follows: (1) best-corrected visual acuity (BCVA) loss coexisting with either of the following—increased latency or reduction of amplitude on visual evoked potential (VEP), impaired color vision, visual field defects, contrast sensitivity impairment, and optic disk swelling—and (2) Barrett's index ≥ 60% in CT. Univariate and multivariate logistic regression analyses assessed the differences in age, gender, eyes, medical history, clinical activity, thyroid hormone and antibodies, uptake ratio (UR) of extraocular muscles in SPECT/CT, and volumetric orbital apex crowding index (VACI) using the generalized estimation equation. Consequently, the receiver operating characteristic curve (ROC) of the significant factors was constructed. *Results.* Univariate analysis revealed significant differences in the clinical activity, free triiodothyronine (FT3), free thyroxine (FT4), thyrotrophin receptor antibody (TRAb) levels, the UR of superior and medial rectus, and VACI between DON and TED (without DON) groups. Multivariate regression analysis revealed that TRAb and VACI were significantly different. ROC analysis showed that the univariate models of TRAb or VACI and the multivariate model were effective indicators of DON, while the multivariate model had the highest area under the ROC curve. *Conclusion.* A combination of TRAb and VACI is an effective indicator for DON.

1. Introduction

Thyroid eye disease (TED), also known as Graves' ophthalmopathy (GO) or thyroid-associated ophthalmopathy (TAO), is one of the most common autoimmune inflammatory disorders of the orbit [1]. The age-adjusted annual incidence of clinically relevant TED is 16 per 100,000 population in women and 2.9 in men [2]. TED is commonly associated with Graves' hyperthyroidism (Graves' disease) [3]. The pathological changes of TED affect periorbital connective tissue, extraocular muscles, and orbital fat tissue, causing ocular irritation, pain, double vision, and in some rare cases reduced vision and blindness [1].

Dysthyroid optic neuropathy (DON) is one of the rarest but most severe complications of TED, which occurs in

approximately 3-8% of cases [4, 5]. The pathogenesis of the DON remains unclear. Previous studies have suggested that mechanical, vascular, and inflammatory components, secondary to an apex syndrome from hyaluronic acid production and adipogenesis enhanced by activated T cells and orbital fibroblasts, may lead to extraocular muscle enlargement and orbital fat expansion and overall increased vascular congestion [5, 6].

If not appropriately treated, DON may cause permanent vision loss; this has been observed in about 30% cases [7]. The current diagnosis of DON relies on the integrative analysis of multiple parameters by experienced clinicians as accurate and simple diagnostic tools are yet lacking. Previous studies have evaluated the clinical data and radiological findings associated with DON. Some of the risk factors associated with TED include age, gender, genetics, smoking, diabetes, thyroid dysfunction, and treatments for hyperthyroidism, which may exert a similar effect on DON [4, 5, 8–13]. However, the sensitivities and specificities of some visual function tests are not sufficient to predict DON. Barrett's index [14], the commonly used muscular index in the clinic to assess orbital apex crowding, cannot directly reflect the degree of muscle volume enlargement in the orbital apex. Therefore, the present study was aimed at identifying new sensitive indicators for detecting early optic nerve damage during the development of DON.

2. Materials and Methods

2.1. Patients. This was a single-center, retrospective study. All the TED patients at the Department of Ophthalmology, Xiangya Hospital, Central South University, Changsha, Hunan, China, between May 2017 and August 2019 were examined. This work has been carried out in accordance with the Declaration of Helsinki (2000) of the World Medical Association. This study was approved by the Ethic Committee of the Xiangya Hospital of Central South University, and all participants provided informed consent.

For each patient, we extracted the following data from the initial visit: gender and age, ophthalmological history, thyroid disease and managements, TED history, clinical features, management, and long-term results.

The ophthalmological examination included eye exophthalmos, best-corrected visual acuity (BCVA), slit-lamp examination, fundoscopy, visual evoked potential (VEP), color vision, visual field, and contrast sensitivity.

Inflammation was clinically evaluated using the clinical activity score (CAS) system by assessing two symptoms (ocular or retrobulbar pain and pain with eye movement) and five signs (conjunctival chemosis, conjunctival erythema, eyelid erythema, eyelid oedema, and swelling/erythema of the caruncle) for each eye. TED was confirmed "active" if CAS was ≥3 (0 to 7) [15].

Serology examination included free triiodothyronine (FT3), free thyroxine (FT4), thyroid-stimulating hormone (TSH), thyroglobulin antibody (TGA), thyroid peroxidase antibody (TPOA), and thyrotrophin receptor antibody (TRAb), which were detected using the electrochemilumi-

nescence immunoassay (Roche Diagnostic Product Co., Ltd., Shanghai, China).

All patients underwent orbital single-photon emission computed tomography (SPECT)/CT (Philips, USA). Briefly, 555 MBq (15 mCi) ^{99m}Tc- (Beijing Atomic High-Tech Co. Ltd., Beijing, China) DTPA (Jiangyuan Pharmaceutical Factory, Jiangsu Institute of Atomic Medicine, Jiangsu, China) was intravenously administered 20 min before imaging. A CT scan with 1 mm layer thickness was performed first, followed by SPECT imaging. Finally, the orbital CT image, SPECT image, and SPECT/CT fusion image were obtained using Philips image processing software.

2.2. Inclusion and Exclusion Criteria. The inclusion criteria were as follows: (1) patients who met the diagnostic criteria of TED [16] (eyelid retraction occurred in association with objective evidence of thyroid dysfunction or abnormal regulation, exophthalmos, optic nerve dysfunction, or extraocular muscle involvement. If eyelid retraction was absent, TED was diagnosed only if exophthalmos, optic nerve dysfunction, or extraocular muscle involvement was associated with thyroid dysfunction or abnormal regulation. The ophthalmic signs may be either unilateral or bilateral; confounding causes, including high myopia, congenital cranial-maxillofacial bone dysplasia, orbital tumor, and orbital nonspecific inflammation, were excluded) and (2) patients who reported to have enlarged extraocular muscles, as detected by SPECT/CT.

The exclusion criteria were as follows: (1) patients who received anti-inflammatory therapy before the first visit and (2) other causes that could explain the visual dysfunction, including cataracts, glaucoma, optic neuropathy, tear film abnormalities, and corneal changes.

Currently, there is no golden standard for the diagnosis of DON. In order to increase the reliability of the study, we referred to Saeed et al.'s clinical diagnostic flow [4] and set relatively stringent criteria. When DON was diagnosed simultaneously and independently by two senior ophthalmologists with at least 3-year experience in the treatment of the orbital disease, the eye was included in the DON group. The diagnostic criteria were as follows: (1) BCVA loss coexisting with either of the following—increased latency or reduction of amplitude on VEPs, impaired color vision, visual field defects, impaired contrast sensitivity, and optic disk swelling—and (2) Barrett's index ≥ 60% in CT [14]. Then, the TED eye with normal vision was included in the TED group (without DON).

2.3. SPECT/CT Imaging Analysis. The uptake ratio (UR) of extraocular muscles and volumetric orbital apex crowding index (VACI) of each eye enrolled were calculated by a senior radiologist blinded to the grouping.

The regions of interest (ROI) of each extraocular muscle were delineated on the coronal plane, respectively. The mean value of the maximum count of the radioactivity in each extraocular muscle on the three levels was taken as the target value; the ROI in the occipital lobe was delineated on the cross section, and the average radioactive count was taken as the nontarget value. The UR was the target/nontarget ratio (T/NT).

TABLE 1: Comparison of basic demographic data and clinical findings between TED patients with and without DON.

Parameter	DON group (16 eyes)	TED group (without DON) (34 eyes)	P
Demographic			
Male	8 (50.0%)	16 (47.1%)	0.870
Right eye	10 (62.5%)	15 (44.1%)	0.225
Age (years)	49.94 (11.48)	49.91 (9.29)	0.994
Clinical history			
Chief complaint			
Exophthalmos/vision loss/others	2/11/3	16/11/7	0.137
History of complaint (months)	7.3 (8.8)	9.4 (6.8)	0.480
Type of thyroid disease			
Hyperthyroidism/euthyroid	16/0	32/2	/
Antithyroid therapy			
ATD/I^{131}	11/5	25/9	0.772
Thyroid function at the first visit			
Hyperthyroidism/euthyroid/hypothyroidism	3/4/9	17/9/8	0.103
History of thyroid dysfunction (months)	29.2 (28.6)	31.19 (49.4)	0.920
BCVA (logMAR)*	0.584 (0.591)	-0.018 (0.055)	0.006
Degree of exophthalmos (mm)	21.6 (4.1)	19.6 (2.7)	0.213
Clinical activity			
CAS (0–7)*	4.17 (1.99)	2.42 (1.14)	0.026
Active (CAS ≥ 3)	12 (75%)	13 (38.2%)	0.106
Thyroid hormone and antibodies			
FT3 (pmol/L)*	4.25 (1.25)	6.25 (2.49)	0.033
FT4 (pmol/L)*	12.8 (4.4)	17.4 (4.9)	0.029
TSH (mIU/L)	20.97 (33.43)	4.13 (7.75)	0.134
TGA (IU/mL)	1144 (1452)	578 (1237)	0.365
TPOA (IU/mL)	176 (173)	176 (191)	0.998
TRAb (IU/L)*	27.0 (14.7)	14.1 (11.8)	0.009
Uptake ratio of extraocular muscles			
Medial rectus**	12.7 (4.2)	10.4 (1.7)	0.070
Superior rectus*	10.2 (3.6)	8.0 (2.3)	0.025
Inferior rectus	11.2 (4.0)	10.4 (2.2)	0.608
Lateral rectus	8.4 (3.6)	8.4 (2.0)	0.506
Mean of four recti	10.62 (3.64)	9.3 (1.3)	0.187
VACI*	6.05 (3.16)	2.42 (1.14)	0.001

*$P < 0.05$, **$P < 0.1$. DON: dysthyroid optic neuropathy; TED: thyroid eye disease; ATD: antithyroid drug; CAS: clinical activity score (of TED); FT3: free triiodothyronine (reference range, 3.1–6.8); FT4: free thyroxine (reference range, 12–22); TSH: thyroid-stimulating hormone (reference range, 0.27–4.20); TGA: thyroglobulin antibody (reference range, 0–115); TPOA: thyroid peroxidase antibody (reference range, 0–34); TRAb: thyrotrophin receptor antibody (reference range, 0–1.75); VACI: volumetric orbital apex crowding index.

The boundary of soft tissue in the orbital apex was recognized, automatically delineated, and manually modified using Philips image processing software according to a previously described approach [17]. The volume of the optic nerve was also manually removed to obtain the extraocular muscle volume. The ratio of the extraocular muscles' volume to the fat volume was calculated to determine the VACI.

2.4. Statistical Analysis. Statistical analysis was performed using IBM SPSS Statistics 24 (International Business Machines Corporation, USA). The normality of the distribution of continuous variables was tested by the Kolmogorov-Smirnov test. The continuous variables were described as mean values ± standard deviation (SD), while the categorical variables were described as numbers and percentages.

Both eyes of each patient were included in this study. The generalized estimation equation was used to increase the statistical power and account for the correlation between two eyes of an individual patient. All variables were assessed by univariate logistic regression analysis; those that were found to be associated ($P < 0.1$) were included in a multivariate model. Consequently, insignificant indicators were removed following a forward stepwise approach in the order of descending P values to reduce the collinearity issues.

The receiver operating characteristic curve (ROC) of the individual parameters within the final multivariate regression model and prognostic values of the multivariate model was developed. The areas under the ROC curves were calculated to descript the ability to indicate the presence of DON. The areas under the ROC curve from each model were then compared for statistical differences (Z test). The optimized Youden index determined the optimal cut points. The level of statistical significance was set at $P < 0.05$ for all the tests.

3. Results

A total of 50 eyes of 12 men (48%) and 13 women (52%) aged 31 to 69 years (mean 49.9 ± 9.9 y) with TED who met the inclusion criteria were included in the final analysis. Among those, 16 eyes of 11 patients were affected by DON, and 5 patients showed bilateral optic neuropathy. The contralateral eyes of 6 one-eye-affected patients were enrolled in the TED group (without DON), while 28 eyes of 14 TED patients without DON were enrolled in the TED group (without DON). The basic demographic data and clinical findings are summarized in Table 1.

The DON group consisted of more elders, males, and right eyes, compared with the TED group, but no statistical difference was observed with respect to age, sex, or lateral eyes.

The most common complaint of DON patients was vision loss and exophthalmos for TED (without DON) patients. The DON patients had a shorter history of thyroid dysfunction and eye complaints and a higher rate of I^{131} therapy than the TED group. On the other hand, most patients in both groups presented hyperthyroidism initially, but hypothyroidism was common in the DON group and hyperthyroidism in the TED group after an examination during the first visit at the eye clinic. However, the clinical history did not differ significantly between the two groups.

The BCVA of DON patients was logMAR (0.584 ± 0.591), which differed significantly from that of TED patients (-0.018 ± 0.055) ($P < 0.05$). The exophthalmos degree was 21.6 ± 4.1 mm for the DON group *vs.* 19.6 ± 2.7 mm for the TED group, with no statistical difference. The clinical activity score (CAS) was significantly different between the DON (4.17 ± 1.99) and TED groups (2.42 ± 1.14) ($P = 0.026$). Furthermore, 75% of DON patients and 38.2% without DON were in an active phase, but the difference was not significant.

Univariate regression analysis showed lower levels of free triiodothyronine (FT3), free thyroxine (FT4), and higher levels of TRAb in the DON group compared to the TED group (4.25 ± 1.25 pmol/L *vs.* 6.25 ± 2.49 pmol/L), 12.8 ± 4.4 pmol/L *vs.* 17.4 ± 4.9 pmol/L, and 27.0 ± 14.7 IU/L *vs.* 14.1 ± 11.8 IU/L, respectively; all $P < 0.05$). In addition, no significant difference was detected in TSH, TGA, or TPOA between the two groups ($P > 0.05$).

The UR of superior rectus was 10.2 ± 3.6 in the DON group *vs.* 8.0 ± 2.3 in the TED group, and the difference was significant ($P < 0.05$). However, no significant difference was detected in the UR of medial rectus, inferior rectus, lateral rectus, and mean ratio of the four recti between the two groups ($P > 0.05$).

TABLE 2: Multivariate factors indicate the presence of dysthyroid optic neuropathy (DON).

| Parameter | B | Std. error | 95% profile likelihood confidence interval | | Hypothesis test | | |
			Lower	Upper	Wald chi-square	df	Sig.
VACI	1.58	0.53	0.54	2.63	8.85	1	0.003
TRAb	0.11	0.05	0.02	0.20	5.87	1	0.015

TRAb: thyrotrophin receptor antibody; VACI: volumetric orbital apex crowding index.

FIGURE 1: Receiver operating characteristic (ROC) curves of the multivariate model, volumetric orbital apex crowding index (VACI), and thyrotrophin receptor antibody (TRAb).

Interestingly, VACI also showed a statistically significant difference between the groups in the univariate model (the means of DON and TED groups were 6.05 ± 3.16 and 2.42 ± 1.14, respectively; $P < 0.05$).

The significant factors of univariate analysis ($P < 0.1$), such as clinical activity, FT3, FT4, TRAb, UR of superior rectus and medial rectus, and VACI, were included in the multivariate model. Table 2 lists the significant variables identified using multivariate regression with the generalized estimation equation. The two variables, VACI and TRAb, were associated with DON. Higher VACI and TRAb values suggested that the patient possibly was more likely to be suffering from DON. The equation was $Y = -7.941.58 \times$ VACI $+ 0.11 \times$ TRAb. The area under the receiver operating characteristic (ROC) curve (AUC) for the predictive value ($Pre = e^Y/(1 + e^Y)$) of the multivariate model was 0.952, and that for the VACI and TRAb was 0.910 and 0.759,
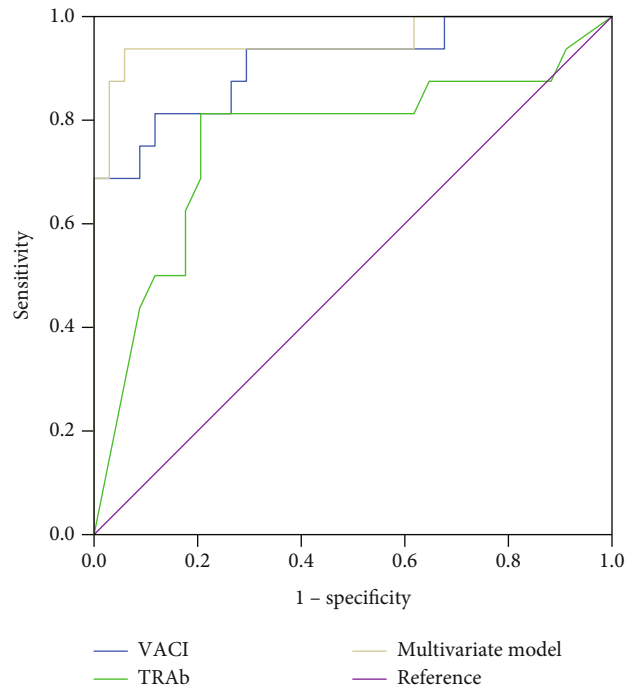
TABLE 3: Parameters of receiver operating characteristic (ROC) curves of the multivariate model, volumetric orbital apex crowding index (VACI), and thyrotrophin receptor antibody (TRAb).

| | The area under the ROC curve | | Cutoff | Youden index | Sensitivity | Specificity |
	Area	95% confidence interval				
VACI	0.910	0.815 1.000	3.11	0.695	81.3%	88.2%
TRAb	0.759	0.597 0.921	17.05	0.607	81.3%	79.4%
Multivariate model	0.952	0.876 1.000	0.31	0.879	93.8%	94.1%

TABLE 4: Diagnostic accuracies of the multivariate model, volumetric orbital apex crowding index (VACI), and thyrotrophin receptor antibody (TRAb).

		DON group	TED group (without DON)	Sum
TRAb	High	13 (true positive 81.3%)	7 (false positive 20.6%)	20
	Low	3 (false negative 18.8%)	27 (true negative 79.4%)	30
VACI	High	13 (true positive 81.3%)	4 (false positive 11.8%)	17
	Low	3 (false negative 18.8%)	30 (true negative 88.2%)	33
Multivariate model	(+)	15 (true positive 93.8%)	2 (false positive 5.9%)	17
	(-)	1 (false negative 6.3%)	31 (true negative 91.2%)	32
Sum		16	34	50

TABLE 5: Z test of receiver operating characteristic (ROC) curves of the multivariate model, volumetric orbital apex crowding index (VACI), and thyrotrophin receptor antibody (TRAb).

	Z value	P
VACI & multivariate model	2.44	0.007
TRAb & multivariate model	2.10	0.018
VACI & TRAb	1.57	0.058

respectively (Figure 1 and Table 3). For the multivariate model, a cutoff of 0.31 (chosen according to an optimal Youden index of 0.879) yielded the best results with a sensitivity of 93.8% and a specificity of 94.1%; 94% of patients were correctly classified using this approach. Moreover, a cutoff of 3.11 in VACI (Youden index 0.695) resulted in a sensitivity of 81.3%, a specificity of 88.2%, and an accurate classification of 86% patients, while for the TRAb, a cutoff of 17.05 IU/L (Youden index 0.607) corresponded to a sensitivity and specificity of 81.3% and 79.4%, respectively, and an accurate classification of 80% of patients. The diagnostic accuracies of the multivariate model, VACI, and TRAb are listed in Table 4.

The AUCs from each model were compared to evaluate the statistical differences using the Z test (Table 5). The AUC of the multivariate model was significantly larger than that of VACI or TRAb, while the AUCs of VACI and TRAb did not differ significantly.

4. Discussion

For patients suffering from DON, which is the most serious vision-threatening complication related to TED, recognition is paramount for timely management [18]. In the present study, we assessed the factors such as age, gender, eyes, clinical history of thyroid disease and TED, type of thyroid disease, antithyroid therapy, degree of exophthalmos, clinical activity, thyroid hormone, antibody levels, UR of extraocular muscles in SPECT/CT, VACI, and the combination of parameters to find an efficient and reliable diagnostic test for DON.

The correlation between age and the development of DON has been reported previously [4] and proven by a multivariable model [8]; however, this association was not detected in our study. This contradiction was observed because some TED patients without extraocular muscle enlargement were excluded in this study.

Male gender was previously associated with DON by one univariate analysis [4], yet the correlation was not present in other preceding multivariable analysis [8] or the current study.

The differences between the two eyes of a patient had not been reported before and were also not analyzed statistically in this study. All the contralateral eyes of the 6 one-eye-affected patients have slight visual impairments (increased latency or reduction of amplitude on VEPs, impaired color vision, visual field defects, or contrast sensitivity impairment), but without BCVA loss, they were enrolled in the TED group (without DON). Owing to the successive onset of the bilateral eyes, quite a few of the TED patients present the condition in both eyes in different degrees. Therefore, the slightly visually impaired eyes might be set towards DON or already had potential optic neuropathy but were excluded based on normal BCVA. However, the diagnosis of the DON eye led to emergency treatments, such as high-dose intravenous glucocorticoids, which might stop the progress of the suspicious eye; however, whether these would convert into DON eventually cannot be judged.

Accumulating evidence indicated that I^{131} therapy is associated with an increased risk of occurrence or

development of TED compared to antithyroid drugs (ATD) and thyroid surgery [19–21]. This phenomenon could result from the increased production of TRAb induced by radioactive iodine- (RAI-) associated leakage of thyroid antigens [19]. However, currently, there is no evidence, including our study, of its direct effect on DON.

Herein, we observed hyperthyroidism predominantly at the first visit in both groups, while the DON group had more hypothyroidism patients, without statistical difference. Both hyper- and hypothyroidism are associated with an elevated risk of progression or deterioration of TED, especially the hypothyroidism after I^{131} therapy for Graves' hyperthyroidism [21]. Nonetheless, the association between thyroid dysfunction and DON needs further investigation.

Thyroid antibodies are closely related to the development and severity of TED, especially the TSH receptor antibodies (TRAb). The expression of the TSH receptor is higher in TED orbital fat compared to that in normal orbital adipose tissues. TRA is a primary autoantigen involved in the pathophysiology of TED, increases the hyaluronic acid synthesis, and enhances adipogenesis in both orbital fibroblasts and preadipocytes [22]. Subsequently, the gradually increased orbital pressure leads to the compression and dysfunction of the optic nerve. Study results performed by several laboratories using different methodologies have identified the parallel between TRAb titers and the clinical features and the course of TED [23]. Ponto et al. [9] have identified TSI (thyroid-stimulating immunoglobulins, one of the four subtypes of TRAb) levels as a useful diagnostic tool for the identification of patients with early onset of DON. The current study confirmed this finding using total TRAbs with the Youden index of 0.607, suggesting that at the TRAb level > 17.05 IU/L, 81.3% TED patients might be at the risk of DON, while 21.6% TED patients without DON would be misdiagnosed.

The concentration influence of TSH, FT3, or FT4 on DON development has not yet been addressed by previous studies, nor have been the other thyroid antibodies, such as TPOA or TGA, which may also influence the extrathyroid manifestation. According to some studies, these disorders appear to predispose to worsening or development of TED; however, the contradictory results reported by other studies make this relationship difficult to interpret [21, 24]. In the present study, these factors did not result as indicators of DON in multivariable analysis.

The correlation of disease activity with the DON has been reported by Khong et al. [8]. Our univariate analysis also indicated that patients with a higher clinical activity score or uptake ratio of superior or medial Rectus were at higher risk of DON; however, when all explanatory variables including TRAb levels were considered, all of the activity indexes, including CAS, phases, or uptake ratios of extraocular muscles, were excluded as DON indicators. Several studies have shown a positive correlation between clinical activity and the levels of TRAb [25]; however, the TRAb levels were not included in Khong et al.'s study. In view of this, we assumed that TRAb levels dictated the incidence risk of DON, but not the clinical activities.

In TED patients, tissue expansion, especially the enlargement of extraocular muscles, occurs within the relatively fixed volume imposed by the bony orbit, resulting in orbital apex crowding, which has been demonstrated to be directly correlated with the development of DON. Nonetheless, to elucidate the degree of orbital apex crowding that leads to DON, accurate, quantizable, and repeatable tests are essential. Previous studies have explored several CT scan parameters for estimating the level of orbital apical crowding, such as linear or area measurements of extraocular muscles (on single coronal image), but volumetric estimates were proven to be a more useful indicator of DON [17]. In our study, 81.3% of TED patients with VACI > 3.11 were at the risk of DON, while 11.8% TED patients without DON were misdiagnosed as DON. Therefore, it could be speculated that other factors may be involved in the process (for example, optic nerve stretching). The cut point was lower than Goncalves' (4.14), which might be attributed to the exclusion of the optic nerve in the calculation of VACI.

The multivariate model of TRAb and VACI was a useful indicator of DON, with a larger AUC than the univariate models of TRAb or VACI. When the predictive value was >0.31, 93.8% of the patients were found to be suffering from DON, while only 5.9% without DON were misjudged.

5. Strengths and Limitations

Rather than age, gender, clinical history, thyroid disease, antithyroid therapy, clinical activity, exophthalmos, and other thyroid hormone and antibody levels, the high levels of VACI and TRAb should be the indicators of DON. These observations revealed that the combination of TRAb and VACI was a sensitive, objective, repeatable, and quantizable new indicator of DON, not contingent on expert experience. To the best of our knowledge, this is the first statistical confirmation of the association between this combined model and DON. Based on the predictive value calculated by TRAb and VACI, 94% of the patients could be correctly classified, and this accuracy was higher than that by TRAb or VACI alone.

The present study had several limitations. Firstly, the number of included patients was relatively small, especially in the DON group. Thus, a sufficient period is required to enlarge the sample size and increase the reliability of this study. Secondly, TSI, which is one of four subtypes of TRAb, showed a significant association with DON relative to other subtypes [25]. However, the detection of TSI has not yet been implemented in clinical practice in China and other countries, while TRAb is an accessible indicator.

In the future studies, we aim to assess a large sample size to increase the reliability, improve the automatic calculation program of the predictive value to report the risk of DON to doctors and patients directly, including the optic nerve stretching index to improve the model, and subsequently observe the dynamic changes in the treatment and improvement of DON.

Data Availability

The data used to support the findings of this study are available from the corresponding author upon request.

Conflicts of Interest

The authors declare that there are no conflicts of interest regarding the publication of this paper.

Authors' Contributions

ZH Deng, L Chen, J Tan, S Wang, and D Liu designed and conceptualized the study. L Chen, J Tan, S Wang, and D Liu provided patients. CZ Jiang, JW Wang, J Yang, and B Xu took charge of patient examinations and data collection and assembly. L Chen performed the statistical analysis. ZH Deng and L Chen prepared the manuscript. J Tan reviewed the manuscript critically. All authors read and approved the final manuscript.

References

[1] Z. Li, D. M. Cestari, and E. Fortin, "Thyroid eye disease: what is new to know?," *Current Opinion in Ophthalmology*, vol. 29, no. 6, pp. 528–534, 2018.

[2] Y. Hiromatsu, H. Eguchi, J. Tani, M. Kasaoka, and Y. Teshima, "Graves' ophthalmopathy: epidemiology and natural history," *Internal Medicine*, vol. 53, no. 5, pp. 353–360, 2014.

[3] D. L. Weiler, "Thyroid eye disease: a review," *Clinical & Experimental Optometry*, vol. 100, no. 1, pp. 20–25, 2017.

[4] P. Saeed, S. Tavakoli Rad, and P. H. L. T. Bisschop, "Dysthyroid optic neuropathy," *Ophthalmic Plast Reconstr Surg*, vol. 34, no. 4S, 4S Supplement 1, pp. S60–S67, 2018, 34.

[5] A. D. Blandford, D. Zhang, R. V. Chundury, and J. D. Perry, "Dysthyroid optic neuropathy: update on pathogenesis, diagnosis, and management," *Expert Rev Ophthalmol.*, vol. 12, no. 2, pp. 111–121, 2017.

[6] R. S. Bahn, "Current insights into the pathogenesis of Graves' ophthalmopathy," *Hormone and Metabolic Research*, vol. 47, no. 10, pp. 773–778, 2015.

[7] A. J. Victores and M. Takashima, "Thyroid eye disease: optic neuropathy and orbital decompression," *International Ophthalmology Clinics*, vol. 56, no. 1, pp. 69–79, 2016 Winter.

[8] J. J. Khong, S. Finch, C. De Silva et al., "Risk factors for Graves' orbitopathy; the Australian Thyroid-Associated Orbitopathy Research (ATOR) Study," *The Journal of Clinical Endocrinology and Metabolism*, vol. 101, no. 7, pp. 2711–2720, 2016.

[9] K. A. Ponto, T. Diana, H. Binder et al., "Thyroid-stimulating immunoglobulins indicate the onset of dysthyroid optic neuropathy," *Journal of Endocrinological Investigation*, vol. 38, no. 7, pp. 769–777, 2015.

[10] B. Rutkowska-Hinc, E. Maj, A. Jabłońska, J. Milczarek-Banach, T. Bednarczuk, and P. Miśkiewicz, "Prevalence of radiological signs of dysthyroid optic neuropathy in magnetic resonance imaging in patients with active, moderate-to-severe, and very severe graves orbitopathy," *Eur Thyroid J.*, vol. 7, no. 2, pp. 88–94, 2018.

[11] H. Lee, Y. H. Lee, S. I. Suh, E. K. Jeong, S. Baek, and H. S. Seo, "Characterizing intraorbital optic nerve changes on diffusion tensor imaging in thyroid eye disease before dysthyroid optic neuropathy," *Journal of Computer Assisted Tomography*, vol. 42, no. 2, pp. 293–298, 2018.

[12] W. M. Wiersinga, "Smoking and thyroid," *Clinical Endocrinology*, vol. 79, no. 2, pp. 145–151, 2013.

[13] S. H. Acharya, A. Avenell, S. Philip, J. Burr, J. S. Bevan, and P. Abraham, "Radioiodine therapy (RAI) for Graves' disease (GD) and the effect on ophthalmopathy: a systematic review," *Clinical Endocrinology*, vol. 69, no. 6, pp. 943–950, 2008.

[14] M. L. R. Monteiro, A. C. P. Gonçalves, C. T. M. Silva, J. P. Moura, C. S. Ribeiro, and E. M. M. S. Gebrim, "Diagnostic ability of Barrett's index to detect dysthyroid optic neuropathy using multidetector computed tomography," *Clinics*, vol. 63, no. 3, pp. 301–306, 2008.

[15] J. Barrio-Barrio, A. L. Sabater, E. Bonet-Farriol, Á. Velázquez-Villoria, and J. C. Galofré, "Graves' Ophthalmopathy: VISA versus EUGOGO Classification, Assessment, and Management," *Journal of Ophthalmology*, vol. 2015, Article ID 249125, 16 pages, 2015.

[16] G. B. Bartley and C. A. Gorman, "Diagnostic criteria for Graves' ophthalmopathy," *American Journal of Ophthalmology*, vol. 119, no. 6, pp. 792–795, 1995.

[17] A. C. Gonçalves, L. N. Silva, E. M. Gebrim, S. Matayoshi, and M. L. Monteiro, "Predicting dysthyroid optic neuropathy using computed tomography volumetric analyses of orbital structures," *Clinics (São Paulo, Brazil)*, vol. 67, no. 8, pp. 891–896, 2012.

[18] L. Bartalena, L. Baldeschi, K. Boboridis et al., "The 2016 European Thyroid Association/European Group on Graves' orbitopathy guidelines for the management of Graves' orbitopathy," *European Thyroid Journal*, vol. 5, no. 1, pp. 9–26, 2016.

[19] K. A. Ponto, S. Zang, and G. J. Kahaly, "The tale of radioiodine and Graves' orbitopathy," *Thyroid*, vol. 20, no. 7, pp. 785–793, 2010.

[20] M. Lantz, T. Planck, P. Asman, and B. Hallengren, "Increased TRAb and/or low anti-TPO titers at diagnosis of Graves' disease are associated with an increased risk of developing ophthalmopathy after onset," *Experimental and Clinical Endocrinology & Diabetes*, vol. 122, no. 2, pp. 113–117, 2014.

[21] M. N. Stan and R. S. Bahn, "Risk factors for development or deterioration of Graves' ophthalmopathy," *Thyroid*, vol. 20, no. 7, pp. 777–783, 2010.

[22] A. Hesarghatta Shyamasunder and P. Abraham, "Measuring TSH receptor antibody to influence treatment choices in Graves' disease," *Clinical Endocrinology*, vol. 86, no. 5, pp. 652–657, 2017.

[23] Y. J. Woo, S. Y. Jang, T. H. T. Lim, and J. S. Yoon, "Clinical association of thyroid stimulating hormone receptor antibody levels with disease severity in the chronic inactive stage of Graves' orbitopathy," *Korean Journal of Ophthalmology*, vol. 29, no. 4, pp. 213–219, 2015.

[24] D. Jarusaitiene, R. Verkauskiene, V. Jasinskas, and J. Jankauskiene, "Predictive Factors of Development of Graves' Ophthalmopathy for Patients with Juvenile Graves' Disease," *International Journal of Endocrinology*, vol. 2016, Article ID 8129497, 9 pages, 2016.

[25] S. Y. Jang, D. Y. Shin, E. J. Lee, and J. S. Yoon, "Clinical characteristics of Graves' orbitopathy in patients showing discrepancy between levels from TBII assays and TSI bioassay," *Clinical Endocrinology*, vol. 80, no. 4, pp. 591–597, 2014.

Hindawi

Retraction

Retracted: Probiotic Supplement Preparation Relieves Test Anxiety by Regulating Intestinal Microbiota in College Students

Disease Markers

This article has been retracted by Hindawi following an investigation undertaken by the publisher [1]. This investigation has uncovered evidence of one or more of the following indicators of systematic manipulation of the publication process:

(1) Discrepancies in scope

(2) Discrepancies in the description of the research reported

(3) Discrepancies between the availability of data and the research described

(4) Inappropriate citations

(5) Incoherent, meaningless and/or irrelevant content included in the article

(6) Peer-review manipulation

The presence of these indicators undermines our confidence in the integrity of the article's content and we cannot, therefore, vouch for its reliability. Please note that this notice is intended solely to alert readers that the content of this article is unreliable. We have not investigated whether authors were aware of or involved in the systematic manipulation of the publication process.

Wiley and Hindawi regrets that the usual quality checks did not identify these issues before publication and have since put additional measures in place to safeguard research integrity.

We wish to credit our own Research Integrity and Research Publishing teams and anonymous and named external researchers and research integrity experts for contributing to this investigation.

The corresponding author, as the representative of all authors, has been given the opportunity to register their agreement or disagreement to this retraction. We have kept a record of any response received.

References

[1] Q. Qin, H. Liu, Y. Yang et al., "Probiotic Supplement Preparation Relieves Test Anxiety by Regulating Intestinal Microbiota in College Students," *Disease Markers*, vol. 2021, Article ID 5597401, 8 pages, 2021.

Research Article

Probiotic Supplement Preparation Relieves Test Anxiety by Regulating Intestinal Microbiota in College Students

Qi Qin, Hui Liu, Yulu Yang, Yifei Wang, Chaofei Xia, Puyuan Tian, Jing Wei, Shengjie Li🆔**, and Tingtao Chen**🆔

National Engineering Research Center for Bioengineering Drugs and the Technologies, Institute of Translational Medicine, Nanchang University, Nanchang, Jiangxi Province 330031, China

Correspondence should be addressed to Shengjie Li; lishengjie1104@126.com and Tingtao Chen; chentingtao1984@163.com

Test anxiety creates barriers to learning and performance, which further affects students' social, behavioural, and emotional development. Currently, the medication to treat test anxiety has not been reported yet. Here, we enrolled 120 students to evaluate the effect of probiotic supplement preparation (PSP) on test anxiety from the aspect of the intestinal microbiota. We found that the intake of PSP alleviated the symptoms of depression and anxiety in students with test anxiety by evaluating their mental state using the Hamilton Depression Rating Scale and Hamilton Anxiety Scale. High-throughput sequencing results indicated that the consumption of PSP increased the abundance of *Streptococcus* and *Akkermansia* that was lowered by the anxiety state in the intestinal microbiota of students. Meanwhile, taking PSP reduced the level of intestinal pathogens of *Fusobacterium* and *Clostridium* as well. In conclusion, our work shows that PSP can reduce test anxiety and restore the disturbed microbiota to the standard level in Chinese college students, rendering the use of PSP a promising strategy for test anxiety.

1. Introduction

Test anxiety is a physiological symptom that is combined with the fear of failure, dread, catastrophizing, and worrying before and during a test, which negatively affects the social, behavioural, and emotional development of students and their feelings about school and themselves [1]. It is a common and potentially serious problem among college students and affects about 20-40% of all students, with a higher prevalence in the students with learning disabilities [1, 2]. A variety of interventions and strategies have been proven beneficial to relieve test anxiety, e.g., using student-friendly tests, enhancing accessibility, fostering motivation, and collaborating with family members and other professionals [1]. Enacting habits to reduce stress, such as exercise, proper nutrition, improving sleep, studying without fear, and meditation, are recommended for treating test anxiety as well [2]. However, the medication to treat test anxiety has not been reported yet.

Growing evidence has explored the potential influence of microbiota on the brain-gut axis in health and disease, including nutrition, immunity, host physiology, and brain development [3, 4]. It has also been suggested that the intestinal microbiota is involved in the modulation of behaviour in stress-related disorders [3, 5, 6]. Studies have indicated that some probiotics can produce neurotransmitters and neuromodulators (e.g., γ-aminobutyric acid, norepinephrine, and dopamine) to modulate opioid and cannabinoid receptors in the gut epithelium and relieve depression and anxiety [7–10].

Although many researchers have indicated the link between intestinal microbiota and mental disorders, little work has been done to evaluate the effect of probiotics on test anxiety in students and their influence on the intestinal microbiota of students. In the present study, the probiotic supplement preparation (PSP) of Hengxin probiotics was used to test the effect of probiotics on test anxiety in Chinese college students.

2. Materials and Methods

2.1. Ethics Statement. All subjects gave their informed consent for inclusion before they participated in the study. The study was conducted in accordance with the Declaration of Helsinki, and the protocol was approved by the Ethics Committee of the Second Affiliated Hospital of Nanchang University (Examination and approval no. is Review [2019] No. (039)).

2.2. Study Groups and Sampling. PSP of Hengxin probiotics was a gift from Harbin Meihua Biotechnology Co., Ltd. (Harbin, Heilongjiang, P.R. China), containing 1.2×10^{10} CFU of *Bifidobacterium longum* subsp. *Longum* BAMA-B05/Bau-B1024, 1.9×10^{10} CFU of *B. lactis* BAMA-B06/Bau-B0111, 1.5×10^{10} CFU of *B. adolescentis*, 3.2×10^9 CFU of *Streptococcus thermophiles*, 4.6×10^9 CFU of *Lactobacillus acidophilus*, and 3.0×10^9 CFU of *L. delbrueckii* subsp. *bulgaricus* per 100 grams of the granule's product, respectively, with a total number of over 10^9 CFU of viable bacterial count per package. The product qualities were also evaluated by the total viable count method and 16S rDNA sequencing before using it.

A total of 300 college students (aged between 18 and 24 years) were enrolled randomly in this study, and 43 of them dropped out due to personal reasons. And then, the eligibility of the rest of the students was assessed by interviewing them about their daily behaviours and health conditions. As a result, 137 students were excluded due to the following reasons, e.g., smoking, drinking, taking antibiotics regularly, and obese and flu sufferers were ruled out as well. Finally, 120 members were selected to respond to questionnaires assessing the depressive and anxiety symptoms at Nanchang University (Table S1). Sixty students without test anxiety were allocated to the healthy group and used as the control one (H group, taking the same package with no probiotics as placebo). The other sixty students with test anxiety were assigned as the treatment group and divided into two subgroups, named BP group meaning before taking the PSP and AP group which took PSP for 15 consecutive days (twice per day, and approximately 12-hour set time between two intakes) (Figure 1). The random fecal samples from the H group ($n = 30$), BP ($n = 30$), and AP ($n = 30$) groups were collected by a stool sampling tube according to the manufacturer's introduction. All the fecal samples were stored at -80°C immediately for DNA extraction [11].

2.3. Depressive and Anxiety Symptoms Analysis. The depressive symptoms of students were evaluated by trained psychiatrists using the Chinese version of the 17-item Hamilton Depression Rating Scale (HAMD-17). The severity of the depressive symptoms was classified using the following severity range for the HAMD score: normal (0–7), mild depression (8–16), moderate depression (17–23), and severe depression (>23). The anxiety symptoms were evaluated using the Chinese version of the 14-item Hamilton Anxiety Scale (HAMA-14), and anxiety symptom severity was classified by the following severity range for the HAMA score: nor-
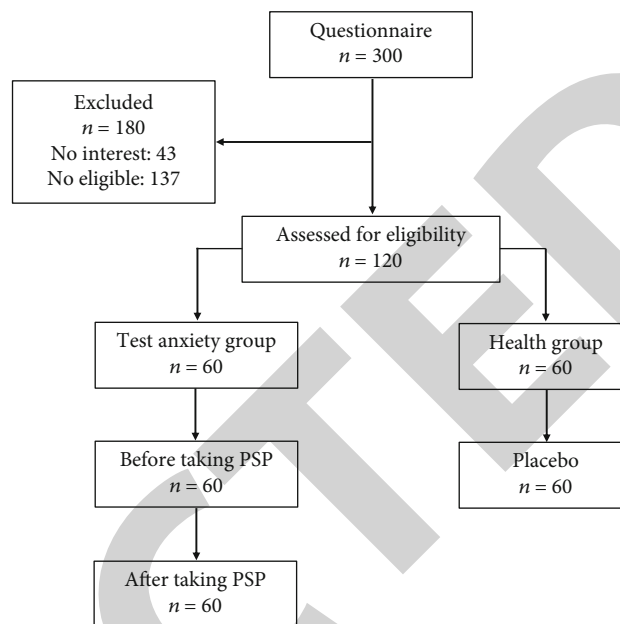

FIGURE 1: Students included in this study. The trial enrolled 300 students, and 120 students (aged between 18 and 24 years) were finally recruited based on the evaluation of depressive and anxiety symptoms at Nanchang University.

mal (0–7), mild or probable anxiety (8–14), moderate or definite anxiety (15–21), and severe anxiety (≥22) [12].

2.4. Genomic DNA Extraction and High-Throughput Sequencing. For the DNA extraction of faeces, a combination of the bead-beating method and Genomic DNA kits (Tiangen Biotech Co., Ltd., Beijing, China) were applied [13]. The concentration and quality of the purified DNA were determined at spectrophotometer (NanoDrop, Thermo Fisher Scientific, Inc., USA). Then, primers 515F/806R (5′-GTGCCAGCMGCCGCGGTAA-3′ and 5′-GGAC TACVSGGGTATCTAAT-3′, respectively) were used to amplify the V4 region of the 16S rDNA genes in each sample, and these PCR products were sequenced with an Illumina HiSeq 2000 platform [14]. The raw reads were deposited in the Sequence Read Archive (SRA) database of NCBI (PRJNA530283).

2.5. Bioinformatics and Multivariate Statistics. FLASH software was used to map overlapped reads (http://ccb.jhu.edu/software/FALSJ/), and low-quality sequences were eliminated by QIIME (v1.8.0, http://qiime.org/) according to the following criteria: (a) raw reads shorter than 160 bp and contained N base; (b) >1 mismatches in the 5′-primer; (c) sequences with more than eight continuous same bases. The obtained sequences were checked by UPARSE package (v 5.2.236) and removed the chimeric ones. Sequences with ≥97% similarity were performed as the same operational taxonomic units (OTUs) using an open-reference OTU picking protocol. The relative abundance of each OTU was assigned as a proportion of the sum of sequences of each sample. The α-diversity (within samples, indexes of observed OTUs,
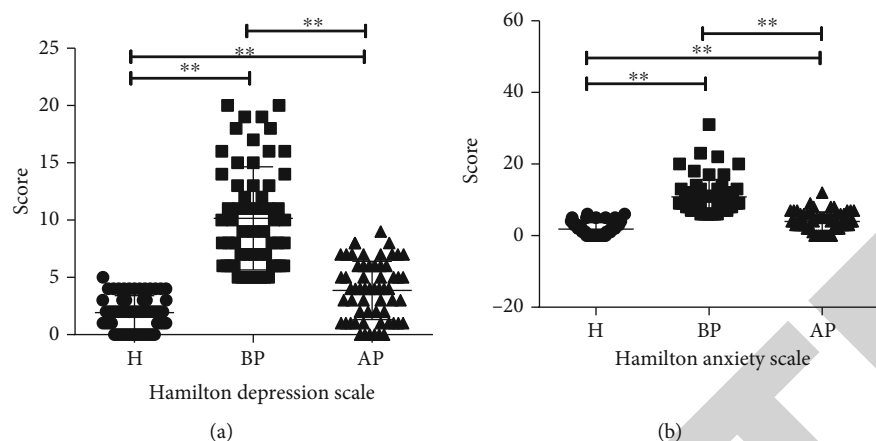
(a)

(b)

Figure 2: PSP improves the mental state of students suffering test anxiety. (a) PSP alleviated students' depression by reducing Hamilton Depression Scale. (b) PSP relaxed the anxiety scale by reducing Hamilton Anxiety Scale. H: students without test anxiety ($n = 60$); BP: students before taking PSP ($n = 60$); AP: students after taking the PSP ($n = 60$). $**p < 0.01$.
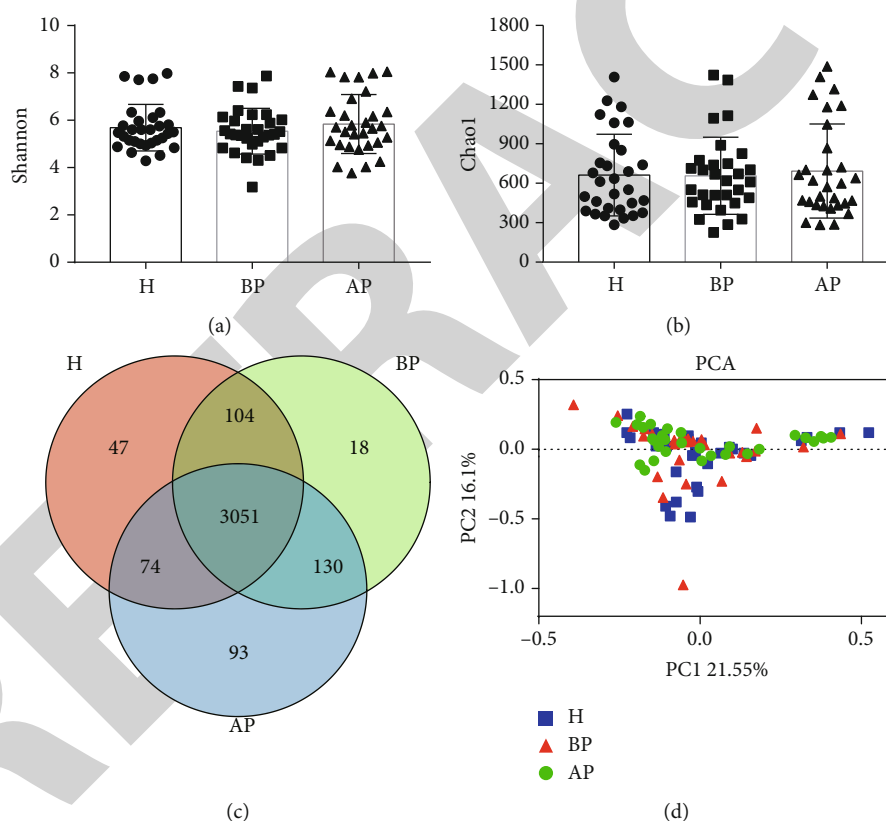

(a)

(b)

(c)

(d)

Figure 3: Effects of PSP on the intestinal microbial diversity in students. (a) Shannon index of fecal microbiota. (b) Chao1 index of fecal microbiota. (c) Venn diagram of fecal bacteria species. (d) PCA analysis of shared genera among microbiomes in the H, BP, and AP groups. H: students without test anxiety ($n = 30$); BP: students before taking PSP ($n = 30$); AP: students after taking PSP ($n = 30$).

Chao1, Shannon) and β-diversity (among samples, PCA, NMDS) were calculated by QIIME software as well.

2.6. Statistical Analysis. Statistical analysis was performed using Prism software version 7.0 (GraphPad Software, San Diego, CA, USA). Data was shown as the mean ± SD. Statistical significance was analysed using a one-way analysis of variance (ANOVA) followed by Tukey's multiple compari-

son test. Error probabilities of $p < 0.05$ were considered statistically significant.

3. Results

3.1. PSP Alleviated Test Anxiety. First, we evaluated the ability of the PSP to improve the mental state of students. As shown in Figure 2, our results indicated that exam pressure
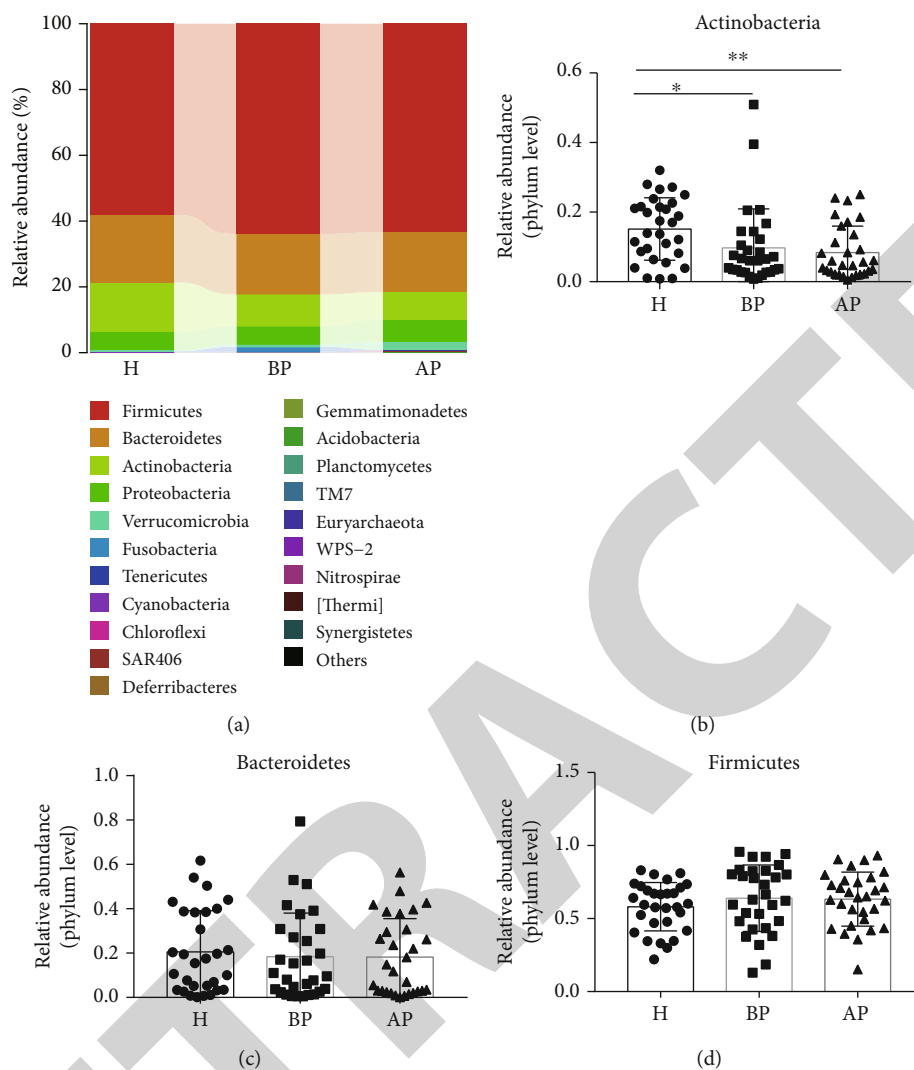
FIGURE 4: PSP has little effect on fecal microbiota composition at the phylum level. (a) The relative abundance of the top 20 bacteriophyta. (b) The relative abundance of *Actinobacteria*, (c) *Bacteroidetes*, and (d) *Firmicutes*. H: students without test anxiety; BP: students before taking PSP; AP: students after taking PSP. $^*p < 0.05$, $^{**}p < 0.01$.

significantly increased students' depression (BP) compared with the students without test anxiety (H) (10.15 vs. 1.92, $p < 0.01$), while the administration of the PSP markedly alleviated students' depression from 10.15 (BP) to 3.87 (AP) ($p < 0.01$) (Figure 2(a)). Similarly, the anxiety scale in the BP group was as high as 10.85, while probiotics significantly reduced the anxiety in the AP group to 3.93 ($p < 0.01$) (Figure 2(b)).

3.2. PSP Had Little Effects on the Microbial Diversity. To evaluate the effect of PSP on microbial diversity, we collected and assessed every 30 fecal samples from the H, BP, and AP groups. It seemed that the PSP had little impact on the Shannon index (5.69, 5.54, and 5.84) and Chao1 index (662, 657, and 692.6) among the H, BP, and AP groups, respectively (Figures 3(a) and 3(b)). The Venn diagram results indicated that 86.76% (3051/3517) of the bacteria were common among the H, BP, and AP groups, yet 18 unique bacteria were found existing in the BP samples (Figure 3(c) and Table S2).

Moreover, the PCA and NMDS results indicated that the samples in the H group, BP, and AP groups clustered together (Figure 3(d) and Figure S1).

3.3. Effects of PSP on the Microbial Community at the Phylum Level. As shown in Figure 4, data for the top 20 microorganism populations at the phylum level were analysed. *Firmicutes*, *Bacteroidetes*, *Actinobacteria*, and *Proteobacteria* constituted the four most common dominant phyla in the H group (0.58, 0.21, 0.15, and 0.05, respectively), BP (0.64, 0.18, 0.10, and 0.05, respectively) group, and AP (0.63, 0.18, 0.08, and 0.07, respectively) group, which accounted for 0.99, 0.97, and 0.97 of the total sequencing number in these three groups, respectively (Figure 4(a)). Then, we further evaluated the relative abundance of *Firmicutes*, *Bacteroidetes*, and *Actinobacteria* in groups H, BP, and AP. Results suggested that the administration of PSP had little effect on the composition of *Firmicutes* and *Bacteroidetes*, while it seemed that the test anxiety could significantly reduce the abundance of
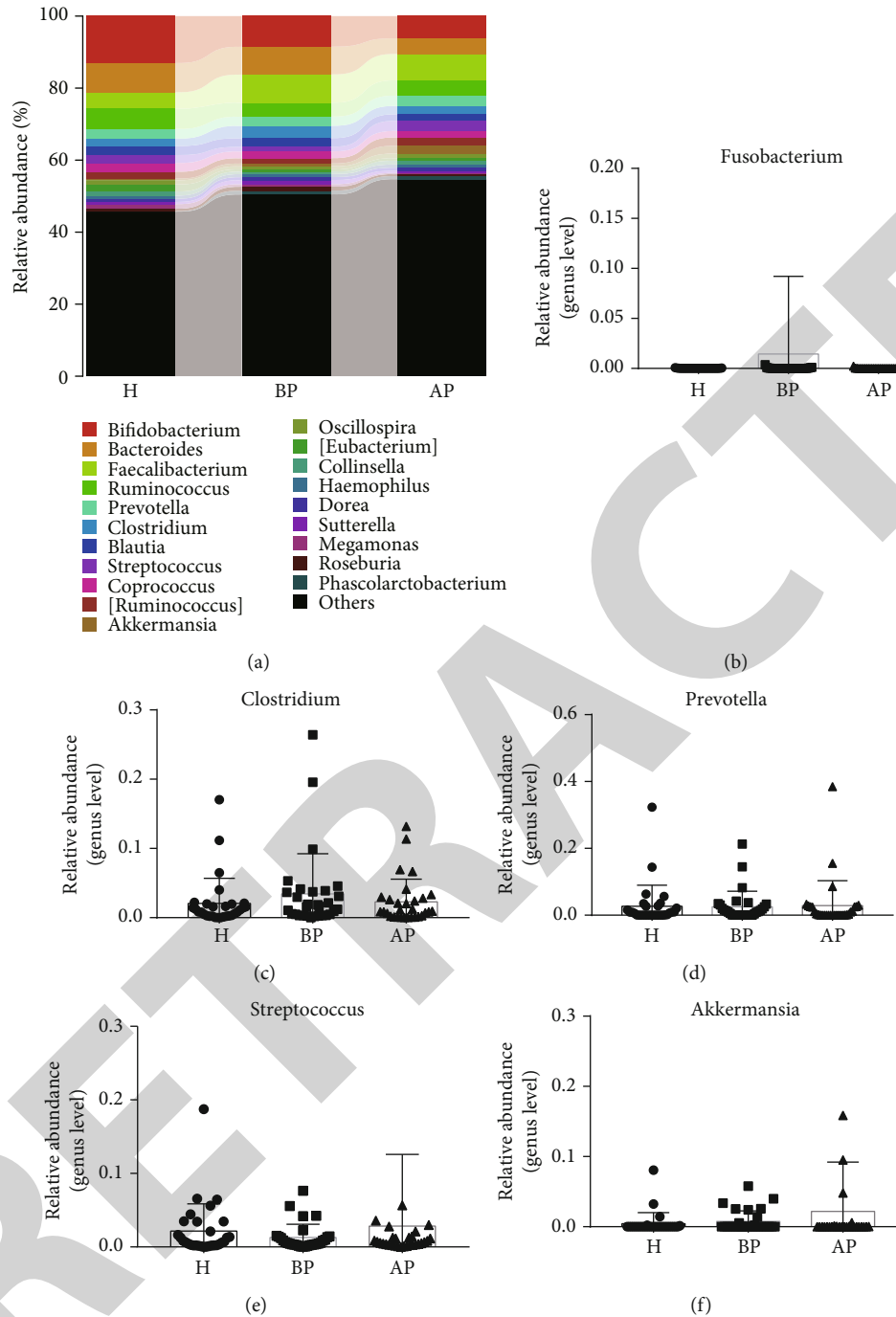
FIGURE 5: PSP enhances the relative abundance probiotics in anxious students. (a) The relative abundance of the top 20 microbes. (b) The relative abundance of *Fusobacterium*, (c) *Clostridium*, (d) *Prevotella*, (e) *Streptococcus*, and (f) *Akkermansia*. H: students without test anxiety; BP: students before taking PSP; AP: students after taking PSP.

Actinobacteria (Figures 4(b)–4(d)). Therefore, it seems that the administration of probiotics has little effect on the microbiota at the phylum level.

3.4. Effects of PSP on the Microbial Community at the Genus Level. Then, the top 20 genera were analysed. *Bifidobacterium*, *Bacteroides*, *Faecalibacterium*, *Ruminococcus*, *Prevotella*, and *Clostridium* accounted for the dominant bacteria in most samples in the H, BP, and AP groups (Figure 5(a)).

To better evaluate the effect of PSP on specific genera, *Fusobacterium*, *Clostridium*, *Prevotella*, *Streptococcus*, and *Akkermansia* were further studied. Our results indicated that students with test anxiety had an increased abundance of the pathogens of *Fusobacterium* (0.00008 vs. 0.01443) and *Clostridium* (0.021 vs. 0.034) and a reduced abundance of *Prevotella* and *Streptococcus* (0.0217 vs. 0.0129), while taking PSP obviously reduced the abundance of *Fusobacterium* (0.01443 vs. 0.0001) and *Clostridium* (0.034 vs. 0.023) and

enhanced that of *Streptococcus* (0.0129 vs. 0.0283) and *Akkermansia* (0.0076 vs. 0.0219) (Figures 5(b)–5(f)).

4. Discussion

Test anxiety is a type of performance anxiety in which people experience extreme distress and anxiety when tested, resulting in impaired learning and reduced performance on tests. Test anxiety has dramatically influenced studies and lives among students in elementary school, middle school, and high school. Here, we evaluated the effectiveness of a multiple probiotics granules product that has been approved by the State Food and Drug Administration of China as a kind of health-care food with the function of enhancing immunity and defecating, on the alleviation of the test pressure. As we know, when students suffer from test anxiety, they feel helpless and anxious, which significantly affects their study, sleep, and diet, and the unhealthy diet and lifestyle, in turn, increases the test anxiety in students.

Research studies have indicated that probiotics have benefits in reducing gastrointestinal discomfort, improving immune health, and relieving constipation [15]. Some work has suggested that people who consume probiotics maintain a healthy balance between anti- and proinflammatory responses, which exerts the potential benefits of gut bacteria on brain health [16]. Kim and Shin indicated that probiotic food consumption has beneficial sound effects on depression [15], and the work performed by Pinto-Sanchez et al. also reported that probiotics successfully reduced depression and increased the quality of life in patients with irritable bowel syndrome (IBS) [6]. As test anxiety is a mild psychological condition, we hypothesized that a probiotic supplement is sufficient to enhance the mental state of students with test anxiety.

In support of our hypothesis, the consumption of PSP alleviated the depression scale and anxiety scale of students. Many reports have indicated that probiotics could reduce various neurological diseases (e.g., Parkinson's disease and Alzheimer's disease) and anxiety caused by illness or depression [6, 16–19]. Thus, it is easy to understand that probiotics will exert a much better effect on the mild psychological condition of test anxiety. In the next step, we further evaluated the impact of probiotics on intestinal microbial diversity, and it seemed that the short period of probiotic consumption reduced the individual differences among students in the AP group compared with students in the H and BP groups, and slightly increased the Shannon index and Chao1 index.

Then, we compared the microbial composition among the H, BP, and AP groups. At the phylum level, test anxiety and probiotics hardly influenced the abundance of *Firmicutes* and *Bacteroidetes*, while could reduce plenty of *Actinobacteria*, and probiotic consumption failed to bring it back to normal levels. *Actinobacteria* is a phylum of gram-positive bacteria with great economic importance, which can produce bioactive metabolites that are useful in human medicine, such as antibacterials, antifungals, antivirals, antithrombotics, immune modifiers, antitumor drugs, and enzyme inhibitors [20]. At the genus level, test anxiety enhanced the abundance of the pathogens *Fusobacterium* and *Clostridium*

and reduced the abundance of *Streptococcus*. However, probiotic administration for 15 days could increase the levels of *Streptococcus* and *Akkermansia*, while reducing the levels of the pathogens *Fusobacterium* and *Clostridium* (Figure 4). As pathogens, *Fusobacterium* and *Clostridium* have been reported to have strong connections with various diseases (e.g., cancers, Alzheimer's disease, and Parkinson's disease), and their overgrowth significantly enhances the deterioration of conditions [21–24]. As probiotics, *Akkermansia*, and *Streptococcus* have been reported to possess benefits in cases of IBS, cancers, infection, obesity, diabetes, and inflammation [25–28]. Although the intestinal microbiota is associated with stress-related disorders, we should not just diagnose the status of anxiety from the aspect of gut microbiota since it would be affected frequently by some other factors, e.g., food habit, drug abuse, and individual differences. But probiotics consumption could be regarded as a kind of treatment and intervention method for relieving human anxiety via modulating the balance of gut micriobiota in the future [29].

5. Conclusion

In the present study, we evaluated the anti-test anxiety effects of Hengxin probiotics. We found that this PSP could significantly reduce test anxiety by reducing the number of pathogens and increasing of probiotics. However, this study has some limitations, e.g., the lack of a group with test anxiety but taking no probiotics (due to the unwillingness of students to take excipients). Additionally, it would have been more informative if some neurotransmitters and metabolites in the faeces were monitored. This is the first study that probiotics are suggested to associate with lower test anxiety in Chinese college student significantly. Our findings provide meaningful information that PSP might play a role in lowering the risk of depression and anxiety in Chinese students.

Data Availability

The datasets used and/or analysed during the present study are available from the corresponding author on reasonable request.

Conflicts of Interest

The authors declare that there is no conflict of interest regarding the publication of this article.

Acknowledgments

Supplementary Materials

Supplementary 1. Figure S1: Nonmetric Multidimensional Scaling (NMDS) analysis of shared genera among microbiomes in the H, BP, and AP groups.

Supplementary 2. Table S1: baseline patient demographics and characteristics. Table S2: the unique bacteria existed in the test anxious students before taking PSP.

References

[1] S. J. Salend, "Teaching students not to sweat the test," *Phi Delta Kappan*, vol. 93, no. 6, pp. 20–25, 2012.

[2] D. Wachelka and R. C. Katz, "Reducing test anxiety and improving academic self-esteem in high school and college students with learning disabilities," *Journal of Behavior Therapy and Experimental Psychiatry*, vol. 30, no. 3, pp. 191–198, 1999.

[3] S. Soldi, S. C. Tagliacarne, C. Valsecchi et al., "Effect of a multi-strain probiotic (Lactoflorene® Plus) on inflammatory parameters and microbiota composition in subjects with stress-related symptoms," *Neurobiology of Stress*, vol. 10, p. 100138, 2019.

[4] C. J. K. Wallace, J. A. Foster, C. N. Soares, and R. V. Milev, "The effects of probiotics on symptoms of depression: protocol for a double-blind randomized placebo-controlled trial," *Neuropsychobiology*, vol. 79, no. 1, pp. 108–116, 2020.

[5] X. F. Liu, S. Q. Cao, and X. W. Zhang, "Modulation of gut microbiota–brain axis by probiotics, prebiotics, and diet," *Journal of Agricultural and Food Chemistry*, vol. 63, no. 36, pp. 7885–7895, 2015.

[6] M. I. Pinto-Sanchez, G. B. Hall, K. Ghajar et al., "Probiotic *Bifidobacterium longum* NCC3001 reduces depression scores and alters brain activity: a pilot study in patients with irritable bowel syndrome," *Gastroenterology*, vol. 153, no. 2, pp. 448–459.e8, 2017.

[7] T. G. Dinan, R. M. Stilling, C. Stanton, and J. F. Cryan, "Collective unconscious: how gut microbes shape human behavior," *Journal of Psychiatric Research*, vol. 63, pp. 1–9, 2015.

[8] W. R. Russell, L. Hoyles, H. J. Flint, and M. E. Dumas, "Colonic bacterial metabolites and human health," *Current Opinion in Microbiology*, vol. 16, no. 3, pp. 246–254, 2013.

[9] C. Rousseaux, X. Thuru, A. Gelot et al., "_Lactobacillus acidophilus_ modulates intestinal pain and induces opioid and cannabinoid receptors," *Nature Medicine*, vol. 13, no. 1, pp. 35–37, 2007.

[10] X. Fang, X. Wang, S. G. Yang et al., "Evaluation of the microbial diversity in amyotrophic lateral sclerosis using high-throughput sequencing," *Frontiers in Microbiology*, vol. 7, p. 1479, 2016.

[11] T. T. Chen, S. Y. Jiang, S. Q. Xiong, M. Wang, D. Zhu, and H. Wei, "Application of denaturing gradient gel electrophoresis to microbial diversity analysis in Chinese Douchi," *Journal of the Science of Food and Agriculture*, vol. 92, no. 10, pp. 2171–2176, 2012.

[12] W. W. Ren, H. H. Qiu, Y. J. Yang et al., "Randomized controlled trial of cognitive behavioural therapy for depressive and anxiety symptoms in Chinese women with breast cancer," *Psychiatry Research*, vol. 271, pp. 52–59, 2019.

[13] X. M. Yu, X. L. Wu, L. Qiu et al., "Analysis of the intestinal microbial community structure of healthy and long-living elderly residents in Gaotian Village of Liuyang City," *Applied Microbiology and Biotechnology*, vol. 99, no. 21, pp. 9085–9095, 2015.

[14] C. Jiang, H. Wang, C. Xia et al., "A randomized, double-blind, placebo-controlled trial of probiotics to reduce the severity of oral mucositis induced by chemoradiotherapy for patients with nasopharyngeal carcinoma," *Cancer*, vol. 125, no. 7, pp. 1081–1090, 2019.

[15] C. S. Kim and D. M. Shin, "Probiotic food consumption is associated with lower severity and prevalence of depression: a nationwide cross-sectional study," *Nutrition*, vol. 63-64, pp. 169–174, 2019.

[16] P. W. J. Burnet and P. J. Cowen, "Psychobiotics highlight the pathways to happiness," *Biological Psychiatry*, vol. 74, no. 10, pp. 708-709, 2013.

[17] D. Gayathri and B. S. Rashmi, "Mechanism of development of depression and probiotics as adjuvant therapy for its prevention and management," *Mental Health & Prevention*, vol. 5, pp. 40–51, 2017.

[18] R. F. Slykerman, F. Hood, K. Wickens et al., "Effect of _Lactobacillus rhamnosus_ HN001 in Pregnancy on Postpartum Symptoms of Depression and Anxiety: A Randomised Double-blind Placebo-controlled Trial," *eBioMedicine*, vol. 24, pp. 159–165, 2017.

[19] L. Steenbergen, R. Sellaro, S. van Hemert, J. A. Bosch, and L. S. Colzato, "A randomized controlled trial to test the effect of multispecies probiotics on cognitive reactivity to sad mood," *Brain Behavior and Immunity*, vol. 48, pp. 258–264, 2015.

[20] G. Mahajan and L. Balachandran, "Antibacterial agents from actinomycetes - a review," *Frontiers in Bioscience*, vol. E4, no. 1, pp. 240–253, 2012.

[21] C. C. Jin, G. K. Lagoudas, C. Zhao et al., "Commensal microbiota promote lung cancer development via $\gamma\delta$ T cells," *Cell*, vol. 176, no. 5, pp. 998–1013.e16, 2019.

[22] C. A. Olson, H. E. Vuong, J. M. Yano, Q. Y. Liang, D. J. Nusbaum, and E. Y. Hsiao, "The gut microbiota mediates the anti-seizure effects of the ketogenic diet," *Cell*, vol. 173, no. 7, pp. 1728–1741.e13, 2018.

[23] V. Gopalakrishnan, B. A. Helmink, C. N. Spencer, A. Reuben, and J. A. Wargo, "The influence of the gut microbiome on cancer, immunity, and cancer immunotherapy," *Cancer Cell*, vol. 33, no. 4, pp. 570–580, 2018.

[24] T. T. Chen, P. Y. Tian, Z. X. Huang et al., "Engineered commensal bacteria prevent systemic inflammation-induced memory impairment and amyloidogenesis via producing GLP-1," *Applied Microbiology and Biotechnology*, vol. 102, no. 17, pp. 7565–7575, 2018.

[25] M. Yassour, M. Y. Lim, H. S. Yun et al., "Sub-clinical detection of gut microbial biomarkers of obesity and type 2 diabetes," *Genome Medicine*, vol. 8, no. 1, p. 17, 2016.

[26] G. L. Hold, "Gastrointestinal microbiota and colon cancer," *Digestive Diseases*, vol. 34, no. 3, pp. 244–250, 2016.

[27] K. C. Johnson-Henry, D. J. Mitchell, Y. Avitzur, E. Galindo-Mata, N. L. Jones, and P. M. Sherman, "Probiotics reduce bacterial colonization and gastric inflammation in H. pylori-infected mice," *Digestive Diseases and Sciences*, vol. 49, no. 7/8, pp. 1095–1102, 2004.

[28] S. H. Wong, L. Y. Zhao, X. Zhang et al., "Gavage of fecal samples from patients with colorectal cancer promotes intestinal carcinogenesis in germ-free and conventional